Charge transport in hybrid films of π-conjugated polymers and semiconductor nanocrystals

Elsa Couderc

UNIVERSITÉ DE GRENOBLE

Thèse

Pour obtenir le grade de

Docteur de l'Université de Grenoble

Spécialité : **Physique des matériaux**

Arrêté ministériel : 7 août 2006

Présentée par

Elsa Couderc

Thèse dirigée par **David Djurado**
et codirigée par **Peter Reiss**

préparée au sein **du Laboratoire d'Électronique Moléculaire, Organique et Hybride, INAC/SPrAM (UMR-5819)**
et de **l'Ecole Doctorale de Physique de Grenoble**

Charge transport in hybrid films of π-conjugated polymers and semiconductor nanocrystals

Thèse soutenue publiquement le ,
devant le jury composé de :

M. Jean-Louis Fave
Chargé de recherche CNRS, Université Pierre et Marie Curie, Rapporteur
M. Bernard Ratier
Professeur de l'Université de Limoges, Rapporteur
M. Daniel Bellet
Professeur de l'Institut National Polytechnique de Grenoble, Examinateur
M. Andreu Cabot
Professeur de l'Université de Barcelone, Examinateur
M. David Djurado
Directeur de recherche CNRS, CEA Grenoble, Directeur de thèse
M. Peter Reiss
Chercheur CEA, CEA Grenoble, Co-Directeur de thèse
M. Jérôme Faure-Vincent
Chercheur CEA, CEA Grenoble, Invité

Ainsi le monde est à l'intérieur de notre esprit,

lequel est à l'intérieur du monde.

Edgar Morin, ***Introduction à la pensée complexe,*** **1990**

Résumé de la thèse en français

Cette thèse porte sur l'étude de couches minces à base de polymères conjugués et de nanocristaux de semi-conducteurs, aussi appelées "hybrides". Ces matériaux composites à base de semiconducteurs absorbent et/ou émettent de la lumière à des longueurs d'ondes contrôlées et conduisent les charges électriques. Ils sont donc considérés pour des applications de bas coût en optoélectronique. Ainsi, des cellules solaires hybrides sont déjà réalisées, mais la compréhension des mécanisme de transport de charge dans ces matériaux est encore très limitée. Nous essayons dans cette thèse d'éclairer cette problématique grâce à des mesures de Temps-de-Vol, où l'on étudie les courants transitoires photo-générés.

Matériaux Dans le premier Chapitre, nous présentons les propriétés principales des nanocristaux de CdSe et du poly(3-hexylthiophène), le polymère conjugué utilisé, avant d'aborder les hétérojonctions hybrides.

Le CdSe massif est un semi-conducteur à gap direct (E_g=1.75 eV), stable sous deux formes cristalline: la structure cubique (zinc blende) et la structure hexagonale (wurtzite); les nanocristaux de CdSe existent également sous ces deux formes cristallines. Les nanocristaux de semiconducteurs sont de taille nanométrique (!) et présentent par conséquent des propriétés de confinement quantique: une bande interdite en énergie plus importante que celle du matériau massif, et des niveaux d'énergie discrets au sein des bandes de valences et de conduction. La variation de la largeur en énergie de la bande interdite avec la taille des nanocristaux de CdSe permet d'ajuster leurs spectres d'absorption et d'émission dans la gamme du visible en modifiant leur taille. Les propriétés optiques peuvent également refléter la présence de défauts structuraux ou chimiques dans les nanocristaux: en effet, certains défauts introduisent des niveaux d'énergie supplémentaires dans les distributions énergétiques et ils sont détectables par exemple grâce à des mesures de PL résolue en temps et/ou en température. De plus, une assemblée de nanocristaux présente une dispersion en taille (de l'ordre de 5 à 10 % pour les nanocristaux de CdSe), résultant en un "désordre énergétique", *i.e.* une dispersion de la distribution énergétique.

Les nanocristaux de CdSe peuvent être préparés par différentes méthodes. La synthèse chimique dite "organométallique" par injection à chaud permet d'obtenir des nanocristaux de tailles ajustables entre 2 et 8 nm avec des faibles polydispersités (5-10 %).De plus, lors de ce type de synthèse, les nanocristaux sont stabilisés en suspension grâce à la répulsion stérique entre de molécules organiques entourant les nanocristaux, appelées "ligands". Ces ligands contrôlent la vie des nanocristaux: synthèse, assemblage, propriétés optiques et électroniques, et propriétés de transport de charges.

Les polymères conjugués sont de longues chaînes carbonées dont les orbitales moléculaires π sont délocalisées le long de la chaîne. Ils peuvent être dopés chimiquement, comme le poly(acétylène) par exemple, et possèdent alors des conductivités importantes (prix Nobel de Chimie 2000 à A. Heeger, A. MacDiarmid et H. Shirakawa). En l'absence de dopage, ce sont des semi-conducteurs, comme le poly(3-hexylthiophene) (P3HT), que nous avons étudié lors de cette thèse. Ils présentent alors une bande interdite en énergie. Un échantillon de polymère conjugué est aussi caractérisée par les tailles de ses constituants (les longueurs des chaînes) et leur polydispersité, ce qui influence la distribution énergétique de l'assemblée. Les porteurs de charges, délocalisés, se couplent aux vibrations du réseau et forment des porteurs de charges spécifiques, appelés polarons et bipolarons dans le cas du P3HT. Sous forme solide, le P3HT présente de plus une structure semi-cristalline, composée de domaines amorphes et de domaines cristallins. Le taux de cristallinité et les directions d'empilement des chaînes peut être ajusté par le choix de poids moléculaires, de la régiorégularité et de la méthode de dépôt des couches minces: un dépôt lent et avec de faibles masses moléculaires conduisent à de plus grandes cristallinités. Enfin, le P3HT a tendance a former des structures supra-moléculaires de formes allongées, les "fibrilles". Selon l'orientation de l'empilement des chaînes, les propriétés de conduction des films de P3HT varient. Il a en effet été montré par des mesures en configuration transistor à effet de champ (field-effect transistor, FET), que la mobilité des porteurs de charges était plus grande dans la direction du π-stacking [1], voir la Fig. I.10 du chapitre I pour une explication graphique. En revanche, le transport de charge perpendiculairement au substrat, mesuré par la méthode de Temps-de-Vol (ou Time-of-Flight, TOF, en anglais), s'avère relativement insensible à la régiorégularité mais se détériore pour des masses moléculaires supérieures à 30-40 kDa [2].

Les hétérojonctions "hybrides" sont dans notre cas définies comme des mélanges en volume de polymère conjugué et de nanocristaux de semi-conducteurs. Elles sont fabriquées par le mélange des composants en solution. Pour réaliser des dispositifs générant du courant sous illumination (cellules solaires, photo-détecteurs), les composants sont choisis de façon à ce que l'alignement des niveaux énergétiques du donneur et de l'accepteur soit de type II, *i.e.* que les niveaux soient disposés en escalier (l'accepteur est la marche inférieure). Cet alignement favorise la dissociation des excitons à l'interface entre donneur et accepteur, même en l'absence de champ électrique appliqué. Cette interface est très importante puisqu'elle est le siège des dissociations, ainsi que celui des recombinaisons bimoléculaires.

Le domaine des cellules solaires hybrides est né en 1996 avec les travaux du groupe d'Alivisatos, à Berkeley [3]. Des nanocristaux de CdSe sphériques, de 4 nm et 5 nm de diamètre, étaient alors utilisés dans une matrice de MEH-PPV. Depuis, la morphologie de l'interface entre donneur et accepteur a été modulée par l'utilisation de nanostructures inorganiques anisotropes (nanobâtonnets, nano-tétrapodes) [4] et la cristallisation spécifique de la phase polymère [5, 6]. Les meilleurs rendements obtenus actuellement sont de 4.1 % pour des fibrilles de P3HT combinées avec des nanocristaux sphériques de CdS (août 2011, [7]).

Les processus physiques ayant lieu dans la couche active hybride influençant le photo-courant récolté sont les suivants: l'absorption et la formation d'excitons, la dissociation des excitons, la diffusion et la dérive des porteurs de charges, les recombinaisons des porteurs de charges. Ces différents mécanismes sont étudiés dans les hybrides et nous avons publié une revue sur le sujet [8]. La formation d'excitons peut être étudiée par des mesures d'absorption photo-induite, et l'évolution de la population excitonique par cette même technique, en variant la fréquence d'excitation ou par des mesures de photoluminescence résolues en temps. La formation de polarons positifs sur le polymère a été observée par résonance paramagnétique électronique sous illumination, mais aucune trace de leur compagnons négatifs sur les nanocristaux n'a pour l'instant été descellée. Des mesures électriques ont mis en évidence de fortes hystérèses dans les caractéristiques courant-tension, qui sont attribuées à la charge des nanocristaux. Enfin, des mesures en configuration FET ont montré des mobilités dominées par les trous et similaires à celles mesurées dans les polymères seuls. Enfin, les recombinaisons sont importantes dans les hybrides, mono-moléculaires pour de basses intensités lumineuse et bi-moléculaires pour de plus fortes intensités lumineuses.

Nous présentons ensuite nos techniques de préparation des échantillons et leurs caractérisations.

La synthèse organométallique de nanocristaux de CdSe a été réalisée à l'échelle du gramme par injection à chaud du précurseur de Se dans un bain contenant solvant, ligands, et le précurseur de Cd, suivant le protocole développé au laboratoire par M. Protière [9]. En variant la température de synthèse, nous avons pu obtenir des nanocristaux de différentes formes: sphériques (250°C), et branchés (230°C). La taille des nanocristaux sphériques peut être ajustée en variant les quantités relatives des précurseurs, ligands et solvants. Dans la suite de notre étude, nous utilisons des nanocristaux sphériques de structure cristalline hexagonale wurtzite (déterminée par diffraction des rayons X), de tailles entre 4 et 7 nm, et émettant entre 620 et 650 nm. Les structures branchées sont un mélange de bipodes, tripodes et tétrapodes, avec des bras de dimensions caractéristiques de 3.8 nm dans la largeur et 6.3 nm dans la longueur (microscopie électronique à transmission). Elles présentent majoritairement la structure hexagonale wurtzite et probablement également la structure cubique zinc blende, et émettent autour de 650 nm.

Le dépôt sous forme de couches minces des nanocristaux a été étudié. Le dépôt à la tournette

permet d'obtenir de films minces, dont l'épaisseur dépend de la concentration de la solution utilisée, homogènes à l'échelle du cm^2 et conformes au substrat. Le dépôt de goutte, suivie d'une évaporation lente, permet de réaliser des films épais (1 μm). Enfin, le dépôt à la raclette permet de réaliser des films d'épaisseurs intermédiaire et relativement homogènes. Les films de nanocristaux présentent couramment des trous ou des craquelures, qui peuvent être comblés par le dépôt successif de deux couches de nanocristaux. Nous avons aussi étudié la formation de couches ultra-minces (inférieures à la monocouche) en fonction du substrat et de traitement de surface du substrat. La rugosité intrinsèque des substrats d'ITO, du même ordre de grandeur que la taille des nanocristaux, domine la répartition de ceux-ci; en revanche, sur des substrats de SiO_2, il est possible d'obtenir une répartition homogène et assez dense (toujours inférieure à la monocouche) en traitant le substrat avec du mercaptopropyltriethoxysilane.

La surface des nanocristaux a été modifiée par échange des ligands de synthèse (acide stéarique, oléylamine), portant de longues chaînes alkyles isolantes, pour de petites molécules qui permettent d'augmenter le couplage électronique entre nanocristaux. En solution, le nouveau ligand est la pyridine. L'échange de ligands provoque une perte de solubilité des nanocristaux dans les solvants auparavant adaptés (hexane, chloroforme), un décalage hypsochromique du premier pic excitonique d'absorption, l'atténuation de la photoluminescence et en spectroscopie infrarouge, l'apparition de pics de vibrations caractéristique d'un composé aromatique, simultanément à la décroissance des pics des chaînes alkyles. L'échange de ligands a également été réalisé sur des films de nanocristaux (en phase solide) pour permettre l'utilisation de plusieurs petites molécules rendant les nanocristaux difficiles à redisperser en solution. Cette étude a été réalisée en collaboration avec A. Lefrançois, en thèse au laboratoire. Les procédures d'échange ont été optimisées pour chaque molécule par des études de spectroscopie infrarouge. L'échange de ligand mène à une diminution de la distance moyenne entre particules, déterminée par rayons X (les surfaces des nanocristaux de 4.1 nm sont espacées de 1.8 nm avant échange et de 0.4 nm après un échange avec l'éthanedithiol). Enfin, le décalage du premier pic d'absorption et une étude électrochimique ont permis de démontrer l'influence des nouveaux ligands sur les niveaux électroniques des nanocristaux: le niveau HOMO, initialement situé à -5.67 eV pour des nanocristaux sphériques de 4.1 nm avec leur ligands de synthèse, est décalé vers des énergies moins profondes pour toutes les molécules utilisées; le décalage est au maximum de +160 meV pour l'éthanedithiol. En revanche, le gap optique augmente ou diminue selon le ligand (il baisse de 10 meV pour l'éthanedithiol et le benzènedithiol et augmente de 20 meV pour la pyridine et la phénylènediamine). Ces résultats sur l'échange de ligands après le dépôt ont été publiés [10].

Nous tentons de comprendre ces modifications énergétiques dans le cadre du changement de l'environnement diélectrique des nanocristaux avec un modèle de constante diélectrique effective. Comme dans [11], nous montrons que les décalages observés ne peuvent être reproduits par ces calculs simples utilisant les constantes diélectriques des ligands *en solution*. Il est fort probable que ces constantes changent lorsque les nanocristaux sont greffés à la surface des nanocristaux, mais ces valeurs n'existent pas à notre connaissance dans la littérature. De plus, des effets de

délocalisation accrue ou diminuée des fonctions d'ondes électroniques sont envisageables mais ne sont pas pris en compte par ce modèle.

Nous utilisons deux types de P3HT: l'un provient de Sigma-Aldrich, est caractérisé par une grande polydispersité (D=3.75), de faibles masses moléculaires (M_n=9.8 kDa) et un faible taux de régiorégularité (91 %) et est appelé "P3HT1". Il est utilisé tel quel. L'autre échantillon provient de Merck et a été soumis à une fractionnation par Soxhlet. La fraction chloroforme contient les plus grandes chaînes et est nommée "P3HT2". Elle possède un indice de polydispersité réduit (D=1.63), des masses moléculaires moyennes (M_n=28.5 kDa), un taux de régiorégularité plus élevé (95.9 %) que le P3HT1.

Nous avons étudié le dépôt de couches minces de P3HT à la tournette et par évaporation lente en fonction du solvant. Les films sont polycristallins, comme le montrent des études de diffraction des rayons X. Le taux de cristallinité est plus important pour les films déposés par évaporation lente à partir d'*ortho*-dichlorobenzène (ODCB) que pour ceux déposés à partir du chloroforme, et les cristallites font alors environ 14 nm. De plus, en considérant que les films peuvent être modélisés par des agrégats H, des études optiques d'absorbance et de photoluminescence permettent de quantifier le couplage inter-moléculaire, de l'ordre de 25 meV pour le film déposé à la tournette à partir de l'ODCB; ainsi que la largeur de la distribution énergétique, de l'ordre de 50 meV pour ce même film.

Enfin, des hétérojonctions hybrides sont fabriquées. En solution, l'atténuation de la photoluminescence du P3HT montre l'occurrence d'un transfert de charge entre le donneur et l'accepteur (la photoluminescence des nanocristaux est plus difficile à détecter car elle est moins intense et superposée à celle du P3HT). Cette atténuation augmente avec le contenu en nanocristaux et est plus importante pour des nanocristaux échangés pyridine que pour les nanocristaux avec leurs ligands de synthèse, témoin d'un couplage électronique accru.

Le dépôt de couches minces hybrides est effectué par trempage, par dépôt à la tournette ou par évaporation lente. La méthode de dépôt couche-par-couche par trempage nécessite l'utilisation de composants spécifiques avec des solvants "orthogonaux", afin de ne pas redisperser les couches déposées auparavant. Nous avons utilisé le système hybride à reconnaissance moléculaire développé au laboratoire par J. De Girolamo [12]. Les hybrides ainsi formés ont des épaisseurs très bien contrôlées (dépôt inférieur à une monocouche à chaque cycle) et présentent la caractéristique intéressante que le P3HT garde un spectre d'absorption très peu décalé vers le rouge, typique de la phase liquide. Les couches déposées à la tournette sont homogènes, autour de 100 nm d'épaisseur. Les couches déposées par évaporation lente sont épaisses, >1 μm, et la dispersion des nanocristaux observées au microscope électronique à balayage y est homogène. Enfin, la cristallinité du P3HT est diminuée par l'ajout de nanocristaux. Les nanocristaux avec ligands pyridine aident à conserver la cristallinité du P3HT pour de plus grandes fractions volumiques que les nanocristaux avec ligands de synthèse.

Mesures de Temps-de-Vol sur des couches hybrides Les matériaux désordonnés présentent des porteurs de charges localisés (interruption de la conjugaison par des défauts pour les polymères conjugués, confinement quantique pour les nanocristaux, localisation faible due au désordre). Ceux-ci se déplacent par sauts, d'un site de localisation à l'autre, en fonction des intégrales de transfert électronique entre sites et des couplages électron-phonon. Ces couplages étant distribués, les porteurs restent plus ou moins longtemps sur un site et le transport est dispersif. Des simulations Monte Carlo ont permis de déterminer une expression de la mobilité en fonction des largeurs de désordres énergétiques et positionnels gaussiens, c'est le modèle de désordre gaussien (GDM en anglais).

Une mesure électrique de Temps-de-Vol (abrégée TOF, pour 'Time of Flight' en anglais) consiste à photo-générer des charges avec une excitation laser rapide (de l'ordre de la nanoseconde), dans une couche d'épaisseur négligeable du film, et de mesurer le courant électrique en sortie dû à la dérive-diffusion du feuillet de charges photo-générées. La brusque baisse du courant marque l'arrivée du feuillet à l'électrode de collecte et permet de calculer la mobilité $\mu_{TOF} = L^2/V.t_{tr}$. t_{tr} est le "temps de transit", c'est-à-dire l'instant de baisse de courant; V est la tension appliquée et L est l'épaisseur de l'échantillon. L'étalement dans le temps du courant est une indication de la dispersivité du feuillet de charge: les phénomènes de diffusion et de relaxation énergétique élargissent le feuillet.

La mobilité des trous dans le P3HT a été étudiée par la méthode de Temps-de-Vol depuis la fin des années 1990 [2, 13–23]. La mobilité est de l'ordre de 5 $.10^{-5} cm^2/Vs$ à $10^{-3} cm^2/Vs$. Elle décroît quand le champ électrique augmente à température ambiante. Ce phénomène est expliqué dans le modèle de désordre gaussien par la présence d'un fort désordre énergétique: à bas champ, les charges sont susceptibles de contourner les obstacles en allant à l'encontre du champ, ce qui n'est plus possible pour des champs forts car c'est trop coûteux énergétiquement.

Enfin, la mobilité des porteurs de charges a été étudiée dans des matériaux hybrides à base de P3HT et de nanobâtonnets de TiO_2 [24, 25] ainsi que dans des hybrides à base de poly(vinylcarbazole) (PVK) et de nanocristaux sphériques de CdS [26]. Dans ces deux études, il est rapporté que la mobilités des trous est améliorée pour de faibles fractions volumiques de nanocristaux (jusqu'à 20 vol% dans le premier cas, et jusqu'à 1 vol%, la fraction maximale étudiée, dans le second). Au delà, la mobilité des trous est détériorée par la présence des nanocristaux.

Dans la partie expérimentale, nous montrons que les films hybrides P3HT:nanocristaux de CdSe, dont l'épaisseur est supérieure à 10 fois la profondeur de pénétration d'une excitation lumineuse à 532 nm (soit 5 μm pour un film hybride contenant 83 % de nanocristaux en poids, soit 49 % en volume), sont adaptés aux mesures de Temps-de-Vol à cette longueur d'onde d'excitation. Ils remplissent en effet les contraintes d'épaisseur optique, de capacitance et de contacts bloquants. Les courants transitoires de trous et d'électrons photo-générés ont été mesurés en changeant le côté d'illumination (Al pour les trous, ITO pour les électrons).

Ils présentent des temps de transit de l'ordre de 10^{-6} s à 10^{-5} s. Nous avons aussi estimé l'incertitude de détermination de la mobilité μ_{TOF}, autour de 10-20 % pour les échantillons hybrides, à partir de celles du temps de transit par la méthode des tangentes, et de l'épaisseur du film, à cause de sa rugosité.

Nous montrons ensuite que l'allure des photo-courants transitoires électroniques dépend de l'intensité lumineuse: la mobilité elle-même n'en dépend pas mais la densité de charge dépend à la fois de l'intensité lumineuse et de la tension appliquée. Cette dépendance par rapport à la tension appliquée peut venir de différents phénomènes dépendants de la tension: la dissociation des excitons, les mécanismes de recombinaison et le piégeage de charge.

Nous étudions la mobilité des trous dans les deux types de P3HT. Les deux échantillons présentent des mobilités décroissantes lorsque le champ électrique augmente. Dans le cadre du modèle de désordre gaussien, nous montrons que l'échantillon présentant la plus grande polydispersité (P3HT1) présente aussi le désordre énergétique le plus grand. Le P3HT1 présente également des mobilités supérieurs à celles du P3HT2, ainsi qu'un désordre positionnel plus faible que le P3HT2, ce qui peut être lié à une taille de cristallites légèrement plus grandes.

Dans les échantillons hybrides basé sur le P3HT1 (non fractionné), la mobilité des trous est plus faible que dans le P3HT1 seul. Dans les échantillons hybrides basés sur le P3HT2, la mobilité dépend de la forme et des ligands des nanocristaux utilisés: elle augmente généralement pour le plus faible volume étudié de nanocristaux (16 %) puis décroît pour des fractions volumiques plus importante, jusqu'à 49 %, la fraction la plus importante étudiée. Nous relions cet effet à un confinement de la phase organique: les nanocristaux empêcheraient les trous d'errer dans des zones de mobilités réduites, comme par exemple les zones amorphes. Pour des fractions volumiques plus importantes de nanocristaux, la perturbation de la cristallinité du polymère est importante et le transport de charge devient moins efficace. La modification de la cristallinité du P3HT dépend de la forme et des ligands des nanocristaux. En effet, les hybrides à cristallisation lente composés de nanocristaux branchées présentent des mobilités plus faibles, tout particulièrement quand ils sont traités avec de la pyridine, ce qui correspondrait à une perturbation de la cristallinité du P3HT plus grande que pour des nanocristaux sphériques ou les ligands de synthèse.

Les mobilités des électrons sont améliorées par la présence des nanocristaux, en accord avec l'idée de formation d'un réseau percolant. Pour les électrons également, la fraction de nanocristaux nécessaire pour obtenir un transport de charge efficace dépend de leur forme et de leur ligands: la fraction critique est plus petite pour les structure branchées que pour les sphères quand les nanocristaux sont recouverts des ligands de synthèse, et pour des champs électriques faibles. Ceci tient à leur anisotropie, qui facilite la percolation. Les mobilités plus faibles mesurées pour les structures branchées traitées avec de la pyridine pourraient découler de l'agrégation des nanocristaux, spontanée à la suite de l'échange de ligands, ou à cause des contraintes liées à la cristallisation du P3HT. Une agrégation mènerait à la dispersion non-aléatoire des nanocristaux et donc relèverait le seuil de percolation.

Nous déterminons la fraction optimale pour les transport de trous et d'électrons à 75 % en poids de nanocristaux (soit 36 % en volume), pour des hybrides composés de P3HT2 et de nanocristaux sphériques avec leurs ligands de synthèse. Pour cette fraction, les électrons comme les trous ont atteint leurs mobilités maximales, un ordre de grandeur supérieure à la mobilité dans le P3HT seul à bas champ. De plus, les mobilités des électrons et des trous sont équilibrées.

Enfin, nous concluons cette partie de mesures de Temps-de-Vol en soulignant les différences entre les cellules solaires hybrides et les échantillons de Temps-de-Vol. Leurs épaisseurs respectives impliquent que l'on sonde davantage de défauts et de pièges lors des mesures de Temps-de-Vol. De plus, les procédés de fabrication de échantillons diffèrent (évaporation lente dans un cas, dépôt rapide à la tournette dans l'autre) et mènent à des degrés de cristallinité variés. La dispersion des nanocristaux dans les deux types d'échantillons peut être différente également. Ces paramètres impliquent des différences de comportements entre échantillons de Temps-de-Vol et cellules solaires, dans le transport de charge, mais aussi dans la génération et la dissociation des excitons, ainsi que dans les mécanismes de recombinaisons.

Simulations Monte-Carlo des expériences de Temps-de-Vol La formalisation du transport par sauts grâce à une équation-maîtresse est présentée en introduction. Une résolution numérique couramment utilisée est la méthode dite de Monte Carlo, qui considère des distributions de probabilités et opère des tirages aléatoires pour générer les charges et les déplacer. Cette procédure permet de mimer le moyennage thermique dans des systèmes matériels. Afin de résoudre l'équation-maîtresse d'évolution du système, la connaissance de différents paramètres est nécessaire. Dans notre cas, il s'agit des expressions des probabilités de sauts, dépendant de la distribution énergétique des sites, des intégrales de transfert électronique et du couplage électron-phonon.

La simulation du transport dans des matériaux organiques avec cette méthode a déjà été utilisé (voir par exemple [27–33] pour des simulations avec la théorie de Marcus pour les fréquences de saut), mais pas pour le P3HT, ni pour les hétérojonctions hybrides. Lors d'un stage de douze semaines à l'Université de Denver dans le groupe de S. Shaheen, j'ai pu apprendre à utiliser un code Monte Carlo pour le transport dans des matériaux organiques, déterminer les paramètres adéquats à la simulation du transport de trous dans le P3HT, puis je l'ai adapté à des hétérojonctions.

Le principe de la simulation est de fabriquer un réseau cubique représentant l'échantillon, et d'attribuer à chaque intersection du réseau, ou "site", une valeur d'énergie de la distribution énergétique définissant la couche active. Ensuite, des porteurs de charges sont générés suivant une distribution de photo-génération, qui prend en compte d'une part la profondeur d'absorption de l'excitation lumineuse, d'autre part la longueur de diffusion des excitons. On créé une file d'attente de porteur de charges: la charge ayant la plus forte probabilité moyenne de saut vers un site premier voisin est la première à se déplacer (sa probabilité moyenne de saut dépend de

l'énergie du site où elle se trouve et de ses voisins, ainsi que de l'occupation des sites voisins). Elle est ensuite replacée dans la file d'attente suivant sa nouvelle probabilité de saut. Les charges se déplacent ainsi une à une et le courant résultant du déplacement des charges est calculé à chaque pas de temps. Lorsqu'une charge arrive à l'électrode, elle est retirée de la course; dans les deux autres directions d'espace, des conditions aux limites périodiques sont appliquées.

Tout d'abord, les différents paramètres de descriptions des matériaux, des expériences, et de nos modèles de sauts sont évalués, grâce à des caractérisations expérimentales (profondeur d'absorption, taille des sites–longueur de délocalisation, etc.) et à des indices de la littérature (distributions énergétiques, ordres de grandeurs des intégrales de transfert électronique et du couplage électron-phonon).

Nous montrons que les distributions énergétiques déterminent la forme des courants transitoires. Pour le P3HT, la distribution énergétique obtenue par dynamique moléculaire par McMahon et Troisi [31] permet de simuler nos courbes expérimentales. Nous utilisons deux types de fréquences de sauts, les sauts activés thermiquement et les sauts de Marcus (ces derniers faisant intervenir un couplage important aux phonons). Les sauts de Marcus permettent de mieux simuler les courbes expérimentales obtenues dans du P3HT1. Les meilleurs courbes simulées sont obtenues grâce à une intégrale de transfert de 10 meV et des énergies de réorganisation (couplages électron-phonon) entre 200 meV et 590 meV selon la tension appliquée. Cette variation des paramètres, nécessaire à l'ajustement des courbes simulées aux courbes expérimentales, peut refléter les approximations de notre modèle numérique, notamment l'absence de corrélations entre les valeurs d'énergie de sites voisins, l'isotropie et l'homogénéité de la couche active et le transport par saut vers les premiers voisins seulement.

Enfin, nous montrons que le transport des trous dans une hétérojonction hybride, composée de P3HT1 et de 16 vol% de nanocristaux sphériques de CdSe avec leur ligands de synthèse, est simulé en considérant que les trous se déplacent dans la phase organique, dont les paramètres ont été définis par les simulations dans les P3HT1 seul, et qu'il leur est extrêmement difficile d'aller sur les nanocristaux.

Nous n'avons pas simulé le P3HT2 et les hybrides fabriqués avec ce P3HT car les simulations n'incluent pas encore d'inhomogénéité de la structure cristalline, qui devraient se traduire par des corrélations spatiales des énergies des sites et des intégrales de transfert.

Des travaux théoriques et expérimentaux parallèles, explorant les phénomènes physiques à différentes échelles de temps et d'espace, devraient permettre de définir plus précisément les paramètres de simulations, notamment en ce qui concerne les anisotropies des couplages électron-électron et électron-phonon. Ces paramètres vont dépendre des conditions de fabrication des échantillons.

En conclusion, nous avons préparé et caractérisé des hétérojonctions hybrides à base de CdSe et de P3HT, en particulier par la technique de Temps-de-Vol. Nous avons montré que le transport de charge est optimal pour une fraction de nanocristaux dans l'hybride, qui dépend

de la nature des nanocristaux (forme, ligands) et de la nature de la matrice organique. De façon à étudier des échantillons identiques à ceux utilisés en applications photovoltaïques, il serait intéressant de se pencher sur la technique d'extraction de courant par rampe de tension (en anglais 'current extraction by linearly increased voltage', CELIV). Enfin, des simulations Monte-Carlo du transport de trous dans les hybrides ont montré que le transport peut être modelisé par un passage seulement dans la phase organique; il serait pertinent d'implémenter des corrélations spatiales pour introduire la notion d'anisotropie dans le transport des trous. Le transport des électrons à travers le réseau de nanocristaux pourrait être simulé également.

Références bibliographiques

[1] H. Sirringhaus, P. J. Brown, R. H. Friend, M. M. Nielsen, K. Bechgaard, B. M. W. Langeveld-Voss, A. J. H. Spiering, Rene A. J. Janssen, E. W. Meijer, P. Herwig, and D. M. De Leeuw. *Two-dimensional charge transport in conjugated polymers.* Nature **401**, 685 (1999).

[2] A. M. Ballantyne, L. Chen, J. Dane, T. Hammant, F. M. Braun, M. Heeney, W. Duffy, I. McCulloch, D. C. B. Donal, and J. Nelson. *The effect of poly(3-hexylthiophene) molecular weight on charge transport and the performance of polymer:fullerene solar cells.* Adv. Funct. Mater. **18**(16), 2373 (2008).

[3] N. C. Greenham, X. Peng, and A. P. Alivisatos. *Charge separation and transport in conjugated-polymer/semiconductor-nanocrystal composites studied by photoluminescence quenching and photoconductivity.* Phys. Rev. B **54**(24), 17628 (1996).

[4] S. Dayal, M. O. Reese, A. J. Ferguson, D. S. Ginley, G. Rumbles, and N. Kopidakis. *The Effect of Nanoparticle Shape on the Photocarrier Dynamics and Photovoltaic Device Performance of Poly(3-hexylthiophene):CdSe Nanoparticle Bulk Heterojunction Solar Cells.* Adv. Funct. Mater. **20**(16), 2629 (2010).

[5] Solenn Berson. *Synthèse, caractérisation et nanostructuration de dérivés du polythiophène pour des applications en cellules photovoltaïques organiques.* PhD dissertation, Université Joseph Fourier (2007).

[6] L. Hartmann, K. Tremel, S. Uttiya, E. Crossland, S. Ludwigs, N. Kayunkid, C. Vergnat, and M. Brinkmann. *2D versus 3D crystalline order in thin films of regioregular poly(3-hexylthiophene) oriented by mechanical rubbing and epitaxy.* Adv. Funct. Mater. page to be announced! (2011).

[7] S. Ren, L-Y. Chang, S-K. Lim, J. Zhao, M. Smith, N. Zhao, V. Bulovic, M. G. Bawendi, and S. Gradečak. *Inorganic-organic hybrid solar cell: bridging quantum dots to conjugated polymer nanowires.* Nano Lett. **11**, 3998 (2011).

[8] P. Reiss, E. Couderc, J. De Girolamo, and A Pron. *Conjugated polymers/semiconductor nanocrystals hybrid materials–preparation, electrical transport properties and applications.* Nanoscale **3**(2), 446 (2011).

[9] Myriam Protière. *Synthèse de nanocristaux fluorescents de semi-conducteurs II-VI et III-V. Augmentation de l'échelle de synthèse.* PhD dissertation, Université Joseph Fourier (2007).

[10] A. Lefrançois, E. Couderc, J. Faure-Vincent, S. Sadki, A. Pron, and P. Reiss. *Effect of the treatment with (di-)amines and dithiols on the spectroscopic, electrochemical and electrical properties of CdSe nanocrystals' thin films.* J. Mater. Chem. **21**, 11524 (2011).

[11] A. Wolcott, V. Doyeux, C. A. Nelson, Gearba R., K. W. Lei, K. G. Yager, A. D. Dolocan, K. Williams, D. Nguyen, and X-Y. Zhu. *Anomalously large polarization effect responsible for excitonic red shifts in pbse quantum dot solids.* J. Phys. Chem. Lett. **2**, 795 (2011).

[12] Julia De Girolamo. *Architectures hybrides auto-assemblées à base de systèmes polyconjugués et de nanocristaux de semi-conducteurs pour le photovoltaïque plastique.* PhD dissertation, Université Joseph Fourier (2007).

[13] A. J. Mozer and N. S. Sariciftci. *Negative electric field dependence of charge carrier drift mobility in conjugated, semiconducting polymers.* Chemical Physics Letters **389**(4-6), 438 (2004).

[14] A. J. Mozer, N. S. Sariciftci, L. Lutsen, D. Vanderzande, R. Österbacka, M. Westerling, and G. Juška. *Charge transport and recombination in bulk heterojunction solar cells studied by the photoinduced charge extraction in linearly increasing voltage technique.* Appl. Phys. Lett. **86**(11), 112104 (2005).

[15] K. Kaneto, K. Hatae, S. Nagamatsu, W. Takashima, A. Pandey, K. Endo, and M. Rikukawa. *Photocarrier rmobility in regioregular P3HT studied by the TOF method.* Jpn J. Appl. Phys. **38**, L1188 (1999).

[16] S. S. P Pandey, W. T. Takashima, S. Nagamatsu, T. E. Endo, Rikukawa M., and K. Kaneto. *Regioregularity vs regiorandomness : effect on photocarrier transport in poly(3-hexylthiophene).* Jpn J. Appl. Phys. **39**(2), 94 (2000).

[17] S. Nagamatsu, S. S. Pandey, W. Takashima, T. Endo, M. Rikukawa, and K. Kaneto. *Photocarrier transport in processable P3AT.* Synthetic Metals **121**, 1563 (2001).

[18] W. Takashima, S. Nagamatsu, S. S. Pandey, T. Endo, Y. Yoshida, N. Tanigaki, M. Rikukawa, S. Yase, and K. Kaneto. *Dispersivity of carrier transport related with molecular arrangement in regioregular poly(3-alkylthiophene).* Synthetic Metals **119**, 563 (2001).

[19] G. Juška, K. Genevičius, K. Arlauskas, R. Österbacka, and H. Stubb. *Charge transport at low electric fields in π-conjugated polymers.* Phys. Rev. B **65**(23), 1 (2002).

[20] S. A. Choulis, Y. Kim, J. Nelson, D. D. C. Bradley, M. Giles, M. Shkunov, and I. McCulloch. *High ambipolar and balanced carrier mobility in regioregular P3HT.* Appl. Phys. Lett. **85**(17), 3890 (2004).

[21] V. Kazukauskas, M. Pranaitis, L. Sicot, and F. Kajzar. *Negative mobility dependence in different regioregular polythiophenes revealed by the charge extraction by linearly increased voltage.* Mol. Cryst. Liq. Cryst. **447**, 141 (2006).

[22] K. Yang, Y. Wang, A. Jain, L. Samulson, and J. Kumar. *Determination of electron and hole mobility of regioregular poly(3-hexylthiophene) by the Time of Flight method.* Journal of Macromolecular Science, Part A **44**(12), 1261 (2007).

[23] R. Mauer, M. Kastler, and F. Laquai. *The impact of polymer regioregularity on charge transport and efficiency of P3HT:PCBM photovoltaic devices.* Adv. Funct. Mater. **20**(13), 2085 (2010).

[24] Chang C-H., Huang T-K., Lin Y-T., Lin Y-Y., Chen C-W., Chu T-H., and W-F. Su. *Improved charge separation and transport efficiency in P3HT-TiO2 nanorod bulk heterojunction solar cells.* J. Mater. Chem. **18**, 2201 (2008).

[25] Li S-S., C-P. Chang, Lin C-C., Lin Y-Y., Chang C-H., Yang J-R., Chu M-W., and Chen C-W. *Interplay of three dimensional morphologies and photocarrier dynamics of polymer/TiO2 bulk heterojunction solar cells.* JACS **133**, 11614 (2011).

[26] K. R. Choudhury, J. G. Winiarz, M. Samoc, and P. N. Prasad. *Charge carrier mobility in an organic-inorganic hybrid nanocomposite.* Appl. Phys. Lett. **82**(3), 406 (2003).

[27] J. Nelson, J. Kirkpatrick, and P. Ravirajan. *Factors limiting the efficiency of molecular photovoltaic devices.* Phys. Rev. B **69**, 035337 (2004).

[28] A. J. Chatten, S. M. Tuladhar, S. A. Choulis, D. D. C. Bradley, and J. Nelson. *Monte Carlo modelling of hole transport in MDMO-PPV: PCBM blends.* Journal of Materials Science **40**(6), 1393 (2005).

[29] J. M. Frost, F. Cheynis, S. M. Tuladhar, and J. Nelson. *Influence of polymer-blend morphology on charge transport and photocurrent generation in donor-acceptor polymer blends.* Nano Lett. **6**(8), 1674 (2006).

[30] J. Nelson, J. J. Kwiatkowski, J. Kirkpatrick, and J. M. Frost. *Modeling charge transport in organic photovoltaic materials: introduction.* Accounts of Chemical Research **42**(11) (2009).

[31] P.D. McMahon and A. Troisi. *Organic semiconductors: impact of disorder at different timescales.* Chem. Phys. Chem. **11**, 2067 (2010).

[32] A. A. Kocherzhenko, F. C. Grozema, S. A. Vyrko, N. A. Poklonski, and L. D. A. Siebbeles. *Simulation of hopping transport based on charge carrier localization times derived for a two-level system.* J. Phys. Chem. C **114**, 20424 (2010).

[33] V. Stehr, J. Pfister, R. F. Fink, B. Engels, and C. Deibel. *First-principles calculations of anisotropic charge-carrier mobilities in organic semiconductor crystals.* Phys. Rev. B **83**(15), 155208 (2011).

Contents

Introduction and motivations

The twentieth century has left us a world of knowledge and of challenges. In natural sciences, great explorations, great discoveries have been made. New observations and analysis techniques were developed, opening an understanding of the world of atoms and molecules. This has eventually led to ever increasing progresses in all fields of technology, described in microelectronics by Moore's law, and most importantly gave birth to our all-technological 21st century. To provide these progresses to the greatest number, efforts are made to cut down the costs of electronic devices and of clean energy supplies, and in particular the energy costs.

One way to do this is to relax the constraints of performance (miniaturization, switching speed, efficiency) and focus on the materials used and their processibilities. Organic materials and colloids are handled in solution, allowing quick and low cost printing of large quantities of simple electronic circuits.

Organic electronics relies on the use of organic compounds exhibiting semi-conducting character for the realization of circuits elements such as field-effect transistors (FET), light-emiting devices (LED), memory devices, etc. Indeed, π-conjugated compounds, *i.e.* organic molecules showing an alternation of single and double bonds, exhibit delocalized charge carriers at the molecular scale. Chemical doping of conjugated polymers enhances their electrical conductivities: doped poly(acetylene) was the first in the spotlight in 1977, which led in 2000 to the award of the chemistry Nobel prize to A. Heeger, A. MacDiarmid and H. Shirakawa. It was later shown that conjugated polymers in their undoped state exhibit semiconducting properties: polythiophene-based field-effect transitors were realized in 1987 [1], poly(*para*-phenylenevinylene) (PPV) was used in 1990 to make light-emitting devices [2] and finally photoinduced charge transfer, a key concept of organic solar cells, was demonstrated between poly[2-methoxy-5-(2'-ethylhexyloxy)-p-phenylenevinylene] (MEH-PPV) and C_{60} in 1992 [3].

While some nanoparticles are produced in natural combustion of organic materials and others were fabricated in vitreous matrices for their optical properties already in the Middle Ages, the relation between their size and their properties has first been foreseen by Faraday in

1856. Science of colloids grew up at the beginning of the twentieth century, notably with the works and Nobel Prizes of Ostwald and Zsigmondy in 1909 and 1925, among others. In the 90's, the preparation of colloidal semiconductor nanocrystals was achieved, leading to their first technological use and commercialization in 2002. Quantum dots consisting of an inorganic core can be seen as tiny crystals or as giant molecules: they exhibit easily tunable discrete emission spectra and continuous absorptions for energies above their band gap. These optical properties respectively won their use in light-emiting devices [4], and triggered research on photovoltaic devices implying nanocrystals blended with conjugated polymers, also known as hybrid solar cells [5], and later on, on devices based solely on quantum-dots [6]. On the other hand, the 3D confinement of charge carriers is intrinsically in opposition to band transport; charge transport occurs *via* hopping and thus depends on wave function overlaps between nanocrystals. Surface ligand engineering aims at modulating these overlaps for different applications.

At the crossroad of organic electronics and semiconductor nanocrystals science, the field of hybrid optoelectronics tries to take advantage of the properties of both components. In the case of hybrid solar cells, first proposed in 1996 by Alivisatos group at UC Berkeley [5], the film-forming and charge transport properties of conjugated polymers and the optical characteristics of semiconductor nanocrystals are exploited. Performances of such devices have increased from 2.6 % [7] to 4.1 % [8] in the last five years and the exploration of the physical phenomena occurring inside the active layer, from the absorption of photons to the extraction of charge carriers, has also started. Processes involving the interface between the donor (polymer) and the acceptor (nanocrystals), such as exciton dissociation, recombinations, as well as effects related to the mechanisms of charge transport, could be the limiting factors in hybrid solar cells, and thus raise particular attention. The work presented in this thesis, at the interface of chemistry, physics and materials sciences, contributes to a better understanding of charge transport in hybrid materials made of conjugated polymers and semiconductor nanocrystals.

In Part I, we introduce the salient properties of both components and of hybrids. We describe nanocrystals preparation in solution and their deposition; we explore the impact of surface ligands on the properties of dense assemblies of nanocrystals. We study different processing methods of P3HT thin films on the basis of optical and morphological studies. Drop-casting will be used for the realization of micrometer thick films apprpriate for electrical Time-of-Flight (TOF) characterizations. Hybrid films are deposited in the same manner and we investigate the structural properties of the P3HT matrix in the presence of nanocrystals by X-ray diffraction.

In Part II, charge transport in disordered materials and its characterization by TOF experiments are presented. We study hybrid films with TOF measurements for different compositions of the films and show that mobilities of charge carriers in hybrid films depend on the nature of both the matrix and the inclusions. We conclude this part by underlining the differences between solar cell devices and our TOF samples.

Finally, Part III is dedicated to Monte-Carlo simulations of hole transport in P3HT and hybrid materials. Within state of the art knowledge of the P3HT density-of-states, of transfer

integrals and of electron-phonon coupling, we discuss the influence of these parameters on simulated transients. We describe the best fits of TOF experimental curves both for P3HT and for hybrid samples, where hole transport is successfully simulated by considering nanocrystals as voids in the P3HT matrix.

We conclude this dissertation by discussing possible extensions of this work and relating it to the current challenges in the field.

December 2010 cover of the *Wired* magazine presents '25 big ideas for 2011'

Featuring our guest stars !

References of the introduction

[1] A. Koezuka, H. ad Tsumura and T. Ando. *Field-effect transisitor with polythiophene thin film.* Synthetic Metals **18**, 699 (1987).

[2] J. H. Burroughes, D. D. C. Bradley, A. J. Brown, R. N. Marks, K. Mackay, R. H. Friend, P. L. Burns, and A. B. Holmes. *Light-emiting-diodes based on conjugated polymers.* Nature **347**, 539 (1990).

[3] N. S. Sariciftci, L. Smilowitz, A. J. Heeger, and F. Wudl. *Photoinduced electron transfer from a conducting polymer to buckminsterfullerene.* Science **258**, 1474 (1992).

[4] V. L. Colvin, M. C. Schlamp, and A. P. Alivisatos. *Light-emitting diodes made from CdSe nanocrystals and a semi-conducting polymer.* Nature **370**, 354 (1994).

[5] N. C. Greenham, X. Peng, and A. P. Alivisatos. *Charge separation and transport in conjugated-polymer/semiconductor-nanocrystal composites studied by photoluminescence quenching and photoconductivity.* Phys. Rev. B **54**(24), 17628 (1996).

[6] I. Gur, N. A. Fromer, Geier M. L., and A. P. Alivisatos. *Air-stable all-inorganic nanocrystal solar cells processed from solution.* Science **310**, 462 (2005).

[7] B. Sun and N. C. Greenham. *Improved efficiency of photovoltaics based on CdSe nanorods and poly(3-hexylthiophene) nanofibers.* Phys. Chem. Chem. Phys. **8**, 3557–3560 (2006).

[8] S. Ren, L-Y. Chang, S-K. Lim, J. Zhao, M. Smith, N. Zhao, V. Bulovic, M. G. Bawendi, and S. Gradečak. *Inorganic-organic hybrid solar cell: bridging quantum dots to conjugated polymer nanowires.* Nano Lett. **11**, 3998 (2011).

Part I

Hybrid materials

Chapter I

Hybrid components and junctions: literature survey

The main properties of colloidal semiconductor nanocrystals and conjugated polymers are introduced. We describe the state of the art in the field of hybrids materials made from these two components. We discuss their structural, electronic and optical properties, focusing on those which influence charge transport.

First, we introduce basic concepts to describe energy levels of CdSe semiconductor nanocrystals, such as size-dependence of the energy gap and disorder. We discuss the synthesis of CdSe nanocrystals by an organometallic route, their functionalization and self-assembly. Types of charge-carriers in nanocrystals are also described.

Concerning conjugated polymers, we focus on the case of poly(3-hexylthiophene) (P3HT). In particular, we correlate the structural properties of P3HT thin films with their charge transport properties.

Finally, we introduce the concept of bulk heterojunction and its application to hybrids made of semiconductor nanocrystals and conjugated polymers. We present in more detail studies of charge generation and charge transport in such hybrids.

1 Semiconductor nanocrystals

Nanocrystals with dimensions between 1 and 10 nm contain a few tens to a few thousands atoms. Due to their size and to the large number of atoms constituting their surfaces, nanocrystals exhibit very specific physical and chemical properties.

Energy bands in bulk semiconductors arise from the delocalization of charge carriers over a very large number of lattice unit cells. When the size of a crystal is reduced to the nanometer scale, energy levels in energy bands are discretized, move away from each other and the gap widens. This quantization is known as *quantum confinement* and therefore semiconductor nanocrystals are also often referred to as 'colloidal quantum dots'. In that respect, nanocrystals are intermediate between large crystals, that exhibit energy bands, and molecules, that exhibit well defined energy levels. Quantum confinement also depends on the shape and possible

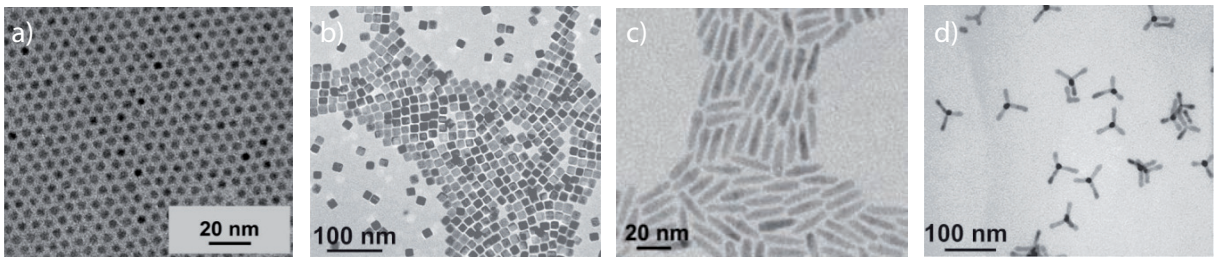

FIGURE I.1 – Transmission electron micrography of nanocrystals of different shapes a) CdSe spherical nanocrystals ('nanodots'); b) PbSe nanocubes; c) CdSe/CdS nanorods; d) CdTe tetrapods. All images were extracted from [1].

anisotropy of the nanocrystals, with the smaller characteristic dimension usually imposing confinement. FIG. I.1 present Transmission Electron Micrography (TEM) images of semiconductor nanocrystals with different shapes: spherical, cubic, elongated, branched.

Moreover, the number of atoms located at the surface of nanocrystals makes up for a large fraction of all atoms in the particle, as it is proportional to $1/r$, where r is the radius of nanocrystals. Moreover, the coordination sphere of surface atoms are incomplete. Therefore, due to their number and to their reactivity, surface atoms influence strongly the properties of nanocrystals. Surface stabilization and passivation is achieved by chemically binding surface atoms to an inorganic crystalline shell (*e.g.* [2]) or to molecular ligands. In the organometallic route, these ligands are organic. The steric hindrance due to long ligands allows for nanocrystals colloidal stability in solution. Organic ligands from the synthesis can be removed or replaced to modify nanocrystals' properties [1, 3–5] as we will see in more detail below.

Various type of nanocrystals are synthesized: elemental (Si, Ge), binary (CdSe, InP), ternary ($CuInS_2$ ...). Different synthetic routes are being developed. Top-down approaches, such as grinding or lithography, divide large bulky material into small pieces. Molecular beam epitaxy, laser pyrolysis and liquid-phase chemical synthesis routes use the bottom-up approach, building nanosized objects from single atoms and molecules.

1.1 Basic physical properties of CdSe quantum dots

We focus here on the characteristics of CdSe nanocrystals prepared by chemical organometallic synthesis. CdSe is by far the most widely studied type of nanocrystals due to its well-mastered synthesis and efficient fluorescence, the wavelength of which can be tuned with the nanocrystal size throughout the visible spectral range, see FIG. I.2.

1.1.1 Crystal structure of CdSe nanocrystals

In the bulk, CdSe is stable in the hexagonal wurtzite and cubic zinc blende phases, represented on FIG I.3.

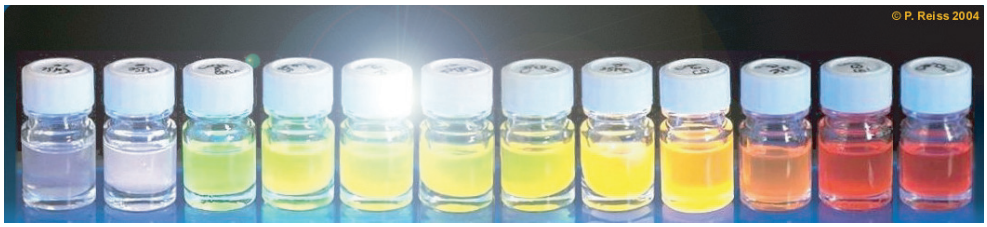

FIGURE I.2 – Emission of CdSe nanocrystals of different sizes While the nanocrystals diameter varies from around 2 nm to 7 nm, the emission of nanocrystals shifts from 480 nm to 650 nm.

Lattice parameters of CdSe are $a = 6.077$ Å for the cubic zinc blende structure and $a = 4.299$ Å and $c = 7.010$ Å for the hexagonal wurtzite structure.

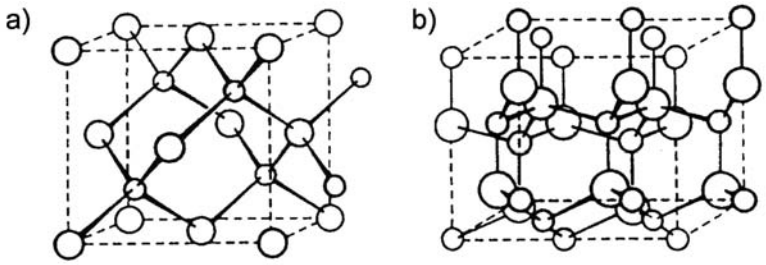

FIGURE I.3 – Crystalline structures of CdSe in a), the cubic zinc blende structure and in b), the hexagonal wurtzite structure.

Both wurtzite and zinc blende phases can be obtained at the nanoscale via different chemical synthesis routes. Lower reaction temperatures ($\lesssim 220°C$) generally lead to the zinc blende phase whereas higher temperatures ($\approx 250-300°$C) lead to the wurtzite phase. Moreover, a transition from the wurtzite structure to the cubic rocksalt phase has been observed at high pressures [6].

1.1.2 Electronic and optical properties of CdSe semiconductor nanocrystals

Electronic and optical properties of semiconductors are strongly related. To understand CdSe nanocrystals properties, we first describe the bulk electronic and optical properties [7].

Properties of bulk CdSe Selenium atoms possess six valence electrons on p orbital, while cadmium atoms possess two valence electrons of a s orbital. The valence band is essentially composed of bonding p orbitals from selenium, occupied with six electrons and sixfold degenerate. The conduction band of bulk CdSe is essentially made of antibonding s orbital from cadmium, occupied by two electrons and doubly degenerate. The conduction band degenerescence is satisfied by spin states and its dispersion curve is parabolic. On the other hand, the valence band degenerescence is partly lifted by the spin-orbit interaction, giving two bands, one with angular momentum $J = 1/2$, the other one with $J = 3/2$. The $J = 3/2$ band is fourfold

degenerate in $\vec{k} = \vec{0}$. For $\vec{k} \neq \vec{0}$, it splits into two bands of different curvatures, $J_z = \pm 3/2$ and $J_z = \pm 1/2$, corresponding to so-called heavy and light holes, respectively.

The crystal potential is taken into account with the use of 'effective masses', that allow to treat electron and hole as free charges and define parabolic dispersion relations. In bulk CdSe, the electron effective mass is $m_e^* = 0.13\ m_e$ and the effective masses of heavy and light holes are respectively $m_{hh}^* = 0.90\ m_e$ and $m_{lh}^* = 0.45\ m_e$.

CdSe possesses a direct energy band gap $E_g = 1.75\ eV$. An electron-hole pair can be created by an optical excitation with photons energies equal or superior to E_g (resonant and non-resonant optical transitions). The electron and hole excited by a non-resonant transition relax by emission of acoustic and optical phonons. They can then recombine radiatively: this is called photoluminescence (PL). The energy of emitted photons is slightly lower than $E_g = 1.75eV$ due to the Coulomb interaction between the electron and hole, (a bound electron-hole pair is called an exciton). The binding energy of the exciton is $E_X = -16\ meV$ in bulk CdSe; its Bohr radius a_X gives its spatial extension, $a_X \approx 5\ nm$.

Size dependance of the energy gap Confining the charges in space results in quantum confinement, *i.e.* leads to the discretization of energy levels inside allowed energy bands and to the widening of the energy gap. In the regime of strong confinement, *i.e.* when the size of the crystal is below the Bohr radius, the difference in energy between the first energy levels of the electron, $1S_e$, and of the hole, $1S_{3/2}$, defines the energy gap E_g, that is related to the radius r of nanocrystals by the following equation:

$$E_{1S_e 1S_{3/2}} = E_g^{eff} = E_g^{bulk} + \frac{\hbar^2 \pi^2}{2r^2}\left(\frac{1}{m_e^*} + \frac{1}{m_h^*}\right) - \frac{1.786e}{4\pi\epsilon_0\epsilon_r r} \tag{I.1}$$

where E_g^{bulk} is the bulk value of the energy gap; m_e^* and m_h^* are respectively the electron and hole effective masses relative to the electron and hole masses m_e and m_h ; ϵ_r is the dielectric constant of the bulk semiconductor relative to the dielectric constant of vacuum.

This relation indicates the theoretical size dependence of energy gaps [8]. When the radius r is very large, the energy gap of the nanocrystals tends toward the bulk value. The second term, in $1/r^2$ expresses quantum confinement energy, in the case of a spherical potential well in which an electron and a hole are confined. The third term, in $1/r$, is the Coulomb attraction energy between the electron and the hole. In CdSe nanocrystals, the Couloumb attraction is stronger than in the bulk and $E_X = 24\ meV$ for a 1.5 Å nanocrystal diameter.

In the field of colloidal quantum dots, the lowest energy level for the electron is also referred to as the 'Lowest Unoccupied Molecular Orbital' (LUMO) and the lowest energy level for holes as the 'Highest Occupied Molecular Orbital' (HOMO).

Very excited states, from 1 eV above the gap, are close enough to overlap and form a continuum. Thus, nanocrystals can absorb light continuously at high energies. At low wavelengths, below 400 nm, optical absorption crosssections of CdSe nanocrystals are higher than those of

atoms and molecules ($8.10^{-15} cm^{-2}$ for a 2.5 nm nanocrystal).

Fine structure and optical transitions In CdSe nanocrystals, the excitonic transition $1S_e 1S_{3/2}$ is degenerate. The fine structure of this transition arises from the electron-hole exchange interaction, from shape asymmetries and from the wurtzite crystalline structure of nanocrystals. The electron-hole exchange interaction is described with the total angular momentum $\vec{F}$: the lowest energy state has a total angular momentum projection $|F_z| = 2$ which is doubly degenerate and can take part in radiative transitions involving single photons. Two $|F_z| = 2$ states, each doubly degenerate, give rise to radiative transitions, and two non-degenerate $|F_z| = 0$ states correspond to radiative transitions that are respectively forbidden and allowed.

The fact that the lowest excitonic transition does not allow for radiative recombination results in the Stokes shift phenomenon, consisting of a shift of energies of emitted and absorbed photons. The Stokes shift is inversely proportional to the particles size because the energy discrepancy between allowed and forbidden radiative transition decreases when the nanocrystals size increases.

Finally, the probability of allowed radiative transitions are defined by their respective oscillator strengths, and also depend on the size of nanocrystals. Thus, the fine structure of CdSe nanocrystals can be studied by their PL at low temperatures. Radiative recombination of excitons, from the radiative transition of lower energy, occurs on the 10 ns time-scale [9]. For comparison, non-radiative intraband transitions in CdSe nanocrystals happen on the 10 ps time-scale [10].

In asymmetric CdSe nanostructures, such as nanorods or nanopods, the fine structure of the lowest energy excitonic transition is modified compared to that of spherical nanocrystals. In nanorods, the lowest excitonic transition is allowed. To the contrary, PL of tetrapods depends on respective sizes of the core and of the arms. To give an example, Pang *et al.* showed that for fixed arm dimensions, smaller core sizes implied that the wavefunction is concentrated in the arms, and eigenstates are defined by the arms dimensions (arm-like states). For larger core sizes, energy levels of the tetrapod became closer and closer to that of the dot (dot-like states). For the ground state, with arms 8 nm long and 4 nm wide, this threshold between arm-like and dot-like states was 2 nm [11].

Correlating CdSe nanocrystals optical spectra and their size as measured by TEM Nanocrystals can absorb photons possessing an energy equal or higher than their energy bandgap. Hence, optical spectra exhibit well defined peaks., called excitonic peaks in absorption spectra. Due to the size dependence of the energy gap, spectra maxima shift hypsochromically (*i.e.* towards smaller wavelengths) when nanocrystals' size decreases, as shown for the absorbance first excitonic peak in Fig. I.4 (A) from [12].

Absorption and emission spectra of CdSe nanocrystals have been correlated to nanocrystal

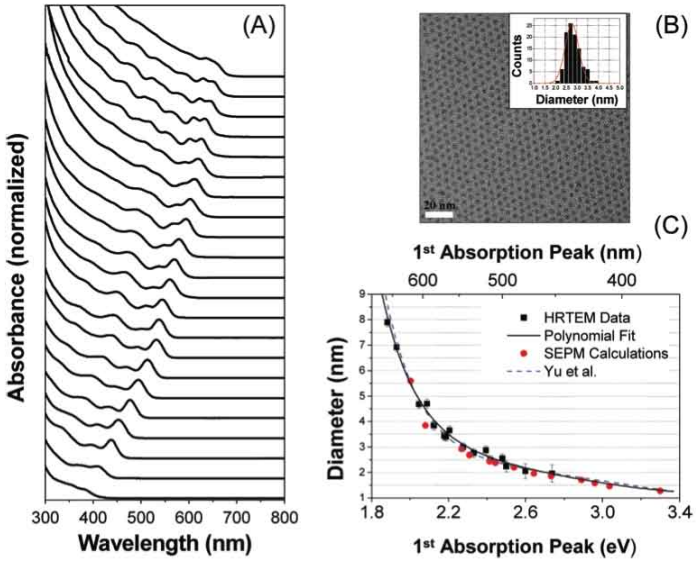

Figure I.4 – Size dependence of absorption spectra from [12], with the original legend: (A) Size-dependent absorption spectra of CdSe nanocrystals dispersed in chloroform. (B) TEM of an ensemble of nanocrystals with a mean size of 2.75 nm. (Inset) Gaussian fit to histogram of measured particle sizes. The standard deviation in this case was determined as 11%. (C) Variation of CdSe nanocrystal diameter with bandgap energy (eV) and first absorption maximum (nm).

sizes as obtained from electron microscopy, see Fig. I.4 (B) and (C) from [12]. This allows to estimate easily the mean nanocrystal diameter D, in nm, from the excitonic peak position λ with :

$$D = 59.60816 - 0.54736\,\lambda + 1.8873\times10^{-3}\,\lambda^2 - 2.85743\times10^{-6}\,\lambda^3 + 1.62974\times10^{-9}\,\lambda^4 \quad \text{(I.2)}$$

It must be emphasized that these values are indications since optical characteristics depend on the shape, solvent and ligands as well as on the size of nanocrystals, as we will explicit in Chapter II.

Defects states and disorder effects In the discussion above, we did not consider chemical impurities and structural defects, nor surface effects. 'Real' nanocrystals possess states which are usually attributed to the incompletion of the coordination spheres of surface atoms. New allowed energy levels for charge-carriers correspond to these defects. They are most noticeable when located within the band gap, as schematized in Fig. I.5. They can be responsible for specific recombination pathways and thus influence the emission spectra of nanocrystals.

Thermal and structural disorders (size dispersion for example) lead to a broadening of energy levels, as pictured in Fig. I.5. Thus, even though at the single nanocrystal scale, we consider discretized energy levels, energy distributions must be used to describe assemblies of

nanocrystals.

Temperature PL spectra allows to study statistical energy distributions of nanocrystals assemblies, including defects states. Time resolved measurements give access to the dynamics of charge relaxation and of charge trapping. For example, Jones *et al.* [13] showed that two distributions of trap states were needed to explain the PL of CdSe nanocrystals at low temperature, one of which was attributed to a broad distribution of non-radiative surface-localized trap states. At low temperature traps states did not modify PL dynamics significantly: the measured average PL lifetime (on the order of 25 ns) was a good indicator of the exciton radiative lifetime. To the contrary, approaching room temperature rendered traps states occupation more probable: measured PL average lifetimes do not correspond to radiative exciton lifetimes.

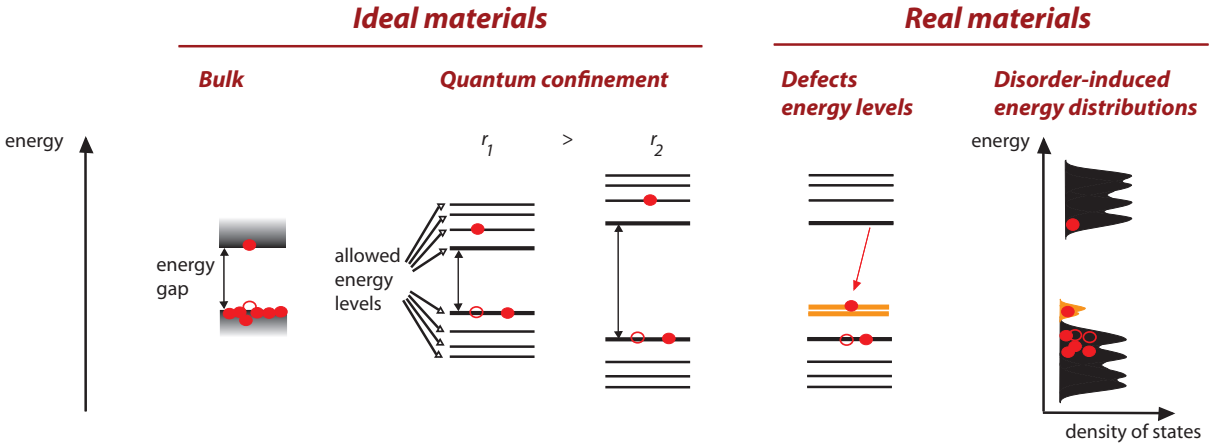

Figure I.5 – Energy levels of semiconductor nanocrystals Effects of quantum confinement (forbidden energy band gap widening), of defects (appearance of energy levels, possibly inside the band gap) and of size dispersion in nanocrystal assemblies are schematically shown.

1.2 Chemistry of quantum dots

We have seen that optical and electronic nanocrystals properties depend on their size. Consequently, it is important to synthesize batches with low size dispersion. 'Good' polydispersities, defined as $\Delta D/D$, with D the average nanocrystal diameter and ΔD the standard deviation around this value, are typically around 5% or 10 %. In order to obtain batches as monodisperse as possible, one must stop the evolution of the nanocrystals' growth, *e.g.* by stabilizing reactive surface atoms with surface ligands.

1.2.1 Synthesis of semiconductor nanocrystals

Liquid-phase chemical synthesis of semiconductor nanocrystals can be divided into two groups: at ambient temperature in aqueous media and at high temperature in organic solvents. The first method is experimentally rather simple but generally yields larger polydispersities than the second one [14].

The second method relies on the temporal separation of nucleation and growth phases. Fast injection of precursors results in a rapid increase of the concentrations of precursors above the nucleation threshold. Subsequent formation of seeds decreases the precursor concentrations and lowers the supersaturation below the nucleation threshold. The short nucleation event is followed by nanocrystals' growth from the precursors remaining in solution. Finally, smaller particles may dissociate due to their large surface energy and contribute to the further growth of larger particles: this is the Ostwald maturation phase. Since this last phase increases the polydispersity, synthesis are ideally stopped before. The reaction time thus controls the size and polydispersity of the obtained sample.

A large number of parameters (type and concentration of precursors and ligands, solvent, temperature) influence the synthesis and can be used to modify the shape of nanocrystals (*e.g.* [15, 16]). To give an example, the synthesis of CdSe spherical nanocrystals has been modified to obtain branched structures. Wurtzite arms have been observed to grow on the {111} facets of zinc blende cores when the reaction temperature was lowered [15]. The use of ligands blocking the arms growth in two directions, thus enhancing the growth in the arm direction, lead to the formation of strongly anisotropic arms [11, 17].

1.2.2 Surface functionalization of semiconductor nanocrystals

Chemically synthesized nanocrystals are covered by a ligand shell made of organic molecules, avoiding their aggregation and allowing their dispersion in colloidal solution. In general, synthesis ligands are long alkyl chains. They interact with surface atoms through coordination bonding and can be exchanged to introduce new functionalities.

Many current issues in nanocrystal science are related to ligands engineering. Controlling the surface of nanocrystals proves to be essential since ligands strongly influence nanocrystals uses:

- Colloidal solubility, in order to disperse nanocrystals in different solvents (*e.g.* water for biomedical applications);
- Electronic and optical properties: the capacity of ligands to complete the coordination sphere of surface atoms of nanocrystals controls trap states, and thus influence recombination dynamics;
- Self-assembly: ligands control the density of nanocrystals' assembly in the liquid and in the solid phase. Specifically-designed ligands can also introduce grafting possibilities for various surfaces or substrates;
- Transport properties throughout nanocrystals assemblies: ligands allow to modulate electronic coupling between nanocrystals and some ligands facilitate charge transport in assemblies where charges are naturally confined [5, 18–21].

a)

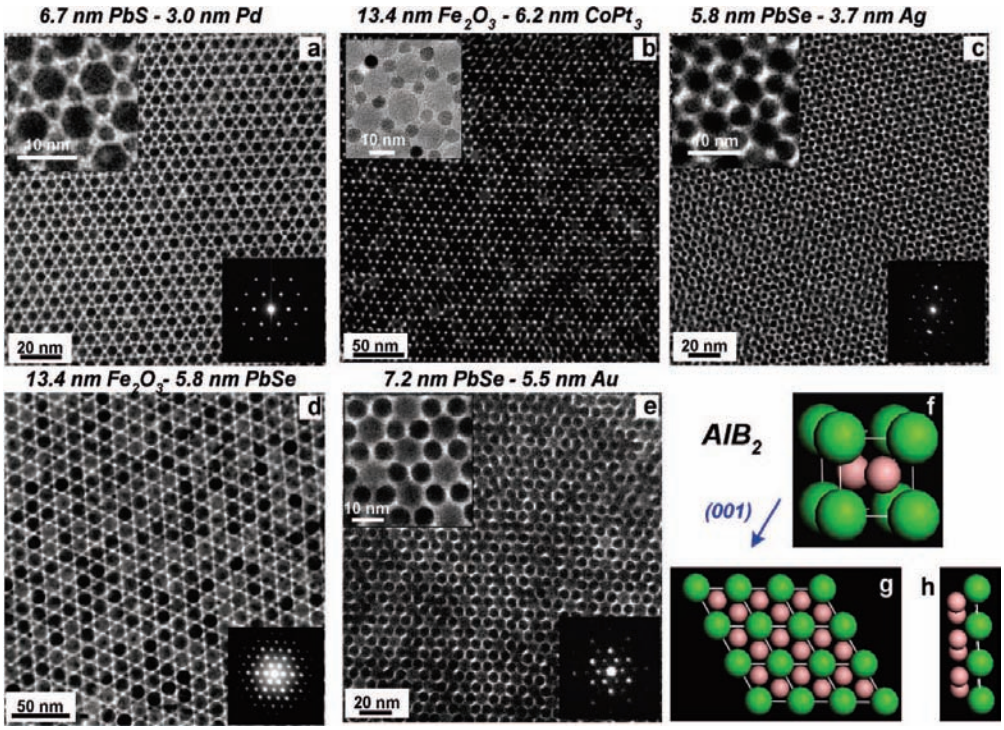

b)

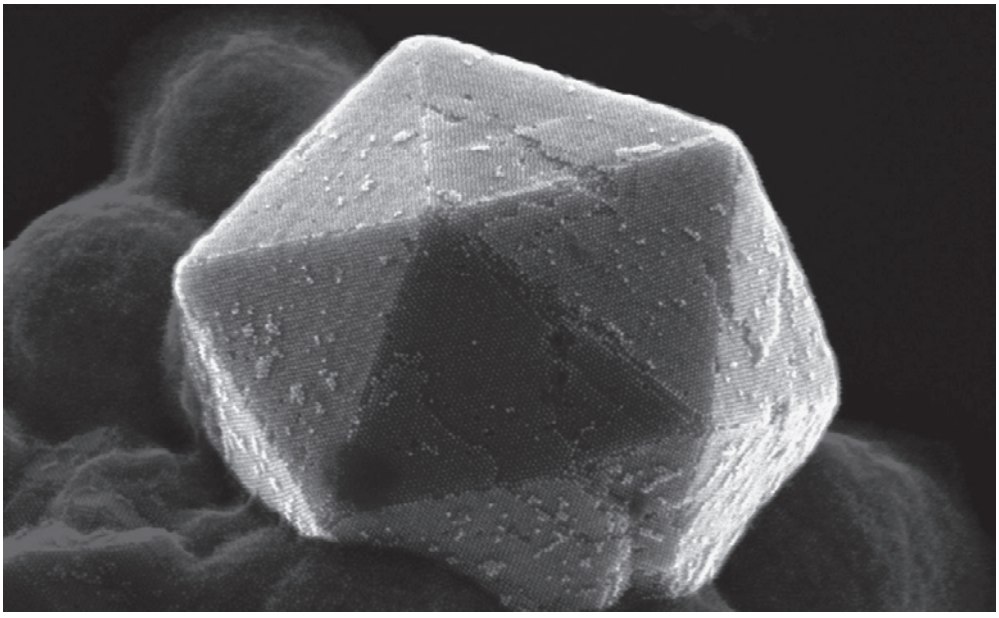

Figure I.6 – 2D and 3D self-assemblies of nanocrystals a) Binary superlattices of nanoparticles from [1] and b) crystal of nanocrystals from [22].

Typical ligand exchange reactions in solution imply nanocrystals dispersed in a solvent for which initial ligands have an affinity. An excess of the new ligands is added and the solution is stirred and heated to facilitate the exchange process. The use of non miscible solvents for the initial and new ligands allows to observe directly the migration of nanocrystals from one phase to another. Ligand exchange reactions can provoke a loss of colloidal solubility, photoluminescence quenching, modification of conductivity, etc. The molecular signature of the new ligands can also be detected by elemental analysis, Nuclear Magnetic Resonance (NMR) and Fourier Transform Infrared (FTIR) spectroscopy.

1.3 Assemblies of semiconductor nanocrystals

Nanocrystals can be assembled into thin films by solvent evaporation. Assemblies of nanocrystals in specific patterns have been obtained by controlling the evaporation or by using external forces (*e.g.* an electric field). For example, it is possible to align nanorods parallel to the substrate plane side-by-side or in a head-to-tail configuration [23, 24]. Vertical configurations, *e.g.* nanorods aligned in a nematic phase (to achieve a comb-like morphology), have been achieved as well [25]. These specific architectures usually extend on the μm or hundreds of μm scale at most. Homogeneous self-assembly at larger scales is still needed from the point of view of optoelectronic applications.

On the other hand, beautiful nanocrystals superlattices have been realized. They can remind us of packing of single atoms into known binary crystal structures, as shown in Fig. I.6 a), or of nanocrystals, in b) !

2 Conjugated polymers

2.1 Introduction

Sharing electronic clouds is not a privilege of dense inorganic crystals. Indeed, all atoms come to assemble their electrons when they are close enough: hybridization of atomic orbitals gives molecular orbitals and chemical bonds.

Conjugated polymers are macromolecules, the main chain of which is made of carbon atoms or hetero-atoms, each carrying a p orbital. The hybridization of p atomic orbitals into sp_2 orbitals, leaves a p_z electron per atom to form π-molecular orbitals. π-orbitals are delocalized on a characteristic length scale called the conjugation length. A one-dimensional chain, with equally spaced sites and a charge per site, is unstable (Peierls instability). To break this perfect order, the period of the polymer chain doubles and an energy gap forms. The energy gap of conjugated polymers depends on the conjugation length (the longer the conjugation length, the smaller the gap). Fig. I.7 schematizes the σ- and π-bonds of two conjugated organic compounds, the benzene aromatic cycle and the poly(acetylene) chain.

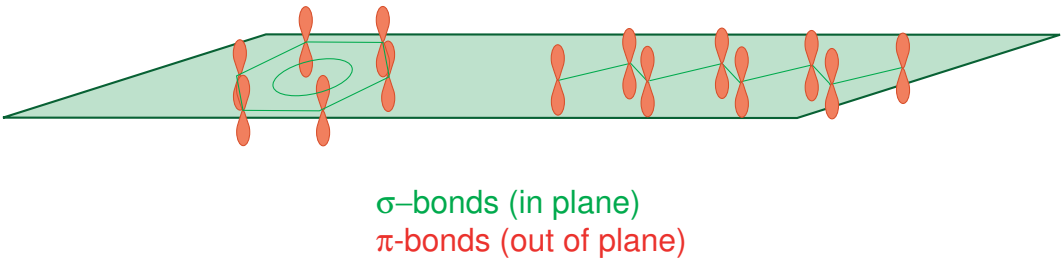

FIGURE I.7 – Chemical bonds and conjugation principle σ- and π-bonds in benzene (left) and poly(acetylene) (right) molecules. Electrons affected to π-bonds are delocalized along the chain: this is called conjugation.

Polymer chains are characterized by their weight average molecular weight M_w and their number average molecular weight M_n:

$$M_w = \frac{\sum_i N_i M_i^2}{\sum_i N_i M_i} \text{ and } M_n = \frac{\sum_i N_i M_i}{\sum_i N_i} \tag{I.3}$$

where N_i is the number of polymer chains of mass M_i. Typically, molecular weights of polymers reach thousands or hundreds of thousands of Daltons. The ratio of weight average on number average molecular weights defines the polydispersity index $D = M_w/M_n$, *i.e.* the dispersion of sizes of polymer chains in a batch. A P3HT sample is considered to have a 'good' polydispersity when it is around or below 2 (P3HT is a well-mastered polymer and such small polydispersity indices are achieved by fractionation).

Finally, a polymer chain is also characterized by its regioregularity index. The polymer backbone possesses side chains, whose anchoring position onto the monomer may vary. The regioregularity index indicates the fraction of monomers with a specific configuration. Usually, regioregularity indexes indicated for P3HT refer to the head-tail head-tail (*i.e.* the monomers bind between the position 2 of the first one and the position 5' of the second one) configuration, for which the orbitals overlap is maximal.

Families of conjugated polymers Conjugated polymers can be classified in different families (see FIG. I.8 for examples): polyenes (they contain one or more sequence of alternating single and double carbon-carbon bonds, *e.g.* poly(acetylene)), aromatic polymers (they are composed of aromatic cycles, *e.g.* poly(*p*-phenylene)), heterocyclic aromatic polymers (they contain a heteroatom in the aromatic cycle, *e.g.* poly(thiophene)), aromatic polymers containing hetero-atoms (they contain hetero-atoms outside the aromatic cycle, *e.g.* poly(aniline)) and polymers composed of different families above (*e.g.* poly(*p*-phenylene-vinylene)).

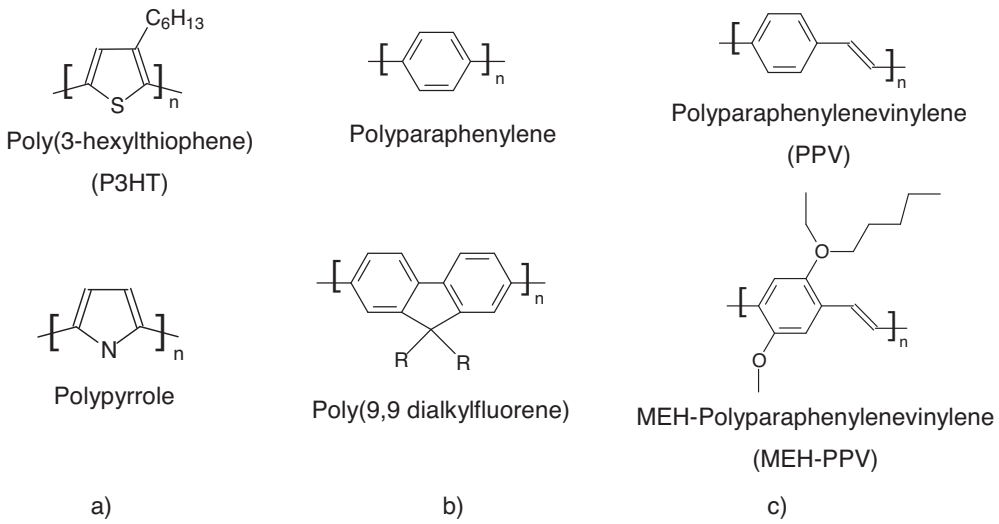

Figure I.8 – Different examples of conjugated polymers a) heterocyclic polymers; b) aromatic polymers; c) mixed polymers, from [26].

2.2 P3HT energy landscape

Polydispersity results in variations of energy states. Moreover, chemical or structural defects interrupt electronic delocalization, provoke variations in the conjugation length and hence of the value of the energy band gap. Defects also introduce defects states in the energy density-of-state (DOS).

Consequently, DOS of conjugated polymer assemblies are rather complex. They are studied by various theoretical methods (see for example [27], to which we will come back in Chapter V) and experimental techniques. To detail an example, Schafferhans *et al.* studied the distribution of traps in P3HT thin films by thermally stimulated current measurements: traps are first filled optically, and the sample is then heated. No voltage is applied and electrical current resulting from charge detrapping is measured as a function of the temperature. This gives the density of traps as a function of their thermal activation energy. A continuous trap distribution was found, with two main contributions. The first contributions has low activation energy (50 meV) and is attributed to the tail of the usual DOS. The second contribution, with an activation energy of 105 meV, strongly increased with exposure to oxygen and the density of oxygen-related traps more than doubled in 50 hours in air [28].

2.3 Charge-carriers in conjugated polymer

Charge carriers can be introduced onto a conjugated polymer chain. This process is called doping. Oxidation or reduction of the polymer chain can be realized chemically or electrochemically, by electrical injection or by photogeneration.

Injecting a charge onto the polymer chain creates a deformation of the chain associated to

a charged defect. Depending on whether the ground state of the polymer chain is degenerate or not, the 'charged defect + chain deformation' is called a soliton, an exciton, a polaron or a bipolaron, as depicted in Fig. I.9.

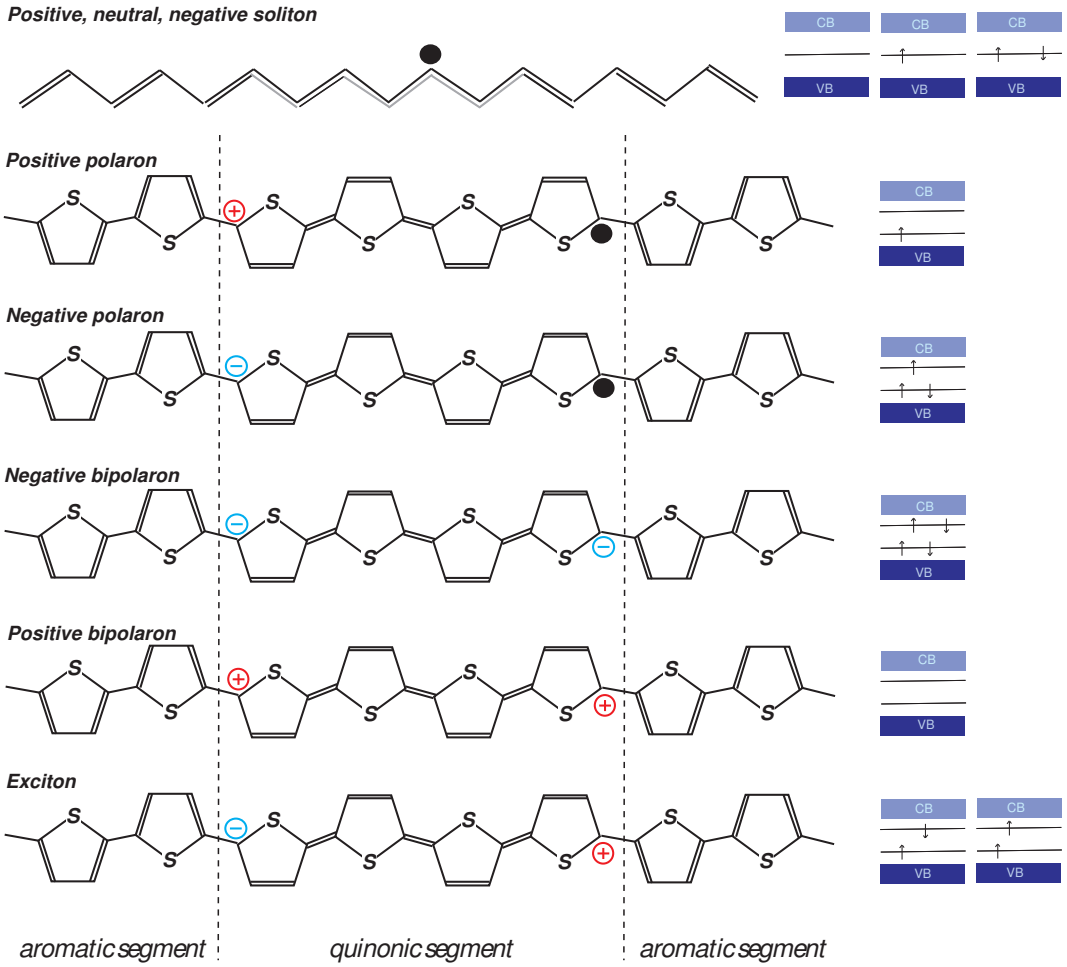

Figure I.9 – Different types of charge carriers on conjugated polymers Here, the polymer is poly(acetylene) on the first line and then poly(thiophene). Black dots represent unpaired neutral spins, red + signs symbolize positive defects and blue - signs negative defects. Note that charged defects are accompanied by chain deformation, *e.g.* the alternance of aromatic and quinonic configurations in the case of poly(thiophene).

Solitons When the energy ground state of a conjugated polymer is doubly degenerate, *i.e.* when its two resonant forms are strictly equivalent energetically speaking, the removal of an electron from the chain results in the creation of a cation radical, *i.e.* an unpaired spin. The charge is annihilated by an anion in solution. Solitons are quasiparticles made of an electrically neutral unpaired spin, mobile along the chain. A discrete energy level associated to this defect appears within the gap.

Polarons Heterocyclic polymer chains such as P3HT are not degenerate in their ground state because aromatic configurations are slightly more stable than quinonic ones (representations of aromatic and quinonic configurations can be found on FIG. I.9 in the case of polythiophene). Soliton formation is thus impossible.

When an electron is taken away from an heterocyclic polymer chain, an effective positive charge is formed, associated to a chain deformation: polarons are quasiparticles of charge +1 and spin 1/2 associated to a quinoic section in an aromatic chain. Two discrete energy levels are formed in the energy gap. Positive polarons form when an electron is taken away from the chain; negative polarons form when an electron is added to the chain.

When identically charged polarons are close enough to each other, they lower their global energy by uniting their chain deformation. The new quasiparticle is a bipolaron, either positive or negative.

Excitons They are generated by photoexcitation of charge-carriers and consist of a bound electron-hole pair associated to a chain deformation. Two discrete energy levels are formed, with one spin on each level, either parallel or anti-parallel.

Stable charged states are polarons and bipolarons. Excitons are unstable and recombine. In the following, when we discuss charge transport in poly(3-hexylthiophene), whose backbone is not degenerate, we refer to diffusion or drift of positive and negative polarons and bipolarons. As often in the community, we also use the terms holes and electrons as shortcuts for negative and positive charge carriers.

2.4 P3HT thin films

Semicrystalline structure Regioregular P3HT is a semi-rigid conjugated polymer with a planar backbone and alkyl side-chains, that confer its solubility in several organic solvents such as chloroform or chlorobenzene. Its conjugated thiophene main chain is planar with possibility of torsions or kinks, detrimental to the conjugation. It self-organizes in a semi-crystalline structure which is composed of crystalline and amorphous domains.

X-ray diffraction (XRD) characterization of P3HT gives insight into its crystalline structure (see [29] for example): when probed as a powder, diffraction peaks (h00) and (020) are found. The first set, (h00), comes from interchain periodicity with the chains separated by alkyl side chains (period 1.6 nm, see FIG. I.10). The (020) peak comes from π-stacking between thiophene ring chains, packed laterally perpendicular to the monomers plane (period 0.38 nm). As generally, the width of XRD peaks is inversely proportional to the crystallite size.

On larger scales, P3HT can organize into anisotropic crystalline structures in an amorphous matrix. These structures (fibrils, needles, ribbons, etc.) can be studied by Atomic Force Microscopy (AFM), as pictured in FIG. I.11.

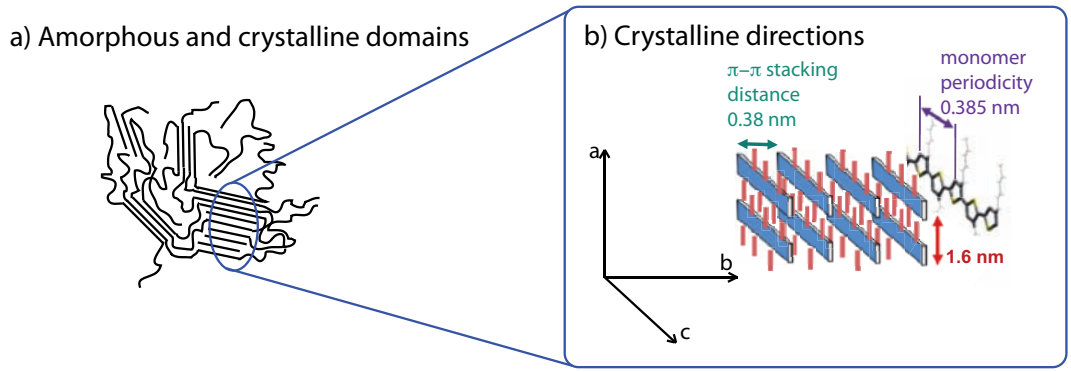

Figure I.10 – P3HT semicrystalline structure a) scheme of crystalline and amorphous domains; b) definition of the crystalline axes.

Crystallization of P3HT thin films depends on the regioregularity, on the molecular weights, on the solvent, on the deposition method and on the substrate.

Solvent evaporation (boiling point, deposition method) rules the organization of P3HT on the substrate, with slow evaporation resulting in higher crystallinity than fast evaporation. In [29] for example, drop-cast films have been shown to crystallize with the $\vec{a}$-axis perpendicular to the substrate plane (edge-on configuration). Spin-coated films on the other hand have more various configurations, depending on the regioregularity and molecular weight. Low M_n (11 and 28 kDa) and high regioregularity (>91 %) led to crystallization with the $\vec{a}$-axis perpendicular to the substrate (edge-on) whereas high M_n (175 kDa) and low regioregularity (81 %) led to the $\vec{a}$-axis parallel to the substrate (flat-on) [30].

Thermal annealing of thin films results in reorganization of P3HT into more crystalline films [31].

As can be seen in Fig. I.11 from [26], the solvent evaporation speed plays a large role in the formation of fibrils. Here, we see that the formation of anisotropic fibrils is favored when the evaporation is slow and for lower M_n.

The substrate has an influence on P3HT crystallization as well. For example, in [32], authors showed that hydropobic substrates with low interfacial free energy favor P3HT crystallization, in opposition to hydrophilic substrates with high interfacial free energy. This effect is limited to the first monolayer.

In conclusion, P3HT thin films tend to be more crystalline when the film forms slowly (slow evaporation), for low molecular weights and for high regioregularities. The formation of anisotropic structures is favored by low molecular weights, except for very slow deposition where high molecular weight lead to fibril formation as well [26].

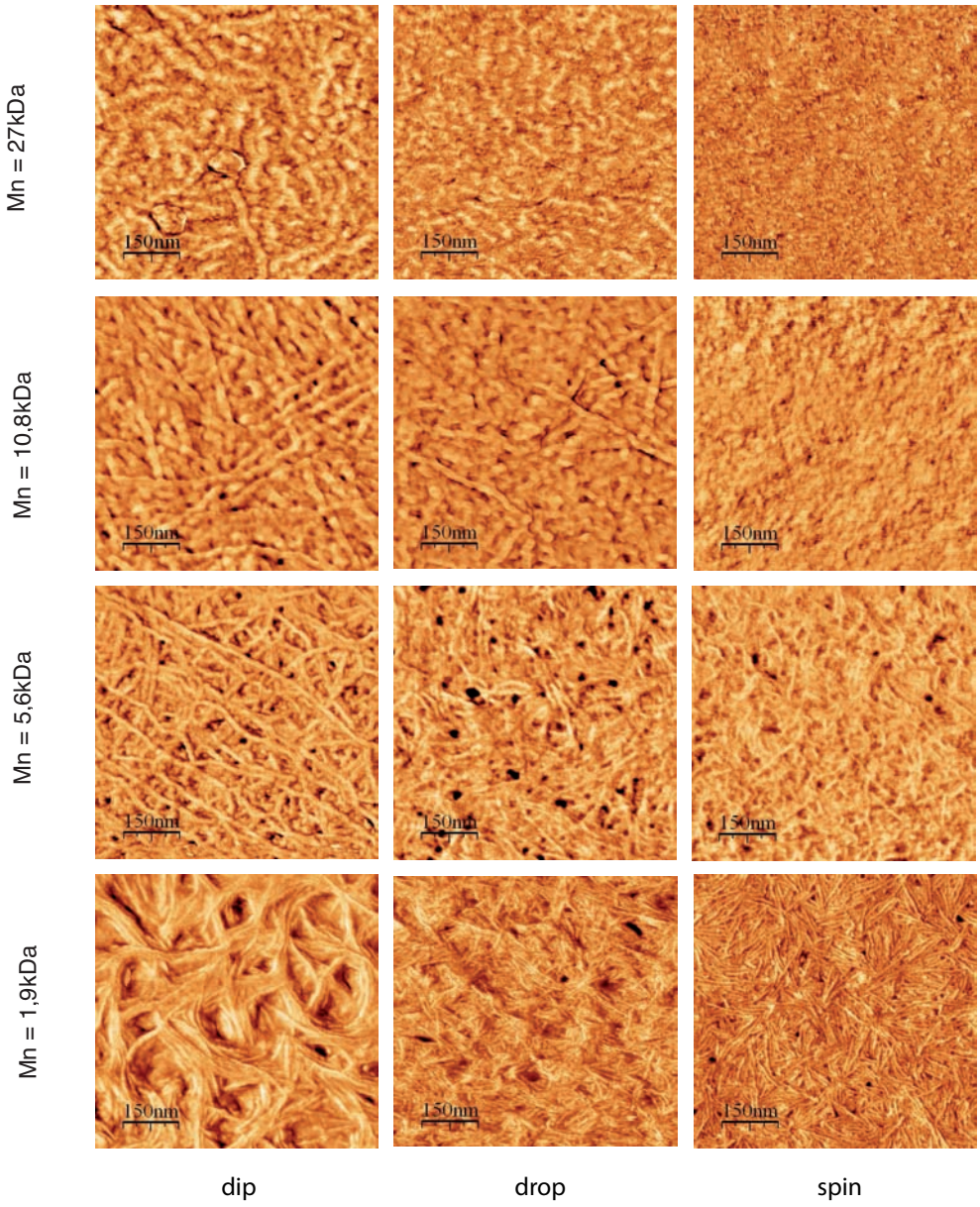

Figure I.11 – AFM phase images of P3HT thin films Evaporation speed is varied through the use of different deposition methods (low evaporation speed for dip-coating, high evaporation speed for spin-coating); the influence of number average molecular masses is explored as well [26]. More fibrillar structures are obtained with low molecular masses and slow evaporation.

Influence of regioregularity and molecular weight on charge transport The crystallinity of P3HT thin films has been shown to strongly influence charge transport properties. Anisotropic crystallization of P3HT at different scales implies that the charge mobility is anisotropic: a film in the edge-on configuration can have high mobilities parallel to the substrate, as probed by field-effect transistor configuration (FET) for example, but lower mobility perpendicular to the substrate, as probed by space-charge-limited current (SCLC) or Time-Of-Flight (TOF) measurements for example[1].

To illustrate this directional effect, let us compare the influence of regioregularity on FET and TOF mobilities. When measured in the FET configuration, regiorandom and regioregular samples exhibit very different mobilities: when going from regioregularity of 70 % to 98 %, the FET saturation mobility was increased by more than 3 orders of magnitude, from 2 $.10^{-5} cm^2/V.s$ to 6 $.10^{-2} cm^2/V.s$ [30]. This is related to the change of crystallinity: high regioregularity samples present large π-stacking parallel to the substrate, which favors the mobilities in this direction. To the contrary, mobilities probed in the TOF configuration were reported to be insensitive to the degree of regioregularity in pristine P3HT. Interestingly, the regioregularity influence on TOF charge mobilities was far more pronounced in the case of blends of P3HT with PCBM [33]. Unluckily, in both these studies [30, 33], not only the regioregularity changed in between samples, but also the molecular weight. As we have seen above, both these factors influence the degree of π-stacking and its direction.

In [34], P3HT hole mobilities were studied in the FET configuration over a large range of M_n. For low boiling point solvents, the authors obtained amorphous films with low mobilities in the whole M_n range probed. For high boiling point solvents, P3HT was better crystallized and the mobility depended on the molecular weight. Mobilities increased with M_n up to a saturation around $10^{-2} cm^2/V.s$ for $M_n > 52kDa$.

In [35], P3HT mobilities were measured by THz spectroscopy, an all-optical technique, and found to increase with molecular weight up to the maximal M_n studied, 153.8 kDa.

Finally, TOF mobilities of pristine and annealed P3HT thin films were determined by Ballantyne *et al.* [36] for molecular weights between 12 and 121 kDa. The mobility decreased with increasing M_n, which was attributed to the entanglement of polymer chains of high M_n. This also suggested that optimal P3HT molecular weights for photovoltaic applications are between 13 and 34 kDa.

3 Hybrid bulk heterojunctions

Fig. I.12 introduces the concept of heterojunction: contacting semiconductor materials with different HOMO and LUMO levels creates a local electric field at the interface between the donor and the acceptor. This interface is of tremendous importance for optoelectronic applications

[1] We will come back to these measurement techniques in Chapter III, dedicated to charge transport and mobility measurements.

since it is a preferential place for 1) exciton dissociation; 2) bimolecular recombination of free charge carriers (monomolecular recombination, *i.e.* recombination of an exciton or of an electron-hole pair from the same exciton, can also occur in one of the two phases).

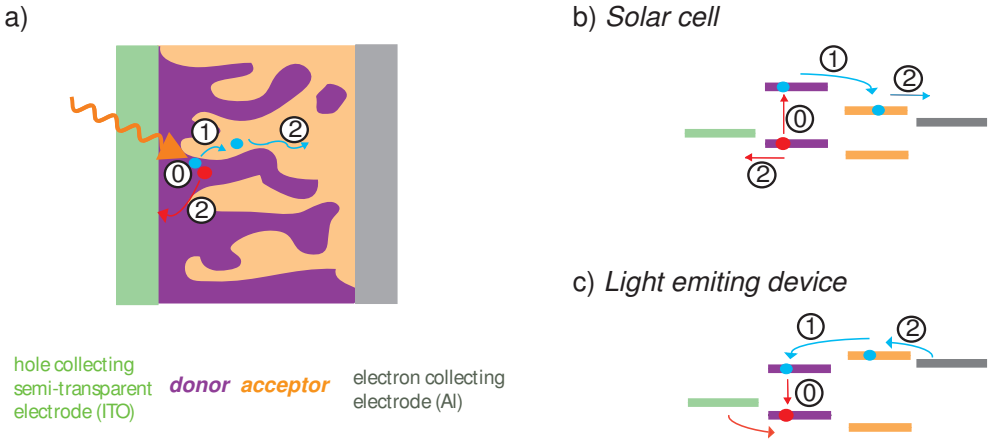

Figure I.12 – Bulk heterojunction a) spatial representation; b) and c) energy-space representation. Conventional nomenclature for electrodes and components of the active layer are indicated in the lower part of a). Processes relative to a solar cell are indicated by numbers in a) and b): (0) generation of en exciton (here on the electron donor); (1) dissociation of the exciton into an electron (blue) and hole (red) pair, here by transfer of the electron onto the acceptor phase; (2) charge transport of electron and hole in their respective favorites phases, towards the collecting electrodes. In the case of light emitting devices in c), the energy diagram presents a different alignment and charges go the other way: (2) charge injection and transport in the active layer; (1) charge trapping on one phase; (0) exciton recombination and photon emission.

Heterojunctions can be built by different techniques. Planar heterojunctions are usually made by evaporation of successive layers. Bulk heterojunctions can be either deposited from a solution containing the different components of the active layer or by first depositing a nanostructured layer (an array of nanowires for example) and adding the second component on top.

The concept of hybrid heterojunctions made of conjugated polymers and semiconductor nanocrystals was first introduced by Colvin et al. [37] for light-emitting devices. Alivisatos group pioneered their use in photovoltaics [38, 39].

3.1 Semiconductor nanocrystals/conjugated polymer hybrid solar cells

In solar cells, from the proof of concept to the best efficiency to date (4.1 %, [40]), materials were varied mostly on the organic side, including for example, poly(phenylene-vinylene), poly(thiophene), poly(vinylcarbazole) and their derivatives, and newer low band gap materials such as PCPDTBT[2]. On the inorganic side, pyridine-treated CdSe nanocrystals of different shapes remained for a long time the only system yielding power conversion efficiencies (PCE) above 1 %. Much effort was put into morphology optimization, for example by varying the

[2]See Appendix 13 for abbreviations.

size and shape of nanocrystals (*e.g.* [41]), by modulating the anisotropic crystallization of the organic phase (*e.g.* [42, 43]) and by controlling the segregation and the respective orientations of both phases (*e.g.* [44, 45]).

Table I.1 gathers power conversion efficiencies of different solar cells technologies, with an emphasis on hybrid devices [46]. It must be noted that the area of the electrodes strongly influences the PCE measurements. First, the sheet resistance of the electrodes increases with the electrode area; second, although perhaps less importantly, due to contour effects, effective current collection surfaces are larger in the case of small areas.

Table I.1 – Power conversion efficiencies (PCE) reported for photovoltaic devices of various types under AM1.5, 100 mW/cm^2, as in [46] In addition to the highest reported value, the numbers in brackets indicate typical values observed for the corresponding device type.

Material	*Device active surface area in cm^2*	*PCE*
Monocrystalline silicon	4	24.4 % (12-16 %)
Polycrystalline silicon	1	20.3 %(9-12 %)
Amorphous silicon	22-24	9.5 % (4-8 %)
Dye-sensitized mesoporous TiO2/redox couple in liquid electrolyte (Grätzel cell)	0.186	10.4 %
Dye-sensitized mesoporous TiO2/MeOTAD(solid state)	0.16	5.0 %
MDMO-PPV/PC70BM	0.1	3.0 %
P3HT/PCBM	0.19	4.9 %
PCPDTBT/PC70BM	0.127	6.1 %
PTB7/PC70BM	0.1	7.4 %
P3HT/CdSe nanodots	0.08	2.0 %
P3HT/CdSe nanorods	0.28	1.6 %
P3HT/CdSe nanorods	0.045	2.6 %
P3HT/CdS nanorods	0.1	2.9 %
MDMO-PPV/CdSe tetrapods	0.045	2.8 %
PCPDTBT/CdSe tetrapods	0.11	3.1 %

To make working devices, energy and morphology constraints are strong. Energy level alignment is crucial, as much at interfaces with electrodes (charge injection or blockade) as at interfaces within the active layer (to favor exciton dissociation). The spatial morphology of the active layer is also very important to ensure optimal exciton and charges diffusion. In organic and hybrid photovoltaic, the optimal morphology is thought to be made of interpenetrating combs, as pictured in Fig. I.12 a). In such architectures, the donor and acceptor phases are

segregated on the 10 nm-length scale, since exciton diffusion lengths in organic materials are around 10 nm. In Fig. I.12 a), we also represented two types of morphological defects: an isolated island, which could act for example as a trap for charges; and a short circuit of the purple phase extending from anode to cathode. Indeed, to avoid short circuits at the interfaces with the electrodes, 'almost but not quite' percolating phases are needed. Avoiding this last kind of defect is in practice often realized by the use of thin charge blocking layers, such as PEDOT:PSS on the Indium Tin Oxide (ITO) electrode to block electrons, or LiF under the Al electrode to block holes, for example.

Energy level alignement at the meso- and nano-scales Interfaces are of tremendous importance in semiconducting devices. Our physical models of interfaces come from the field of bulk inorganic semiconductors. As we have seen before, these materials are: 1) defect-less to a large extent, at least compared to our objects of study; 2) very large in size, *i.e.* made of a large number of atoms. These two characteristics allowed the formulation of band theory and are also exactly what distinguishes bulk inorganic semiconductors from our nanostructured organic and hybrid materials.

At the device scale, the uniform field representation is usually used to picture the internal electric field. Recent works from the organic electronics field started exploring spatial distributions of the applied electric field, depending on the active layer thickness and field intensity. For example, P3AT devices between ITO and Al electrodes were studied by field-induced photoluminescence quenching [47]. A depletion layer forms at the interface with Al, making the field larger at this interface and thus dissociation of excitons more efficient.

Finally, it should be kept in mind that energy levels depend not only on the material characteristics (on the charge carrier delocalization length and its dispersion in the assembly), but also on the batch and on processing conditions of a particular sample. For example, ITO has a work function comprised between -4.8 eV and -5.1 eV. In the literature, P3HT HOMO level is set between -4.6 eV and -5.2 eV depending on the source (*e.g.* [48, 49]). As we will see in the next Chapter, nanocrystals' energy levels depend on many factors, including of course their size but also their surface chemistry.

3.2 Charge generation and transport in hybrid bulk heterojunctions

In 2011, we published a review on hybrid materials for photovoltaics in Nanoscale, [46]. Its Section 5 deals with Charge generation and transport in hybrids, and the following paragraph is its summary.

Electronic properties of hybrid materials consisting of conjugated polymers and semiconductor nanocrystals have been studied with various experimental techniques in the last fifteen years. Spectroscopic studies allow the characterization of the hybrid materials on their own,

whereas electrical measurements strongly depend on the film morphology, on the interfaces with the electrodes and on the electrode materials.

Exciton generation upon illumination has been proved by the appearance of photo-induced absorption bands [50]. The lifetimes of these excitons have been studied by photoluminescence decay experiments [51, 52] and [photo-induced absorption] PIA frequency measurements [50, 53]. Their diffusion seems to be thermally activated [54].

Whereas photoluminescence quenching indicates the dissociation of excitons into free charge carriers or energy transfer (*i.e.* the creation of an exciton on the lower gap component of the hybrid) [52, 53, 55], only positive polarons on the polymers have been observed by light-induced electron spin resonance [LESR] [50, 55] and photo-induced absorption (PIA) [50, 52, 53, 56] and no sign of their negative counterparts has been detected yet. The positive polarons exhibited long lifetimes that are distributed in such wide ranges as the μs to ms range or longer, as found by LESR signal decay studies and PIA frequency measurements. The latter tend to indicate dispersive recombination processes in the most recent studies [55, 57].

Electrical characterizations exploring a wide range of parameters such as temperature and light intensity have been rather rare until now [38, 58, 59]. Dark and photocurrents have been described by a space-charge limited current model associated with a field dependent mobility. Temperature dependence indicated the thermal activation for energies corresponding to material parameters. Studies of the current dependence on the illumination wavelength gave mostly an absorbance sensitizer role to the nanocrystals rather than the desired electron transport role [60, 61]. Current hystereses have been reported when scanning the applied voltage back and forth [62–64]. These hystereses are more important when nanocrystals are decoupled, either by the use of type I core/shell nanocrystals or of insulating surface ligands, or by blending them with an insulating polymer and are attributed to nanocrystals' charging. Finally, mobilities have been measured by time-of-flight measurements [65, 66] and with field effect transistor configuration [60, 62, 63]. The obtained hole mobilities were relatively close to those measured in pristine polymer films, with the exception of ref. [65], where the nanocrystals were directly synthesized in the polymer matrix. The transport was dominated by holes in the hybrids investigated in these reports.

Recombination is likely to be the dominating efficiency-limiting process in hybrid materials. It has been shown to be dispersive in many samples by studying the short circuit photocurrent as a function of light intensity, either monomolecular at low light intensities (low charge-carrier density) or bimolecular at higher light intensities. These findings are coherent with the widely distributed lifetimes of free charge carriers mentioned above, as well as with the idea that hybrid materials are of highly disordered nature.

In contrast with all organic blends (*e.g.* with PCBM as an electron acceptor), electrons have neither been detected spectroscopically so far nor have charge transport studies shown their large contribution. Many efforts are underway to improve the transport by enhancing mobilities through the use of anisotropic nanocrystals and crystalline polymers and through

reducing trapping and recombinations.

4 Conclusion

In this introductory chapter, we presented the main features of semiconductor nanocrystals, conjugated polymers and hybrids made of these components. We focused on photo-generation and transport of charge-carriers. Descriptions of materials based on energy distributions and energy levels alignment have been introduced and will serve in the analysis of materials properties and of transport measurements as well as in their simulations.

Chapter II

Materials used in our work

In order to study electrical transport in hybrid materials, we have decided to use a well-documented heterojunction: CdSe nanocrystals blended in solution with poly(3-hexylthiophene). These materials present several advantages: availability, well known physico-chemical properties and successful use in hybrid heterojunctions solar cells.

P3HT is commercially available in its regioregular form, and its fractionation procedure is well established. CdSe nanocrystals are one of the first type of II-VI semiconductor nanocrystals to have been synthesized by the organometallic route. Syntheses leading to low polydispersity (5-10%) and excellent optical properties have been optimized in our laboratory. More importantly for our study that requires large quantities of nanocrystals, our laboratory developped a versatile gram-scale synthesis for CdSe nanocrystals of various sizes and shapes [14].

Deposition methods, structural properties and transport properties of P3HT are well known. Likewise, the functionalization of CdSe nanocrystals, their self-assembly and transport properties have been extensively studied.

Finally, bulk heterojunctions made of P3HT and CdSe nanocrystals have held the record efficiency, 2.8%, for hybrid heterojunctions for a few years [67, 68]. Only recently, have they been overtaken by a 3.1% efficiency blend of PCDTBT and CdSe nanorods [69] and by a 4.1% efficiency blend of P3HT fibrils and CdS nanocrystals [40].

In conclusion, the CdSe/P3HT heterojunction is appropriate system for fundamental studies. It is an ideal starting point for developping charge transport characterization methods, which could be used for studying future more refined, efficient and environmentally-benign hybrids heterojunctions in solar cells and photodetectors.

In this Chapter, we present all the steps that precede and condition charge transport experiments: synthesis, surface functionalization and characterization of CdSe nanocrystals; preparation and optimization of the deposition of P3HT thin films and finally the preparation of hybrids in solution, their deposition as thin films and their characterization.

1 Preparation and characterizations of CdSe nanocrystals

1.1 Large-scale synthesis of CdSe nanostructures

Comparably large quantities of nanocrystals are required for their integration in optelectronic devices. For example, many hybrid solar cells use polymer:nanocrystals weight ratio of 1:9. For spin-coated hybrids, rather large polymer concentrations and a high volume are needed, *e.g.* 30 mg/mL and 300 μL, so that 90 mg of nanocrystals are needed to make a single sample–the full amount of a typical lab synthesis ! In order to limit subtle variations between samples, such as surface chemistry, it is interesting to use large batches of nanocrystals.

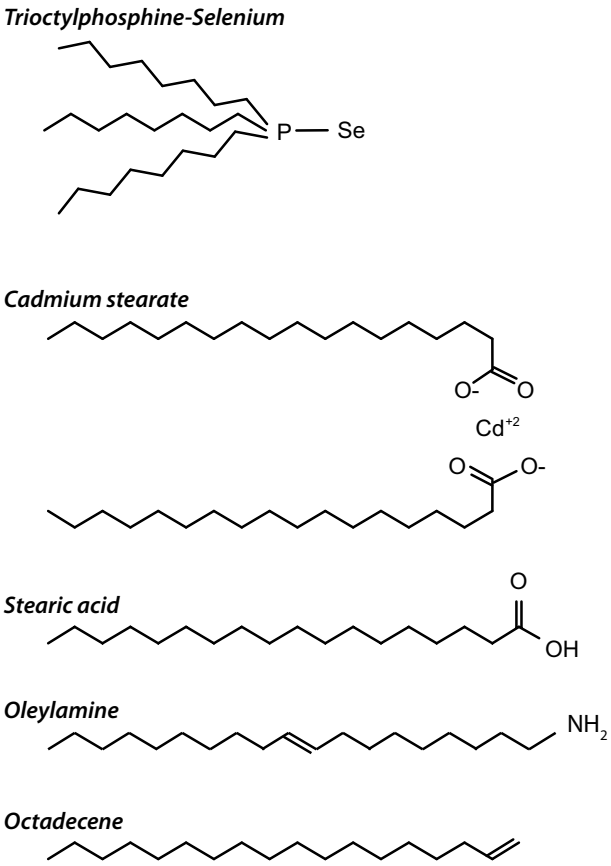

FIGURE II.1 – Precursors, ligands and solvents used in the gram-scale synthesis of CdSe nanocrystals

Experimental protocol(s) Fast injection of Se precursor into a heated mixture of solvent, ligands and Cd precursor, at high temperature and under inert atmosphere, is a typical method for CdSe nanocrystals synthesis [70]. For the gram-scale synthesis [14, 71], a large reactor with a powerful mechanical stirring is used. A peristaltic pump allows for the fast injection of large volumes (100 mL in 1 s), required for the separation of nucleation and growth phases in the hot-injection method. All compounds used in our synthesis are shown in FIG. II.1 and the detailled experimental protocol can be found in Appendix 1.

Spherical nanocrystals of different sizes, referred to as *nanodots*, have been obtained by Myriam Protière, at a reaction temperature of 250°C by varying the quantity of precursors and/or ligands and solvents [14].

Branched structures have been obtained by lowering the reaction temperature to 230°C. We have obtained a mixture of bipods, tripods and tetrapods and will refer to them as *nanopods*. It is possible that the selectivity towards tetrapods (*i.e.* obtaining a dominating fraction of tetrapods over the other branched morphologies) could be enhanced by lowering further the reaction temperature [15].

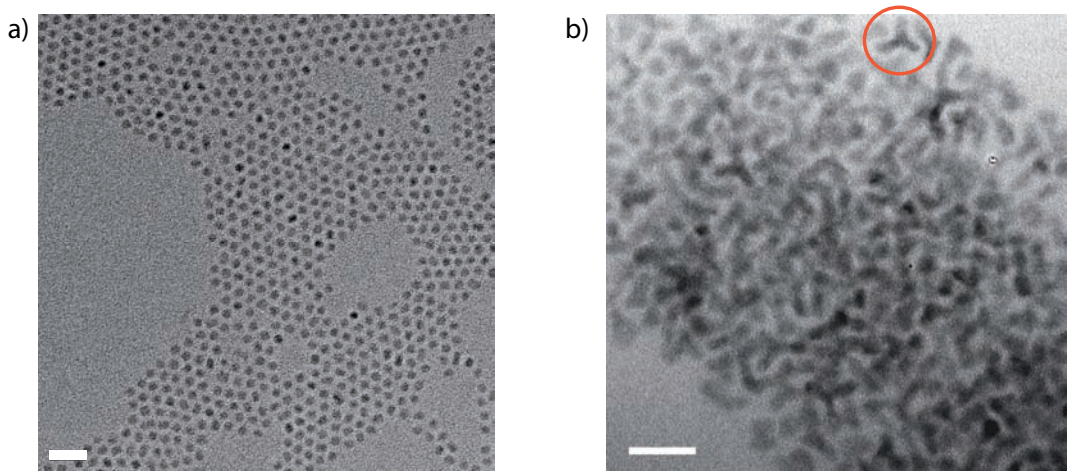

Figure II.2 – Transmission Electron Microscopy images of synthesized nanocrystals In a), 4.1 nm spherical nanocrystals; in b), branched nanocrystals. A nicely oriented tripod or tetrapod is circled in red. Scale bars are 20 nm.

Structures of the obtained nanocrystals TEM images of the nanocrystals are presented in Fig. II.2: in a), spherical nanocrystals of 4.1 nm in diameter, with a polydispersity $\Delta D/D = 7.5\%$; in b), branched nanostructures or nanopods, with core and arm diameters of 3.8 nm and an arm length of 6.3 nm.

The powder XRD profiles of 4.1 nm spherical and branched nanocrystals are shown in Fig. II.3.

The XRD profile of spherical nanodots, Fig. II.3 a), shows that they exhibit the CdSe hexagonal wurtzite structure. The corresponding peaks of bulk wurtzite CdSe are indicated as red bars. In comparison to the bulk values, the nanodot peaks at $2\theta = 41.5°$ and at $53.6°$ are strongly attenuated. This is usual in CdSe nanocrystals and is attributed to defects with the zinc blende cubic structure along the (001) direction [72].

The XRD diffractograms of the nanopods, Fig. II.3 b), shows relatively similar peaks. Here too, the peaks at $2\theta = 41.5°$ and at $53.6°$ have lower relative intensities than what is found in the CdSe wurtzite bulk (red bars). Moreover, the intensities of the peaks located at $2\theta = 29.53°$, $49.14°$ and $58.38°$ peaks are also modified with respect to the intensities of corresponding peaks in the spectra of the nanodots. In Fig. II.3, red and black bars correspond respectively to the bulk CdSe peaks in the wurtzite and zinc blende structure. The peaks of which relative intensities are modified between the diffractorgrams of the dots and of the pods are those that imply both the wurtzite *and* the zinc blende contribution. This is consistent with the coexistence of the two phases in the pods, in opposition to a single wurtzite phase in the dots. Indeed, Luyen *et al.* observed the formation of branched structure, with first the growth of zinc blende cores, followed by the growth of wurtzite arms with $(00\bar{1})$ direction on the $\{111\}$ zinc blende facets of the core, when lowering the reaction temperature (rather than wurtzite cores in the case of

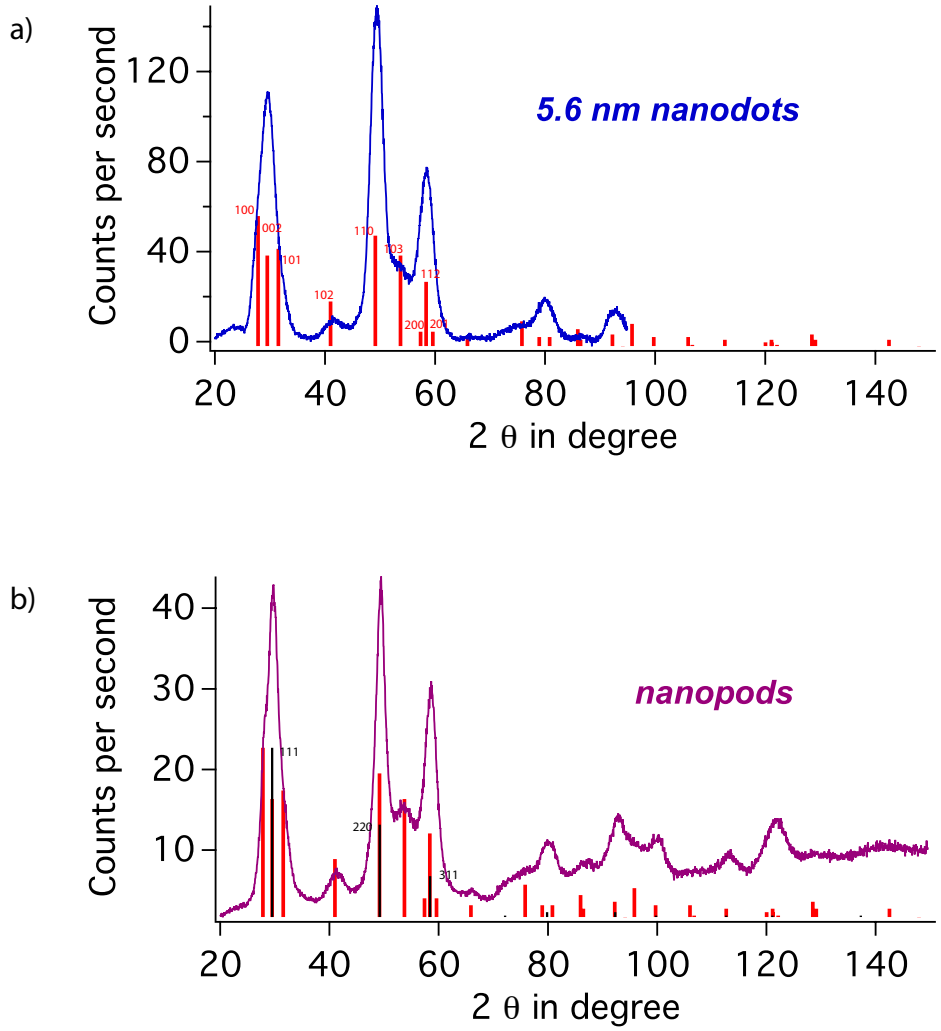

Figure II.3 – X-ray diffraction profiles of the obtained CdSe nanocrystals In a) the diffractogram obtained for spherical 5.6 nm nanocrystals; in b) the diffractogram obtained for nanopods; theoretical peaks for the hexagonal wurtzite structure of bulk CdSe from are indicated as red bars and the ones for the zinc blende structure of bulk CdSe in black (from the JCPDS catalog). Experimental profiles were obtained with Co Kα, $\lambda = 1.789$Å.

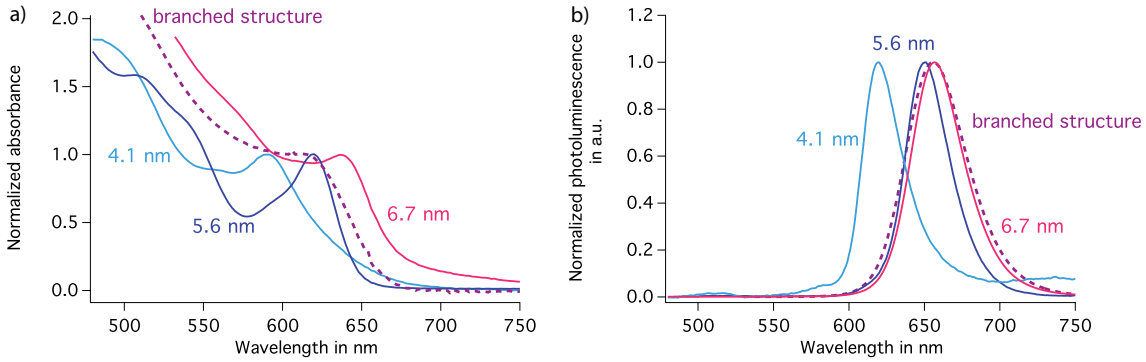

Figure II.4 – Optical absorption and emission of nanocrystals In a) UV-visible absorption spectra around excitonic peaks positions; in b) photoluminescence spectra, with an excitation wavelength of 400 nm.

higher reaction temperatures leading to nanodots) [73].

The deconvolution of the diffractogram obtained with the nanopods in detailed in the Section concerning hybrid films, in Fig. II.24.

Optical characterization We present UV-visible absorption and photoluminescence spectra of nanodots and nanopods in Fig. II.4.

The positions of the absorbance first excitonic peaks, Fig. II.4 a), allows for estimating the nanocrystals diameters using reported correlations between TEM imaging of spherical nanocrystals and their optical spectra [12]. We give in Fig. II.4 the diameters obtained for our nanodots.

The energy band gaps of spherical nanocrystals can be extracted from the maximum of emission spectra. The values, summarized in Table II.1, show the effect of quantum confinement, with larger band gap for smaller nanocrystals.

Table II.1 – Energy band gap E_g of the spherical nanocrystals, obtained from the position of the PL maxima.

Nanocrystals' diameter	4.1 nm	5.6 nm	6.7 nm
E_g	2.00 eV	1.91 eV	1.87 eV

Another effect of quantum confinement can be found in the Stokes shift between the first excitonic peak in absorption and the emission peak for the different sizes of nanodots, namely 50 meV for 6.7 nm nanocrystals, 90 meV for 5.6 nm nanocrystals and 100 meV for 4.1 nm

nanocrystals. The spacing of energy levels in each energy 'bands' increases when the confinement is enhanced and this implies larger Stokes shifts for smaller nanocrystals.

In the case of nanopods, the evaluation of the size can not be done in a straightforward way from the absorption spectrum because confinement in anisotropic structures depends on the detailed aspect ratio. Similarly, the electronic levels of such complex structures require specific investigations, see for example [11].

1.2 Nanocrystals thin film deposition

We have optimized several parameters for the deposition of nanocrystals thin films. Depending on the constraints related to the subsequent use of the films (*e.g.* ligand, thickness, roughness), it was necessary to develop specific deposition methods. As a rule of thumb, concentrated solutions give thicker films. Highly concentrated solutions (*e.g.* 80 mg/mL) cannot be filtered and aggregates of nanocrystals are present on the film, increasing drastically the surface roughness (aggregates can create peaks of 100 nm above the mean surface). While high roughnesses are detrimental for electrical characterizations in sandwich configuration, they could be exploited to build layered heterojunctions with high interfacial area.

Experimental procedures for thin film deposition can be found in Appendix 8.

Spin-coating To obtain very thin and homogeneous films, spin-coating at high speed is the easiest and most reproducible method. Modifying the concentration between 10 mg/mL and 80 mg/mL allows to tune the thickness of the obtained films between 70 nm to 250 nm. The main drawback of the spin-coating method is the loss of a large amount of matter during the spinning process.

Drop-casting Films of large thicknesses can be obtained by drop-casting a small volume of concentrated nanocrystals dispersion: for example, depositing 10 μL at 80 mg/mL resulted in a film thickness of 1 μm. Using a mixture of solvents such as hexane and octane avoids unidirectional evaporation fronts (*e.g.* the coffee stain effect in the case of hexane) and allows to obtain more homogeneous thicknesses on the whole substrate.

Doctor-blade Doctor-blading is an interesting intermediate between spin-coating and drop-casting. This technique allows to use very small volumes of nanocrystals, typically a few μL, without significant loss of matter. The blade spreads the solution more evenly on the substrate than the spontaneous spreading of the drop during drop-casting: this allows to make thin films of good quality, in the 50 nm range for example, which could not be realized by drop-casting.

Doctor-blading requires the use of solvents with intermediate boiling points: if the solvent evaporates too fast (with chloroform for example), the blade does not spread the solution well, and if the solvent evaporates too slowly (orthodichlorobenzene for example), de-wetting appears before the film is dry; surface functionalization should avoid this to some extent. A

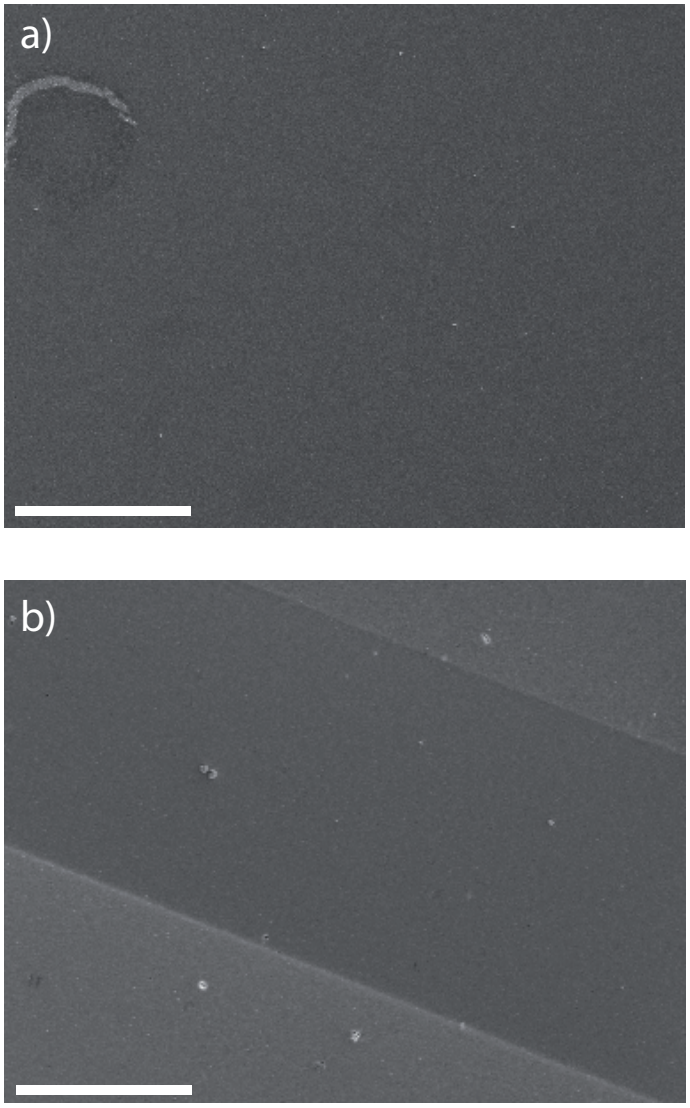

Figure II.5 – Nanocrystals thin films made by doctor blading a) on ITO: one still sees the characteristic structures of the ITO surface (the peak-to-valley roughness of the ITO substrate ranges around 30 nm). The film is thin enough (50 nm) to be conform to the substrate. The film RMS roughness is 5 nm, a little larger than that of ITO, 3 nm. On the upper left corner, a crack leaves the substrate apparent. In b), nanocrystals are deposited on a thermal SiO_2 substrate with patterned gold electrodes (clear zones). Here also, the film is mostly homogeneous and has a low roughness (RMS roughness 1 nm) but presents some pinholes. Roughnesses were determined by AFM imaging. Scale bars are 10 μm.

subtle equilibrium needs to be found between the viscosity of the solution, the boiling point of the solvent and the blade speed.

For low concentrations ($\approx$ 15mg/mL), we doctor-bladed very thin films ($\approx$ 50 nm) on SiO_2 and on ITO substrates. These films are quite homogeneous, as shown by Scanning Electron Microscopy (SEM) imaging. Fig. II.5 presents examples of doctor-bladed thin films on two kinds of substrates: in a) ITO and in b) SiO_2 with patterned gold electrodes. SEM images and RMS roughnesses measured by AFM (Nanosurf Mobile S) show that such thin films of nanocrystals are conform to the substrate (3 nm RMS roughness for ITO and 5 nm RMS roughness for nanocrystals films; 1 nm RMS roughness both for SiO_2 substrates and nanocrystals thin films).

Circumventing pin-holes SEM and AFM can probe relatively small surfaces compared to electrode areas needed in macroscopic electrical characterizations (tens of μm^2 *vs* a few mm^2). Actually, when examining larger surfaces, one sees small cracks or holes that can lead to short circuits (a crack can be seen on the upper left corner of Fig. II.5, for example). These cracks and holes are observed for all different deposition techniques of thin films presented here. Thicker films deposited by drop-casting present large surface roughnesses but usually no cracks or holes going all the way down to the substrate, therefore avoiding short circuits. Cracks and holes are worsened when the films are rinsed with ethanol, acetone, or acetonitrile. We circumvented this issue by repeating the deposition procedure a second time. The cracks have never been found to form throughout two successive layers.

Substrate functionalization Finally, in order to increase the affinity between nanocrystals and substrate, we treated the substrates with mercaptopropyltriethoxysilane (MPTES) or ethanedithiol (EDT). The first molecule, MPTES, has three hydrolizable triethoxy groups facilitating the binding to a SiO_2 substrate [74], and one thiol group of high affinity to the surface of CdSe. The second molecule, EDT, has two thiol groups, meant to bind to the substrate (*e.g.* tin atoms of ITO substrates) and to nanocrystals. Experimental procedure for substrates functionalization can be found in Appendix 7. We tested the effects of these surface functionalizations on SiO_2 and ITO substrates by depositing nanocrystals by dip coating (SiO_2) and doctor blading (ITO). SEM images of the obtained nanocrystal assemblies are shown in Fig. II.6.

Nanocrystals deposited by dip-coating[1] on SiO_2 before MPTES treatment form non homogenous patterns: in some zones, they are densely packed (sometimes forming bilayers), and are absent in other zones. After treatment with MPTES, nanocrystals disperse themselves nicely on the substrate to create a denser, more homogeneous sub-monolayer.

On the other hand, MPTES and ethanedithiol treatment on ITO substrates do not seem to

[1]Manual dip coating in a 10 mg/mL nanocrystals solution was performed to deposit sub-monolayers of nanocrystals, see Appendix 8.

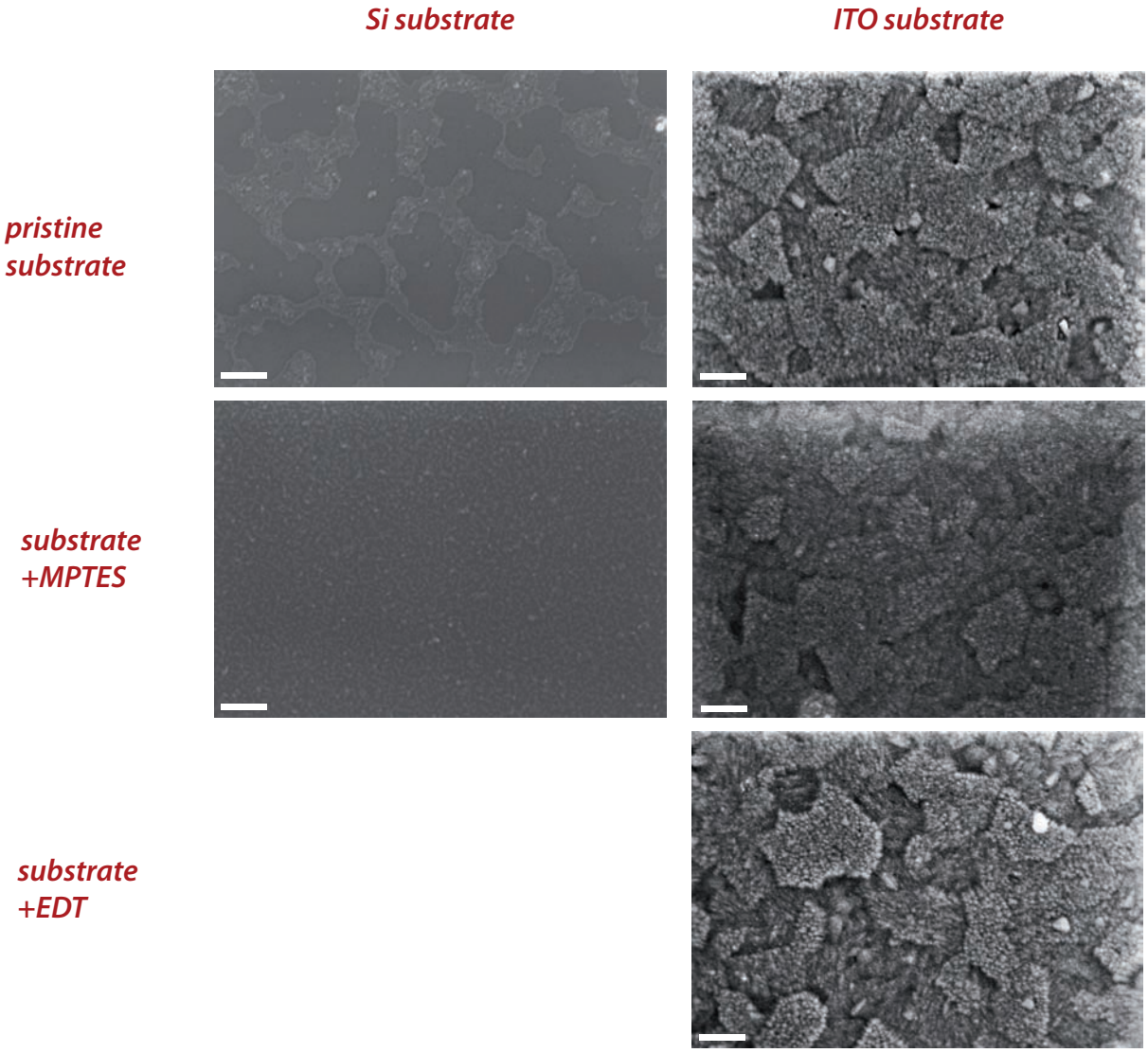

Figure II.6 – Comparison of nanocrystals depositions on SiO_2 and ITO substrates with different types of substrates functionalizations Films are deposited by dip-coating on SiO_2 and by doctor-blading on ITO. Scale bars are 200 nm.

change drastically the repartition of nanocrystals on the substrate. In this case, ITO roughness (3 nm RMS and 30 nm peak-to-valley measured by AFM) dominate the nanocrystals deposition: one must use larger concentrations to form continuous thin films.

In conclusion, substrate functionalization has been successful in the case of SiO_2, using MPTES. In the case of ITO, the deposition of small amounts of nanocrystals is dominated by ITO roughness (nanocrystals tend to aggregate in valleys); the deposition of larger amounts of nanocrystals results in quite homogeneous and conform films, making it difficult to evaluate the impact of surface functionalization.

1.3 Nanocrystals surface functionalization

We have seen in Chapter I, 1.2, that surface ligand exchange is required to enhance conductivity of nanocrystals thin films [5, 18–21]. This is true in particular when the synthesis ligands are long alkyl chains, as in our case (stearic acid and oleylamine, see Fig. II.7). Nanocrystals surface atoms should have a stronger affinity for the new ligands than for the old ones in order for ligand exchange to take place.

Traditionally, ligand exchange reactions were carried out in solution and nanocrystals were recovered in solution. This permits the easy processing of ligand-exchanged nanocrystals. The challenge is to find compatible ligand/solvent couples (and in the specific case of hybrids preparations, the solvent should also be compatible with the polymer).

These limitations have triggered novel surface treatment procedures, where the ligand exchange takes place *after* thin film deposition [5, 20, 21]. Spin-coated thin films (≈ 30 nm) are soaked into a solution of new ligands, that diffuse throughout the film.

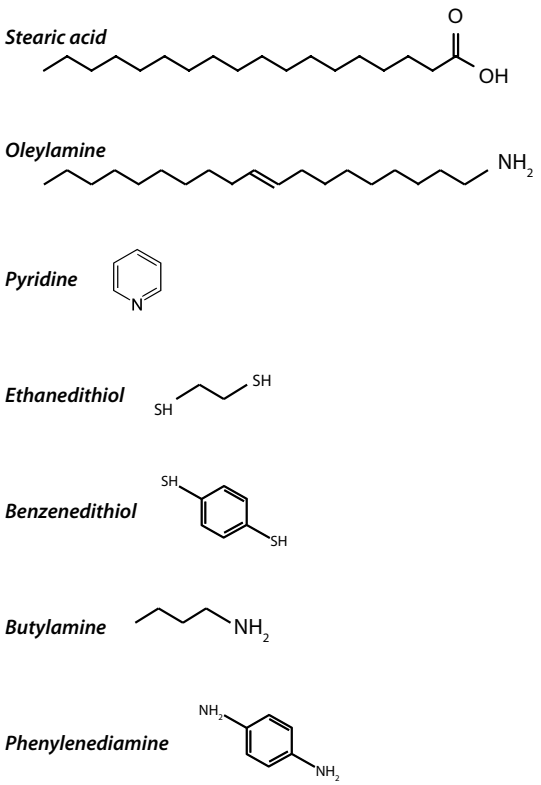

Figure II.7 – Molecules used as ligands in our study

We have developed and optimized ligand treatment protocols both in solution and as thin films to replace stearic acid and oleylamine from the synthesis for smaller molecules, see Fig. II.7.

1.3.1 Solution-phase ligand exchange

In solution, we have treated nanocrystals with pyridine, which is known to bind weakly to the Cd atoms at the surface of CdSe nanocrystals (*e.g.* [75–77]).

Consequently, to perform ligand exchange, we must introduce enough pyridine to bind to surface Cd atoms. Pyridine is added to a chloroform dispersion of nanocrystals. The solution is stirred and heated under reflux and under argon atmosphere. Nanocrystals are recovered by precipitation in hexane and dispersed in pure pyridine for storage. Indeed, it has been shown that due to their small size, pyridine molecules shield only weakly the nanocrystals' Van der Waals attraction. When the nanocrystals are dispersed in pyridine, the dispersion is stable over long times; whereas in other solvents, with the reduced affinity of the ligands towards the solvent, attraction forces dominate and lead to the formation of nanocrystals' dimers or trimers, depending on the concentration of nanocrystals. This microscopic associations eventually lead to macroscopic aggregation [76].

The calculation for the excess of ligand and the experimental procedure are detailed in Appendix 2.

The success and reproducibility of ligand exchange reactions were evaluated from the following experimental indications of surface modification:

- loss of solubility in solvents that were adequate before ligand exchange (chloroform, hexane);
- nanocrystals' photoluminescence quenching, with an example in Fig. II.8 b);
- modification of FTIR spectra, with an example in Fig. II.9.

From the loss of solubility, we found that long ligand exchange times ($\approx$ 12 h) gave more reproducible results than shorter exchange times as were used initially (between 10 min and 1 h, [68]). We attribute this to a variability of the degree of the ligand exchange: may some synthesis ligands (stearic acid and oleylamine) remain at the surface of nanocrystals, and nanocrystals retain their solubility.

First, optical characterizations of 4 nm nanocrystals before and after ligand exchange are presented in Fig. II.8: in a), absorption spectra; in b), PL spectra for different exchange times.

Treating nanocrystals with pyridine in solution provoked a hypsochromic shift of the absorption first excitonic peak. Its displacement is here around 13 nm (50 meV) but can vary slightly from batch to batch, probably depending on the degree of exchange.

Moreover, the PL of the nanodots is very rapidly quenched by the ligand exchange, with a quenching of already 94 % after 2 minutes of exchange, see Fig. II.8 b). This indicates the quick formation of non-radiative decay pathways for excitons. Moreover, we observe an hypsochromic

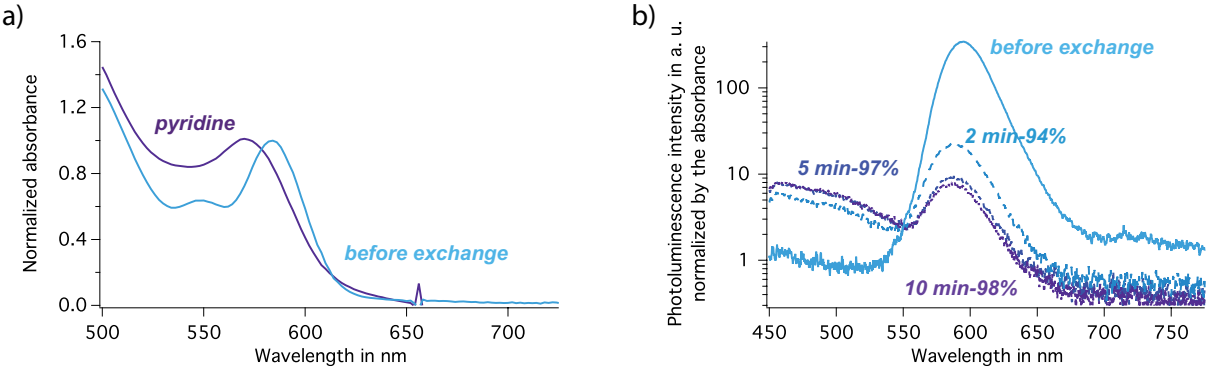

FIGURE II.8 – Optical absorbance and photoluminescence of 4 nm pyridine treated nanocrystals a) the first excitonic peak is blue shifted, here by 13 nm; b) the photoluminescence is blueshifted as well and also quenched by pyridine treatment. The quenching increases with the reaction time.

shift of the PL maximum, as for the first excitonic peak in the absorption spectrum. The shift is here about 7 nm (30 meV).

These blue shifts correspond to a larger effective gap and to a smaller effective diameter of nanocrystals. This indicates that the presence of pyridine enhances the effect of exciton confinement. We will see in the next paragraph that the shift direction depends on the ligand and we will discuss this phenomena at the very end of the Section.

Furthermore, we present in FIG. II.9 the FTIR characterization of solution-phase pyridine exchange. The intensities of peaks relative to aliphatic C-H bonds and to COO^- bonds have decreased during after the treatment, indicating removal of oleylamine and stearic acid. The N-H peak at 3200 cm^{-1} is a signature of both oleylamine and pyridine so it can not be used to estimate the binding of pyridine onto the surface of nanocrystals. To the contrary, the aromatic C-H peak at 800 cm^{-1} is here characteristic of pyridine only. We conclude here by remarking that pyridine has been shown by X-ray photoelectron spectroscopy (XPS) to desorb from the surface of CdSe nanocrystals in vacuum and at room temperature [75]; it is probable that we detect pyridine here because our FTIR measurements were performed at ambient pressure.

Finally, it must be remarked that in the case of pyridine ligand exchange, the nanocrystals must be redispersed in pyridine or in a solvent mix including pyridine. This is commonly observed and is explained by continuous adsorption and desorption of pyridine molecules due to the weak binding nature of pyridine molecules at the surface of CdSe nanocrystals [78]. The fact that pyridine must be present in solution prohibits simple H^1 NMR analysis: although, in principle, bound molecules can be distinguished from free molecules in solution by different peak widths and positions, the very low amount of bound pyridine molecules renders their signal negligible in comparison to that of free molecules in solution.

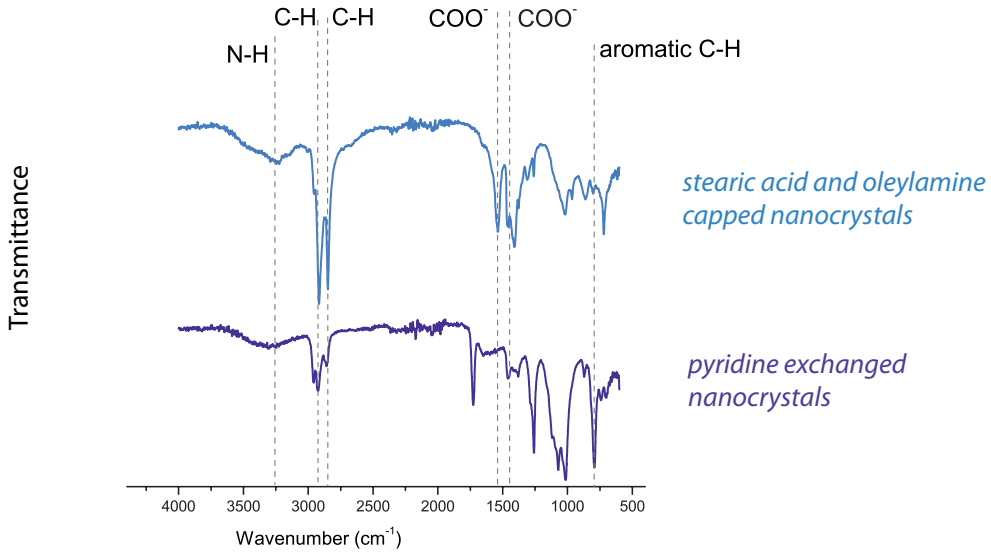

Figure II.9 – FTIR spectra of 4.1 nm nanocrystals before and after solution-phase pyridine exchange in solution.

All these experimental checks of surface treatment prove that synthesis ligand are at least partly removed: losses of solubility and of photoluminescence show that surface passivation is lessened. Additionally, the appearance of aromatic C-H peaks in the FTIR spectra shows that pyridine molecules are present after ligand exchange.

1.3.2 Ligand exchange after thin film deposition [5]

Ligand exchange after thin film deposition enables to test different small molecules that prohibit redispersion of nanocrystals in solution, due to their small size and insufficient sterical repulsion and/or cross-linking character. We used ethanedithiol, benzenedithiol, butylamine and phenylenediamine and pyridine, see Fig. II.7. These molecules possess one or two thiol or amine anchoring groups and aliphatic or aromatic spacers.

Ligand exchange reactions in the solid state are performed by soaking spin-coated thin films (around 30 nm) in a solution of the new ligand in acetonitrile. Films are then rinsed with acetonitrile and dried in the glovebox. Experimental procedures are described in Appendix 3. This study has been performed by Aurélie Lefrançois in our laboratory.

Ligand concentration and reaction times have been optimized for each ligand thanks to FTIR spectroscopy. Spectra are shown in Fig. II.10. Exchanges with thiol-based molecules are quicker than with amine-based molecules. The C-H peaks around 2800 cm^{-1} from alkyl chains in stearic acid and oleylamine decrease in intensity for all new ligands. Contrarily to ligand treatment in solution with pyridine, FTIR spectra also exhibit peaks from new ligands bonds. Amine-treated nanocrystals exhibit a N-H peak at 3200 cm^{-1}. The concomitant decrease of

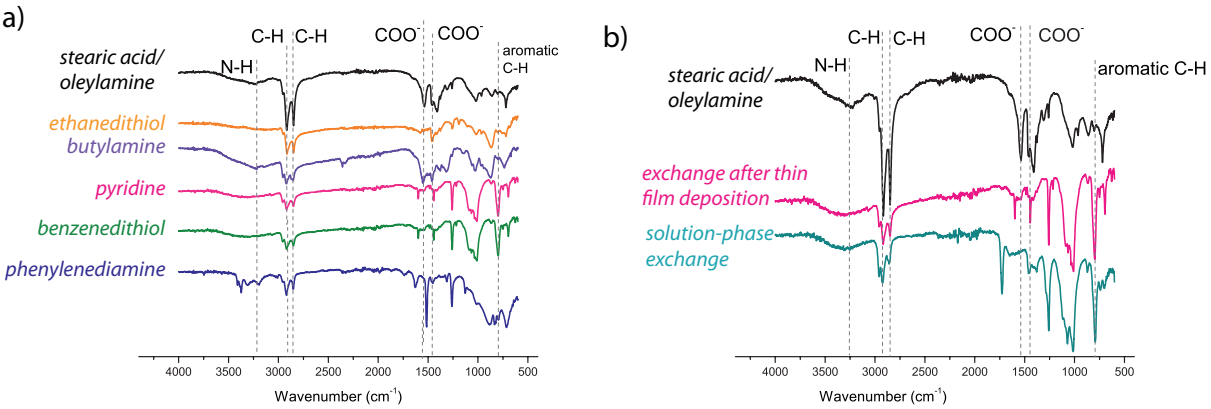

Figure II.10 – FTIR spectra of chemically treated nanocrystals in a), FTIR spectra for synthesis ligands, ethanedithiol, butylamine and pyridine; b) as a comparison, FTIR spectra of nanocrystals treated with pyridine, in solution and after thin film deposition.

C-H peaks shows that these N-H peaks do not only arise from initial oleylamine ligands, but also from the new amine-based ligands. Films treated with aromatic ligands (pyridine, benzenedithiol, phenylenediamine) exhibit a new peak at 800 cm^{-1} corresponding to aromatic C-H bonds. Finally, no new peak is observed for films treated with thiol-based ligands, as in [79]. We interpret this as the formation of thiolate that have high binding energies to CdSe nanocrystals. This explains why thiol treatment proceeds faster and more efficiently than amine treatment.

As in the case of ligand exchange in solution, optical spectra were subject to important changes. For all ligands, the photoluminescence is completely quenched, indicating that the new surface ligands introduce non-radiative decay channels. UV-visible absorption shows that the first excitonic peak is shifted. For thiol-based molecules, the shift was bathochromic (towards longer wavelengths), whereas for pyridine and phenylenediamine, the peak was hypsochromic (as in the case of the pyridine exchange in solution). In the case of butylamine only, the peak does not shift noticeably.

In Table II.2, we present the values of the energy band gap, calculated from the position of the excitonic peak $\lambda_{excitonic\ peak}$ and under the hypothesis that the Stokes shift $\Delta\lambda_{Stokes}$ is not modified by ligand exchange: $E_g^{optical} = 1240/(\lambda_{excitonic\ peak} + \Delta\lambda_{Stokes})$ in eV, with wavelengths in nm.

Optical absorption and emission allow to estimate the band gap of nanocrystals. Positioning the HOMO and the LUMO energy levels relatively to other materials energy levels requires the knowledge of their absolute positions and the use of other techniques, such as Scanning Tunneling Microscopy (STM), Ultraviolet Photoelectron Spectroscopy (UPS) or electrochemistry (*e.g.* [80]).

To investigate the HOMO energy levels after ligand exchange, electrochemical measurements

Table II.2 – Energy gap from optical characterization before and after ligand exchange

Ligand	$E_g^{optical}$ 4.1 nm	$E_g^{optical}$ 5.6 nm
Stearic acid/oleylamine	2.00 eV	1.91 eV
Phenylenediamine	2.02 eV	-
Ethanedithiol	1.99 eV	1.88 eV
Benzenedithiol	1.99	-
Butylamine	-	1.91 eV
Pyridine	2.02 eV	-

have been performed on 4.1 nm spherical CdSe nanocrystals capped with different ligands [5]. The LUMO energy levels could not be measured with confidence due to the sensitivity to air, the setup at that time being outside the glovebox.

Nanocrystals were deposited as thin films from a hexane:octane solution onto the Pt work electrode and measured in 0.1 M tetrabutylammoniumhexafluorophosphate in anhydrous acetonitrile, *vs* ferrocene/ferrocinium. Intensities of signals arising from nanocrystals rather than from the ligands or from the electrolyte are usually low. Consequently, the more sensitive differential pulse voltammetry (DPV) technique was used rather than cyclic voltammetry.

Typical oxidation DPV curves are presented in Fig. II.11. The oxidation curve of 4.1 nm nanocrystals before ligand exchange exhibits an oxidation peak at 0.87 V. The oxidation curve of phenylenediamine in solution presents two oxidation peaks, that we also find in the spectrum of ligand-exchanged nanocrystals. On this last curve, we see that the oxidation peak was shifted by 50 mV to 0.82 V.

The position of the peak allows to determine the HOMO energy level of nanocrystals with the equation:

$$E_{HOMO} = -e\ (V_{ox} + 4.8)eV \tag{II.1}$$

Measured oxidation potentials and the corresponding HOMO energy levels for pyridine, ethanedithiol and phenylenediamine treated thin films are shown in Table II.3. HOMO energy levels were raised for all ligand exchanges performed in comparison to the HOMO energy level of nanocrystals with synthesis ligands. The HOMO maximal shift was +160 meV for ethanedithiol-treated nanocrystals.

Finally, we performed small angle X-ray diffraction measurements to determine the average

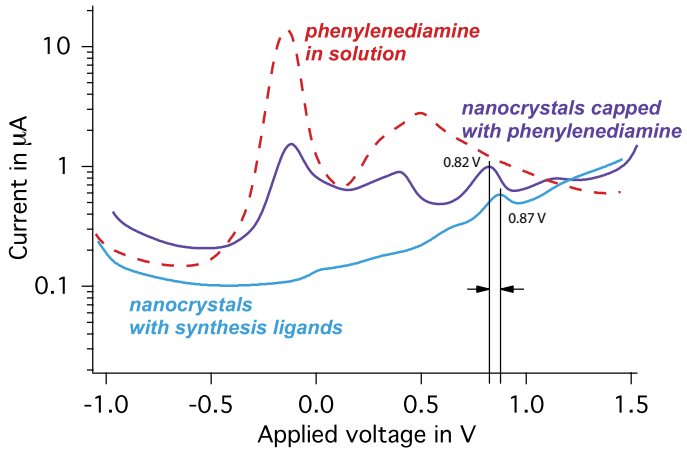

Figure II.11 – Oxidation curves of 4.1 nm nanocrystals before and after ligand exchange, and of the new ligand in solution, as measured by DPV The nanocrystals were deposited by drop-casting from a 9:1 hexane:octane solvent mix onto the Pt work electrode and were measured in 0.1 M tetrabutylammoniumhexafluorophosphate in anhydrous acetonitrile, against ferrocene/ferrocinium. The reference electrode was Ag and the counter electrode Pt. The scan speed was 10 mV/s.

Table II.3 – HOMO level of 4.1 nm CdSe nanocrystals, from DPV measurements Electrochemical measurements of HOMO energy levels of drop-cast 4.1 nm nanocrystal thin films, capped with different ligands [5].

	Stearic acid/oleyamine	Pyridine	Ethanedithiol	Phenylenediamine
Oxydation peak	$0.87V$	$0.80V$	$0.71V$	$0.82V$
HOMO	**-5.67 eV**	**-5.60 eV**	**-5.51 eV**	**-5.62 eV**

distance between nanocrystals on the films, before and after exchange. In Fig. II.12, the XRD diffractogram obtained for a spin-coated film of 4.1 nm CdSe nanocrystals before ligand exchange and after EDT treatment by soaking the film 6 minutes in an 0.1 M EDT in acetonitrile solution are shown. The steep baselines come from the experimental geometry. The peak/shoulders arise from coherent diffraction on the periodic lattice of nanocrystals.

Before exchange, the average distance d between the centers of adjacent 4.1 nm nanocrystals is 5.7 nm, as obtained from the position of the diffraction peak with the formula $d = \lambda/2\sin\theta$, where λ is the wavelength of the X-ray radiation. This corresponds to a distance between the surfaces of neighboring nanocrystals of 1.6 nm. For 5.6 nm nanocrystals (not shown), the average distance between centers was 7.5 nm, resulting in a distance between surfaces of around 0.9 nm.

After the exchange with EDT, the diffraction peak is less well defined, indicating a lower

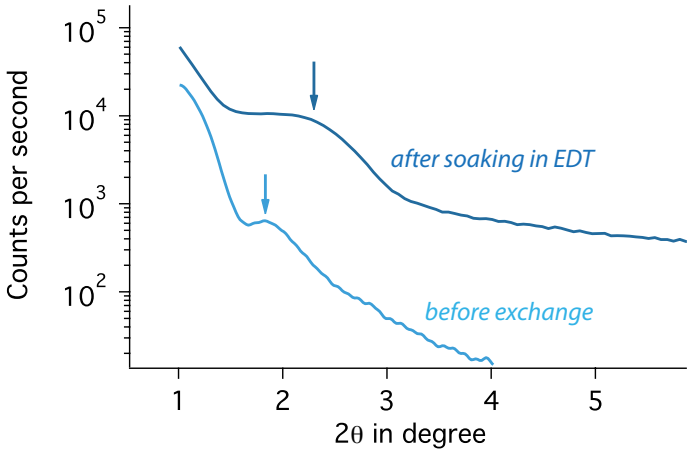

FIGURE II.12 – Small angle X-ray diffraction profiles of a 4.1 nm nanocrystals film before and after ligand exchange The arrows indicate the angles used to determine the interparticle distances.

degree of order in the film. The average distance between adjacent centers of 4.1 nm nanocrystals is estimated between 4.1 and 4.9 nm. This can correspond to a distribution of surface-surface distances, from direct contact to by 0.4 nm.

1.3.3 Modification of the energy gap due to ligand exchange

Optical absorption and electrochemistry measurements show that the nanocrystals' energy level positions and energy gaps change, depending on the nature of their surface ligands. This modification is a widely observed phenomena (*e.g.* [20, 21, 81–83] among many others) and finds several different explanations in the literature, namely:

- enhanced or reduced delocalization of the exciton into the ligand shell [83];
- change of the dielectric constant of the surrounding media–this was used to model successfully solvatochromism [84] and was evoked to explain the Stark shift [85];
- coupling of exciton wavefunctions from different quantum dots [86].

Here we focus on an explanation by a change in the dielectric constant of the surrounding media. Solvatochromism of CdSe nanocrystals has been successfully explained by such a model, as well as the absorption shift measured between the liquid and the solid phases.

Change in dielectric constant First, we calculate the effective constant ϵ_{eff} of an assembly of nanocrystals in an organic matrix (the ligands), depending on the dielectric constant of the matrix and the proportion of nanocrystals in the matrix (*a priori* related to the size of ligands). Then, we calculate the optical gap modification of a CdSe nanocrystal in a matrix of dielectric constant ϵ_{eff}.

Bruggeman's equation for effective media is:

$$\sum_i \delta_i \frac{\epsilon_i - \epsilon_{eff}}{\epsilon_i + (n-1)\epsilon_{eff}} = 0 \tag{II.2}$$

where i is the index on the different phases, δ_i the volumic fraction occupied by phase i, ϵ_i the dielectric constant of phase i and ϵ_{eff} the effective dielectric constant of the complex material. n is the number of Euclidian dimensions of the system, 3 in our case.

We consider two phases: the nanocrystals and the ligand 'sea'. The nanocrystals can occupy maximally 74 % of the volume (close-packing of spheres). A random close-packing leads to an occupied fraction of 64 %.

For nanocrystal films before ligand exchange, used as a reference, we use the dielectric constant of stearic acid: $\epsilon_{AS} = 2.3$ and a random close packing of spheres. We consider spheres made of nanocrystals+ligand coronae. From small angle X-ray diffraction measurements, we have determined average interparticle distances to be 7.5 nm (for 5.6 nm nanocrystals) and 5.65 nm (for 4.1 nm nanocrystals), and we use these values as the diameter of randomly close-packed spheres. We obtain $\epsilon_{eff} = 3.36$ (for 5.6 nm nanocrystals) and $\epsilon_{eff} = 3.26$ (for 4.1 nm nanocrystals).

Following Jdira *et al.* [87], we relate the optical gap of a nanocrystal to its HOMO/LUMO gap and polarization energy Σ and Coulombic attraction between electron and hole J_{e-h} energies by :

$$E_{opt} = E_{HOMO/LUMO} + 2\Sigma - J_{e-h} \tag{II.3}$$

And we calculate the polarization and Coulombic energies from the mismatch of dielectric constants of nanocrystals ϵ_{NX}[2] *vs* the surrounding medium ϵ_{eff}:

$$\Sigma = \frac{\epsilon_{NX} - \epsilon_{eff}}{\epsilon_{NX}\ (\ \epsilon_{NX} + \epsilon_{eff})} (1/\alpha - 0.376\alpha + 0.933) \frac{e^2}{8\pi\epsilon_0 r_{NX}} \quad \text{with} \quad \alpha = \frac{\epsilon_{NX}}{\epsilon_{NX} + \epsilon_{eff}} \tag{II.4}$$

and

$$J_{e-h} = (\ \frac{1}{\epsilon_{eff}} + \frac{0.79}{\epsilon_{NX}}\ )\ \frac{e^2}{4\pi\epsilon_0 r_{NX}} \tag{II.5}$$

The polarization energies are $\Sigma = 56\ meV$ (for 5.6 nm nanocrystals) and $\Sigma = 79\ meV$ (for 4.1 nm nanocrystals), while Coulombic attraction energies are $J_{e-h} = 205\ nm$ (for 5.6 nm nanocrystals) and $J_{e-h} = 284\ nm$ (for 4.1 nm nanocrystals).

[2]The dielectric constant of CdSe nanocrystals is different from the dielectric constant of bulk CdSe due to polarization effects at the surface. We use $\epsilon_{NX} = 8$ as measured in [88].

To obtain the energy shifts measured optically for EDT-treated nanocrystals by using $\epsilon_{EDT} = 2.2$, the nanocrystals phase needs to account for 59 % of the total volume (for 5.6 nm nanocrystals) or 44 % of the total volume (for 4.1 nm nanocrystals). These values are lower than in the case of a random close-packing of spheres and indicate that the ligand sea is not limited to coronae around nanocrystals. This is in agreement with the evaluation of [20].

For butylamine and pyridine ligands, we could not reproduce the optical shifts with the dielectric constants 5.4 and 12.5 found for these molecules in solution. This leads us to one of the limits of the effective medium model. Ligands, if bound to the surface, will not have the same dielectric properties as free molecules in solvents. Moreover, ligand-nanocrystal interactions most probably modify electronic states of both the ligand molecule and the nanocrystal. This can result in modification of nanocrystals couplings (*e.g.* tunneling probabilities) or of the extension of wave functions. These phenomena are not taken into account by the simple effective medium model. In conclusion, there is more to our optical absorption shifts than an effective medium approximation of the change in the dielectric constant, as was also pointed out in [20, 21, 89] for PbSe nanocrystal thin films.

In conclusion, we have synthesized, deposited and functionalized nanocrystals. Spin-coating, drop-casting and doctor-blading have been performed to realize thin films of different thicknesses and allow for different electrical measurements by reducing roughnesses and eliminating pinholes. Ligand exchange after thin film deposition has been performed for five different small molecules, and surface modifications have been characterized.

2 Characterization and deposition of P3HT

2.1 Material parameters

We use commercially available regioregular poly(3-hexylthiophene) from Sigma-Aldrich and Merck. As we have seen in the previous chapter, charge transport in P3HT depends on molecular weights, so we fractioned the commercial batch from Merck with the following solvent sequence: acetone, hexane, dichloromethane, tetrahydrofuran and chloroform [90], as detailled in Appendix 4.

The Sigma-Aldrich sample and the fractions of the P3HT from Merck were studied by absorbance, photoluminescence, and size-exclusion chromatography (SEC), see Fig. II.13. SEC was performed at the Warsaw University of Technology, in Poland, by M. Zagorska, using polystyrene standard. For further studies, we used:

1. P3HT1 (from Sigma-Aldrich), with low molecular weight M_n=9.8 kDa, high polydispersity index D=3.75 and low regioregularity RR (indicated as > 90 % by the supplier, measured 91 % by H^1 NMR, see Appendix 4 and [91]);

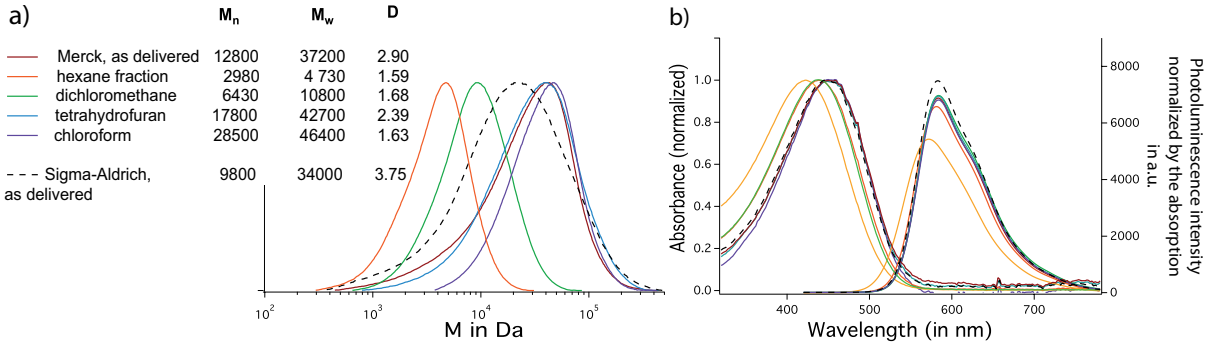

FIGURE II.13 – Steric exclusion chromatography, absorbance and photoluminescence of the different P3HT batches in a) results of the size-exclusion chromatography of P3HT1 from Sigma-Aldrich and of P3HT from Merck and its fractions (the chloroform fraction is referred to as P3HT2 in the following); b) absorbance and photoluminescence (excitation 400 nm) of these samples. The table gives values of molecular weight in number M_n and mass M_w and polydispersity indices D for each fraction.

2. P3HT2 (chloroform fraction from Merck), with higher molecular weight M_n=28.5 kDa, low polydispersity index D=1.63 and higher regioregularity (RR 95.9 % given by the supplier).

2.2 P3HT thin films

P3HT can be deposited as a thin films by a large variety of methods. We have explored and optimized drop-casting under solvent saturated atmosphere and spin-coating. Appendix 8 gives the precise experimental procedures.

2.2.1 Deposition methods: spin-coating, drop-casting

Depending on the characterization techniques, we need to process films of different thicknesses. OPV, CELIV, absorbance measurements call for thin films (100-200 nm) whereas TOF measurements necessitate thicker films ($> 1\ \mu m$).

Spin-coating is ideal to realize a homogeneous thin film with a small roughness. For example, film thicknesses ranging from 40 nm to 300 nm have been obtained by using chlorobenzene (CB) and varying the P3HT concentration from 10 mg/mL to 40 mg/mL.

Drop-casting In order to make thicker films, we use low concentrations of P3HT in orthodichlorobenzene (ODCB) and drop-cast the solution onto the substrate. As much solution as possible before overflow is deposited on the substrate, and the film is left to evaporate under a Petri dish. Full evaporation of the film takes around one week. The obtained films are 1 to several μm thick and mirror-like (RMS roughnesses measured by profilemeter are 50 nm for 5 μm thick films).

2.2.2 P3HT structural arrangement in thin films

We have studied the influence of the deposition method and of the solvent on the structural properties of the films by grazing incidence X-ray diffraction (GIXRD) measurements and by optical absorption and emission studies.

Grazing incidence X-ray diffraction We studied the crystalline structure of P3HT by GIXRD in order to probe the crystallinity of samples in the direction perpendicular to the substrate and in a thin region at the surface of the films.

In Fig. II.14 a), we present the experimental GIXRD profiles of P3HT thin films obtained with P3HT1 by spin- and drop-casting from ODCB and chloroform ($CHCl_3$) solutions, on ITO substrates. Diffraction profiles are dominated by the (100) peak, located at $2\theta = 6.3°$ (λ=1.789 Å), corresponding to the interchain periodicity of 1.6 nm. The distribution of orientation of the chains was checked by rocking ω scans and we found that P3HT films are truly polycrystalline, presenting all orientations of the crystallites (3D powders). This crystallinity is very pronounced in the case of ODCB drop-cast films, that also exhibits second and third order diffraction peaks: the solvent evaporation in this case is very slow so that polymer chains have time to organize in a more regular fashion. All films also exhibit a large peak around $2\theta = 28°$, that corresponds to π-stacking, with a periodicity of 0.38 nm.

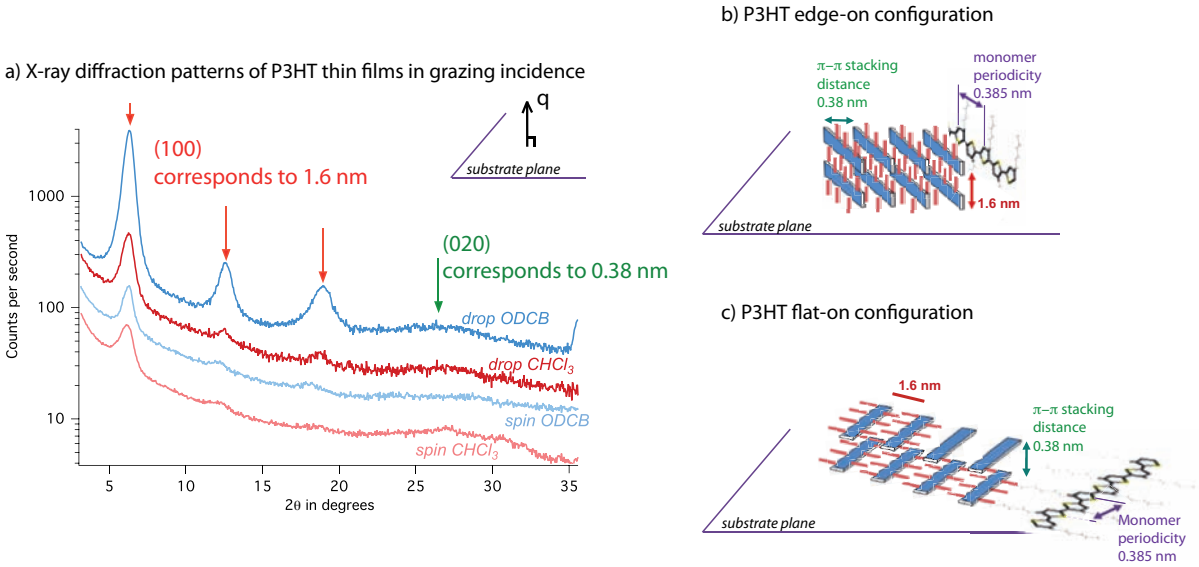

Figure II.14 – X-ray diffraction profiles of P3HT1 thin films, obtained in grazing incidence In a): diffractograms of samples made with P3HT1 by different deposition methods and obtained with λ = 1.789Å. Intensities were normalized by counting times and traces shifted vertically for clarity. We indicate the peak nomenclature and the periods in real space to which they correspond. In b) and c), schematic views of the edge-on and flat-on crystalline configurations of P3HT.

Moreover, the width Δ of the diffraction peaks gives the coherence length ξ of crystalline domains through the application of the Scherrer formula $\xi = K\lambda/\Delta\cos\theta$, where K is the the shape-factor (0.9 for spherical domains) and λ the wavelength of the X-ray radiation, 1.789 Å. With this formula, we found coherence lengths of 140 Å for the drop-cast film from ODCB, 135 Å for the spin-coated film from ODCB, 118 Å for the drop-cast film from $CHCl_3$ and 99 Å for the spin-coated film from $CHCl_3$. Thus, ODCB-based films exhibit larger crystalline domains than $CHCl_3$-based ones.

Finally, drop-cast films of P3HT1 and P3HT2 from ODCB solutions are compared in Fig. II.15. The quality of diffractograms is very similar, with three intense orders of diffraction in the (h00) directions and a π-stacking signal at $2\theta = 28°$. The widths of the (100) peaks give slightly different crystallite sizes for both P3HT films, namely 140 Å for P3HT1 and 130 Å for P3HT2.

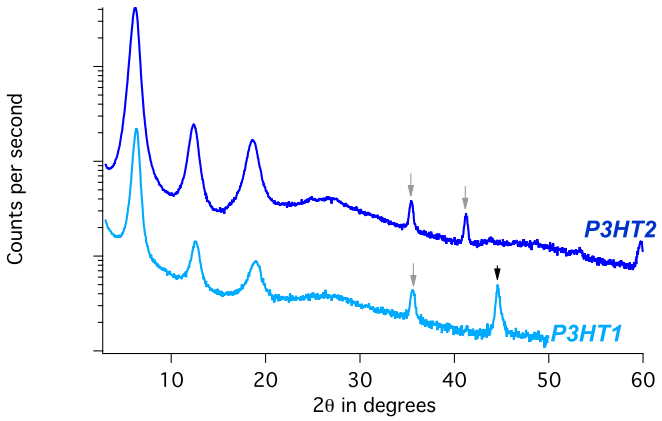

Figure II.15 – GIXRD profiles of P3HT thin films The films were made with P3HT1 and P3HT2. Intensities were normalized by counting times and traces shifted vertically for clarity. The black arrow indicates the signal of Al (upper electrode); the gray ones are from ITO (substrate).

Optical characterizations Fig. II.16 present absorption spectra and PL spectra of P3HT1 solutions and thin films (spin and drop-cast) for three different solvents: $CHCl_3$, CB and ODCB, which boiling points are 61°C, 132°C and 180.5°C, respectively. The use of one or the other thus influences thin film deposition rates and crystallinities.

The results are summarized in Table II.4. From this table, we see that the peak positions depend on 1) whether P3HT1 is in the liquid or in the solid phase; 2) the deposition method. While peak positions of thin films do not depend on the solvent, peak intensities depend strongly on the three factors (liquid *vs* solid, solvent, deposition method).

Peak attribution and analysis was made following the works of Spano *et al.* [92, 93]. Using $CHCl_3$ and isodurene, the authors found that emission in regioregular P3HT arises from weakly

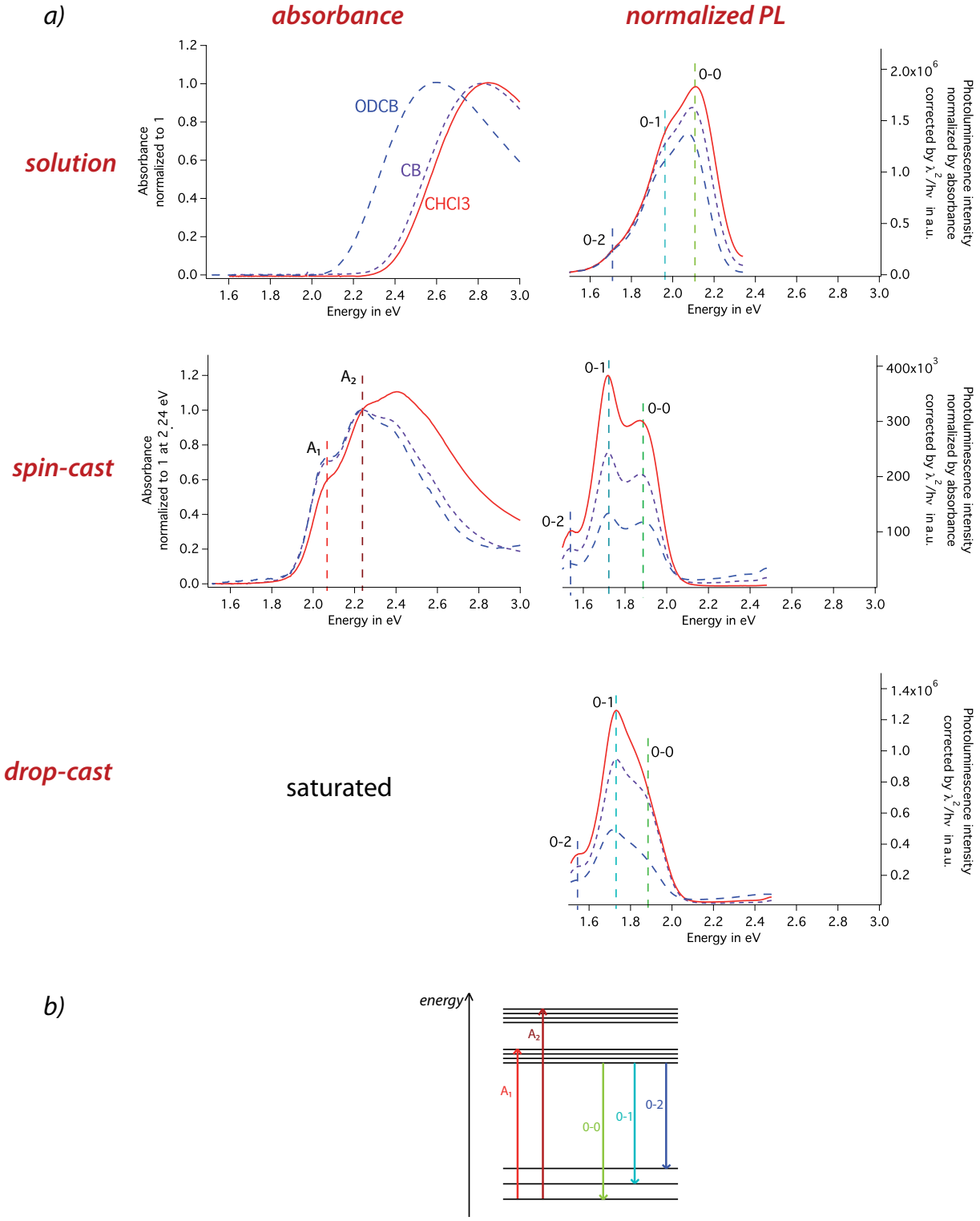

Figure II.16 – Optical characterizations of P3HT1 thin films a) UV-vis absorption and PL spectra of P3HT1 spin-coated thin films and solutions with different solvents (the absorbance of drop-cast films is too large to be measured); b) assignement of the optical transitions for a weakly coupled H-aggregate, as in [92]. Excitation wavelength for PL measurements: 480 nm.

coupled H-aggregates (*i.e.* from interchain excitons in π-stacked materials).

Solutions Absorption spectra of P3HT1 solutions are rather broad and featureless. Photoluminescence spectra are narrower, and exhibit vibronic structures, with the appearance of two shoulders around 640 nm and 720 nm. These observations are similar to the findings of Banerji *et al.* [94] for P3HT in CB. In presence of important conformational disorder in solution, the absorption of a photon can lead to numerous excited states, resulting in a featureless absorption band. The relaxation leads to a common emitting state, namely an intrachain exciton, that is more localized than the excited states probed by absorption, and less influenced by disorder, leading to a more structured emission spectrum.

Table II.4 – Energy values from P3HT1 optical spectra Energy gaps are deduced from the absorption edge. Position of absorption and PL peaks are indicated, with maxima in bold. Stokes shift are calculated from the difference between the emission maximum and the absorption edge [94].

		Band gap	Absorption		Emission			Stokes
			A_1	A_2	0-0	0-1	0-2	shift
Solution	$CHCl_3$	**2.32 eV**	2.76 eV		**2.12 eV**	1.96 eV	1.72 eV	0.2 eV
	CB	**2.29 eV**	2.73 eV		**2.10 eV**	1.95 eV	1.72 eV	0.19 eV
	ODCB	**2.26 eV**	2.70 eV		**2.08 eV**	1.93 eV	1.72 eV	0.18 eV
Spin	$CHCl_3$	**1.92 eV**	2.07 eV	2.25 eV	1.89 eV	**1.72 eV**	1.55 eV	0.2 eV
	CB	**1.91 eV**	2.06 eV	2.25 eV	1.89 eV	1.72 eV	1.55 eV	-
	ODCB	**1.91 eV**	2.06 eV	2.23 eV	**1.90 eV**	1.72 eV	1.55 eV	0.01 eV
Drop	$CHCl_3$	-	-	-	1.54 eV	**1.74 eV**	1.85 eV	-
	CB	-	-	-	1.54 eV	**1.74 eV**	1.85 eV	-
	ODCB	-	-	-	1.54 eV	**1.72 eV**	1.85 eV	-

Spin-cast films Absorption and emission spectra of spin-cast films are very different from those in solution. All peaks are shifted towards smaller energies and amplitudes are modified due to the semi-crystalline structure of P3HT1 thin films. The energy gap is smaller than in solution and does not depend on the solvent, with a value of 1.91 eV. This corresponds to a larger delocalization (conjugation) length, and is due to a decrease in conformational disorder since P3HT1 organizes on the substrate.

Absorption spectra present vibronic structures. The relative intensities of the peaks depend

on the solvent: different excitations pathways are favored by different configurations.

Spano *et al.* have developed a method to deduce the magnitude of the exciton bandwidth[3] W from the relative intensity of A_1 and A_2 peaks [93], assuming a Huang-Rhys factor of 1:

$$\frac{I_{A_1}}{I_{A_2}} = \left(\frac{1 - 0.24W/E_p}{1 + 0.073W/E_p}\right)^2 \tag{II.6}$$

E_p is the energy of the vibrational mode dominating the transition, taken as the energy of C=C stretch ($E_p = 0.18eV$). From this formula, the exciton bandwidth W is 153 meV for the film spin-coated from $CHCl_3$, 106 meV for the one spin-coated from CB-based and 98 meV for the one spin-coated from ODCB. This means that the intermolecular coupling decreases when the film is deposited from a solvent with higher boiling point, under the assumption that films can be modeled by H-aggregates. This can moreover be related to the enhancement of crystallization. Indeed, an inhomogeneous film with a mix of crystallized and amorphous domains, as opposed to an amorphous film, may present lower *average* intermolecular electronic couplings than more homogeneous, isotropic films.

Finally, in emission spectra, 0-1 transitions dominate for all solvents. From [34], we take:

$$\frac{I_{0-0}}{I_{0-1}} = \frac{(1 - 0.24W/E_p)^2}{2e^{-2}(1 + 0.073W/E_p)^2}\frac{\sigma^2}{W^2} \tag{II.7}$$

with σ the half width at $1/e$ maximum of the Gaussian distribution of site-energy disorder. From this equation, we see that more intense 0-1 transitions relative to 0-0 transitions indicate a larger exciton bandwidth and/or smaller energy disorder. From the emission spectra of spin-cast films, with the values of the exciton bandwidth determined above by absorption spectroscopy, we find $\sigma = 59$ meV for the film spin-coated from $CHCl_3$, 45 meV for the one spin-coated from CB and 44 meV for the one spin-coated from ODCB.

Drop-cast films Absorbance of drop-cast films can not be measured because of their large absorption. Consequently, we present only their PL spectra. These show no red shift compared to spin-coated films. Peaks from the 0-1 and 0-2 transitions keep the same relative intensities than in spin-cast films. Peaks from the 0-0 transitions lose in relative intensity compared to the 0-1 transition. As detailed above, this is an indication for a decreased disorder and/or larger exciton bandwidth (larger intermolecular coupling) in comparison to spin-cast films.

Conclusion In conclusion, we have developed P3HT1 thin film processing for different thicknesses, in order to use them for different characterizations, and to use the deposition protocols as a base for hybrid thin film deposition. Spin-casting produces thin films ($\approx$ 100 nm) of good quality: thickness homogeneity over the whole surface, low roughness, crystallinity. Drop-casting, particularly processed from ODCB, can produce thick films ($> 1\ \mu m$) of very good

[3]The exciton bandwidth W is four times the intermolecular coupling energy for a one-dimensional linear aggregate [34].

quality: low roughness, high crystallinity, low disorder and/or high intermolecular coupling.

3 Hybrid blends and thin films

In this Section, we present the processing of hybrid materials, from their blending in solution to the film depositions and characterizations.

When preparing donor-acceptor blends in solution, the most practical way is to use mass ratios of the components. On the other hand, volume ratios of the components are more relevant when studying optical and transport properties of thin films. In Table II.5, we present typical weight ratios used in organic and hybrid photovoltaics and the corresponding volume ratios, for P3HT:CdSe and P3HT:PCBM heterojunctions.

Table II.5 – Weight *vs* volume proportions of acceptors in P3HT:CdSe and P3HT:PCBM heterojunctions Calculated with the following density values: bulk CdSe 5.81g/cm^3; P3HT 1.1 g/cm^3; PCBM 1.72 g/cm^3.

$m_{P3HT} : m_{acceptor}$	*Fraction of acceptor in weight*	*Fraction of acceptor in volume*	
		P3HT:CdSe	*P3HT:PCBM*
1:1	50 wt%	16 vol%	39 vol%
1:3	75 wt%	36 vol%	66 vol%
1:5	83 wt%	49 vol%	76 vol%
1:9	90 wt%	63 vol%	85 vol%

For a similar weight ratio, the volume occupied by the PCBM is larger than that occupied by CdSe nanocrystals. This is one of the many factors to take into account when comparing all-organic and hybrid solar cells.

A limit for blending nanocrystals and polymers in solution is the possible aggregation of nanocrystals at high concentrations.

In a donor-acceptor heterojunction of type I, schematized on Fig. II.17 a), excitons can dissociate at the interfaces between donor and acceptor phases. This phenomenon can be studied by measuring the PL of the blends: the quenching of the PL of both materials indicates an effective charge transfer preventing exciton recombination. Fig. II.17 shows PL quenching for hybrid solutions made of P3HT1 and 6.7 nm nanodots with b) synthesis ligands and c) pyridine ligands. While the fluorescence of CdSe nanocrystals is not detected due to the overlap with that of P3HT, PL quenching of P3HT increases with the amount of nanocrystals added to the blend. Due to stronger electronic couplings between hybrid compounds, the quenching of

the PL of P3HT is more efficient for pyridine-treated nanocrystals than for nanocrystals with synthesis ligands.

Hybrid solution blending and handling procedures can be found in Appendix 5. When the nanocrystals were treated with pyridine, they are dispersed in a 1:9 pyridine:S solvent mix (S = ODCB, $CHCl_3$, etc.) to ensure colloidal stability; resulting in a hybrid solution in a 1:19 pyridine:S solvent mix.

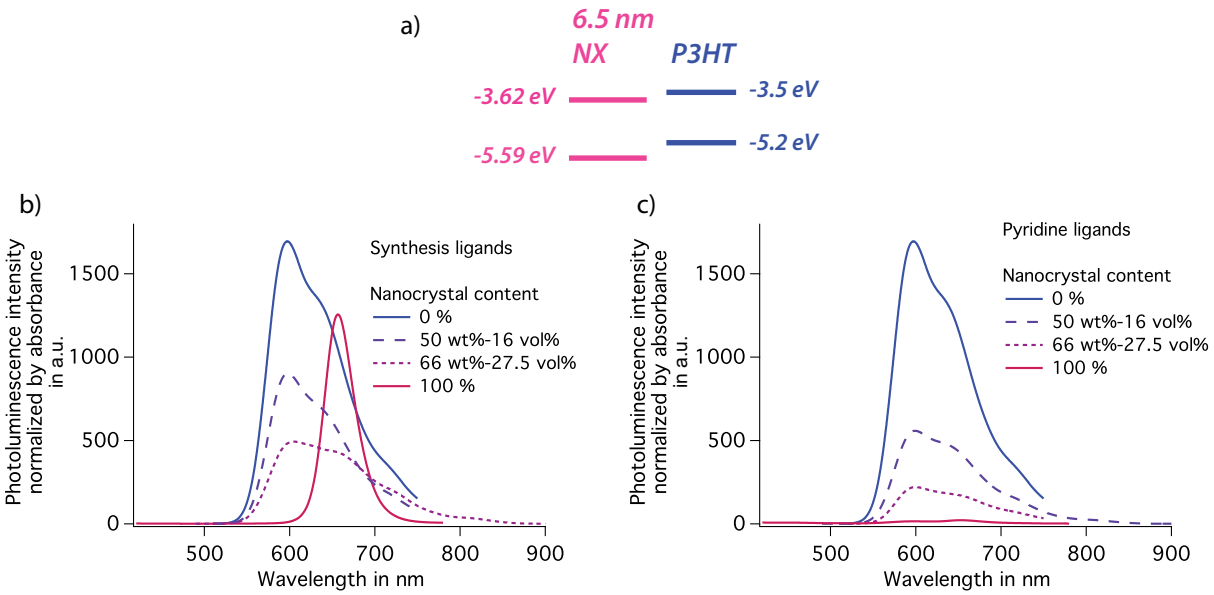

Figure II.17 – Charge transfer and PL quenching in hybrid solutions in a) the energy diagram of an hybrid, using the energy levels of 6.5 nm nanocrystals with synthesis ligands from [95]; in b) and c) PL of hybrid solutions made with 6.7 nm nanocrystals with: in b) synthesis ligands and in c) pyridine ligands (1:19 pyridine:ODCB solvent mix). Pure P3HT and nanocrystals PL spectra are given for comparison. These studies were done with P3HT1 and with an excitation wavelength of 450 nm for the P3HT and hybrid solutions and of 400 nm for the nanocrystal solution.

3.1 Film deposition

We have used different techniques to deposit hybrid bulk heterojunctions[4]: Layer-by-Layer dip-coating when the components can not be blended in solution due to various solubilities; spin- and drop-casting when components can be mixed in solution. Film deposition protocols are detailled in Appendix 8.

Dip-coating To build-up hybrid thin films in a Layer-by-Layer fashion, dip-coating is an interesting technique.

[4]Planar heterojunctions can be obtained by a variety of techniques by depositing the P3HT layer first and nanocrystals on top: it is easier to find a solvent that disperse nanocrystals without redissolving the underlying P3HT layer.

We used specifically functionalized nanocrystals and P3HT, developed by Julia De Girolamo [96–98] and shown on Fig. II.18. The 1-(6-mercaptohexyl)thymine (MHT) ligands on the nanocrystals and the diaminopyrimidine groups on P3HT bind *via* triple hydrogen bonds. To proceed to the Layer-by-Layer deposition and at the same time avoid the redispersion of any of the two phases in the second one during the deposition, nanocrystals and polymers are dispersed in orthogonal solvents, respectively a 1:10 mix of DMF:methanol and chlorobenzene.

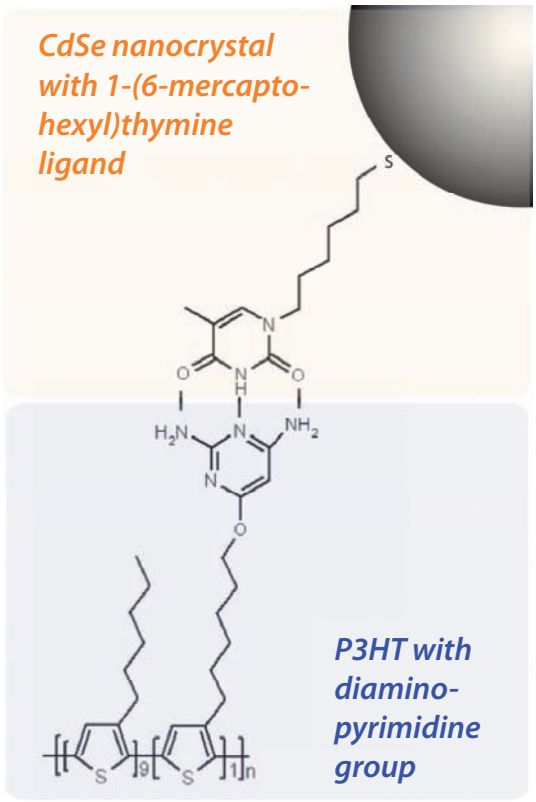

Figure II.18 – Triple hydrogen bonding between specifically functionalized nanocrystals and functionalized P3HT This system was developed and optimized by Julia De Girolamo [96] and used for dip-coating of hybrid thin films.

We focused on the automatization of the successive depositions of sub-monolayers of polymer and nanocrystals by a dip-coating procedure, to finally obtain a dense hybrid film. Using high boiling point solvents and rinsing steps after the deposition of each layer allowed to control very nicely the thickness of the films. A very good dispersion of nanocrystals in the polymer matrix is observed. On the other hand, one does not control the nanocrystals:polymer ratio. This technique moreover necessitates specific solubilities of components: the solvent of polymer should not be able to redisperse nanocrystals and vice versa; in consequence, it is not applicable for pyridine-treated nanocrystals and P3HT. On a more practical point of view, one downside of this technique is that it is time consuming.

Spin-coating Spin-coating is an easy, quick and efficient technique to make thin films that are homogeneous at the *mm* scale, of small roughnesses (5-10%) and of thicknesses up to 400 nm. Unfortunately, the loss of materials during the spinning process is too high to allow to make a large number of samples by this method.

Drop-casting Drop-casting can be used to realize hybrid thin films with a nanocrystals content up to 83 wt%-49 vol%. Higher contents of nanocrystals resulted in macroscopic cracking of the films, which is attributed to a lack of polymer matrix, playing the role of mortar, or cement, for these very slowly formed films. Thicknesses of films obtained by drop-casting were a little higher than to those of P3HT-only films. For example, drop-casting a ODCB solution of P3HT

(10 mg/mL) and nanocrystals (up to 49 mg/mL of nanocrystals for a 83 wt%-49 vol% hybrid) resulted in 5-8 μm films, in comparison to 5 μm for P3HT films. RMS roughnesses of hybrid films deposited by drop-casting were also larger than those of P3HT-only film, $\geq$ 7 % *vs* 1 % in the case of the P3HT films.

Time-of-Flight characterizations necessitate films thick enough to fully absorb the excitation light pulse in a thin layer of the device (500 nm for P3HT-only devices; 7 μm for hybrid films with a 83 wt%-49 vol% content in nanocrystals, see Chapter IV, 2.2). Drop casting is the cleanest and most reproducible method to make films of this thickness, although large roughnesses increase uncertainties on measured mobility values.

3.2 Optical characterizations of hybrid films

The characterizations of hybrid thin films made with CdSe nanocrystals is complicated, in comparison to P3HT or nanocrystals-only thin films, because P3HT and CdSe nanocrystals features superimpose and/or the components interact. For example, the first excitonic absorption peak of CdSe is located between 580 and 620 nm depending on their sizes, and P3HT deposited as a thin film absorbs below 650 nm. Similarly, the first X-ray diffraction peak of CdSe nanocrystals are located around 2θ=27°, 29° and 31° and overlap with the π-stacking peak of P3HT at 28°, as will be detailed in Fig. II.24. PL spectra of hybrid thin films combine 1) the addition of the photoluminescence of both components and 2) the interactions between the components resulting in possible charge transfer, depending on their degree of coupling, so the PL intensities are modified.

Optical absorption of hybrid thin films We present in Fig. II.19 the absorbance of two different kinds of hybrid thin films. The first one, in a), shows the absorbance of a spin-coated 1:9 polymer:nanocrystals (4.1 nm dots with pyridine ligands) blend; the second one in b) shows the absorbance built-up as the number of (nanocrystals+polymers) layers increases during dip coating, with 4.3 nm nanocrystals capped with MHT ligands.

In both cases, the absorptions of polymer and nanocrystals combine to cover a wide range of the solar spectrum, nonetheless leaving the wavelengths above 650 nm unabsorbed[5].

In a), we see the strong shift of the polymer absorption band between solution and film: the polymer absorbs below 550 nm in solution and below 650 nm when deposited on a substrate. This results in a well-visible nanocrystals' excitonic peak in solution. To the contrary, the nanocrystals influence on thin film absorption is only visible at lower wavelengths, below 450 nm, *i.e.* below the polymer absorption band.

This superposition of the absorption features of the hybrid components is not as strong in the case of the dip-coated film: in b), the polymer absorption band is visible at low wave-

[5]This is one of the reasons why CdSe nanocrystals and P3HT are progressively replaced by smaller band gap compounds.

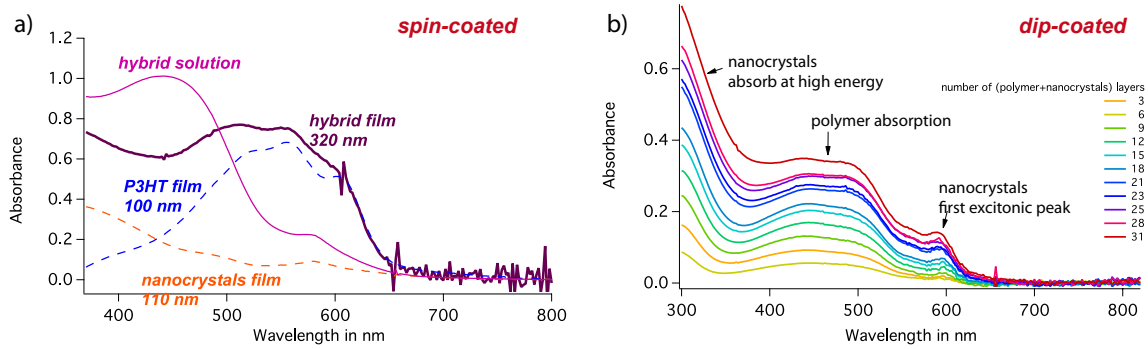

Figure II.19 – Absorbance of hybrid thin films in a) the UV-visible absorption spectrum of a spin-coated hybrid thin film with P3HT2 and 4.1 nm nanodots capped with pyridine in a 1:9 P3HT:nanocrystals weight ratio (1:19 pyridine:ODCB solvent mix), the spectra of spin-coated thin films of both components separately, and the spectrum of the hybrid solution before spin-coating; in b) the UV-visible spectra of a dip-coated hybrid thin film during its fabrication layer-by-layer, resulting in a final thickness of 90 nm, containing specially functionalized P3HT and 4.3 nm CdSe nanocrystals, as in [96].

lengths, comparable to solution absorption. Indeed, molecular recognition and dip coating combined results in a very good dispersion of nanocrystals in the polymer matrix, preventing any organization of the organic phase, hence its solution-like absorption spectrum.

Photoluminescence of hybrid thin films The photoluminescence spectra of thick drop-cast hybrid films (2 μm), made with P3HT and with nanocrystals of 4 and 6.7 nm, capped with synthesis ligands, are presented in Fig. II.20, with the appearance of the nanocrystals emission peaks indicated by arrows. These features can superpose to the emission of P3HT, as we can see here in the case of 6.7 nm nanocrystals. Consequently, the study of crystallization and order in P3HT, presented in the Section on P3HT films and based on relative intensities of photoluminescence peaks, is not possible for the larger nanocrystals. On the other hand, smaller nanocrystals emit at smaller wavelengths and contributions for nanocrystals and polymer can be distinguished. In the hybrid with 4 nm nanocrystals, the 0-0 transition of the P3HT (675 nm) gains in relative intensity with respect to the 0-1 transition (725 nm), when compared to the P3HT film. This indicates a larger disorder and/or a smaller intermolecular coupling than in the P3HT-only film, which can be intuitively understood by the disruption of order when nanocrystals are present in the film.

The thicknesses of the films prevent any reliable absorption measurements and hence any normalization relative to the absorbance, *i.e.* to the quantity of matter in the films. Any comparison of the intensities of different films is impossible. Consequently, PL quenching, and hence charge transfer, can not be studied in our case[6].

[6]For thinner films, the influence of the substrate can also play on PL intensities, rendering evaluation of PL quenching difficult as well.

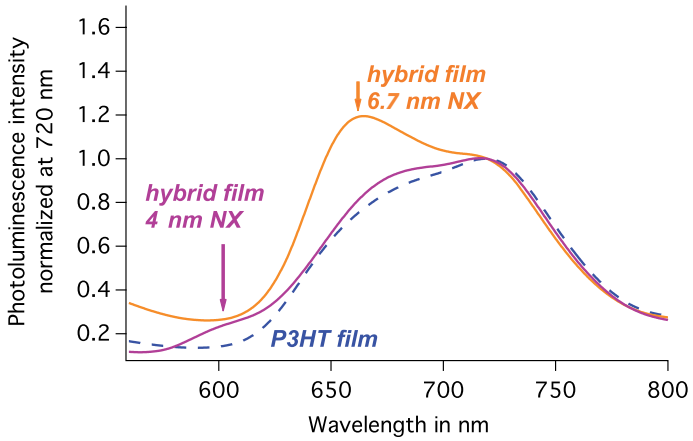

Figure II.20 – Photoluminescence of thick hybrid films drop-cast from ODCB, and based on nanocrystals of 4 and 6.7 nm with synthesis ligands. Thus, hybrids PL spectra possess nanocrystal (abbreviated NX on the figure) contributions at different wavelengths, indicated by the colored arrows. The nanocrystals were capped with synthesis ligands. The photoluminescence intensities have been normalized to 1 at 720 nm. These studies were done with P3HT1.

3.3 Morphological characterizations of hybrid films

We studied the morphology of drop-cast hybrid thin films with a profilemeter for thickness and roughness measurements, with SEM for the internal morphology of the active layer and with XRD for the crystalline properties.

Thicknesses and roughnesses Thicknesses and roughnesses were determined by profilemeter measurements. As for P3HT-only and nanocrystal-only film, the hybrid films of thicknesses below 100 nm (deposited by spin-coating) were conform to the substrate surface. Moreover, roughnesses of hybrid films were higher than for P3HT-only films. The RMS roughness went up from 4 % to around 10 % between a P3HT film and a hybrid film both deposited by spin-coating. This effect was even more pronounced in the case of drop-cast films: absolute RMS roughnesses were between 50 nm (1 %) for P3HT-only thin films and were $>$ 350 nm (7 %) for hybrid films. Hybrids containing pyridine-treated nanocrystals presented higher RMS roughnesses, on average 16 % , than hybrids based on nanocrystals with synthesis ligands, 9 %.

Scanning electron microscopy of hybrid thin films Fig. II.21 pictures cross sectionnal imaging of a 1.3 μm hybrid thin film, with 16 vol% of 4.1 nm CdSe nanocrystals capped with synthesis ligands. The film and substrate were cut neatly before insertion into the SEM vacuum chamber. We observed nanocrystals (clear dots) in different zones throughout the film.

Grazing incidence X-ray diffraction in hybrid thin films We studied different hybrid thin films by GIXRD measurements.

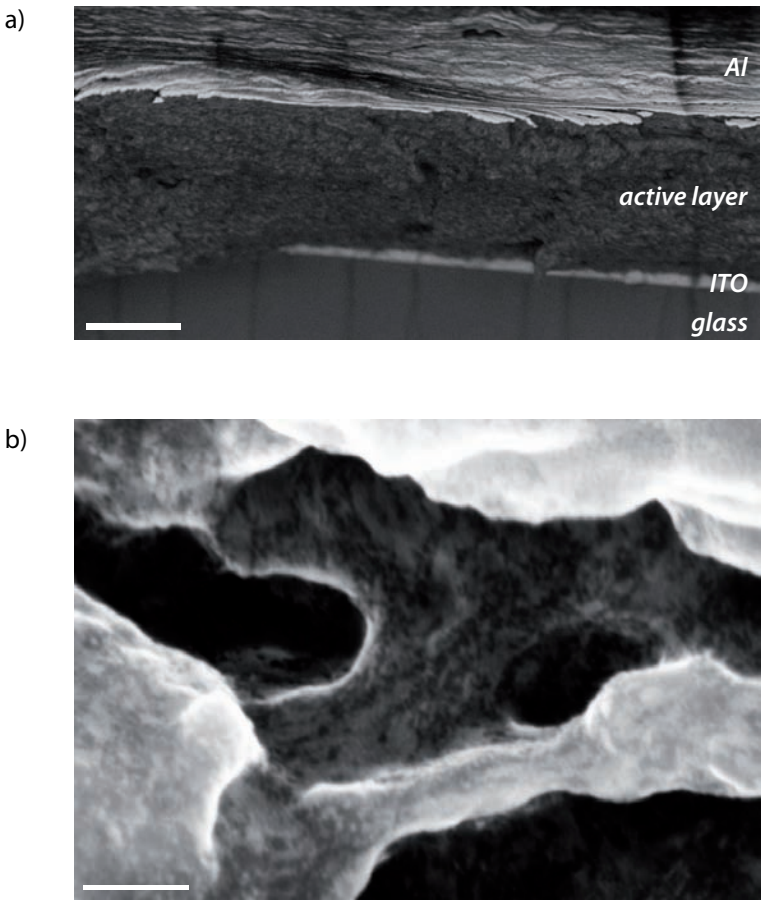

Figure II.21 – SEM cross section imaging of an hybrid device with 16 vol% of 4.1 nm CdSe nanocrystals capped with synthesis ligands, drop-cast from ODCB using P3HT1. In a), working distance 5 mm, high voltage 2.5 kV, scale bar 1 μm: all layers of the device can be identified. From the bottom, we see the glass substrate, the ITO electrode, the 1.3 μm active layer and the Al electrode. In b), working distance 4.7 mm, high voltage 5 kV, scale bar 100 nm: clear dotted zones are nanocrystals.

First, the diffractogram of a hybrid film made of P3HT1 and 16 vol% 6.7 nm nanodots capped with their pyridine ligands is shown in Fig. II.22, and the corresponding profile for pristine P3HT1 is given as a reference (the same as in Fig. II.14). In this hybrid profile, peaks characteristics of the nanodots are found at 2θ=30°, 2θ=49° and 2θ=58° (indicated as orange dots). While the P3HT (100) peak (2θ=6.3°) is intense and the second and third order diffraction peaks (2θ=6.3°, 18.9°) are clearly visible in the case of pristine P3HT1, the hybrid film only exhibits the first order of diffraction. This indicates that the degree of crystallinity of P3HT1 is much lower in the hybrid film than in the pristine P3HT1 film, and thus shows that the *nanodots contribute to worsen the degree of crystallization of P3HT1.*

Then, in Fig. II.23, we present diffraction profiles of hybrid thin films based on P3HT2 and different fractions of nanopods: a) with the synthesis ligands; b) with pyridine ligands.

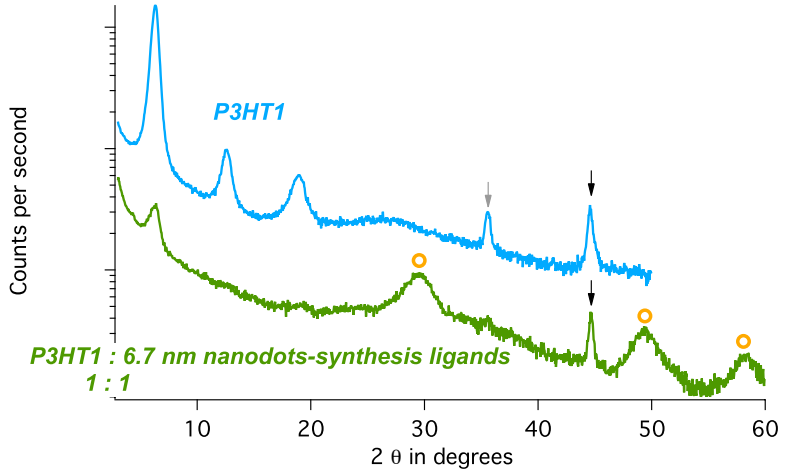

Figure II.22 – Grazing incidence X-ray diffractogram of an hybrid thin film, using P3HT1 and 6.7 nm nanodots (orange dots indicate peaks from the nanodots diffraction); and the spectrum for P3HT1 for reference; both films were drop-cast from ODCB. Intensities were normalized by the counting time. Black and gray arrows indicate Al and ITO signals.

In these GIXRD diffractograms, we see the respective features of P3HT and of nanopods, with 1) the relative intensity of the nanocrystals signals increasing coherently with the volume of nanopods in the matrix, 2) the features of P3HT2 degrade progressively and disappear for the 1:5 sample in Fig. II.23 a). There are two different effects: first, the volume fractions change and influence the relative intensities of nanopods *vs* P3HT2 peaks; secondly, the P3HT2 crystallinity worsens, as shown by the progressive disappearance of the second and third order of diffraction of the P3HT (h00) for larger fractions of nanocrystals. *The larger the fraction of nanocrystals in the hybrid, the less crystalline P3HT is.*

Rocking ω scans around the (100) peak showed that the crystallites of P3HT are randomly oriented, in pristine P3HT and in hybrids. We evaluated the size of the crystallites from the width of the (100) peak of P3HT2. Except for the 1:5 hybrid (in Fig. II.23 a)) where this peak is barely visible so the evaluation could not be made, all crystallite sizes were identical: 109 Å. In comparison, the crystallites in pristine P3HT2 were larger, 130 Å. This indicates that *the addition of nanopods provokes a diminution of the average size of P3HT2 crystallites, similar for all studied nanocrystals fractions.*

For equal amounts of nanopods, the hybrids with pyridine-treated nanopods exhibit clearer (h00) peaks than the hybrids based on nanopods capped with synthesis ligands. This is a sign of a better crystallization of the P3HT2 in pyridine-treated hybrids, closer to that of pristine P3HT2.

Moreover, for all hybrid diffractograms, we fitted the nanopod peaks around 2θ=30° with

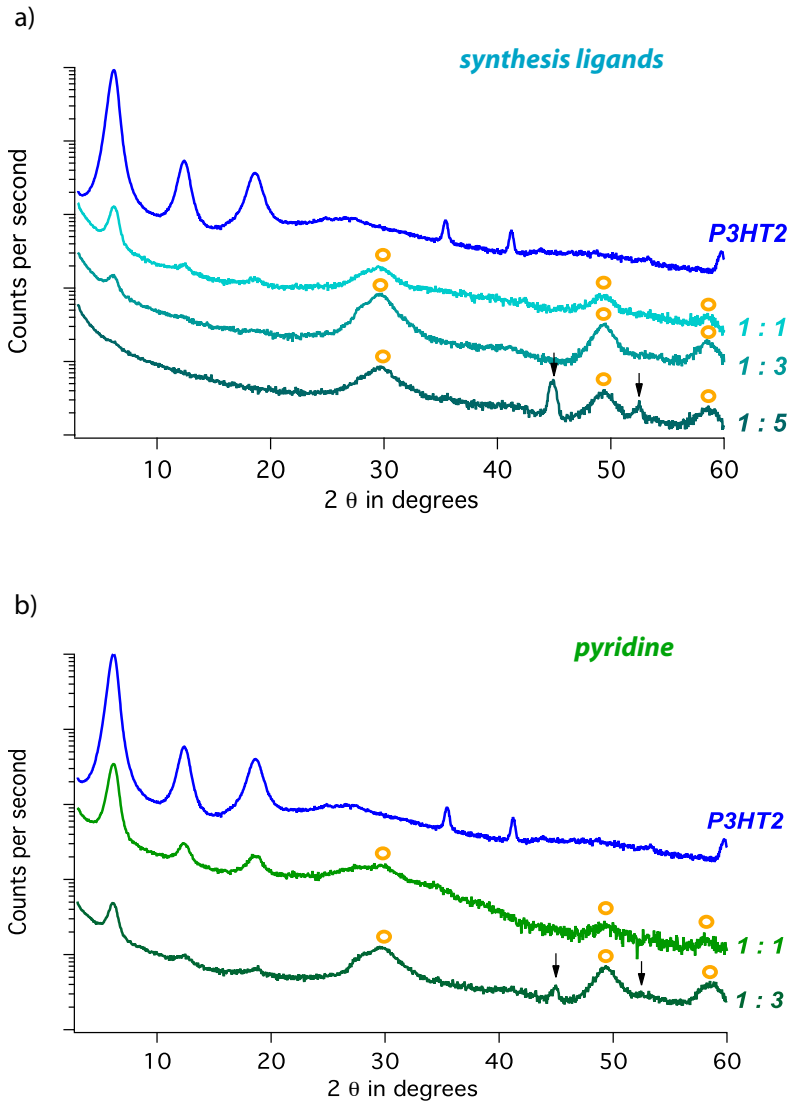

Figure II.23 – Grazing incidence X-ray diffractograms of hybrids thin films based on P3HT2 and nanopods in a) with their synthesis ligands, in b), treated with pyridine; the diffractogram of P3HT2 is shown as reference. All films were drop-cast from a) ODCB for hybrids based of nanopods with synthesis ligands, b) ODCB:pyridine 19:1 in the case of the hybrid made with pyridine-treated nanopods. Peaks from the nanopods are indicated by orange dots. Intensities were normalized by the counting time. Black arrows indicate Al Bragg peaks.

(100), (002) and (101) peaks of the CdSe nanopods hexagonal wurtzite structure. In Fig. II.24, we present typical diffractograms and their fits: in a), nanopods only; in b), pristine P3HT2; in c), a hybrid sample based on P3HT2 and 16 vol% (1:1) of CdSe nanopods capped with pyridine; in d), a hybrid with a similar amount of nanopods, but capped with synthesis ligands. The hybrid with pyridine-treated nanopods exhibits features of both P3HT2 (π-stacking) and nanopods (wurtzite structure). The hybrid with nanopods capped synthesis ligands does not show a clear

signal from the π-stacking of P3HT. Thus, our experimental results show that *hybrids based on P3HT2 exhibit a better structuration perpendicular to the substrate with pyridine-capped nanopods than with synthesis ligands.* This can be due to the presence of pyridine in solution.

Finally, the fact that both 1:1 samples in Fig. II.23 show three orders of diffraction for the (h00) peaks of P3HT2 contrasts with the findings of Fig. II.22, where the number of crystalline domains of P3HT1 was diminished already by the addition of a similar volume of nanocrystals. This can be due to 1) the different nature of the P3HT matrix (P3HT2 is less sensitive to the addition of a small volume of nanocrystals than P3HT1) and/or to 2) the different nature of nanocrystals, either their shape (spherical in Fig. II.22 *vs* branched in Fig. II.23) or the effective volume they occupy.

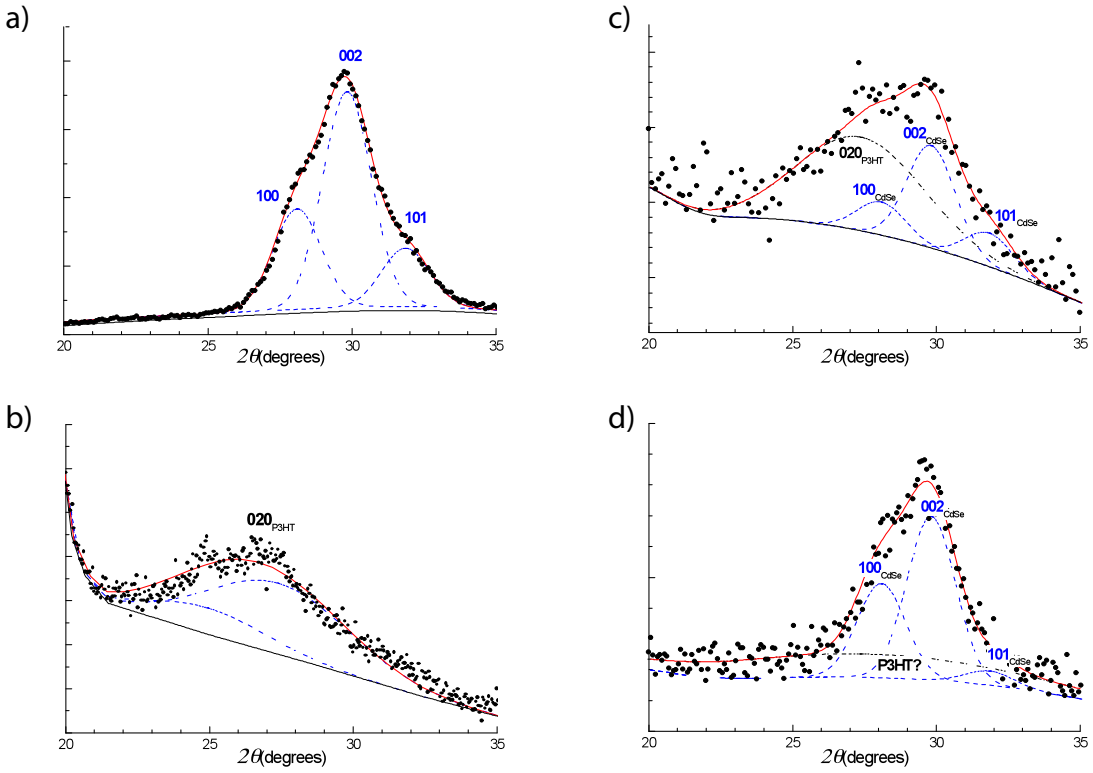

Figure II.24 – Zooms of the grazing incidence X-ray diffractograms We focus on the 20°-35° 2θ range of the X-ray profiles of a) CdSe nanopods only (powder diffractogram); b) pristine P3HT2; c) hybrid based on P3HT2 and 16 vol% of pyridine-treated nanopods; d) hybrid based on P3HT2 and 16 vol% of nanopods capped with their synthesis ligands. Films on b) and d) were drop-cast from ODCB, the film on c) from ODCB:pyridine 19:1.

In conclusion, GIXRD measurements of P3HT and hybrid films have shown that the presence of nanocrystals with synthesis ligands damages the crystallization of P3HT perpendicular to the substrate in terms of numbers of crystalline domains. The crystalline periodicity in this direction disappears progressively for increasing volumes of nanocrystals, depending on the

nature of P3HT and on the nature of nanocrystals. On the other hand, nanocrystals capped with pyridine put off the degradation of the P3HT crystallization, compared to hybrids with similar amounts of nanopods capped with synthesis ligands.

4 Conclusion

Synthesis of CdSe nanocrystals of different sizes and shapes (spherical, branched) was performed on a large scale to obtain grams of colloidal nanocrystals. Spherical CdSe nanocrystals crystallize in the wurtzite phase, while CdSe branched structure exhibit XRD diffractograms composites of cubic zinc blende and hexagonal wurtzite CdSe structures. Photoluminescence allowed to determine the energy band gaps of spherical nanocrystals of different sizes: E_g=2.00 eV for 4.1 nm nanocrystals, E_g=1.91 eV for 5.6 nm nanocrystals and E_g=1.87 eV for 6.7 nm nanocrystals. Surface ligand exchanges before or after thin film deposition were performed with small molecules, including pyridine and compounds with thiol or amine anchoring groups and aliphatic or aromatic spacers. Ligands influence nanocrystals energy levels, with measured shifts of the HOMO level towards shallower energies, up to +160 meV for phenylenediamine-treated nanocrystals. We deposited nanocrystals by spin-coating, drop-cast and doctor-blade to obtain films of different thicknesses. We evaluated different substrate surface treatments to enhance the affinity between nanocrystals and the substrate and were able to densify sub-monolayers of CdSe nanocrystals on SiO_2 substrates thanks to a treatment with mercaptopropyltriethoxysilane.

P3HT was fractioned and its deposition by spin-coating and drop-casting was studied. Film thicknesses can be varied from several tens of nm to several μm homogeneously at the mm^2 scale, adapted for different characterization techniques, including electrical characterizations. GIXRD showed that drop-casting with a high boiling point solvent leads to a higher degree of crystallization, with distributed orientations of the crystallites. The analysis of optical characterizations in terms of H-aggregates allowed to deduce values of the interchain electronic couplings, and values of energetic disorder, respectively around 25-40 meV and around 50 meV for spin-coated films. Drop-cast films exhibit reduced disorder and/or larger intermolecular coupling.

Finally, we blended P3HT and CdSe nanocrystals in solution to make hybrids. We observed PL quenching in solution, proving charge transfer between components. We deposited hybrid films by spin-coating and drop-casting to obtain film thicknesses up to 400 nm and between 2 and 10 μm, respectively. SEM cross sectional imaging of devices showed that nanocrystals are dispersed throughout the polymer matrix. Optical characterizations indicated the presence of both polymer and nanocrystals in the films. In the case of 4.1 nm CdSe nanocrystals, the PL of drop-cast films led to estimate that ordering of the P3HT matrix is destroyed partially in the

presence of nanocrystals (in the H-aggregate model). In the case of larger CdSe nanocrystals, the overlap between the features of the two components prevented more precise analysis. Finally, GIXRD characterizations showed that the polycrystalline structure of P3HT is perturbed by the presence of nanocrystals. For hybrids based on nanocrystals with synthesis ligands, the crystallinity of P3HT had almost disappeared for the largest probed amounts of nanocrystals (1:1 $\leftrightarrow$ 50 wt% $\leftrightarrow$ 16 vol% of nanodots in P3HT1; 1:5 $\leftrightarrow$ 83 wt% $\leftrightarrow$ 50 vol% of nanopods in P3HT2). In hybrids based on pyridine-treated nanopods, the P3HT crystallinity is temporarily preserved in comparison to hybrids made with nanopods with synthesis ligands with similar volumes fractions of nanocrystals.

References of part I

[1] D. V. Talapin, J-S. Lee, M. V. Kovalenko, and E. V. Shevchenko. *Prospects of colloidal nanocrystals for electronic and optoelectronic applications.* Chem. Rev. **110**(1), 389 (2010).

[2] P. Reiss, M. Protiere, and L. Li. *Core/shell semiconductor nanocrystals.* Small **5**(2), 154 (2009).

[3] M. V. Kovalenko, M. Scheele, and D. V. Talapin. *Colloidal nanocrystals with molecular metal chalcogenide surface ligands.* Science **324**, 1417 (2009).

[4] M. V. Kovalenko, M. I. Bodnarchuk, and D. V. Talapin. *Nanocrystal superlattices with thermally degradable hybrid inorganic-organic capping ligands.* JACS Communications **132**, 15124 (2010).

[5] A. Lefrançois, E. Couderc, J. Faure-Vincent, S. Sadki, A. Pron, and P. Reiss. *Effect of the treatment with (di-)amines and dithiols on the spectroscopic, electrochemical and electrical properties of CdSe nanocrystals' thin films.* J. Mater. Chem. **21**, 11524 (2011). 10, 17, 40, 43, 45, 46

[6] S. H. Tolbert and A. P. Alivisatos. *Size dependence of a first order solid-solid phase transition: the wurtzite to rock salt transformation in CdSe nanocrystals.* Science **265**, 373 (1994).

[7] S. Carayon. *Propriétés de fluorescence de nanocristaux de semiconducteurs II-VI.* PhD dissertation, Université Joseph Fourier (2005).

[8] L. E. Brus. *Electron-electron and electron-hole interactions in small semiconductor crystallites: the size dependence of the lowest excited electronic state.* J. Chem. Phys. **80**(9), 4403 (1984).

[9] S. A. Crooker, T. Barrick, J. A. Hollingsworth, and V. I. Klimov. *Multiple temperature regimes of radiative decay in CdSe nanocrystal quantum dots : Intrinsic limits to the dark-exciton lifetime.* Appl. Phys. Lett. **82**(17), 2793–2795 (2003).

[10] P. Guyot-Sionnest, B. Wehrenberg, and D. Yu. *Intraband relaxation in CdSe nanocrystals and the strong influence of the surface ligands.* J. Chem. Phys. **123**, 074709 (2005).

[11] Q. Pang, L. Zhao, Y. Cai, D. P. Nguyen, N. Regnault, N. Wang, S. Yang, W. Ge, R. Ferreira, G. Bastard, and J. Wang. *CdSe nano-tetrapods : controllable synthesis, structure analysis, and electronic and optical properties.* Chem. Mater. **17**, 5263 (2005).

[12] J. Jasieniak, L. Smith, J. van Embden, P. Mulvaney, and M. Califano. *Re-examination of the size-dependent absorption properties of CdSe quantum dots.* J. Phys. Chem. C **113**(45), 19468 (2009).

[13] M. Jones, S. S. Lo, and G. D. Scholes. *Signatures of exciton dynamics and carrier trapping in the time-resolved photoluminescence of colloidal CdSe nanocrystals.* J. Phys. Chem. C. **113**(43), 18632 (2009).

[14] Myriam Protière. *Synthèse de nanocristaux fluorescents de semi-conducteurs II-VI et III-V. Augmentation de l'échelle de synthèse.* PhD dissertation, Université Joseph Fourier (2007). 16, 31, 32

[15] Y-W. Jun, S-M. Lee, N-J. Kang, and J. Cheon. *Controlled synthesis of multi-armed CdS nanorod architectures using monosurfactant system.* JACS (18), 5150 (2001).

[16] S. Asokan, K. M. Krüger, V. L. Colvin, and M. S Wong. *Shape-controlled synthesis of CdSe tetrapods using cationic surfactant ligands.* Small **3**, 1164 (2007).

[17] W. W. Yu, Y. A. Wang, and X. Peng. *Formation and stability of size-, shape-, and structure-controlled CdTe nanocrystals: ligand effects on monomers and nanocrystals.* Chem. Mater. **15**, 4300 (2003).

[18] G. Konstantatos, I. Howard, A. Fischer, S. Hoogland, J. Clifford, E. Klem, L. Levina, and E. H. Sargent. *Ultrasensitive solution-cast quantum dot photodetectors.* Nature **442**(7099), 180 (2006).

[19] G. I. Koleilat, L. Levina, H. Shukla, S. H. Myrskog, S. Hinds, A. G. Pattantyus-Abraham, and E. H. Sargent. *Efficient, stable infrared photovoltaics based on solution-cast colloidal quantum dots.* ACS Nano **2**(5), 833 (2008).

[20] M. Law, J. M. Luther, Q. Song, B. K. Hughes, C. L. Perkins, and A. J. Nozik. *Structural, optical, and electrical properties of PbSe nanocrystal solids treated thermally or with simple amines.* JACS **130**(18), 5974 (2008).

[21] J. M. Luther, M. Law, M. C. Beard, Q. Song, M. O. Reese, R. J. Ellingson, and A. J. Nozik. *Schottky solar cells based on colloidal nanocrystal films.* Nano Lett. **8**(10), 3488 (2008).

[22] K. J. M. Bishop, C. E. Wilmer, S. Soh, and B. A. Grzybowski. *Nanoscale forces and their uses in self-assembly.* Small **5**(14), 1600 (2009).

[23] D. Steiner, D. Azulay, A. Aharoni, A. Salant, U. Banin, and O. Millo. *Photoconductivity in aligned CdSe nanorod arrays.* Phys. Rev. B **80**(19), 1 (2009).

[24] A. Persano, M. De Giorgi, A. Fiore, R. Cingolani, L. Manna, A. Cola, and R. Krahne. *Photoconduction properties in aligned assemblies of colloidal cdse/cds nanorods.* ACS Nano **4**(3), 1646 (2010).

[25] H. J. Snaith, G. L. Whiting, B. Sun, N. C. Greenham, W. T. S. Huck, and R. H. Friend. *Self-organization of nanocrystals in polymer brushes. Application in heterojunction photovoltaic diodes.* Nano Lett. **5**(9), 1653 (2005).

[26] J-M. Verilhac. *Transistors organiques à base de dérivés du polythiophène, effets de la structure moléculaire et supramoléculaire.* PhD dissertation, Université Joseph Fourier (2006).

[27] P.D. McMahon and A. Troisi. *Organic semiconductors: impact of disorder at different timescales.* Chem. Phys. Chem. **11**, 2067 (2010). 20

[28] J. Schafferhans, A. Baumann, C. Deibel, and V. Dyakonov. *Trap distribution and the impact of oxygen-induced traps on the charge transport in poly(3-hexylthiophene).* Appl. Phys. Lett. **93**(9), 093303 (2008).

[29] T. Thurn-Albrecht, R. Thomann, T. Heinzel, and S. Hugger. *Semicrystalline morphology in thin films of poly(3-hexylthiophene).* Colloid Polym. Sci. **282**(8), 932–938 June (2004).

[30] H. Sirringhaus, P. J. Brown, R. H. Friend, M. M. Nielsen, K. Bechgaard, B. M. W. Langeveld-Voss, A. J. H. Spiering, Rene A. J. Janssen, E. W. Meijer, P. Herwig, and D. M. De Leeuw. *Two-dimensional charge transport in conjugated polymers.* Nature **401**, 685 (1999). 23, 25

[31] S. Lilliu, T. Agostinelli, E. Pires, M. Hampton, J. Nelson, and J. E. Macdonald. *Dynamics of crystallization and disorder during annealing of P3HT/PCBM bulk heterojunctions.* Macromolecules **44**(8), 2725 (2011).

[32] G. L. Destri, T. F. Keller, M. Catellani, F. Punzo, K. D. Jandt, G. Marletta, and M. Catellani. *Crystalline monolayer ordering at substrate/polymer interfaces in poly(3-hexylthiophene) ultrathin films.* Macromol. Chem. Phys. **212**, 905 (2011).

[33] Y. Kim, S. Cook, S. M. Tuladhar, S. A. Choulis, J. Nelson, J. R. Durrant, D. D. C. Bradley, M. Giles, I. McCulloch, C-S Ha, and M. Ree. *A strong regioregularity effect in self-organizing conjugated polymer films and high-efficiency polythiophene:fullerene solar cells.* Nature Materials **5**, 197 (2006).

[34] J-F. Chang, J. Clark, N. Zhao, H. Sirringhaus, D. W. Breiby, J. W. Andreasen, M. M. Nielsen, M. Giles, M. Heeney, and I. Mcculloch. *Molecular-weight dependence of interchain polaron delocalization and exciton bandwidth in high-mobility conjugated polymers.* Phys. Rev. B **74**, 115318 (2006).

[35] O. Esenturk, J. S. Melinger, and E. J. Heilweil. *Terahertz mobility measurements on poly(3-hexylthiophene) films: Device comparison, molecular weight, and film processing effects.* J. Appl. Phys. **103**(2), 023102 (2008).

[36] A. M. Ballantyne, L. Chen, J. Dane, T. Hammant, F. M. Braun, M. Heeney, W. Duffy, I. McCulloch, D. C. B. Donal, and J. Nelson. *The effect of poly(3-hexylthiophene) molecular weight on charge transport and the performance of polymer:fullerene solar cells.* Adv. Funct. Mater. **18**(16), 2373 (2008). 25

[37] V. L. Colvin, M. C. Schlamp, and A. P. Alivisatos. *Light-emitting diodes made from CdSe nanocrystals and a semi-conducting polymer.* Nature **370**, 354 (1994).

[38] N. C. Greenham, X. Peng, and A. P. Alivisatos. *Charge separation and transport in conjugated-polymer/semiconductor-nanocrystal composites studied by photoluminescence quenching and photoconductivity.* Phys. Rev. B **54**(24), 17628 (1996). 26, 29

[39] W. U. Huynh. *Nanocrystal-polymer solar cells.* PhD dissertation, University of California at Berkeley (2002).

[40] S. Ren, L-Y. Chang, S-K. Lim, J. Zhao, M. Smith, N. Zhao, V. Bulovic, M. G. Bawendi, and S. Gradečak. *Inorganic-organic hybrid solar cell: bridging quantum dots to conjugated polymer nanowires.* Nano Lett. **11**, 3998 (2011). 26, 31

[41] S. Dayal, M. O. Reese, A. J. Ferguson, D. S. Ginley, G. Rumbles, and N. Kopidakis. *The Effect of Nanoparticle Shape on the Photocarrier Dynamics and Photovoltaic Device Performance of Poly(3-hexylthiophene):CdSe Nanoparticle Bulk Heterojunction Solar Cells.* Adv. Funct. Mater. **20**(16), 2629 (2010). 27

[42] Solenn Berson. *Synthèse, caractérisation et nanostructuration de dérivés du polythiophène pour des applications en cellules photovoltaïques organiques.* PhD dissertation, Université Joseph Fourier (2007). 27

[43] L. Hartmann, K. Tremel, S. Uttiya, E. Crossland, S. Ludwigs, N. Kayunkid, C. Vergnat, and M. Brinkmann. *2D versus 3D crystalline order in thin films of regioregular poly(3-hexylthiophene) oriented by mechanical rubbing and epitaxy.* Adv. Funct. Mater. page to be announced! (2011). 27

[44] S. Gupta, Q. Zhang, T. Emrick, and T. P. Russell. *"Self-corralling" nanorods under an applied electric field.* Nano Lett. **6**(9), 2066 (2006).

[45] M. Brinkmann, D. Aldakov, and F. Chandezon. *Fabrication of oriented and periodic hybrid nanostructures of regio-regular poly(3-hexylthiophene and CdSe nanocrystals by directional expitaxial solidification.* Adv. Mater. **19**, 3819 (2007).

[46] P. Reiss, E. Couderc, J. De Girolamo, and A Pron. *Conjugated polymers/semiconductor nanocrystals hybrid materials–preparation, electrical transport properties and applications.* Nanoscale **3**(2), 446 (2011). 27, 28

[47] V. Singh, S. S. Pandey, W. Takashima, and K. Kaneto. *Role of morphology on photoluminescence quenching and depletion width formed at the interface of aluminum and poly(3-alkylthiophene).* Jpn J. Appl. Phys. **48**(6), 061503 (2009).

[48] D Aldakov, F Chandezon, R De Bettignies, M Firon, P Reiss, and A Pron. *Hybrid organic-inorganic nanomaterials : ligand effects.* EPJ-Applied physics **265**, 261–265 (2007).

[49] W. C. Tsoi, S. J. Spencer, L. Yang, A. M. Ballantyne, P. G. Nicholson, A. Turnbull, A. G. Shard, Craig E. Murphy, D. D. C. Bradley, J. Nelson, and J-S. Kim. *Effect of crystallization on the electronic energy levels and thin film morphology of P3HT:PCBM blends.* Macromolecules **44**(8), 2944 (2011).

[50] M. Pientka. *Photogeneration of charge carriers in blends of conjugated polymers and semiconducting nanoparticles.* Thin Solid Films **451-452**, 48 (2004).

[51] W. Huang, J. Peng, L. Wang, J. Wang, and Y. Cao. *Impedance spectroscopy investigation of electron transport in solar cells based on blend film of polymer and nanocrystals.* Appl. Phys. Lett. **92**(1), 013308 (2008).

[52] K. M. Noone, N. C. Anderson, N. E. Horwitz, A. M. Munro, A. P. Kulkarni, and D. S. Ginger. *Absence of photoinduced charge transfer in blends of PbSe quantum dots and conjugated polymers.* ACS Nano **3**(6), 1345 (2009).

[53] D. S. Ginger and N. C. Greenham. *Photoinduced electron transfer from conjugated polymers to CdSe nanocrystals.* Phys. Rev. B **59**(16), 10622 (1999).

[54] T. Stoeferle, U. Scherf, and R. F. Mahrt. *Energy transfer in hybrid organic/inorganic nanocomposites.* Nano Lett. **9**(1), 453 (2009).

[55] M. D. Heinemann, K. von Maydell, F. Zutz, J. Kolny-Olesiak, H. Borchert, I. Riedel, and J. Parisi. *Photo-induced charge transfer and relaxation of persistent charge carriers in polymer/nanocrystal composites for applications in hybrid solar cells.* Adv. Funct. Mater. **19**(23), 3788 (2009).

[56] Y. C. Tseng, M. Tzolov, E. H. Sargent, P. W. Cyr, and M. A. Hines. *Control over exciton confinement versus separation in composite films of polyfluorene and CdSe nanocrystals.* Appl. Phys. Lett. **81**(18), 3446 (2002).

[57] M. Wang, J. K. Oh, T. E. Dykstra, X. Lou, G. D. Scholes, and M. A. Winnik. *Surface modification of CdSe and CdSe/ZnS semiconductor nanocrystals with poly(N,N-dimethylaminoethylmethacrylate).* Macromolecules **39**(10), 3664 (2006).

[58] I. Gur, N. A. Fromer, and A. P. Alivisatos. *Controlled assembly of hybrid bulk-heterojunction solar cells by sequential deposition.* J. Phys. Chem. B **110**(50), 25543 (2006).

[59] L-G. Yang, F. Chen, H. Xu, M. Wang, and H-Z. Chen. *Charge transport at hybrid bulk heterojunction based on CdS nanopillar arrays embedded in a conducting polymer.* J. Appl. Phys. **106**(7), 073701 (2009).

[60] T. Rauch, M. Böberl, S. F. Tedde, J. Fürst, M. V. Kovalenko, G. Hesser, U. Lemmer, W. Heiss, and O. Hayden. *Near-infrared imaging with quantum-dot-sensitized organic photodiodes.* Nature Photonics **3**, 332 (2009).

[61] S. A. McDonald, P. W. Cyr, L. Levina, and E. H. Sargent. *Photoconductivity from PbS-nanocrystal/semiconducting polymer composites for solution-processible, quantum-size tunable infrared photodetectors.* Appl. Phys. Lett. **85**(11), 2089 (2004).

[62] C-C. Chen, M-Y. Chiu, J-T. Sheu, and K-H. Wei. *Photoresponses and memory effects in organic thin film transistors incorporating poly(3-hexylthiophene)/CdSe quantum dots.* Appl. Phys. Lett. **92**(14), 143105 (2008).

[63] M-Y. Chiu, C-C. Chen, J-T. Sheu, and K-H. Wei. *An optical programming/electrical erasing memory device: organic thin film transistors incorporating core/shell cdse@znse quantum dots and poly(3-hexylthiophene).* Organic Electronics **10**(5), 769 (2009).

[64] J. H. Ham, D. H. Oh, S. H. Cho, J. H. Jung, T. W. Kim, E. D. Ryu, and S. W. Kim. *Carrier transport mechanisms of nonvolatile write-once-read-many-times memory devices with InPZnS core-shell nanoparticles embedded in a polymethylmethacrylate layer.* Appl. Phys. Lett. **94**(11), 112101 (2009).

[65] A. A. R. Watt, D. Blake, J. H. Warner, E. A. Thomsen, E. L. Tavenner, H. Rubinsztein-Dunlop, and P. Meredith. *Lead sulfide nanocrystal: conducting polymer solar cells.* J. Phys. D: Appl. Phys. **38**(12), 2006 (2005).

[66] K. R. Choudhury, J. G. Winiarz, M. Samoc, and P. N. Prasad. *Charge carrier mobility in an organic-inorganic hybrid nanocomposite.* Appl. Phys. Lett. **82**(3), 406 (2003). 29

[67] B. Sun and N. C. Greenham. *Improved efficiency of photovoltaics based on CdSe nanorods and poly(3-hexylthiophene) nanofibers.* Phys. Chem. Chem. Phys. **8**, 3557–3560 (2006).

[68] T. Jiu, P. Reiss, S. Guillerez, R. De Bettignies, S. Bailly, and F. Chandezon. *Hybrid Solar Cells Based on Blends of CdSe nanorods and P3AT nanofibers.* IEEE Journal of selected topics in quantum electronics **16**(6), 1619 (2010).

[69] S. Dayal, N. Kopidakis, D. C. Olson, D. S. Ginley, and G. Rumbles. *Photovoltaic devices with a low band gap polymer and CdSe nanostructures exceeding 3% efficiency.* Nano Lett. **10**(1), 239 (2010).

[70] S. G. Kwon and T. Hyeon. *Formation mechanisms of uniform nanocrystals via hot-injection and heat-up methods.* Small (2011).

[71] M. Protière, N. Nerambourg, and P. Reiss. *Rational design of the gram-scale synthesis of nearly monodisperse semiconductor nanocrystals.* Nanoscale Research Letters **6**, 472 (2011).

[72] C. B. Murray, D. J. Norris, and M. G. Bawendi. *Synthesis and characterization of nearly monodisperse CdE (E=S, Se, Te) semiconductor crystallites.* JACS **115**, 8706 (1993).

[73] T. N. Luyen, L. B. Hai, N. X. Nghia, and P. T. Nga. *Effect of reaction temperature and ligand concentration on the shape of CdSe nanocrystals.* Int. J. Nanotechnol. **8**(3/4/5), 214 (2011).

[74] K. Huang, O. Renault, J-P. Simonato, B. Grévin, J. De Girolamo, P. Reiss, R. Demadrille, and H. Benmansour. *Multiple hydrogen-bond-assisted self-assembly of semiconductor nanocrystals on silicon surfaces and nanowires.* J. Phys. Chem. C. **113**, 21389 (2009).

[75] J. E. Bowen Katari, V. L. Colvin, and A. P. Alivisatos. *X-ray photoelectron spectroscopy of CdSe nanocrystals with applications to studies of the nanocrystal surface.* J. Phys. Chem. **98**, 4109 (1994).

[76] H. Mattoussi, A. W. Cumming, C. B. Murray, and M. G. Bawendi. *Characterization of CdSe nanocrystallite dispersions by small angle x-ray scattering.* J. Chem. Phys. **105**, 9890 (1996).

[77] X. Peng, M. C. Schlamp, A. V. Kadavanich, and A. P. Alivisatos. *Epitaxial growth og highly luminescent CdSe/CdS core/shell nanocrystals with photostability and electronic accessibility.* JACS **119**, 7019 (1997).

[78] X. Ji, D. Copenhaver, C. Sichmeller, and X. Peng. *Ligand bonding and dynamics on colloidal nanocrystals at room temperature: the case of alkylamines on CdSe nanocrystals.* JACS **130**, 5726 (2008).

[79] B. von Holt, S. Kudera, A. Weiss, T. E. Schrader, L. Manna, W. J. Parak, and M. Braun. *Ligand exchange of CdSe nanocrystals probed by optical spectroscopy in the visible and mid-IR.* J. Mater. Chem. **18**(23), 2728 (2008).

[80] M. Soreni-Harari, N. Yaacobi-Gross, D. Steiner, A. Aharoni, U. Banin, O. Millo, and N. Tessler. *Tuning energetic levels in nanocrystal quantum dots through surface manipulations.* Nano Lett. **8**(2), 678 (2008).

[81] S. K. Sarkar, N. Chandrasekharan, S. Gorer, and G. Hodes. *Reversible adsorption-enhanced quantum confinement in semiconductor quantum dots.* Appl. Phys. Lett. **81**(26), 5045 (2002).

[82] S-H. Kang, Ch. K. Kumar, Z. Lee, V. Radmilovic, and E. T. Kim. *Effects of surface ligands on the charge memory characteristics of CdSe/ZnS nanocrystals in TiO2 thin film.* Appl. Phys. Lett. **95**(18), 183111 (2009).

[83] M. T. Frederick and E. A. Weiss. *Relaxation of exciton confinement in CdSe quantum dots by modification with a conjugated dithiocarbamate ligand.* ACS Nano **4**(6), 3195 (2010).

[84] C. A. Leatherdale and M. G. Bawendi. *Observation of solvatochromism in CdSe colloidal quantum dots.* Phys. Rev. B **63**, 165315 (2001).

[85] U. T. D. Thuy, N. Q. Liem, D. X. Thanh, M. Protière, and P. Reiss. *Optical transitions in polarized CdSe, CdSe/ZnSe, and CdSe/CdS/ZnS quantume dots dispersed in various polar solvents.* Appl. Phys. Lett. **91**, 241908 (2007).

[86] O. I. Micic, S. P. Ahrenkiel, and A. J. Nozik. *Synthesis of extremely small InP quantum dots and electronic coupling in their disordered solid films.* Appl. Phys. Lett. **78**(25), 4022 (2001).

[87] L. Jdira, P. Liljeroth, E. Stoffels, D. Vanmaekelbergh, and S. Speller. *Size-dependent single-particle energy levels and interparticle Coulomb interactions in CdSe quantum dots measured by scanning tunneling spectroscopy.* Phys. Rev. B **73**(11), 1 (2006).

[88] T. D. Krauss and L. E. Brus. *Charge, polarizability and photoionization of single semiconductor nanocrystals.* Phys. Rev. Lett. **83**(23), 4840 (1999).

[89] A. Wolcott, V. Doyeux, C. A. Nelson, Gearba R., K. W. Lei, K. G. Yager, A. D. Dolocan, K. Williams, D. Nguyen, and X-Y. Zhu. *Anomalously large polarization effect responsible for excitonic red shifts in PbSe quantum dot solids.* J. Phys. Chem. Lett. **2**, 795 (2011). 49

[90] M. Trznadel, A. Pron, and M. Zagorska. *Preparation and properties of fractionated regioregular poly(3-alkylthiophenes).* Synthetic Metals **101**, 118 (1999).

[91] G. Barbarella, A. Bongini, and M. Zambianchi. *Regiochemistry and conformation of poly(3-hexylthiophene) via the synthesis and the spectroscopic characterization of the model configuration triads.* Macromolecules **27**, 3039 (1994).

[92] F. C. Spano, J. Clark, C. Silva, and R. H. Friend. *Determining exciton coherence from the photoluminescence spectral line shape in poly(3-hexylthiophene) thin films.* J. Chem. Phys. **130**(7), 074904 (2009).

[93] J. Clark, C. Silva, R. H. Friend, and F. C. Spano. *Role of intermolecular coupling in the photophysics of disordered organic semiconductors : aggregate emission in regioregular polythiophene.* Phys. Rev. Lett. **98**, 206406 (2007).

[94] N. Banerji, S. Cowan, E. Vauthey, and A. J. Heeger. *Ultrafast relaxation of the poly(3-hexylthiophene) emission spectrum.* J. Phys. Chem. C **115**(19), 9726 (2011).

[95] C. Querner, P. Reiss, S. Sadki, M. Zagorska, and A. Pron. *Size and ligand effects on the electrochemical and spectroelectrochemical responses of CdSe nanocrystals.* Phys. Chem. Chem. Phys. **7**, 3204 (2005).

[96] Julia De Girolamo. *Architectures hybrides auto-assemblées à base de systèmes poly-conjugués et de nanocristaux de semi-conducteurs pour le photovoltaïque plastique.* PhD dissertation, Université Joseph Fourier (2007). 58, 60

[97] J. De Girolamo, P. Reiss, M. Zagorska, R. De Bettignies, S.. Bailly, J-Y. Mevellec, S. Lefrant, J-P. Travers, and A. Pron. *Layer-by-layer assembled composite films of side-functionalized poly(3-hexylthiophene) and CdSe nanocrystals: electrochemical, spectroelectrochemical and photovoltaic properties.* Phys. Chem. Chem. Phys. **10**, 4027 (2008).

[98] J. De Girolamo, P. Reiss, and A. Pron. *Hybrid materials from diaminopyriminide-functionalized poly(hexylthiophene) and thymine-capped CdSe nanocrystals : part II. Hydrogen bond assisted Layer-by-Layer molecular level processing.* J. Phys. Chem. C **112**, 8797 (2008).

Part II

Charge transport measurements in thin films

Chapter III

Time-of-Flight charge transport characterizations in disordered materials: concepts and results from the literature

Disordered semi-conducting materials exhibit localized charge carriers. In these materials, charge transport occurs by hopping between localization sites. Here, we present the traditional[1] Time-of-Flight measurement technique and how to derive mobility from photocurrent transients. We discuss dispersive transport and the notion of apparent mobility. Finally, we present TOF measurements and results on P3HT and hybrid thin films from the literature.

A short introduction to hopping transport

Charge carriers in conjugated polymers and semiconducting nanocrystals are localized on the nanometer or tens of nanometers range. In conjugated polymers, the conjugation phenomenon (delocalization) is interrupted by morphological defects, such as chemical impurities, lack of backbone planarity and irregular chain packing. In isolated nanocrystals, the wavefunction localization is due to electronic confinement. In denser assemblies of nanocrystals (in the solid phase for example), when interparticle distances are small or when dielectric environment is adequate, wavefunctions of different nanocrystals overlap [1]. In the case of solution-processed thin films, this is related to the nature and size of ligands surrounding the nanocrystals. In addition to confinement-related localization of wavefunctions, the structural disorder, related to random interruptions of the conjugation in conjugated polymers and to random packings of both type of components, gives rise to weak localization: wave packets are back-scattered by randomly distributed defects, the interferences of back-scattered waves induce the localization of charge carriers.

Because wavefunctions are localized, the overlap of wavefunctions on different localization

[1] Time-of-Flight refinements have been developed, such as integral TOF, Space-Charge Limited regime TOF and Current Extraction by Pulse Voltage measurements.

sites are small. Transport occurs by hopping between localized sites: all charges are essentially 'trapped' on a site for some amount of time, called 'dwell time' and given by the inverse hopping rate. It has to be remarked that this use contrasts with the term 'trap' in the inorganic community. In inorganic materials, while the majority of states are by essence delocalized, traps represent a minority of electronic states, are spatially localized and are isolated energetically from the main band in the DOS (as in FIG. I.5 in Chapter I).

Finally, polymer and nanocrystals assemblies present distributed values of site energies and of electronic couplings. They are described mathematically by the 1) energetical disorder distribution and 2) positional disorder distribution.

We detail here the Gaussian Disorder Model (GDM), developed by Bässler (*e.g.* [2]). The site energy distribution is assumed to be a Gaussian of width σ. At low charge densities, excited charges relax by hopping and eventually reach an equilibrium energy level $E_\infty = -\sigma^2/k_BT$. There, few sites are available for hopping. Charge transport is then thermally activated, with $\mu = \mu_0\ exp\{-(2\sigma/3k_BT)^2\}$, and occurs at a mean energy $E_{transport} = -5\sigma^2/9k_BT$: this is the *quasi-equilibrium transport regime*.

Including the effect of a Gaussian distribution of wavefunction overlaps, or transfer integrals, of width Σ, Monte Carlo simulations allowed to derive an expression for the mobility:

$$\mu_{GDM}(T,E) \;=\; \mu_0\ exp\Big\{ -(\frac{2\sigma}{3k_BT})^2 \;+\; C\ \sqrt{E}\ [\ (\frac{\sigma}{k_BT})^2 - \Sigma^2]\ \Big\} \qquad \text{(III.1)}$$

where T is the temperature, E the electric field, C a numerical factor, σ the energetic disorder (width of the distribution of sites energies), and Σ the positional disorder (width of the distribution of transfer integrals). The $\mu = f(\sqrt{E})$ dependence is commonly referred to as Poole-Frenkel dependence. Initially though, the Poole-Frenkel model derived from charge trapping by charged Coulomb traps and $\mu \propto exp(\beta\sqrt{E}/k_BT)$, where $\beta = 2e^{3/2}/(4\pi\epsilon\epsilon_0)^{1/2}$.

In the initial model by Bässler, disorders are uncorrelated; Cordes *et al.* developed a Correlated Disorder Model [3, 4].

1 Time-of-Flight experiments in disordered materials and the mobility concept

1.1 Description of a typical ToF experiment

In a TOF experiment, a short laser pulse is sent on an optically thick sample to photogenerate charge carriers in a thin portion of the sample, close to the illumination electrode. A constant voltage is applied to allow one type of carriers to drift through the film and electrical current is measured. When contacts are appropriately designed, choosing the polarity of the applied bias enables to measure one or the other type of charge carriers. Another possibility is to change the illumination electrode and keep the same applied bias voltage. The principle of

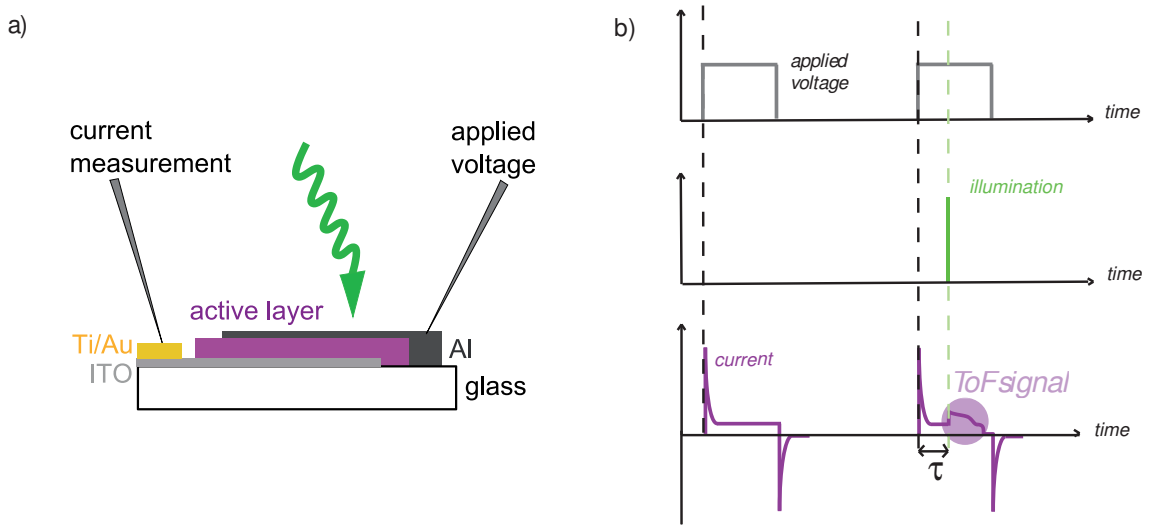

Figure III.1 – Time-of-Flight measurement in a), one of the configuration used; in b) its chronogram. A square voltage pulse is applied. After a time τ long enough for the sample to relax, it is excited optically with laser pulse. Photocurrent is recorded.

TOF experiments in depicted in Fig. III.1. In a), the measurement configuration is depicted and in b) a chronogram of the experiment shows the application of a voltage pulse and the resulting current, with or without the optical excitation.

TOF measurements are widely used to extract effective mobilities in different materials, including disordered materials. The mobility μ, defined as the proportionality coefficient between the drift-velocity $\vec{v}$ and the electric field $\vec{E}$, is calculated from the measured value of the transit (or arrival) time t_{tr}:

$$\mu = \frac{L^2}{t_{tr}.V} \tag{III.2}$$

where L is the sample thickness when the sample is fully depleted and V the applied voltage. The transit time t_{tr} corrsponds in principle to the arrival of the fastest charges and is determined by the intersection of tangents before and after the current drops [5], as is schematized in Fig. III.2.

Some conditions need to be satisfied in order to analyze current transients with the TOF method: the sample must have blocking contacts, must be optically thick, and satisfy some capacitance constraints. Namely, the photo-generated charge must be much smaller than the capacitive charge stored at the electrodes and the response time of the RC circuit must be much smaller than the transit time of charges. These conditions can be fulfilled by adjusting the electrode area, sample thickness, or the illumination intensity. We will review these requirements more precisely in the next Chapter.

1.2 Dispersion of transit times

In FIG. III.2, we pictured charge carrier densities evolution and corresponding measured currents for different stereotypical cases that we examine qualitatively. Both the charge density $n(\vec{r},t)$ and the charge velocity $v(\vec{r},t)$ depend on space and time (respectively because of space and time dependences of generation, collection, recombination and of transport mechanisms, applied electric field, morphology, etc.). Hence, the current density $j(t)$ depends on the time after illumination. We neglect recombinations, so the only factor to reduce the charge density $n(t)$ is when charges arrive to the electrode.

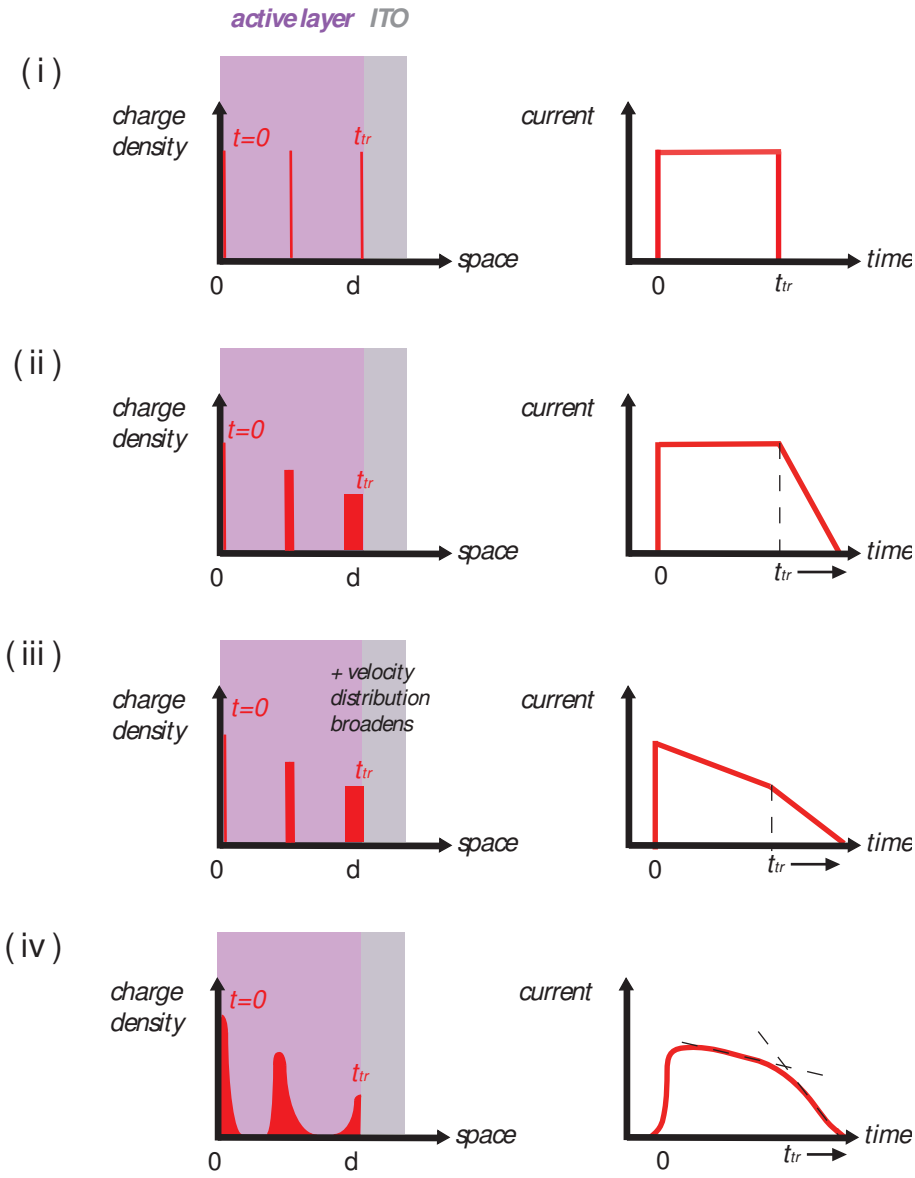

FIGURE III.2 – Time-of-Flight typical transients

In case (i), the charge generation occurs on a very thin layer and charges drift without dispersion to the other electrode. The lack of dispersion would be due to the absence of diffusion and to the absence of traps. The recorded current is constant until the arrival of charges to the collecting electrode, when it falls to zero.

In case (ii), the charge density broadens with time. This can be due to 1) diffusion or 2) a dispersion of the drift-velocity value that is constant in time (consider a set of percolating pathways, each with a different hopping time, for example; this also means that charges have reached quasi-equilibrium). Charges arrive at different times to the collecting electrode. From the time the first charge arrives to the collecting electrode, the current falls gradually to zero. We have a distribution of arrival times.

In case (iii), the velocity dispersion increases with time and its average decreases (*e.g.* because of trapping or because charges relax towards their equilibrium energy). Therefore, the current falls gradually from the rise of photocurrent. If the velocity dispersion is not too large, we can still see a drop of the recorded photocurrent related to decreases in the total number of carriers, *i.e.* related to arrival times.

Finally, in a more realistic case, charges are not homogeneously generated, case (iv). They thus have different distances to cover to reach the collecting electrode. This implies a supplementary dispersion of arrival times.

In terms of mobility: in case (i), the mobility takes a single value for all charges and t_{tr} gives access to this value. In cases (ii), (iii) and (iv), if there is an inflection point, it corresponds to the arrival time of the fastest charges: $n(t)$ starts decreasing, so does $j(t)$. The transit times then leads to the highest mobility value. In case (ii), velocities are distributed and constant in time and the dispersion in transit times can be analyzed as a dispersion of mobilities around the equilibrium average mobility. In case (iii), the velocity distribution evolves with time so that the dispersion of transit times gives the mobility distribution averaged over time. Finally in case (iv), the supplementary dispersion of transit times does not reflect any supplementary dispersion of mobilities but rather of distances to cover.

Diffusion and the Einstein relation As mentioned above, the dispersion of transit times Δt_{tr} can arise from a spread of the charge sheet due to diffusion (case (ii)). In this case, and when the Einstein relation $D/\mu = k_B T/e$ holds, one has [2]:

$$\frac{\Delta t_{tr}}{t_{tr}} = \frac{t_{1/2} - t_{tr}}{t_{1/2}} = \sqrt{\frac{2k_B T}{eV}} \tag{III.3}$$

where $t_{1/2}$ is the time at which the current has decreased by half its initial amplitude.

It has been observed experimentally in organic films that this $\Delta t_{tr}/t_{tr}$ relation does not hold. It is instead larger than predicted by Eq. III.3 and is merely independent on voltage.

Also, Einstein relation has been shown not to hold either for organic materials. N. Tessler and Y. Roichman [6] have derived analytically a generalized Einstein relation for organic semi-

conductors under the assumptions of a Gaussian DOS and quasi-equilibrium. Both these studies show that effective diffusion coefficients are larger than expected from the classical Einstein's relation, which seems in accordance with the experimentally observed $\Delta t_{tr}/t_{tr}$.

Disorder and equilibration The fact that transport occurs *via* successive localizations and hops with different dwell times implies that charges do not drift uniformly, resulting in larger dispersion of transit times: this is *anomalous* or *dispersive transport*. It has been studied with the Continuous-Time Random Walk (CTRW) model and by the Multiple Trapping (MT) and release model (see for example PhD dissertations of Wong [7] and Bange [8]).

Scher and Montroll have studied a CTRW model [5]. In the absence of disorder, the dwell time takes a single value and the current decay is exponential. When some disorder is introduced via a power distribution of dwell times $t^{-(1+\alpha)}$, the current decays in $t^{-(1-\alpha)}$ before t_{tr} and $t^{-(1+\alpha)}$ after t_{tr}. This results in the sum of pre- and posttransit slopes equals to 2. Experimentally, deviations from the Scher-Montroll relations have been found. Since Rudenko and Arkhipov have later shown that this power distribution of dwell times is correct for an exponential distribution of traps only (*e.g.* [9]), this could be related to different shapes of DOS. Nonetheless, slopes of the current transients are used to compare transport dispersivities of different samples, and formalized in the values of α_{pre} and α_{post}.

Finally, above considerations suppose that the quasi-equilibrium transport regime is reached, *i.e.* that charge carriers have relaxed to their equilibrium energy level. Especially when charges are generated with excess energy, non equilibrium transport may become important [10]. Relaxation of charge carriers within the DOS implies a decrease of the mean mobility and an increase of the mean diffusion coefficient, as shown in [11]. In [12], Monte Carlo simulations were performed to study the influence of disorder, field and time on the Einstein relation. D/μ increases above k_BT/e with increasing disorder and field and is shown to relax with time. Here relaxation is related to energy relaxation of charges, *i.e.* to a non-equilibrium regime.

Mobility distributions In conclusion, mobility is not a well-defined parameter for disordered materials with distributed DOS and/or distributed transfer integrals. Charge mobility measurements, such as TOF, SCLC and others, give access to effective or apparent mobility values. These values do not depend only on the material but also on processing conditions of the sample and on experimental conditions (field, temperature, charge density, etc.). Several works have emphasized the interest of investigating mobility distributions (*e.g.* [5, 13]) rather than apparent mobilities.

2 Time-of-flight on P3HT films

Hole mobilities in P3HT have been studied a lot in these last 15 years. We review experiments and their interpretations in this section. An example of TOF hole mobilities in P3HT as a

function of the applied electric field and for different temperatures is shown in FIG. III.3, from [14].

Hole mobilities were measured between 5 $.10^{-5} cm^2/Vs$ and $10^{-3} cm^2/Vs$ (for both regioregular and regiorandom P3HT, abreviated respectively rR-P3HT and rr-P3HT in the following) for all studied electric fields, *i.e.* approximatively 10^4 to 10^6 V/cm.

To the best of our knowledge, few reports include electron mobilities. When measured, *in vacuo*, they are balanced with hole mobilities. In [15], mobilities were approximately constant above 1.2 $.10^5$ V/cm, with $\mu_h = 3 .10^{-4}$ cm^2/Vs and $\mu_e = 1.5 .10^{-4}$ cm^2/Vs. In [16] mobilities were approximately constant for all field reported, *i.e.* between 6 $.10^4$ V/cm and 1.4 $.10^6$ V/cm, with $\mu_h = 4.5.10^{-4}$ cm^2/Vs and $\mu_e = 3.8 .10^{-4}$ cm^2/Vs.

Electric field dependence In rR-poly(3-alkylthiophene) (P3AT), at low fields, mobilities decreased with increasing electric field, and stabilized for fields larger than 10^5 V/cm (*e.g.* [14–18]). This phenomenon is observed above 280 K, as illustrated in FIG. III.3. In the case of rr-P3AT, this negative field dependence was not observed. To the contrary, mobilities of rr-P3HT samples increased rapidly with the electric field, and this increase was more pronounced for long alkyl side-chains [18]. In rr-P3HT, hole mobilities at low fields were 10 times smaller in amplitude than those of rR-P3AT samples [19])

Mauer *et al.* showed that the hole mobilities strongly depend on the degree of regioregularity. For rr-P3HT samples, TOF transients were too dispersive to be analysed. In a 94 % rR-P3HT sample, the mobility at room temperature was around 5 $.10^{-5} cm^2/V.s$ and it decreased very slightly with increasing field. When the regioregularity was further increased to $>$ 98 %, the hole mobility increased to around 4 $.10^{-4} cm^2/V.s$. Unfortunately, very regioregular samples with large molecular weights are difficult to obtain. More particularly, in this study, very high regioregularity samples ($>$ 98 %) possessed molecular weights $M_w \approx 25kDa$, while lower regioregularity samples had $M_w \approx 60kDa$. This renders difficult the evaluation of the effect of the regioregularity by itself [20].

In [21], the influence of P3HT molecular weight on charge transport was studied by TOF (see also Chapter I). Mobilities of rR-P3HT annealed samples were measured as a function of the electric field. Low molecular weight (13 kDa) resulted in a room temperature mobility constant with the electric field above 1.6 $.10^5$ V/cm , while higher molecular weight (121 kDa) exhibited increasing mobilities with the electric field between 6.2 $.10^4$ V/cm and 3.6 $.10^5$ V/cm.

In conclusion, in rR-P3HT samples, a negative field mobility dependence for electric fields lower than 10^5 V/cm has been reported by different groups.

Temperature dependence Mozer *et al.* studied doctor-bladed P3HT films. The measured transients were relatively non dispersive at room temperature, as shown by current plateaus before the transit time and short current tails after the transit time. Transients became more and more dispersive at lower temperatures, indicating a transition from non-dispersive transport

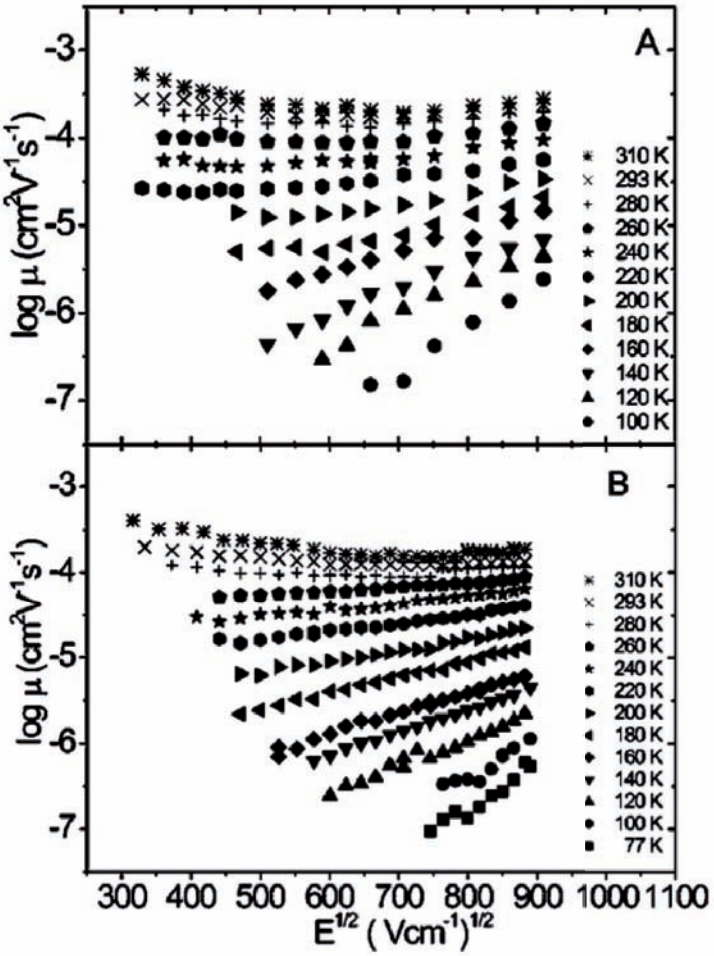

Figure III.3 – Time-of-Flight transients in P3HT from [14]. A and B show TOF characterizations of different P3HT (different suppliers, Rieke and Starck, and different thicknesses, 4.6 μm and 3.6 μm, respectively) as a function of the applied electric field and of the temperature. Films were deposited from 90mg/mL from chloroform solutions by doctor-blading.

to dispersive transport when the temperature increases [14, 22].

Moreover, below 260K, mobilities exhibited a positive electric field dependence, illustrated in III.3, from [14]. In [21], low molecular weight P3HT (13 kDa) also exhibited this transition from negative to positive field dependance when the temperature was decreased below 260 K.

In the constant field-mobility region (above 10^5 V/cm), hole mobilities in P3AT films were thermally activated, with activation energies around 100 meV and increasing notably with the alkyl side-chain length [17, 18].

Dispersivity The analysis of pretransit slopes showed that transport was more dispersive for P3AT spin coated samples than for drop cast samples [23][2].

[2]Other than this report, any influence of the film processing was not reported and is difficult to make out: deposition methods used in different studies vary, sometimes even in the same study. Doctor blade is used in

Alkyl chains lengths were not found to clearly influence dispersivities [23].

The negative mobility dependance as a function of the electric field for fields lower than 10^5 V/cm, has been observed by TOF by different groups [14, 15, 24]. While it has been argued that the negative field mobility dependence was an artifact of TOF measurements related to the reorganization of the electric field during the transit (*e.g.* [25]), the observation of the same phenomena with the CELIV technique [14, 24] finally led to consider this negative field mobility dependance as a real physical phenomenon. The explanation raised most of the time relies in the GDM for the mobility field dependence, Eq. III.1:

$$\mu_{GDM}(T,E) \;=\; \mu_0 \; exp\Big\{ -(\frac{2\sigma}{3k_BT})^2 \;+\; C\;\sqrt{E}\;\big[\;(\frac{\sigma}{k_BT})^2 - \Sigma^2\big]\;\Big\} \tag{III.4}$$

where the field dependence can be negative if $\Sigma \;>\; \sigma/k_BT$, *i.e.* if the positional disorder is greater than the energetic disorder (and $C > 0$). Indeed, when transfer integrals vary a lot, charges can go around an obstacle, *i.e.* a low probability hop, by going sideways or backwards, against the field direction. When the electric field increases, the energy cost needed to go against the field becomes prohibitive; dwelling times are large for hops in all directions, and the mobility decreases.

Fits to the GDM were performed and gave for example $10^{-3} cm^2/Vs$ for the mobility prefactor μ_0, $10^{-4} cm^{1/2}/V$ for the fit parameter C, 70 meV for the energetic disorder σ and 3 for the positional disorder Σ (Σ is normalized by k_BT) [14]. Similar values were obtained in other studies [21, 24], with a larger $\Sigma \;=\; 9.5$ in the case of [24].

In the case of rr-P3AT, it has been observed by TOF that mobilities increased with the field [19]. In the GDM framework, one can argue that the equilibrium between energetic and positional disorders are displaced when the regioregularity is changed, which is coherent with the observation of different film morphologies. Indeed, the positional disorder could depend strongly on the regioregularity *via* the amount and orientation of the molecular packing.

A complementary explanation was proposed for the negative field mobility dependance, relying on the spatial inhomogeneity of the electric field [26, 27]. These works account for the spatially inhomogeneous electric field at the interfaces with the electrodes (depletion) in calculations of transit times. Transit times are then composites of drift and diffusion processes. There has been some debate on this depletion effect. Indeed, depletion implies that current transient should be thickness dependent, while [15] and [14] measured thickness independent mobilities.

[14], spin coating in [15, 16, 19, 21, 23] and drop casting in [17, 23, 24].

Doping by oxygen and moisture It is well known that the shallow ionization potential of P3HT implies that it is easily *p*-doped (for example by oxygen). The effects of oxygen, light and moisture on electrical characteristics and on solar cells performances of samples containing P3HT have been studied. P3HT has been shown to degrade under the influence of light, moisture and oxygen combined. In [28] for example, impedance spectroscopy measurements showed an increase of the acceptor density in P3HT thin films within a few tens of minutes under light and oxygen influence. The doping on the other hand remained stable under sole influences of light or oxygen.

In [29], FET characteristics were measured in air and very quick degradation of the characteristics were also shown (a few minutes), while de-doping to the contrary was very long (150 hrs under secondary vacuum). Saturation mobilities of field effect transistors were found to degrade in the first day of air exposure but remained stable afterwards. In [30], the influence of moisture and oxygen were investigated separately on P3HT-based FET characteristics. When the samples were stored in dry oxygen atmosphere, the mobility did not evolve, while degradations were much stronger when samples were stored in atmospheres with high relative humidities.

Importantly, Schafferhans *et al.* studied the effect of oxygen on the charge mobility with the CELIV technique. For P3HT-only thin films, they showed that the mobility decreased by 2 orders of magnitude after 100h of oxygen exposure [31]. For P3HT-PCBM heterojunctions, the degradation was stabilized compared to P3HT-only devices, with a decrease of mobility only by a factor 2 in the same conditions. Furthermore, the degradation due to oxygen was found to be accelerated by light [32].

In conclusion, P3HT electrical characteristics are modified by oxygen, moisture and light. Doping occurs very quickly and is reversible by pumping under secondary vacuum for 150 hrs (thin film FET measurements, [29]). The combined influence of oxygen and light decreased mobilities. High humidity also has been shown to accelerate tremendously FET degradation.

Electrical fatigue A recent study shows the influence of electrical stress on TOF transients in PPV derivatives [33]. Hole transport was shown to fade with electrical fatigue: transients became more dispersive, mobility decreased and became more dependent on the applied electric field. Although no similar study has been published about P3HT, this phenomenon is also likely to occur.

3 Time-of-Flight measurements in hybrids

A few TOF studies of hybrids consisting of conjugated polymers and semiconducting nanocrystals have been published.

In 2003, Choudhury *et al.* studied hole transport in hybrids based on PVK and CdS nanodots (with diameters <14 nm) [34]. Devices consisted of ITO, a selenium charge generation

layer, the spin coated hybrid blend (the maximal CdS fraction was 5 wt%, *i.e.* around 1 vol%[3]) and Ag electrodes. A 10 ns pulsed laser at 532 nm was shone through the ITO/Se layer. The authors found a Poole-Frenkel dependence of the hole mobility as a function of temperature and electric field, very similar to that of PVK alone[4]. Mobilities depended on the film thickness for 2.9 to 5.9 μm thick films. Finally, the hole mobility improved with increasing content of CdS nanodots.

More recently, Chen *et al.* studied hole and electron transport in hybrids made of P3HT and pyridine-treated TiO_2 nanodots or nanorods, by the TOF and CELIV techniques [35, 36]. TOF samples consisted of 2 μm thick drop cast hybrid layers between 1) ITO and Al electrodes for electron current measurements with the illumination through ITO and 2) Al-coated ITO (35 nm of Al) and an Al counter electrode for hole current measurements, with the illumination through Al-coated ITO.

P3HT transients currents were dispersive; addition of TiO_2 nanodots or nanorods rendered the plateau region better defined, indicating a less dispersive transport for both electrons and holes. Furthermore, electron and hole mobilities increased by one order of magnitude for hybrids containing nanodots and by more than one order of magnitude in the case of nanorods, compared to pristine P3HT samples. Mobilities were only weakly dependent on the electric field for all samples, contrasting with some studies presented in the previous Section. Interestingly, optimal PV devices contained 50 wt% of TiO_2 nanocrystals (21 vol%[5]) and TOF measurements also showed optimal mobilities for this ratio. Mobilities increased with the content of nanocrystals up to 50 wt%, while samples made of 70 wt% of nanocrystals (38 vol%) exhibited reduced mobilities and a negative field-dependence [35].

Finally, the authors correlated charge generation and separation (absorbance, photoluminescence, time-resolved photoluminescence) and charge transport to the active layer morphology (X-ray, electronic tomography by scanning transmission electron microscopy with high-angle annular dark-field) [36]. They attributed the enhancement of hole transport to a morphology change of the P3HT matrix, showing 'nanodomains' confined by the presence of nanocrystals, and more strictly by nanorods than by nanodots. Moreover, the nanorods' intrinsic anisotropy improved the connectivity of the electron transporting phase and nanorods-based samples proved to have more distinct organic *vs* inorganic phases, particularly in the direction perpendicular to the substrate. This is thought to facilitate transport in this direction of interest for transport.

[3] CdS density is 4.82 g/cm^3.
[4] PVK hole mobility increases with the electric field, contrarily to hole mobility in P3HT.
[5] TiO_2 density is 4.23 g/cm^3.

4 Other mobility measurement techniques [37]

Performing traditional Time-of-Flight measurements requires thick samples. Due to varying processing conditions, they can differ from typical OPV samples in terms of active layer structural and morphological properties. Consequently, alternative charge transport measurement techniques have also been used in the growing field of organic photovoltaics. With different configurations and experimental conditions, they may lead to different values of mobilities. Different methods probe different scales; the larger the surface or volume probed, the more sensitive to purity and order of the materials. Other than TOF, electrical measurements of the mobility include:

Field effect transistor configuration Charge carriers are accumulated in a very thin conduction channel between the two electrodes by the application of a gate voltage inducing a capacitive effect at the interface with the dielectric substrate. Usually, these electrodes are both either at the bottom or at the top of the active layer and the accumulation channel is located on the substrate. This technique thus allows to study charge transport in the direction parallel to the substrate. Recently, several groups have developed vertical Field-Effect transistors to study charge transport perpendicular to the substrate [38]. FET measurements are affected by structural properties and defects at the interface with the dielectric layer, by its nature and by contact resistances.

Space-charge limited current In space-charge conditions, the current is limited by a large density of injected charge carriers, which electrostatic repulsion prevents more charges of being injected. Low mobilities of charge-carriers often lead to the build-up of a space-charge zone. In the absence of traps, current-voltage characteristics of unipolar samples in the space-charge limited regime follow the Mott-Gurney law:

$$J_{SCLC}(V) = \frac{9}{8}\epsilon\epsilon_0\mu\frac{V^2}{L^3} \tag{III.5}$$

where L is the sample thickness, V the applied voltage. The V^2 dependence of current is reached for high voltages (at lower fields, the dependance is linear). Especially at high fields, a field dependent mobility should be considered (such as the Poole-Frenkel dependence $\mu = \mu_0 exp(\beta\sqrt{V/d})$).

This technique requires good injecting contacts, so that current is limited by the bulk properties of the device, not by the injection. It has been emphasized in [39] for example that the I(V) characteristics can depend on the nature of contacts when the transport is limited by injection, thus restricting proper determinations of the mobility.

Current extraction by linearly increased voltage (CELIV) Charge-carrier are extracted from the active layer by the application of voltage ramp. This technique allows to

determine the charge-carrier density as well as their mobility. Here one measures sandwich-type samples and charge carriers are intrinsic, doping charges or photo-generated charges in photo-CELIV (charge carriers are photo-generated by a laser pulse at a time t_{del} before the voltage ramp starts). This technique is applicable to thin films with relatively high conductivities, contrarily to TOF. Recent analyses include recombinations [8].

Pulse-radiolysis Time-Resolved Microwave Conductivity (PR-TRMC) This technique is different from the other ones because it is contact-less and probes materials locally, *e.g.* on the scale of the single polymer chain or portion of chain. PR-TRMC thus gives upper limits for mobility values when mobilities are limited by interchain transport, as it is the case in polymer thin films.

One of the differences between these techniques to study charge transport is the thickness of active layers. Table III.1 summarizes thicknesses of typical samples, applied voltages ranges and the subsequent applied field.

Table III.1 – Typical values of thicknesses, applied voltages and fields in different electrical characterizations

Technique	*Thickness*	*Applied voltage*	*Applied electric field*
OPV/SCLC	100 nm	1 V	10^5 V/cm
TOF	5 μm	100-1000 V	$10^4 - 10^6$ V/cm
CELIV	100 nm [40]-1 μm[14]	2-10 V	$2.10^4 - 10^6$ V/cm

5 Conclusion

Charge mobility in disordered materials and some mobility measurement techniques have been introduced, with an emphasis on the dependence of mobility values on the nature and processing of samples, experimental conditions, and history of the sample. Traditional Time-of-Flight measurements and analysis were described.

We focused on reports of TOF measurements of P3HT and hybrid thin films. Hole mobility in P3HT exhibits a negative field dependence at room temperature, attributed a to large positional disorder; this negative field dependence disappears at low temperature. Regioregular P3HT samples deposited by solvent slow evaporation exhibited less dispersive transients than

spin coated samples, with higher mobilities than in regiorandom samples. Degradation of P3HT samples due to oxygen, light, moisture and/or electrical stress was presented by various electrical methods, among them TOF. Finally, TOF measurements on hybrids consisting of PVK:CdS nanodots and on P3HT:TiO_2 nanodots or nanorods were presented. In both studies, inorganic fractions were kept relatively small. Electron and hole transports both became more efficient upon the addition nanocrystals, especially in the case of nanorods-based hybrids. An optimum for hole and electron mobilities was reached for 50 wt% (21 vol%) of TiO_2 nanocrystals, before deteriorating for larger ratios.

Chapter IV

Time-of-Flight measurements in P3HT and hybrid films

Our Time-of-Flight setup and experiments are described. We first introduce the studied samples, the measurement configuration, and current voltage characterizations of hybrids. We detail our TOF measurements and the obtained results for charge transport in P3HT and hybrid thin films in terms of mobility and dispersivity.

1 Time-of-Flight setup

We built a setup compatible for Time-of-Flight and Current Extraction by Linearly Increased Voltage (CELIV) measurements[1].

The laser is a Crylas Nd:YAG laser emitting at 532 nm or 355 nm, with a modulable output power up to 100 μJ in each 1 ns pulse.

The laser beam is split into two secondary beams: one is going to a photodiode that detects the laser pulse, and triggers the generation of voltage pulses and the mechanical shutter; the other beam can be attenuated by optical densities before being focused into an optical fiber for transmission to the sample, see Fig. IV.1.

All measurements are performed in a Faraday cage and care has been taken to limit electrical noise.The sample holder is horizontal and allows for illumination either through the bottom or the top electrode. Contacts are made by probes equipped with micro-manipulators. Voltage pulses and ramps are generated by Agilent 33220A waveform generator and a Trek 601C voltage amplifier if needed. Current is directly measured and recorded by a Tektronik digital oscilloscope DPO 7104 1GHz thanks to a 50 Ω terminated probe and a current amplifier when needed. All electronics are synchronized on the laser pulse detection by a Stanford Research System delay generator DG535.

Photocurrent measurement in the TOF configuration follow triggering by both the photodiode and the mechanical shutter signals. The acquisition is commanded via a home-made

[1]Nicolas Bruyant and the ANR Myosotis have been the architects of this experimental setup.

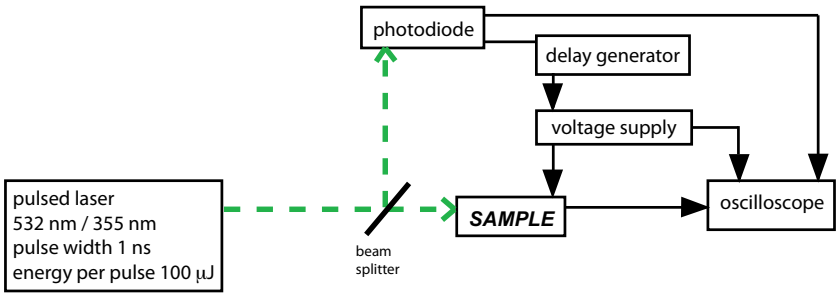

Figure IV.1 – TOF setup

LabView program that allows to choose various delay times and voltage levels.

This setup allows measurements down to the nanosecond range, for currents down to 5 μA at 400 MHz.

2 Studied devices

Indium Tin Oxide (ITO) substrates were prepared by etching ITO in warm aqua regia to make conducting ITO lines on glass, 1 to 5 mm wide. Substrates were cleaned by a wet procedure and by UV-ozone. Films were deposited by drop casting solutions of polymer, nanocrystals or hybrid blends onto the substrate as explained in Chapter II, left to dry for one week, before annealing in a Büchi oven. For electrical characterizations, aluminum electrodes were deposited on top of the active layer to cross with ITO lines and obtain 2 to 6 'pixels' with areas between 1 mm^2 and 25 mm^2. Active layer thicknesses and roughnesses were measured with an Ambios XP-2 stylus profilometer. All steps of sample preparation are detailed in Appendices.

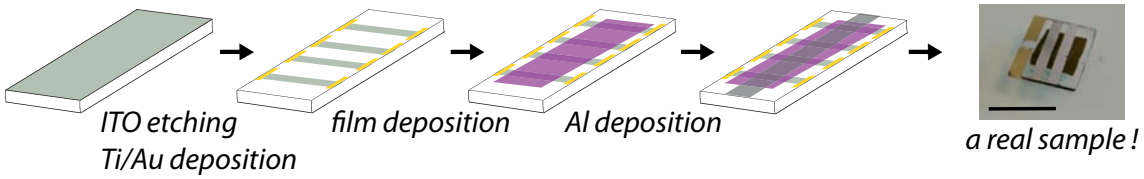

Figure IV.2 – TOF device making On the picture of the real sample, the areas of the pixels are 4 mm^2 and the scale bar is 1.2 cm.

2.1 Active layer compositions

We varied different parameters in the composition of samples:

- the nature of the P3HT matrix, by using two types of P3HT: i) P3HT1, with M_n=9.8 kDa, D=3.75 and a regioregularity around 91%; ii) P3HT2, with $M_n = 28.5\ kDa$, $D = 1.63$ and a regioregularity of 95.9%;

- the nature of the nanocrystals, by varying the shape (spherical, branched) and ligands (synthesis, pyridine);

- the proportions of the components, between 0 % of nanocrystals to 83 wt%-49 vol% of nanocrystals.

A more precise list of samples is presented in Section 3. To analyze photocurrent transients with the traditional Time-of-Flight method described above, several conditions need to be respected. Here we list them and check that our P3HT and hybrid samples fulfill these conditions.

2.2 Optical thicknesses

The sample must be optically thick, *i.e.* its thickness L must be much larger than the penetration depth δ of the excitation beam. In the following reasoning, we take $L/\delta \geq 10$.

We measured the penetration depth for P3HT thin films to be 50 nm for 532 nm illumination (500 nm for a 355 nm illumination). Consequently, P3HT samples with thicknesses above 0.5 μm (5 μm) fulfill the optical thickness condition for a 532 nm (355 nm) illumination.

For 6.7 nm CdSe nanocrystals thin films, penetration depths of a 532 nm illumination are around 1.3 μm when they are capped with synthesis ligands and 600 nm when they are capped with pyridine (the film density increases). They decrease to 350 nm and 190 nm respectively for a 355 nm illumination wavelength.

Thus, hybrid films with 49 vol% nanocrystals capped with synthesis ligands were the less absorbing samples that we studied. They have a penetration depth of around 700 nm (425 nm) for a 532 nm (355 nm) illumination, calling for samples thicknesses $\geq 7\ \mu m$ (4.25 μm).

2.3 Capacitance constraints

The geometrical capacitance of a typical sample is $C_{geom} = \epsilon\epsilon_0 S/L$, where ϵ is the relative dielectric constant of the active layer, S the area of the sample and L its thickness. For P3HT, ϵ is around 3, leading to a geometrical capacitance :

$$C_{geom} \approx 2.10^{-11}\ F \tag{IV.1}$$

calculated with the parameters used in our measurements: $S = 0.04\ cm^2$ and $L = 5\ \mu$m.

For hybrid materials, the effective dielectric constant is expected to be larger than for P3HT-only: for 16% in volume of inclusions with a dielectric constant of 8, Bruggeman's effective medium theory gives $\epsilon_{eff}^{16\%} = 3.6$; $\epsilon_{eff}^{36\%} = 4.4$ for 36% of nanocrystals and finally $\epsilon_{eff}^{49\%} = 4.9$ for 49% of nanocrystals. Thus, the geometrical capacitances of hybrid samples are a little larger than those of P3HT-only films.

For TOF analysis, the sample capacitance C_{sample} must fulfill two conditions:

$$\underbrace{C_{min} = \frac{Q_\gamma}{V}}_{1} << C_{sample} \underbrace{<< C_{max} = \frac{L^2}{\mu V R}}_{2} \tag{IV.2}$$

1. The condition $C_{sample} >> C_{min} = Q_\gamma/V$ ensures that the total amount Q_γ photo-generated charges is much smaller than the number of capacitive charges accumulated at the electrodes so that space-charge effects do not perturbate the internal field.

   We evaluate the maximal number Q_γ^{max} of photo-generated charge carriers from the 532 nm laser pulse energy (60 μJ), the attenuation due to the Al electrode (10^{-4} for a 60 nm thick electrode) and the ratio of the electrode area (0.04 cm^2) to the total illuminated area (1 cm in diameter): $Q_\gamma^{max} \approx 10^{-10}C$. For a typical applied voltage of 100 V, this leads to a lower bound for the capacitance:

   $$C_{min} \approx 1.3.10^{-12}F \tag{IV.3}$$

   Here we considered that all photons transmitted through the Al electrode are absorbed and converted into free charges.

   An experimental check of this condition relies on integrating the photocurrent to obtain the total number of charges collected (this procedure also neglects recombinations).

   Let us note that the condition $C_{sample} >> Q_\gamma/V$ is mathematically equivalent to the condition $t_\sigma >> t_{tr}$ under the assumption that the sample can be described as a parallel plate capacitor and that it is fully depleted. Indeed, the dielectric relaxation time writes $t_\sigma = \epsilon\epsilon_0/\sigma$, where σ is the conductivity; the transit time writes $t_{tr} = L^2/\mu V$.

   High light-pulse intensities result in the space-charge limited TOF regime (SCLC-TOF), see for example [41] for SCLC-TOF measurements on P3HT.

2. The condition $C_{sample} << L^2/\mu V R$ is equivalent to having a very small circuit decay time RC compared to the transit time of charges in a fully depleted sample: $t_{RC} << t_{tr}$. This ensures that the decay current of the circuit after the voltage rise does not affect the transit time determination.

   With a sample thickness of 5 μm, a mobility of $10^{-3}cm^2/V.s$, an applied voltage of 100 V and a load resistance of 50 Ω, the maximal capacitance of the sample is:

   $$C_{max} \approx 5.10^{-8}\ F \tag{IV.4}$$

   This correspond to a maximal decay time $R.C_{max} \approx 2.5 \times 10^{-7}s$.

   TOF experiments with $t_{RC} >> t_{tr}$ are called *integral TOF*. They are usually performed

with thinner samples, and the quantity studied is the collected charge rather that the current.

2.4 Contacts and energy levels

For a electron (hole) mobility measurement,

- the contact at the illuminated electrode must be blocking for electrons (holes) to ensure measurement of photo-generated charge carriers and not injected ones;
- the contact at the collecting electrode must be blocking for holes (electrons) in order to avoid recombinations in the active layer during drift.

In the paragraph below, we refer to four contacts, for electrons and holes at each electrode.

Our anode is ITO and its energy level is aligned to the HOMO of P3HT, ruling out a blocking contact for holes at the interface with ITO[2]. In our case, then, the ideal configuration for measurement of both electrons and holes current within a single sample, in order to rule out any possible variability from sample processing, is with an energy electrode level E1 aligned to the LUMO of the active layer and the other electrode energy level E2 aligned to the HOMO, see Fig. IV.3. Then, illuminating through E1 allows to measure holes and illuminating through E2 allows to measure electrons. This principle contrasts with the commonly advertised procedure, that consists of inverting the sign of the applied bias, rather than the illumination side, to measure different types of charges and is similar to that used in [16] for example. Both procedures are not strictly equivalent since the charge generation and collection occur at different interfaces.

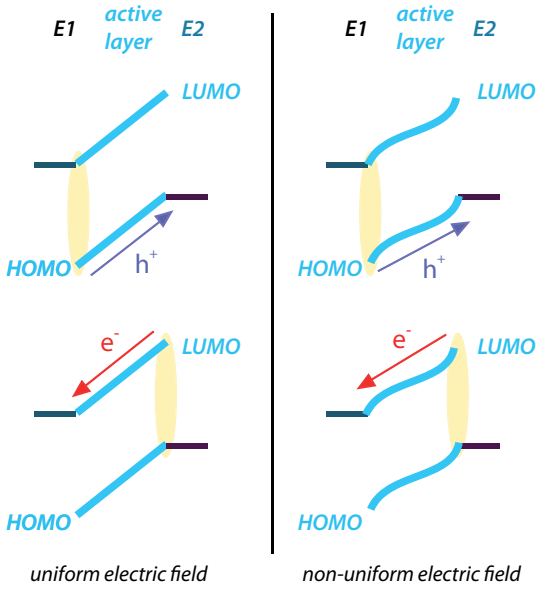

Figure IV.3 – Ideal energy levels for TOF measurements E1 and E2 are the electrodes energy levels; HOMO and LUMO are the energy levels of the active layer, in the uniform and non-uniform electric field representations.

The electric field at the interface with the illuminated electrode must be strong in order to optimize exciton dissociations. In the case of P3HT, it has been shown that the signal is more important when the sample is illuminated

[2]Although for OPV, thin layers of Ca under Al and of PEDOT-PSS on top of ITO are used to optimize electron and hole blockade, we minimized the number of intermediate layers to have simpler devices, easier to interpret. Moreover, PEDOT-PSS is usually used to reduce the roughness of the ITO substrate. For TOF (thick) samples, ITO roughness is not a limiting factor.

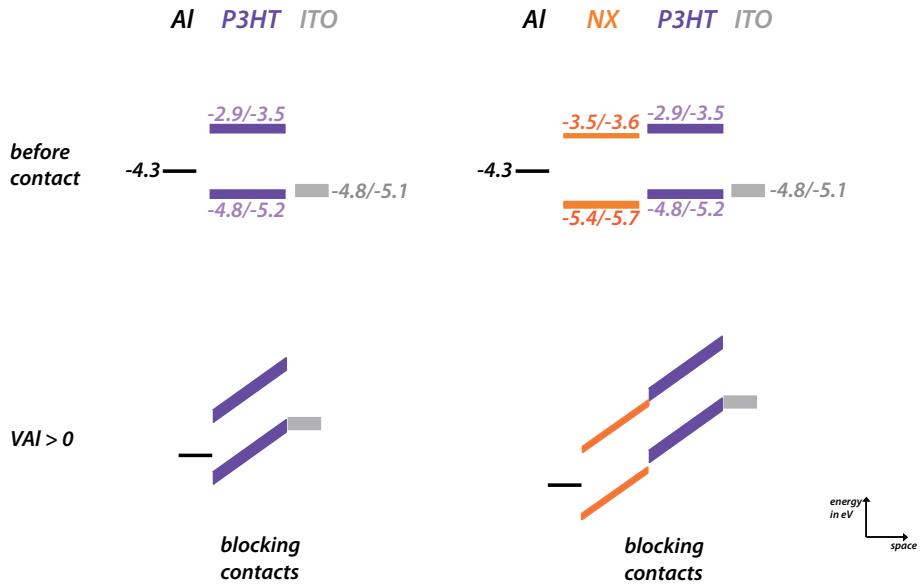

Figure IV.4 – Energy diagram of devices for P3HT-only devices and hybrid devices, in the uniform electric field representation. Energy levels were obtained from electrochemistry or from the literature. The width of the lines is an indicator of the range of values found (depending on the size of nanocrystals or on the source).

through the Al electrode, and this has been explained by the formation of a strong electric field in the depletion zone at the Al interface [27].

In Fig. IV.4, energy levels for P3HT and hybrid thin films are represented. Al, ITO and P3HT energy levels are drawn from the literature. Nanocrystals' HOMO energy levels were measured by electrochemistry and are gathered in Chapter II, Table II.3. Nanocrystals' LUMO level measurements can be found in [42]. For TOF measurements, the applied bias were always $V_{ITO} = 0\ V$, $V_{Al} - V_{ITO} = V_{Al} > 0\ V$.

2.5 Current-voltage characteristics

Current-voltage characteristics were measured in the dark with a Keithley 2636A; we present the dark I(V) curve of a hybrid device in Fig. IV.5 a), showing a diode behavior.

Current-voltage characteristics allow an analysis with equivalent electrical circuit as pictured in Fig. IV.5 b), [43]. R_s is the series resistance (contacts), R_{sh} is the shunt resistance (active layer). The diode represents the blocking nature of one of the contacts. Finally, the current generator, present only under illumination, represents charge generation and extraction from the active layer. The collection of charges leads to a shift of the I(V) curve. The performance of the solar cell is described by the values of the short-circuit current I_{sc}, the open-circuit voltage V_{oc} and the Fill Factor, defined graphically by the ratio of the collected power to the maximal expectable power $P_{th} = I_{sc}.V_{oc}$.

Samples presented in the following have thicknesses above 3 μm and exhibited shunt resis-

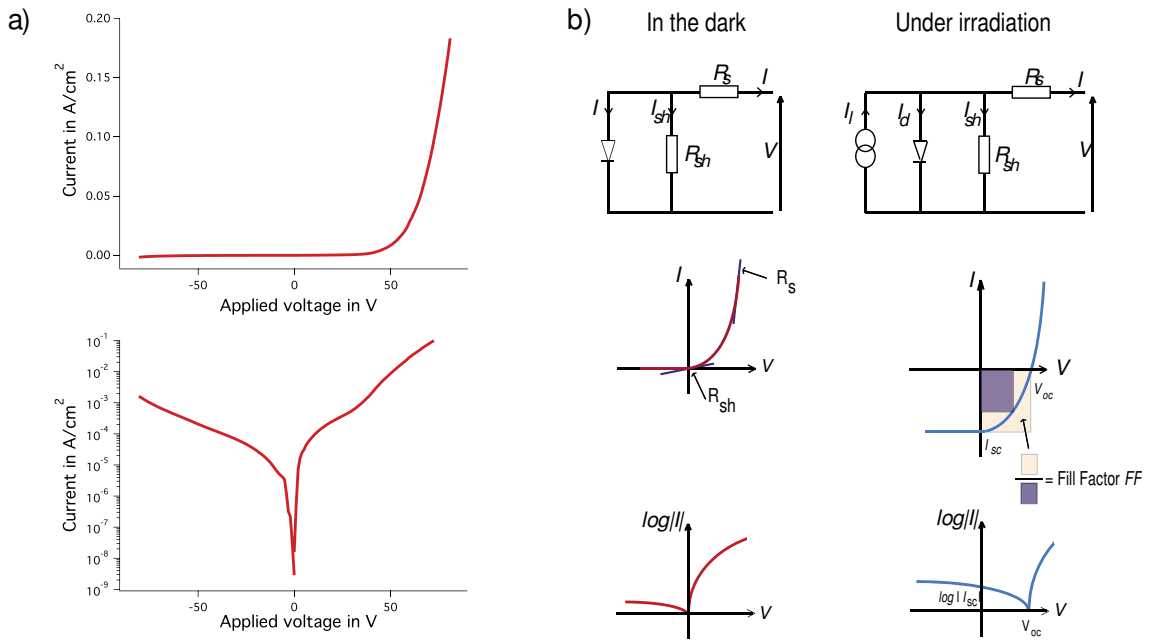

Figure IV.5 – Current-voltage characteristics and equivalent circuit representations of a hybrid device in the diode configuration. In a), dark I(V) curves in linear and lin-log representations of a 7 μm thick hybrid film, containing 75 wt% (36 vol%) of nanodots capped with synthesis ligands. In b), the definitions of the variables used frequently to characterize solar cells.

tances between 50 kΩ and 20 MΩ, estimated from the slope of the current-voltage characteristics for low voltages. These shunt resistances correspond to active layer resistivities, with hundreds of $\Omega.cm$ for P3HT-only samples and $10^3 - 10^5$ $\Omega.cm$ for hybrid samples.

3 Typical Time-of-Flight transients of organic and hybrid thin films

A voltage pulse is applied to the sample; after the capacitive current has decayed to a stable value, charges are photogenerated by a 1 ns laser pulse, shone through the Al or the ITO electrode, for hole and electron detection respectively. The voltage pulse is cut when the photocurrent has decayed and the sample is allowed to relax before the next laser pulse. Transients are averaged over 50 runs. Raw data sets are treated before extraction of transit times: i) the observable is a voltage across a 50 Ω resistor; it is converted to a current density; ii) the origin of time is taken at the photocurrent maximum; iii) the baseline (dark current) is subtracted. Data sets are usually 10^5 points and are not filtered nor resampled unless necessary for further analysis.

In this Section, we present an example of TOF analysis for a 7 μm thick hybrid film, made of a P3HT2 matrix containing 75 wt% (36 vol%) of 4.1 nm nanodots capped with synthesis ligands.

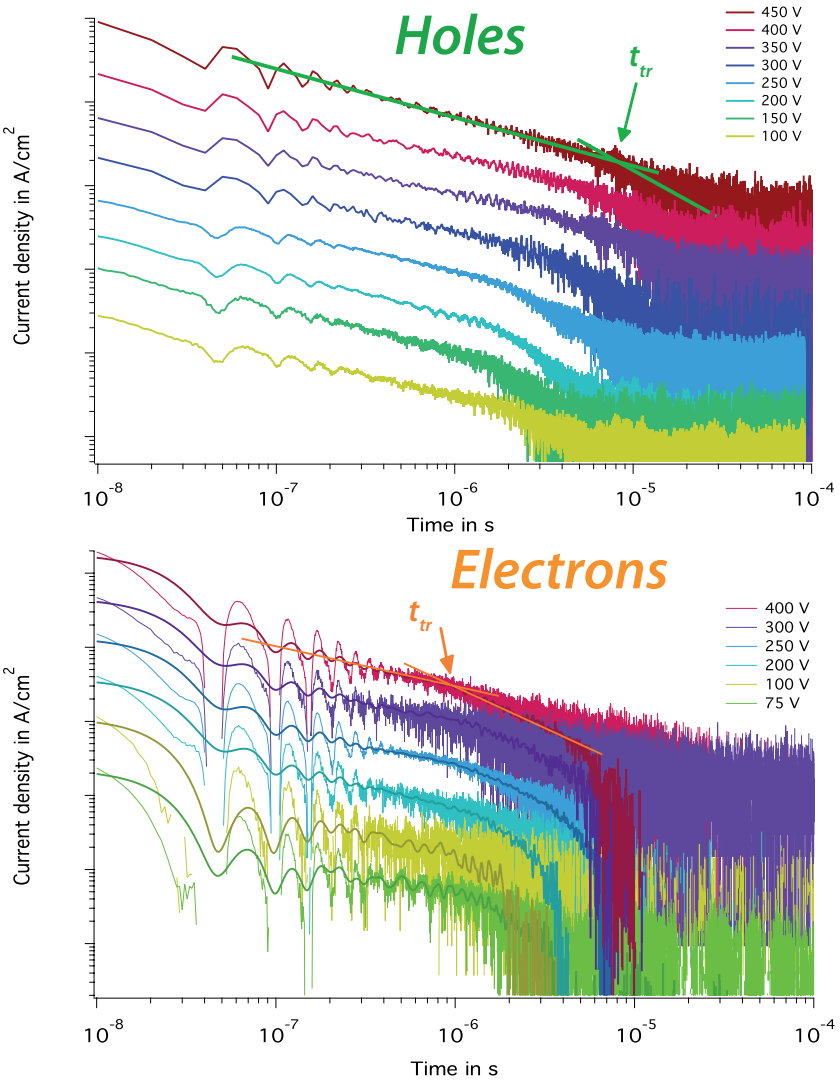

Figure IV.6 – TOF transients of a hybrid sample in the log-log representation. The sample is 7 μm thick and contains 75 wt% (36 vol%) of 4.1 nm nanodots capped with synthesis ligands. The externally applied voltage was varied between 75 V and 450 V. The upper graph shows traces recorded with illumination through Al and $V = V_{Al} > 0V$ and consists of unfiltered data, whereas the lower graph shows traces recorded with illumination through ITO and $V = V_{Al} > 0V$ and presents both the unfiltered data and the filtered data (low-pass Hanning filter; end of pass band 10^{-6}; start of reject band 2.10^{-2}), for easier visualization. Here, lines and arrows indicate fits and transit time positions. Curves were shifted vertically for clarity.

FIG. IV.6 shows hole and electron photocurrent transients for different applied voltages. Linear parts of the transients on log-log plots are fitted with $t^{-(1-\alpha_{pre})}$ before the current drop and by $t^{-(1+\alpha_{post})}$ after the current drop, where α_{pre} and α_{post} are the dispersivity coefficients. The intersection of the fitting curves gives the transit time t_{tr}.

We observed dispersive transients, as shown by the current tails at long times. α coefficients do not vary significantly with the applied voltage.

The mobility is computed from the transit time t_{tr} with the help of EQ. III.2, corrected for the penetration depth δ of the 532 nm illumination in the hybrid material and for the built-in voltage V_{bi} due to the difference of work functions of electrodes:

$$\mu_{xp} = \frac{v}{E} = \frac{(L-\delta)}{t_{tr}} \frac{L}{(V-V_{bi})} \tag{IV.5}$$

where L is the sample thickness and V the externally applied voltage. While the correction due to the built-in voltage $V_{bi} \approx 0.5\ V$ is relatively negligible compared to the externally applied voltages, δ reached 10 % of the film thickness L for some hybrids samples.

Uncertainties in the determination of the mobility include: 1) the thickness variation dL, taken as the standard deviation around the mean thickness. $dL/L \approx 10\%$ in the roughest samples used for mobility determination (rougher samples tended to give unexploitable transients); 2) the error on the determination of t_{tr} by the tangent method; dt_{tr}/t_{tr} was usually around $3-10\%$.

Probing the electronic signal by variation of the illumination intensity and wavelength

We varied the illumination intensity to probe the influence of photo-generated charge densities on the allure of current transients.

FIG. IV.7 shows transients obtained with different transmissions (optical densities) of the 532 nm illumination through ITO, with various applied voltages, for the same hybrid sample.

First, while a full transmission results in readable transients for all voltages, low transmissions impeach the readability of transients: a photosignal exists but it is too low to be analyzed by the TOF method. Secondly, the transmission threshold to have a good signal depends on the voltage: the higher the voltage, the less transmitted photons are needed to obtain decent TOF photocurrents. Finally, when electron transit times can be derived, we find that they do not depend on the optical transmission within experimental uncertainties. This last observation shows that the electron mobility does not change with the photo-generated charge carrier density, at least in the range of optical intensities probed here.

These observations show that the charge carrier density increases with the number of incident photons. This can be explained with complementary arguments: i) a larger exciton generation, ii) a more efficient exciton dissociation, iii) a smaller proportion of charges recombining and/or

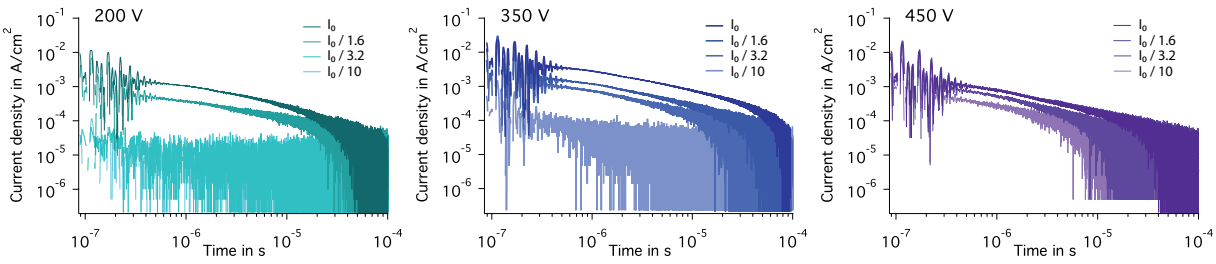

Figure IV.7 – Comparison of photocurrents obtained with different 532 nm illumination intensities for the same sample than Fig. IV.6 and various applied voltages.

iv) a smaller proportion of charges stuck on long-lived trap states. While the first reason in itself (larger exciton generation) cannot explain the voltage dependance of the threshold, the next three should all depend on the applied voltage.

This study shows that electron mobilities do not depend on the light intensity but that the photocurrents themselves do. While these findings of course calls for further investigation of the electron photocurrent dynamics, for example thanks to temperature-dependent measurements, it is worth to note that this intensity-dependent shape of TOF current transient is similar to what was reported in P3HT:PCBM organic blends [20].

Electric energy scale

With applied fields between 5.10^4 V/cm and 10^6 V/cm, electric energies are between 5 meV/nm and 100 meV/nm and are thus comparable to 1) the thermal energy at room temperature; 2) the energies at play in the materials (energetical and positional disorders for example). The competition between these energies most likely influences the dependance of the mobility on the electric field.

List of studied samples

Table IV.1 presents the samples of which TOF mobilities are presented here.

4 In pristine P3HT

The TOF measurements in pristine P3HT serve as references for the discussion of the mobilities in hybrids.

Hole mobilities in P3HT1 and P3HT2 thin films are presented in Fig. IV.8. They lie between 10^{-4} and 10^{-3} cm^2/V.s for both samples. P3HT1 exhibits slightly higher TOF hole mobilities than P3HT2. This could be related to the size of crystallites, larger in P3HT1 (140 Å) than in P3HT2 (130 Å), see Chapter II, 2.2.2.

Table IV.1 – Samples measured by TOF

Type of active layer	*Nanocrystals' proportion, weight and volume*	*Shape of nanocrystals*	*Surface functionalization of nanocrystals*
P3HT1	0 %	-	-
P3HT2	0 %	-	-
Hybrid (P3HT1)	50 wt% - 16 vol%	spherical 6.7 nm	synthesis ligands
Hybrid (P3HT2)	50 wt% - 16 vol%	spherical 4.1 nm	synthesis ligands
	75 wt% - 36 vol%	spherical 4.1 nm	synthesis ligands
	83 wt% - 49 vol%	spherical 4.1 nm	synthesis ligands
Hybrid (P3HT2)	75 wt% - 36 vol%	spherical 4.1 nm	pyridine
Hybrid (P3HT2)	50 wt% - 16 vol%	branched	synthesis ligands
Hybrid (P3HT2)	50 wt% - 16 vol%	branched	pyridine
	75 wt% - 36 vol%	branched	pyridine

In both samples, hole mobilities decrease with increasing electric field at least at low fields; P3HT2 exhibits a stable mobility value above $\sqrt{E} = 700(V/cm)^{1/2}$. This negative electric field dependance of the mobility at low fields cannot be fitted by the Poole-Frenkel model, where the mobility is in $exp(\beta\sqrt{E})$, with $\beta > 0$. However, this negative dependance, as well as the order of magnitude of the measured mobilities, are in complete accordance with previous reports (see Chapter III, 2 and the references therein, *e.g.* [14–18]).

Also, both curves could be fitted to the Gaussian Disorder Model (GDM), with fit parameters indicated in Table IV.2.

$$\mu_{GDM}(T,E) \;=\; \mu_0 \; exp\Big\{ -(\frac{2\sigma}{3k_BT})^2 \;+\; C\;\sqrt{E}\;\big[\;(\frac{\sigma}{k_BT})^2 - \Sigma^2\big]\;\Big\} \tag{IV.6}$$

The GDM fit parameters are in agreement with the values reported in the literature. Of course, these fits would be more accurate with more constraining data points, obtained for example by varying the temperature, which is not possible yet in our setup.

From the point of view of material parameters, a higher energetical disorder in P3HT1 reflects the higher polydispersity of this sample compared to the polydispersity of P3HT2. Moreover, the larger crystallites of P3HT1 leads to a reduced positional disorder, probably

among other factors.

In the case of P3HT2, we could also measure the electron mobility, which was balanced with the hole mobility and will serve as a reference for the discussion of electron mobilities in hybrids.

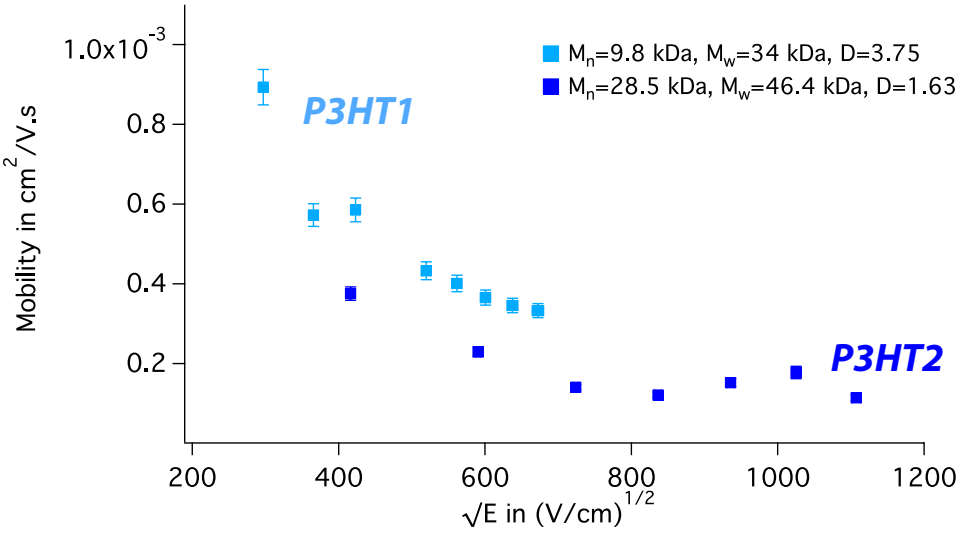

Figure IV.8 – TOF holes mobilities in P3HT1 and P3HT2 samples Due to clear inflection points of the transients and very low surface roughnesses, errors bars are smaller than the markers' size. The polymers have been measured in slightly different electric field ranges due to different qualities of the photosignals.

Table IV.2 – Gaussian Disorder Model fit parameters for both our P3HT samples and from the literature.

GDM parameters	P3HT1	P3HT2	Values from the literature [14] - [44]
σ	70 meV	46 meV	75 meV - 58 meV
Σ	2.2	4.1	3 - 9.5
μ_0	1.7 10^{-3}cm^2/Vs	2.3 10^{-3}cm^2/Vs	5 10^{-3}cm^2/Vs - 5.3 10^{-3}cm^2/Vs
C	8.3 10^{-4} (cm/V)$^{1/2}$	1.6 10^{-4} (cm/V)$^{1/2}$	1.4 10^{-4} (cm/V)$^{1/2}$ - 6 10^{-4} (cm/V)$^{1/2}$

5 Hole transport in hybrids

In order to understand the influence of nanocrystals on hole transport in hybrid materials, we present hole TOF measurements in hybrid films made with two types of P3HT and CdSe nanocrystals of different natures (shape, ligands), as presented in TABLE IV.1. We first present experimental observations and then discuss the mobility values in relation to the material parameters.

5.1 In hybrids with P3HT 1

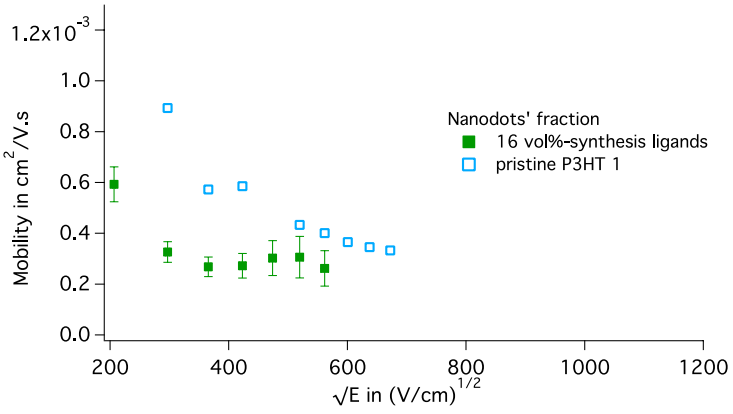

FIGURE IV.9 – TOF holes mobilities in a hybrid sample made with P3HT1 and 6.7 nm nanodots capped with synthesis ligands and compared to pristine P3HT1. The error bars for the mobility in pristine P3HT1 are not indicated because they are smaller than the marker's size, see FIG. IV.8.

The mobility measured in a hybrid film made with P3HT1 and 16 vol% of 6.7 nm nanodots capped with synthesis ligands is presented as a function of the square root of the electric field in FIG. IV.9. The hole mobility decreases in the presence of nanocrystals, in comparison to the mobility in pristine P3HT1.

5.2 In hybrids with P3HT 2

We studied hybrid films made with various contents of P3HT2 and nanocrystals with different shapes and ligands.

FIG. IV.10 presents hole mobilities in hybrids based on P3HT2 and a) 4.1 nm nanodots with synthesis ligands, b) 4.1 nm nanodots with pyridine, c) nanopods with synthesis ligands, d) nanopods with pyridine. As in pristine P3HT, mobilities generally decrease with the increasing electric field.

In a), hole mobilities are larger in hybrids with small fractions of CdSe nanocrystals (16 vol% and 36 vol%) than in pristine P3HT2. For hybrids containing 49 vol% of nanocrystals,

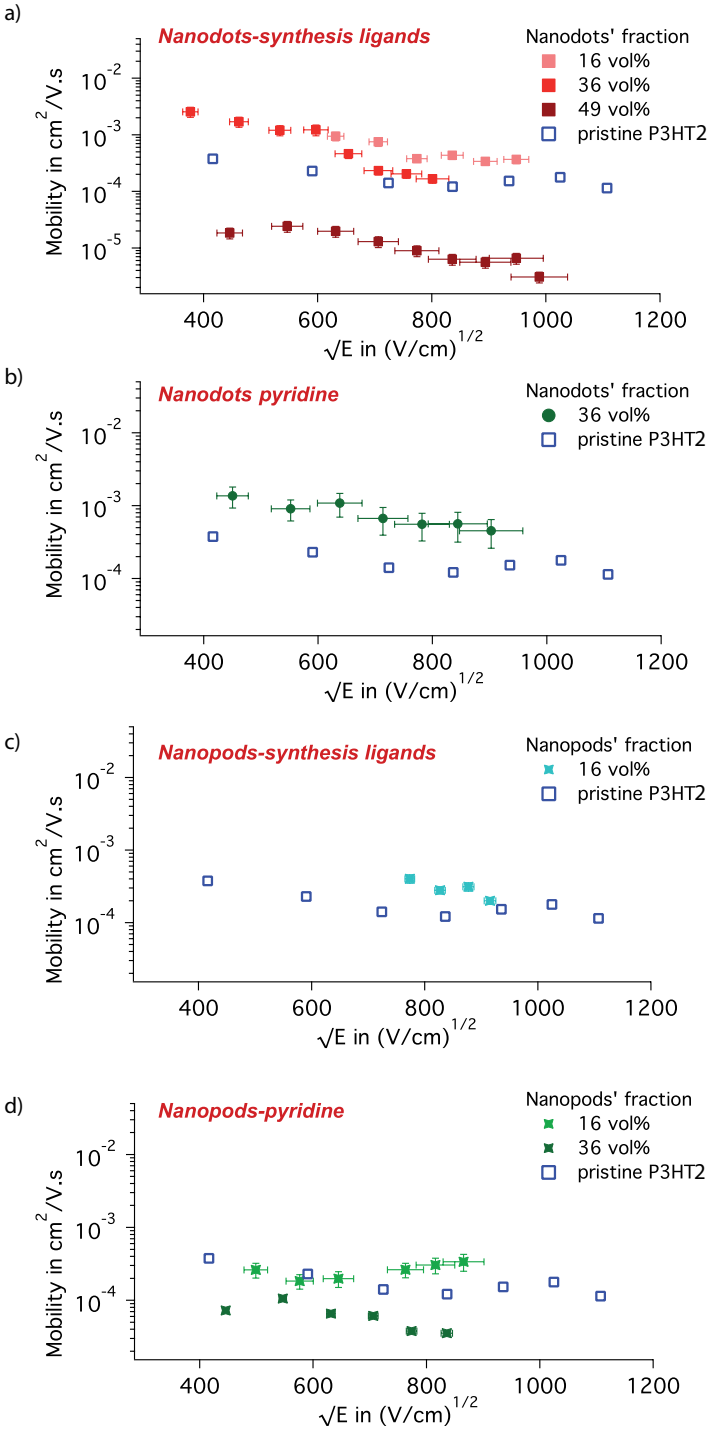

Figure IV.10 – TOF holes mobilities in hybrid samples made of P3HT2 and a) 4.1 nm nanodots with synthesis ligands, b) 4.1 nm nanodots with pyridine, c) nanopods with synthesis ligands, d) nanopods with pyridine. Note the different mobility scale for the first graph. Fractions not represented could not be measured due to low sample quality. The error bars for the mobility in pristine P3HT2 are not indicated because they are smaller than the marker's size, see Fig. IV.8.

mobilities decrease dramatically by 1 to 2 orders of magnitude.

In b), the hole mobility is improved by the addition of 36 vol% of nanodots treated with pyridine.

In c), the mobility is slightly higher for 16 vol% of nanopods with synthesis ligands than for prisitine P3HT2, especially for electric fields below 900 $V/cm^{1/2}$.

Finally, for nanopods treated with pyridine, in d), the hole mobility for 16 vol% of nanopods is slightly better than that of pristine P3HT2, especially at higher fields. It deteriorates for a higher content of nanocrystals, 36 vol%.

In summary, the hole mobility is improved by the presence of low contents of nanocrystals in the hybrid blend and deteriorates for higher amounts of nanocrystals. The experiments show that the amount of nanocrystals leading to a maximal hole mobility actually depends on the nature of nanocrystals: it is around 16 to 36 vol% for nanodots with synthesis ligands and lies around 16 vol% of nanopods capped with pyridine. Such behavior, *i.e.* the increase of hole mobility in P3HT upon addition of small volumic fractions of nanocrystals, has also been reported in [34–36].

We also observed a modification of the dispersivity of transients, evaluated from the slopes of the transients before the transit time, upon addition of nanocrystals. Smaller fractions of nanocrystals result in less dispersive transients (higher value of α_{pre}), as can be seen from the values of the dispersivity coefficient α_{pre} in Table IV.3. When the fraction of nanocrystals further increases, the dispersitivity decreases.

The values reported here for hole transport are of the same order than those found for rR-P3HT drop cast (0.9) and spin-coated (0.6) samples in [23]. Moreover, reduced dispersivities upon the addition of small volumes of acceptor have similarly been reported in [35] concerning P3HT:TiO_2 nanorods, and in [45] about P3HT:PCBM heterojunctions.

Table IV.3 – Hole transient dispersivities for P3HT and hybrids made with a) 4.1 nm nanodots with synthesis ligands; b) nanopods with synthesis ligands.

Nanocrystals' proportion, in weight and volume	*Dispersivity coefficient* α_{pre}	
	Dots-synthesis	*Pods-pyridine*
0 %	0.5	0.5
50 wt% - 16 vol%	0.9	0.85
75 wt% - 36 vol%	0.5	0.75
83 wt% - 49 vol%	0.5	-

In conclusion, the measurements of mobilities and dispersivities show that small volume fractions of nanocrystals result in more efficient hole transport than in pristine P3HT, and larger fractions in less efficient hole transport.

Effects of the nanocrystals' shape and surface ligands We gather in FIG. IV.11 the hole mobilities obtained in hybrids for 16 vol% in a) and for 36 vol% in b), to make out the influence of the shapes and ligands of nanocrystals.

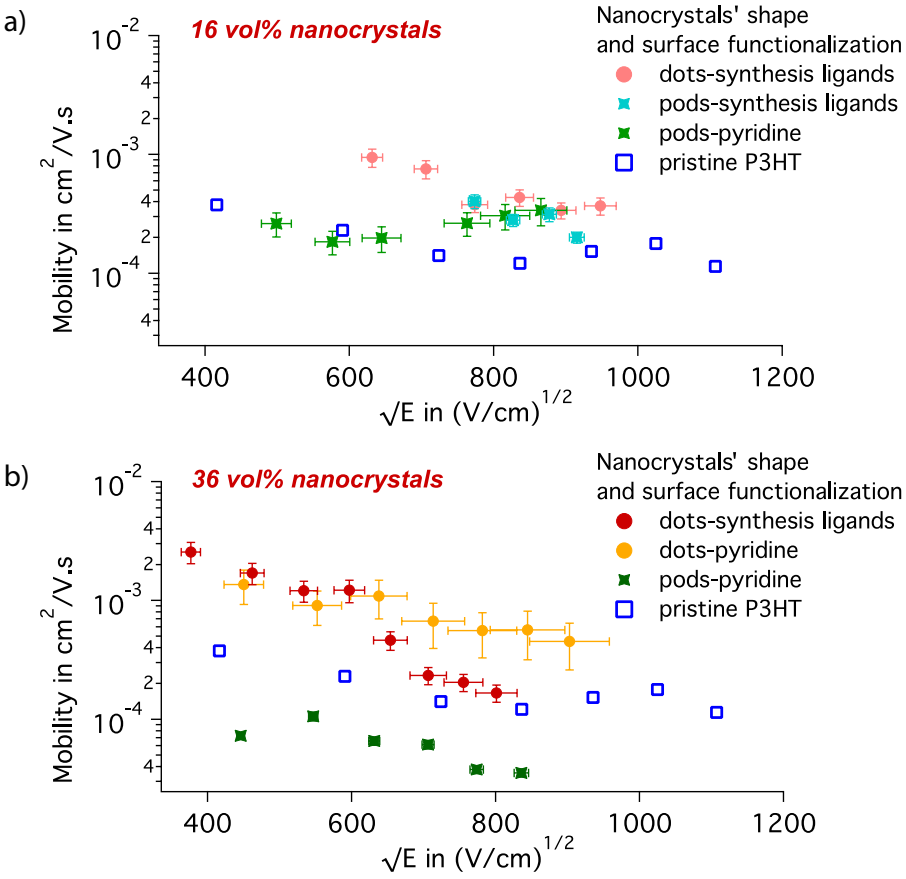

FIGURE IV.11 – Hole mobilities in hybrid samples made with nanocrystals of different shapes and with different surface ligands in a), 16 vol% and in b) 36 vol%.

For 16 vol% of nanocrystals, FIG. IV.11 a), hole mobilities are similar above 750 V/cm$^{1/2}$ for all samples probed, whatever the shape and ligands of nanocrystals. At lower electric fields, the hole mobility in nanopods-pyridine based hybrids is lower than that of hybrids made with nanodots with their synthesis ligands.

For 36 vol% of nanocrystals, FIG. IV.11 b), hole mobilities in hybrids containing nanodots are similar at lower electric fields and differ at higher fields: above 600 (V/cm)$^{1/2}$, hybrids made with nanodots with pyridine exhibit higher mobilities than those with nanodots with synthesis

ligands. The opposite behavior is observed for hybrids containing nanopods. When nanopods were treated with pyridine, the hole mobility is much lower than in P3HT2 and other hybrids (36 vol%). On the other hand, hybrids based on nanopods with their synthesis ligands exhibit intermediate values of mobility.

Hole transport modifications in the presence of nanocrystals

In conclusion, hole transport in the direction perpendicular to the substrate depends a) on the nature of the P3HT matrix; b) on the nature of nanocrystals (shape and ligands); c) on the content of nanocrystals.

Qualitatively, two effects thus need to be discussed: 1) the improvement of transport upon addition of small volumes of nanocrystals and 2) the degradation of transport for larger volumes of nanocrystals. We work out these effects within the common paradigm that P3HT is the hole transporting layer.

The first effect may come from the combination of several factors. First, a change of the polymer packing could lead to enhanced charge transport. We have seen in Chapter II, 3.3 that the presence of nanocrystals implies that the P3HT crystallites are smaller (109 Å in hybrids *vs* 130 Å in pristine P3HT2). Moreover, in small fractions, the nanocrystals do not perturb much the crystallization of P3HT2. Nanocrystals could confine the hole transporting phase and prevent the roaming of charge carriers in low mobility domains, for example the amorphous ones. Indeed, although we have not been able to check this point in our samples, it was shown in [46] that nanocrystals gathered in the amorphous domains of P3HT in hybrid films deposited by directional epitaxy crystallization.

This holds only up to a certain amount of nanocrystals. Above a critical fraction of nanocrystals (which precise value depends on the nature of P3HT and on that of nanocrystals), the degradation of the crystallinity of P3HT is too important to ensure efficient charge transport and the hole mobility decreases. Large and correlated degradations of the crystallinity (GIXRD, Chapter II) and of the mobility have been observed in the hybrids made of i) 16 vol% of 6.7 nm nanodots in P3HT1 and ii) 36 vol% of pyridine-treated nanopods in P3HT2. Finally, the presence of a large number of obstacles (nanocrystals) on the way of holes prevents efficient drift through the active layer.

6 Electron transport

In order to understand if and how the electrons conduction goes through the nanocrystalline phase, we studied hybrid samples based on P3HT2 and containing various amounts of nanocrystals of different natures (shape, ligands). We first present experimental results and then turn

to the discussion based on material parameters.

FIG. IV.12 presents electron mobilities in P3HT2 and in hybrid films made with P3HT2 and a) 4.1 nm nanodots with synthesis ligands nanocrystals, b) nanopods with synthesis ligands and c) nanopods with pyridine.

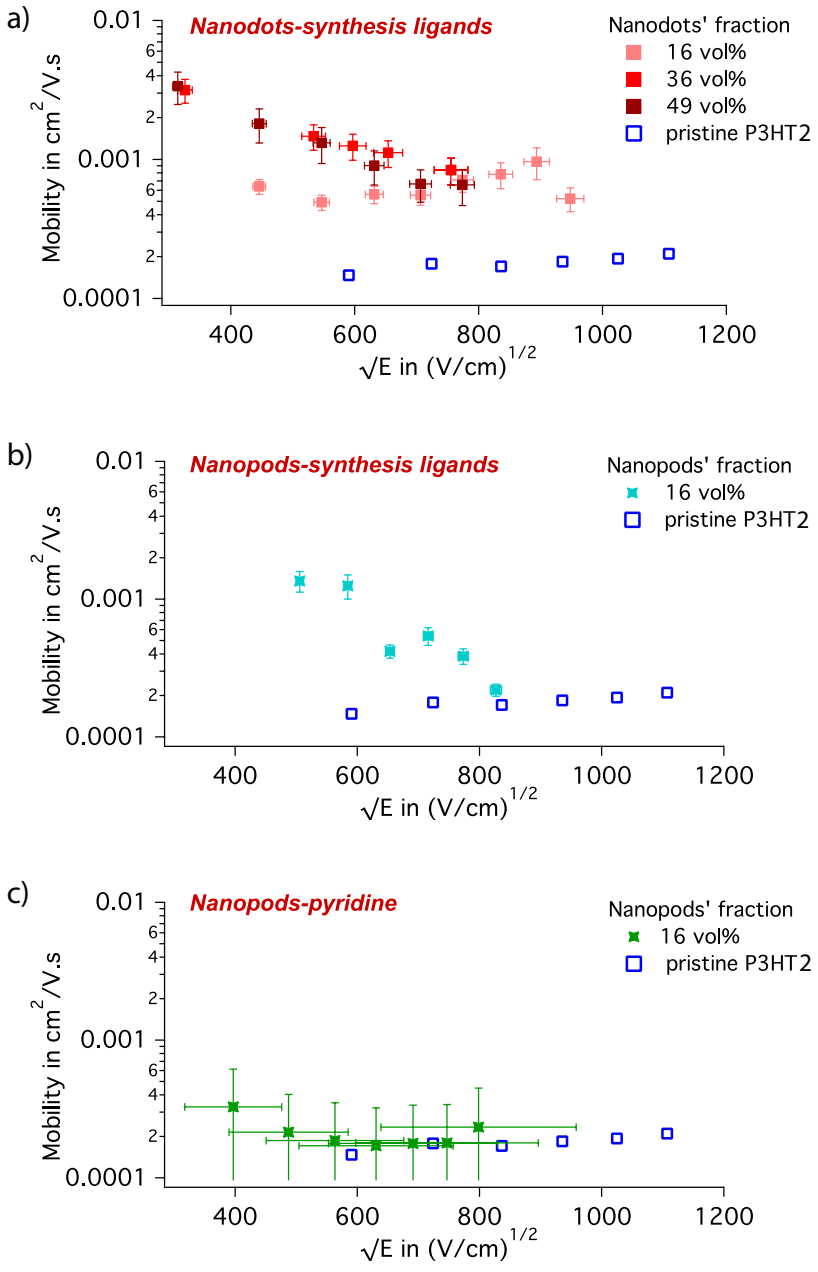

FIGURE IV.12 – TOF electron mobilities in hybrid samples made with a) nanodots capped with synthesis ligands, b) nanopods with synthesis ligands, c) nanopods with pyridine.

In a), the electron mobility at low fields increases with increasing amount of nanodots, up to a saturation level, at 36 vol%, from which the mobility did not improve anymore.

In b), the electron mobility in the 16 vol% blend is higher than in pristine P3HT2.

Finally, in c), the mobility for 16 vol% is very close to that of pristine P3HT2.

In the case of electron currents, dispersivities trends are less clear than in the case of hole currents. Dispersivities are globally lower for larger fractions of nanocrystals (α_{pre} approaches 1), see TABLE IV.4.

TABLE IV.4 – Electron transients dispersivities for P3HT and hybrids

Nanocrystals' proportion, in weight and volume	*Dispersivity coefficient α_{pre}*		
	Dots-synthesis	*Pods-synthesis*	*Pods-pyridine*
0 %	0.4	0.4	0.4
50 wt% - 16 vol%	0.7	0.65	0.45
75 wt% - 36 vol%	0.6	-	-
83 wt% - 49 vol%	0.9	-	-

Effects of the nanocrystals' shape and surface ligands In FIG. IV.13, we gather the mobilities obtained for 16 vol% of nanocrystals, for different shape and ligands in order to better visualize and understand their influence.

For nanocrystals with their synthesis ligands, at low field, electron mobilities are higher in nanopods-based hybrids than in nanodots-based ones. At high fields, it is the opposite: electron mobilities are higher in the case of nanodots-based hybrids than in the case of nanopods-based hybrids. Pyridine-treated nanopods lead to mobilities comparable to that of P3HT2.

Electron transport modifications in the presence of nanocrystals

It is believed that electron transport occurs through the nanocrystalline phase. The intrinsic confinement of wave functions results in hopping transport, provided the network of nanocrystals is dense enough to allow for reasonable hopping probabilities. In our case, nanocrystals are spread in the polymer matrix, and transport is thought to be conditioned by the existence of a percolating network. In the framework of percolation theories, the critical volume fraction is defined as the fraction above which a path can be found to percolate through the layer.

For nanodots with synthesis ligands, the mobility is larger in the hybrid with 36 vol% of nanocrystals, compared to pristine P3HT2 and to the hybrid with 16 vol% of nanocrystals.

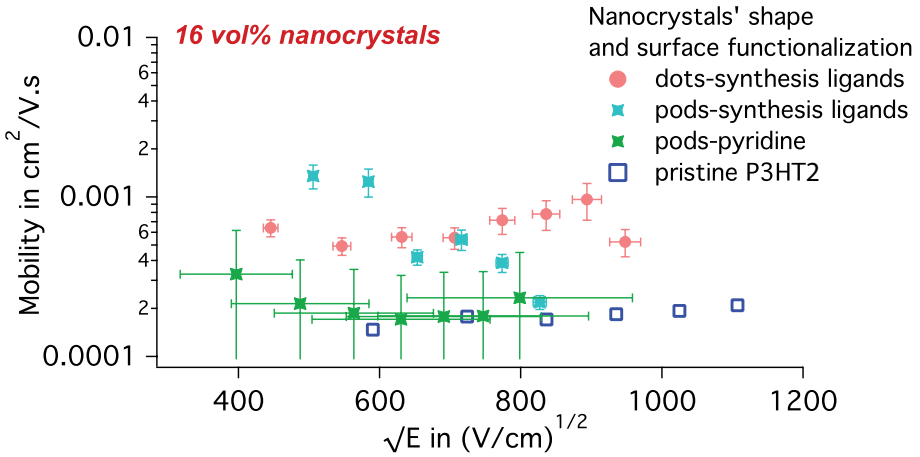

Figure IV.13 – Electrons mobilities in hybrid samples made with nanocrystals of different shapes and with different surface ligands with 16 vol% nanocrystals

This is in agreement with the order of magnitude for the percolation threshold for a random packing of spheres in a 3D matrix, 29 vol%. In this framework, the fact that the mobility does not increase further for a higher volume of nanocrystals (49 vol%) means that transport is percolation-limited: the opening of new percolation pathways does not enhance further the effective mobility value.

Moreover, the effect of the content of nanocrystals depends on their shape and ligands. In the hybrid with 16 vol% of nanopods treated with pyridine, the crystallinity of P3HT2 is preserved (see Chapter II, Fig. II.23), and the mobility is similar to that in P3HT2. This suggests that the crystallinity of P3HT constrains the dispersion of nanocrystals, causing an inhomogeneous dispersion of the nanocrystals in the polymer matrix. This inhomogeneous dispersion could also be caused by microscopic aggregation of nanocrystals after ligand exchange. Such a aggregation, that we could not check with SEM or AFM imaging, would influence the value of the percolation threshold, and modify the resulting mobility.

In conclusion, the electron transport in hybrids probed by TOF measurements changes upon addition of nanocrystals. It is altogether more efficient or similar to electron transport in pristine P3HT. Whether the measured electron mobility increases or not depends on the nature (shape, ligands) of the nanocrystalline inclusions.

7 TOF mobilities *vs* hybrid solar cells performances: discussion

From the dependences of hole and electron transports reported above, we determined the optimal P3HT:nanocrystals weight ratio to be 1:3 (*i.e.* 75 wt%-36 vol% of nanocrystals) for the system P3HT2:nanodots capped with synthesis ligands. At this ratio, both electron and hole TOF mobilities reach their maximal measured values. This is comparable to the optimal ratio

of 21 vol%, reported for TOF measurements in P3HT:TiO_2 nanorods in [35, 36].

This contrasts with the optimal 1:9 weight ratio (63 vol%) usually found in the literature for hybrid solar cells. Unfortunately, we have not been able to make 1:9 thick films for TOF studies: drop casting with large amounts of nanocrystals resulted in macroscopic film cracking.

This discrepancy can originate from differences in charge transport mechanisms, but also in absorption, exciton dissociation and recombination processes.

While OPV and TOF devices are both in the diode configuration, they have different thicknesses. Larger thicknesses imply that the TOF measurement is more sensitive to chemical or structural defects than charge transport characterizations in thinner films. In addition, we have seen that the morphology of the active layer varies with the processing and thickness. P3HT is less crystalline in spin-coated samples than in our TOF samples. It is possible that the crystallinity of P3HT is ameliorated upon addition of nanocrystals in spin-coated films, resulting in an even more positive impact on transport properties. Moreover, the dispersion of nanocrystals probably depends on the processing conditions as well. Finally, in the case of oriented anisotropic nanocrystals with a characteristic length of the order of the device thickness, a percolation regime should be reached in thin OPV samples for very low volume fractions of nanocrystals.

These morphological arguments support the idea of different charge transport regimes in OPV devices and in our TOF samples, made by drop-casting. Additionally, the performance of photovoltaic devices is set by many other factors than charge transport, namely, absorption, dissociation and recombinations, all influencing the charge carrier density. We have seen that higher amounts of photogenerated charge carriers resulted in less dispersive charge transport. The enhanced absorption due to CdSe nanocrystals is really effective for wavelengths below 450 nm (that P3HT does not absorb) or under white illumination. TOF experiments probe a single wavelength, and in our case a wavelength corresponding the maximum absorbance of P3HT. Consequently, we have only probed the influence of nanocrystals on the transport of charge, not on their density. Both exciton dissociation and recombinations involve the interfaces between P3HT and nanocrystals. Therefore, an optimal device to enhance dissociation and limit recombination depends on the interface area and morphology, which can be tuned thanks to the amount and nature of nanocrystals.

8 Conclusion and outlook

Hybrid samples with thicknesses above 10 times the penetration depth of a 532 nm illumination are suitable for Time-of-Flight measurements, as assessed by the usual conditions of optical thickness, capacitance constraints, and blocking contacts (typically, this thickness is 5 μm). Hole and electron transients, with typical transit times between 10^{-6} s to 10^{-5} s, were measured by varying the illumination side.

Electron photocurrents depend on the illumination intensity. The mobility is not intensity-

dependent; but the charge density does depends on both the intensity and the voltage, which can be explained from the voltage dependence of exciton dissociation, recombinations and trapping.

We studied the hole TOF mobilities in two types of P3HT. Both samples present mobilities decreasing with increasing electric field. In the framework of the Gaussian Disorder Model, this is attributed to large positional disorder compared to the energetical disorder. Our fits showed that the energetical disorder in the film made with the P3HT with higher polydispersity, lower molecular weights and lower regioregularity (P3HT1) is larger than in the other film with contrasting parameters (P3HT2). This is coherent with the larger polydispersity index. Moreover, P3HT1 exhibits higher mobilities and a lower positional disorder parameter than P3HT2, possibly in correlation with larger crystallites.

In hybrid samples based on P3HT1, the hole TOF mobility decreases upon addition of nanocrystals. In hybrid samples based on P3HT2, the mobility depends on the shape and ligands of the nanocrystals; it is globally enhanced for low fractions of nanocrystals (50 wt%-16 vol%) and diminished for larger fractions of nanocrystals (probed up to 83 wt%-49 vol%). Indeed, we have seen in the previous Chapter that the presence of nanocrystals changes the crystallinity of P3HT. For low contents of nanocrystals, the main observed change is in the crystallite size, so we suggest that nanocrystals confine the hole transport layer and thus contribute to improved hole transport, for example by neutralizing low mobility regions. When the content of nanocrystals is large, the crystallinity of the P3HT matrix disappears and charge transport becomes less efficient.

TOF electron mobilities are enhanced by the presence of nanocrystals, in accordance with the idea of the formation of a percolation network. Here too, the fraction of nanocrystals needed for efficient transport varies with their shape and ligands: it is smaller for nanopods than for nanodots when they are capped with their synthesis ligands, at low fields. This can be explained by their anisotropy, that facilitates percolation. The lower electron mobilities measured for nanopods with pyridine are attributed to the possible aggregation of nanocrystals (constrained by the P3HT crystallization or spontaneous after ligand exchange), which would lead to a non random dispersion of nanocrystals and increase the percolation threshold.

Finally, in the case of P3HT2 and nanodots with synthesis ligands, the optimal fraction of nanocrystals both for electron and hole transport is 75 wt%-36 vol%. For this ratio, electron and hole mobilities are balanced, one order of magnitude larger than in pristine P3HT2 at low fields. Differences in thicknesses and morphologies of the active layer could explain the discrepancy between this optimal ratio and the one reported for hybrid solar cells.

References of part II

[1] D. V. Talapin, J-S. Lee, M. V. Kovalenko, and E. V. Shevchenko. *Prospects of colloidal nanocrystals for electronic and optoelectronic applications.* Chem. Rev. **110**(1), 389 (2010).

[2] P. M. Borsenberger, L. T. Pautmeier, and H. Bässler. *Scaling behavior of nondispersive charge transport in disordered molecular solids.* Phys. Rev. B **48**(5), 3066 (1993).

[3] Cordes H., Baranovskii S. D., K. Kohary, Thomas P., Yamasaki S., Hensel F., and Wendorff J-H. *One dimensional hopping transport in disordered organic solids I: analytic calculations.* Phys. Rev. B **63**, 094201 (2001).

[4] K. Kohary, Cordes H., Baranovskii S. D., Thomas P., Yamasaki S., Hensel F., and Wendorff J-H. *One dimensional hopping transport in disordered organic solids II: Monte Carlo simulations.* Phys. Rev. B **63**, 094202 (2001).

[5] H. Scher and E. W. Montroll. *Anomalous transit-time dispersion in amorphous solids.* Phys. Rev. B **12**(6), 2455 (1975).

[6] Y. Roichman and N. Tessler. *Generalized Einstein relation for disordered semiconductors: implications for device performance.* Appl. Phys. Lett. **80**(11), 1948 (2002).

[7] K-Y. Wong. *Electronic structure and Time-of-Flight measurement for organic molecules and polymers.* PhD dissertation, (2003).

[8] S. Bange. *Transient optical and electrical effects in polymeric semiconductors.* PhD dissertation, Potsdam University (2009).

[9] V. Arkhipov, E. Emelianova, and G. Adriaenssens. *Effective transport energy versus the energy of most probable jumps in disordered hopping systems.* Phys. Rev. B **64**(12), 1 (2001).

[10] B. Movaghar, M. Grüunewald, B. Ries, H. Bässler, and D. Würtz. *Diffusion and relaxation of energy in disordered organic and inorganic materials.* Phys. Rev. B **33**(8), 5545 (1986).

[11] V. R. Nikitenko, H. von Seggern, and H. Bässler. *Non-equilibrium transport of charge carriers in disordered organic materials.* J. Phys.: Condens. Matter **19**, 136210 (2007).

[12] R. Richert, L. Pautmeier, and H. Bässler. *Diffusion and drift of charge carriers in a random potential: deviation from Einstein's law.* Phys. Rev. Lett. **63**(5), 547 (1989).

[13] N. Rappaport, Y. Bar, O. Solomeshch, and N. Tessler. *Mobility spatial distribution function: comparative method for conjugated polymers/molecules.* Appl. Phys. Lett. **89**(25), 252117 (2006).

[14] A. J. Mozer, N. S. Sariciftci, L. Lutsen, D. Vanderzande, R. Österbacka, M. Westerling, and G. Juška. *Charge transport and recombination in bulk heterojunction solar cells studied by the photoinduced charge extraction in linearly increasing voltage technique.* Appl. Phys. Lett. **86**(11), 112104 (2005).

[15] S. A. Choulis, Y. Kim, J. Nelson, D. D. C. Bradley, M. Giles, M. Shkunov, and I. McCulloch. *High ambipolar and balanced carrier mobility in regioregular P3HT.* Appl. Phys. Lett. **85**(17), 3890 (2004).

[16] K. Yang, Y. Wang, A. Jain, L. Samulson, and J. Kumar. *Determination of electron and hole mobility of regioregular poly(3-hexylthiophene) by the Time of Flight method.* Journal of Macromolecular Science, Part A **44**(12), 1261 (2007).

[17] K. Kaneto, K. Hatae, S. Nagamatsu, W. Takashima, A. Pandey, K. Endo, and M. Rikukawa. *Photocarrier rmobility in regioregular P3HT studied by the TOF method.* Jpn J. Appl. Phys. **38**, L1188 (1999).

[18] S. Nagamatsu, S. S. Pandey, W. Takashima, T. Endo, M. Rikukawa, and K. Kaneto. *Photocarrier transport in processable P3AT.* Synthetic Metals **121**, 1563 (2001).

[19] S. S. P Pandey, W. T. Takashima, S. Nagamatsu, T. E. Endo, Rikukawa M., and K. Kaneto. *Regioregularity vs regiorandomness : effect on photocarrier transport in poly(3-hexylthiophene).* Jpn J. Appl. Phys. **39**(2), 94 (2000).

[20] R. Mauer, M. Kastler, and F. Laquai. *The impact of polymer regioregularity on charge transport and efficiency of P3HT:PCBM photovoltaic devices.* Adv. Funct. Mater. **20**(13), 2085 (2010).

[21] A. M. Ballantyne, L. Chen, J. Dane, T. Hammant, F. M. Braun, M. Heeney, W. Duffy, I. McCulloch, D. C. B. Donal, and J. Nelson. *The effect of poly(3-hexylthiophene) molecular weight on charge transport and the performance of polymer:fullerene solar cells.* Adv. Funct. Mater. **18**(16), 2373 (2008).

[22] A. J. Mozer and N. S. Sariciftci. *Negative electric field dependence of charge carrier drift mobility in conjugated, semiconducting polymers.* Chemical Physics Letters **389**(4-6), 438 (2004).

[23] W. Takashima, S. Nagamatsu, S. S. Pandey, T. Endo, Y. Yoshida, N. Tanigaki, M. Rikukawa, S. Yase, and K. Kaneto. *Dispersivity of carrier transport related with*

molecular arrangement in regioregular poly(3-alkylthiophene). Synthetic Metals **119**, 563 (2001).

[24] V. Kazukauskas, M. Pranaitis, L. Sicot, and F. Kajzar. *Negative mobility dependence in different regioregular polythiophenes revealed by the charge extraction by linearly increased voltage.* Mol. Cryst. Liq. Cryst. **447**, 141 (2006).

[25] G. Juška, K. Genevičius, K. Arlauskas, R. Österbacka, and H. Stubb. *Charge transport at low electric fields in π-conjugated polymers.* Phys. Rev. B **65**(23), 1 (2002).

[26] Hirao A., Nishizawa H., , and Sugiuchi M. *Diffusion and drift of charge carriers in molecularly doped polymers.* Phys. Rev. Lett. **75**(9), 1787 (1995).

[27] K. Kaneto, S. S. Pandey, and W. Takashima. *Photocarrier transport in non-uniform field based on Schottky cell for the TOF measurement in P3AT films.* Jpn J. Appl. Phys. **40**, 4933 (2001).

[28] Meijer E. J., Mangnus A.V.G., Huisman B.-H., 't Hooft G.W., de Leeuw D.M., and Klapwijk T.M. *Photoimpedance spectroscopy of P3HT metal–insulator–semiconductor diodes.* Synthetic Metals **142**, 53 (2004).

[29] J-M. Verilhac. *Transistors organiques à base de dérivés du polythiophène, effets de la structure moléculaire et supramoléculaire.* PhD dissertation, Université Joseph Fourier (2006).

[30] Y. Liu, L. Wu, P.T. Lai, and Q. Zuo. *Air-stability analysis and improvement of poly(3-hexylthiophene) field-effect transistors.* Semicond. Sci. Technol. **24**, 095013 (2009).

[31] J. Schafferhans, A. Baumann, C. Deibel, and V. Dyakonov. *Trap distribution and the impact of oxygen-induced traps on the charge transport in poly(3-hexylthiophene).* Appl. Phys. Lett. **93**(9), 093303 (2008).

[32] J. Schafferhans, A. Baumann, A. Wagenpfahl, C. Deibel, and V. Dyakonov. *Oxygen doping of P3HT:PCBM blends: influence on trap states, charge carrier mobility and solar cell performance.* Organic Electronics **11**(10), 1693 (2010).

[33] Stegmaier K., A. Fleissner, Janning H., Yampolskii S., Melzer C., and von Seggern H. *Influence of electrical fatigue on hole transport in PPV-based organic light-emiting diodes.* J. Appl. Phys. **110**, 034507 (2011).

[34] K. R. Choudhury, J. G. Winiarz, M. Samoc, and P. N. Prasad. *Charge carrier mobility in an organic-inorganic hybrid nanocomposite.* Appl. Phys. Lett. **82**(3), 406 (2003).

[35] Chang C-H., Huang T-K., Lin Y-T., Lin Y-Y., Chen C-W., Chu T-H., and W-F. Su. *Improved charge separation and transport efficiency in P3HT-TiO2 nanorod bulk heterojunction solar cells.* J. Mater. Chem. **18**, 2201 (2008).

[36] Li S-S., C-P. Chang, Lin C-C., Lin Y-Y., Chang C-H., Yang J-R., Chu M-W., and Chen C-W. *Interplay of three dimensional morphologies and photocarrier dynamics of polymer/TiO2 bulk heterojunction solar cells.* JACS **133**, 11614 (2011).

[37] V. Coropceanu, J. Cornil, D. A. da Silva Filho, Y. Olivier, R. Silbey, and J-L. Brédas. *Charge transport in organic semiconductors.* Chem. Rev. **107**(4), 926–52 April (2007).

[38] A. J. Ben-Sasson, E. Avnon, E. Ploshnik, O. Globerman, R. Shenhar, G. L. Frey, and N. Tessler. *Patterned electrode vertical field effect transistor frabricated using block copolymer nanotemplates.* Appl. Phys. Lett. **95**, 213301 (2009).

[39] Z. B. Wang, M. G. Helander, M. T. Greiner, J. Qiu, and Z. H. Lu. *Carrier mobility of organic semiconductors based on current-voltage characteristics.* J. Appl. Phys. **107**, 034506 (2010).

[40] G. Juška, K. Arlauskas, R. Österbacka, and H. Stubb. *Time-of-flight measurements in thin films of regioregular poly(3-hexylthiophene).* Synthetic Metals **109**(1-3), 173 (2000).

[41] G. Juška, M. Viliunas, K. Arlauskas, and J. Kočka. *Space-charge limited photocurrent transients: the influence of bimolecular recombination.* Phys. Rev. B **51**(23), 16668 (1995).

[42] C. Querner, P. Reiss, S. Sadki, M. Zagorska, and A. Pron. *Size and ligand effects on the electrochemical and spectroelectrochemical responses of CdSe nanocrystals.* Phys. Chem. Chem. Phys. **7**, 3204 (2005).

[43] P. Reiss, E. Couderc, J. De Girolamo, and A Pron. *Conjugated polymers/semiconductor nanocrystals hybrid materials–preparation, electrical transport properties and applications.* Nanoscale **3**(2), 446 (2011).

[44] V. Kazukauskas, M. Pranaitis, V. Cyras, L. Sicot, and F. Kajzar. *Negative mobility dependence on electric field in poly(3-alkylthiophenes) evidenced by the charge extraction by linearly increasing voltage method.* Thin Solid Films **516**(24), 8988 (2008).

[45] S. M. Tuladhar, D. Poplavskyy, S. A. Choulis, J. R. Durrant, D. D. C. Bradley, and J. Nelson. *Ambipolar charge transport in films of methanofullerene and poly(phenylenevinylene)/methanofullerene blends.* Adv. Funct. Mater. **15**, 1171 (2005).

[46] M. Brinkmann, D. Aldakov, and F. Chandezon. *Fabrication of oriented and periodic hybrid nanostructures of regio-regular poly(3-hexylthiophene) and CdSe nanocrystals by directional expitaxial solidification.* Adv. Mater. **19**, 3819 (2007).

Part III

Monte Carlo simulation of Time-of-Flight transients

Chapter V

Modeling charge transport in disordered materials: the basics

MATHEMATICAL DESCRIPTION OF HOPPING TRANSPORT and its parametrization are introduced. We present hopping rates frequently used in descriptions of polymeric and nanocrystalline systems.

1 Why hopping ?

Idealized transport mechanisms can be described by a system Hamiltonian allowing intersite electronic, phononic and electron-phonon couplings [1]:

$$H = H_{el} + H_{ph} + H_{el-ph} \tag{V.1}$$

The electronic Hamiltonian H_{el}, the phononic Hamiltonian H_{ph} and the electron-phonon coupling H_{el-ph} can each be detailed as:

$$H_{el} = \sum_i \epsilon_i a_i^\dagger a_i - \underbrace{t \sum_i a_i^\dagger a_{i+1}}_{V_{el-el}} , \tag{V.2}$$

$$H_{ph} = \sum_i \hbar\omega_0 (b_i^\dagger b_i + \frac{1}{2}) , \tag{V.3}$$

$$\text{and} \quad H_{el-ph} = \sum_i g\hbar\omega_0 (b_i^\dagger + b_i) a_i^\dagger a_i . \tag{V.4}$$

The ϵ_i are the onsite energies and $a_i^\dagger$, a_i, $b_i^\dagger$, b_i are respectively the electron and phonon creation and annihilation operators.

t is the electronic transfer integral. It is related to the electron wavefunction overlap. Here, electrons are only coupled to electrons on adjacent sites ($i \leftrightarrow i+1$) of a cubic lattice and the transfer integral t is assumed constant.

g is the electron-phonon coupling strength, related to the Huang-Rhys factor $S = g^2$, and ω_0 is the phonon frequency.

Relative values of the inter-site electronic interaction V_{el-el} of the electron-phonon coupling H_{el-ph} and of the temperature determine the regime of charge transport:

- If the electron-phonon coupling is sufficiently small, electrons and phonons are decoupled and charge carriers can be described as delocalized wave packets. Transport is bandlike, and carriers are scattered by impurities and phonons. Thus, the mobility decreases with increasing temperature. If H_{el-ph} is not negligible but small enough to be treated as a perturbation, electrons are 'dressed' by phonons, into quasi-particles called polarons. The transfer integral is then modified to a smaller, effective transfer integral. Charge carriers are still delocalized and transport still occurs through energy bands, at least for sufficiently low temperatures.
- On the other hand, if t is very small, the localizing term H_{el-ph} dominates over the delocalizing term t and charge carriers are localized on particular molecules. In this case, transport occurs via thermally activated hopping and the mobility increases with increasing temperature. At high temperatures, it decreases due to phonon scattering.

Multi-scale approaches Influences of phonon and conformational dynamics on charge transport in soft matter have been recently emphasized. The 2008 and 2010 reviews [1, 2] of A. Troisi and coworkers point out the importance of comparing time scales of phonons dynamics and charge dynamics. Individual charge dynamics take place on the picosecond scale, whereas full devices may require evaluation of dynamics over much larger scales, in hundreds of nanosecond or microsecond scales. Nuclear dynamics at intermediate time scales (picoseconds to nanoseconds) influences strongly charge transport. Finally, structural fluctuations on very long time scales, sometimes longer that the operation times of the device, can modulate transport properties.

Different works focus on studying physical processes in devices at their respective time and space scales (*e.g.* [3–5]). The aim is to derive macroscale properties (such as charge mobility) based on meso- and nanoscale conformations (localization length), transfer integrals and electron-phonons couplings.

Quantitatively evaluating the transfer integral t and the electron-phonon coupling strength S in conjugated polymers and nanocrystals' solid assemblies is not straightforward. We presented in Chapter III qualitative arguments for charge carrier localization in these assemblies: finite chain dimensions and interruption of the conjugation for conjugated polymers and confinement of wave packets for nanocrystals. Moreover, it has been shown that transport occurs via hopping in P3HT thin films [6] and in CdSe nanocrystals assemblies [7, 8]. Consequently, hopping

transport was thus was suggested for both charge carriers in hybrid thin films made of P3HT and CdSe nanorods [9] and demonstrated for hole transport in hybrids films made of PVK and CdS nanocrystals [10].

2 Mathematical descriptions of hopping transport

Charge-carriers in polymeric and nanocrystalline assemblies can be described by localized wave packets. They can thus both be treated by hopping transport equations. Under the hypothesis of an uncorrelated system, hopping is a random and memoryless process (also called Markovian process), consisting of discrete displacements of charge carriers between localized states.

2.1 Master equation

Let us describe the active layer as a set of N sites occupied by M charge carriers. Hopping from site i to site j occurs with a rate $\nu_{i\to j}$. The state of the system is described by occupations η_i of all sites. The probability $P(\{\eta\})$ that the system is in the state $\{\eta\} = (\eta_1, \eta_2, ...)$ evolves following a master equation [11]:

$$\frac{\partial P(\{\eta\})}{\partial t} = -\sum_{i,j,j\neq i} \nu_{i\to j}\ \eta_i(1-\eta_j)\ P(\{\eta\},t)\ +\ \sum_{i,j,j\neq i} \nu_{j\to i}\ \eta_j(1-\eta_i)\ P(\{\eta\}_{i\leftrightarrow j},t) \quad \text{(V.5)}$$

where $\{\eta\}_{i\leftrightarrow j}$ is the state where occupations of sites i and j are all exchanged. The negative sign indicates charge carriers leaving site i whereas the positive sign shows arrival of a charge carrier on site i. The number of possible states is very large in real systems, so the exact solution of such an equation is beyond our reach.

If we neglect correlations of occupational probabilities, $P(\{\eta\})$ can be factorized and writes $P(\{\eta\}) = P(\eta_1)P(\eta_2)P(\eta_3)....$ This is the mean-field approximation. Nonetheless keeping the condition that two charge carriers cannot occupy the same site at the same time (this condition is equivalent to electrostatic repulsion when the degeneracy due to spin is neglected), the previous equation simplifies to:

$$\frac{\partial P_i}{\partial t} = -\sum_{j\neq i} \nu_{i\to j}\ P_i(t)\ (1-P_j(t))\ +\ \sum_{j\neq i} \nu_{j\to i}\ P_j(t)\ (1-P_i(t)) \quad \text{(V.6)}$$

where $P_i(t)$ is the probability of occupation of site i.

Correlations Electrostatic interactions in disordered media depend on the charge configuration at a given time and can not be treated through the average occupancies of sites, as is done for band-like semiconductors [12]. Including treatment of electrostatic interactions is thus difficult. Nonetheless, electrostatic interactions can be neglected if the charge carrier density is very low in comparison to the inverse electrostatic repulsion volume. In P3HT, the repulsion

length is 16 nm, so that the critical density is $\rho_c = (16\ nm)^{-3} = 2.4 \times 10^{17}\ cm^{-3}$. If the charge density is below this critical density ρ_c, it is correct to neglect electrostatic interactions between charges.

Correlations related to morphology, like aggregates of nanocrystals or anisotropic coupling of conjugated polymer chains, can be implemented through sites properties.

Most common approaches to solve the master equation are numerical: the Monte Carlo approach and the approach introduced by Yu *et al.* [13]. The Monte Carlo approach for solving the Master Equation for hopping transport is summarized in Fig. V.1. The general idea is to randomly generate charge carriers on a lattice, to rank them in increasing dwell time order, and to have charges hop in this order until no charges remain on the lattice. The procedure will be detailed in the next Chapter for our particular problem.

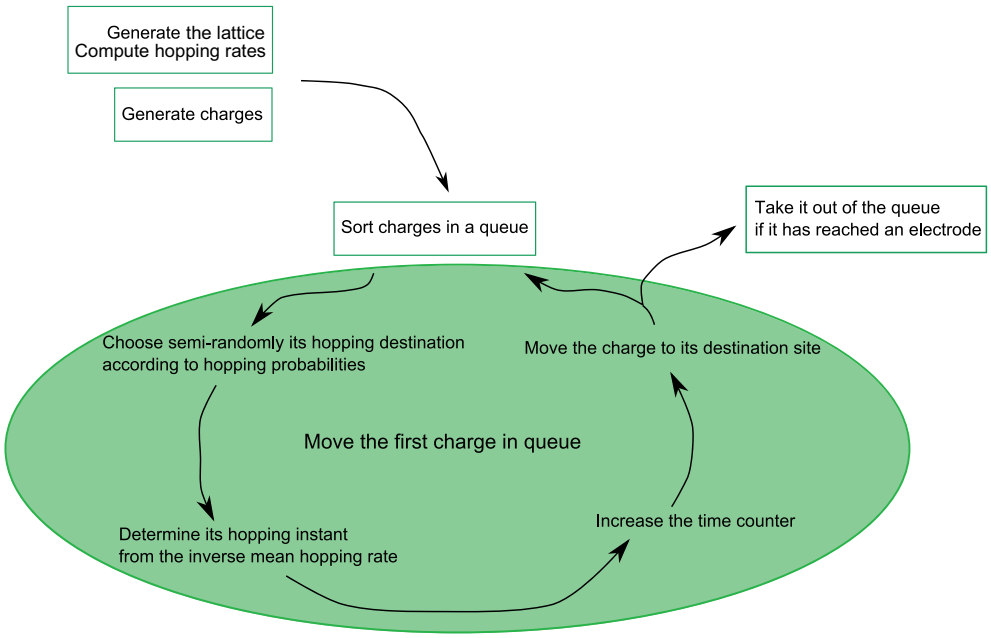

Figure V.1 – Principle of the Monte Carlo simulation of hopping transport This scheme is inspired from [5].

2.2 Hopping rates

As inputs to the master equation, one needs expressions for occupational probabilities and hopping rates, *i.e.* for the probability of a charge to transfer from one point to another in space, time, and energy.

Space and energy dependance

At zero temperature, one expects hops downward in energy. When the temperature increases, upward hops may be thermally activated by coupling to lattice phonons. Moreover, the amplitudes of wave functions decrease exponentially with distance so that transition rates should also depend exponentially on the distance between departure and destination sites as well. This leads to a general expression of the hopping rate from site i to site j:

$$\nu_{i\to j} \;=\; \nu_0 \; e^{-\frac{\Delta E_{ij}}{kT}} \; e^{-2\alpha r_{ij}} \text{ with } \Delta E_{ij} \;=\; \begin{cases} E_j - E_i & \text{if } E_j > E_i \\ 0 & \text{else} \end{cases} \tag{V.7}$$

ν_0 is the attempt-to-hop frequency. ΔE_{ij} is the energy difference between the destination and departure sites (in the case of an external electric field, it includes its influence). α is the inverse localization length (or cut-off inverse length) and $r_{ij} = |r_i - r_j|$ is the distance between origin and destination sites. This general expression is often referred to as the *Miller-Abrahams hopping rate* [14]. It can also been seen as a phenomenological basis for formalizing temperature and distance dependences of most hopping rates.

Variable range hopping Mott noticed that there is a competition between energy and space dependences so that hops to close sites are not always the most probable : a charge can hop to a far away site if the site is close enough in energy. This is *variable range hopping*. It leads to a specific temperature dependance for conductivity $\sigma \propto e^{(T_0/T)^{1/4}}$. Variable range hopping has been shown to become non negligible at low temperatures in conjugated polymers [15].

More precise expressions for ν_0, E_i and α can be derived in different models, depending on the described system.

Hopping rates used in descriptions of transport in nanocrystals assemblies

Transport in nanocrystal assemblies has been modeled by thermally activated hopping of electrons in nanocrystalline TiO_2 in [16] and by resonant tunneling in [17], using:

$$\nu_{i\to j} = \nu_0 e^{-\Delta x_{edge}\sqrt{\frac{2m^*}{\hbar^2}(E_{vac}+(E_i+E_j)/2)}} \tag{V.8}$$

where Δx_{edge} is the smallest edge-to-edge distance between initial and arrival quantum dots and m^* is the electron effective mass.

Hopping rates used in descriptions of transport in conjugated polymers

In disordered organic conductors, the coupling to the phonons is rather strong, with the Huang-Rhys factor $S \approx 0.5 - 2$. This has led to the dominant use of the *Marcus theory* to describe

hopping in organic materials [2, 4, 5, 18–21]:

$$\nu_{i\to j}^{Marcus} = \nu_0\, e^{-\frac{\left(E_j-E_i+\lambda\right)^2}{4\lambda kT}} \text{ , with } \begin{cases} \nu_0 &= \frac{2\pi}{\hbar}|t|^2\frac{1}{\sqrt{4\pi\lambda k_B T}} \\ \lambda &= S\hbar\omega_0 \end{cases} \tag{V.9}$$

To obtain the latest expression V.9, two strong assumptions have been made: the transfer integral is small enough to be treated as a perturbation in the Fermi Golden rule and phonons can be treated classically.

$$\begin{cases} |t| &<< \lambda \\ \hbar\omega_0 &<< k_B T \end{cases} \tag{V.10}$$

Two derivations of the Marcus hopping rate can be found in Appendice 11.

Inverted regime Marcus rate as a function of ΔE_{ij} is symmetric towards λ (see Fig V.2). It increases with $-\Delta E_{ij}$ until a maximum rate is reached for $-\Delta E_{ij} = \lambda$ and then decreases. This last region is called the inverted regime. It corresponds to an increased vibrational energy needed to reach the curve crossing as the acceptor well is lowered. Hops with a difference in free energy close to λ will be favored in comparison to hops with larger energy differences. This means that hops towards deep traps are little likely to happen.

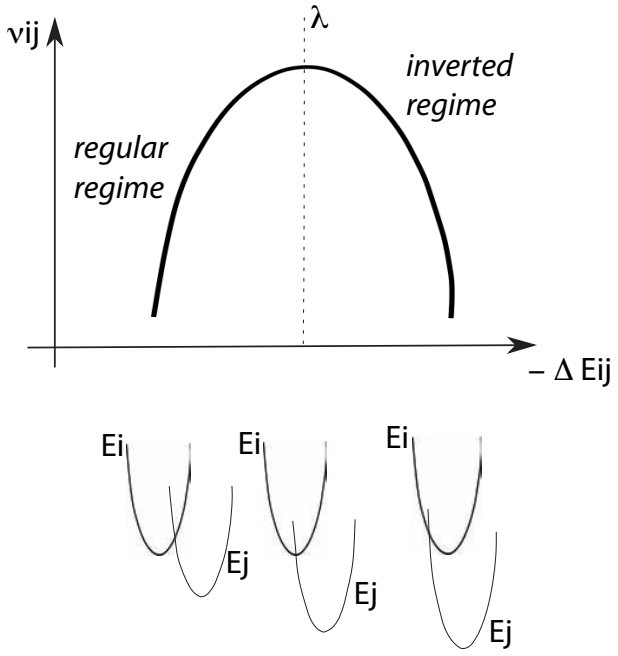

Figure V.2 – Hopping rate dependance on the difference of free energy between the initial and final sites When $-\Delta G^0$ increases, the hopping rate reaches a maximum for $-\Delta G^0 = \lambda$ and then decreases again.

The condition $\hbar\omega_0 << k_BT$, used to derive the classical high temperature limit of the Marcus hopping rate, is a little liberal in organic materials. In particular, charge carriers can couple to high energy phonons, for example intramolecular stretch vibrations. These can exceed the thermal energy [22], in which case the above condition does not hold.

In this Chapter, we presented the formalization of hopping transport in polymeric and nanocrystals assemblies by the master equation. The master equation can be solved numerically thanks to a Monte Carlo procedure for given expressions of hopping rates. We have introduced the Miller-Abrahams hopping rate as well as the high temperature limit of the Marcus hopping rate, that both depend on materials parameters.

Chapter VI

Monte Carlo simulations of hole transport in TOF experiments in hybrid materials

Monte Carlo simulations are used to explore probability distributions over numerous runs. Since disordered materials are described statistically, with energy and morphology distributions, the Monte Carlo technique is particularly adapted to simulate transport in disordered materials.

In this Chapter, we first present the experimental data sets that we simulated: hole photocurrents generated in Time-of-Flight experiments and obtained in the following films: 1) a P3HT1 film and 2) a hybrid film, based on P3HT1 and 6.7 nm nanodots capped with synthesis ligands (see Fig. IV.9 for the corresponding measured mobilities and below for the photocurrent). We detail the principle of the simulations[1] and discuss orders of magnitudes of the different simulation parameters, for our materials and experiments. These factors influence the allure of simulated photocurrents, and we study how. Finally, we present simulated photocurrents and show that nanocrystals can be seen as voids in the transport lattice.

1 Experimental data

We focus here on the simulation of hole current transients in two samples:

- a 2.2 μm thick film made with P3HT1 (see Fig.II.13 in Chapter II for characteristics) ;
- a hybrid thin film based on P3HT1 and containing 50 wt%-16 vol% 6.7 nm CdSe nanocrystals with synthesis ligands, also 2.2 μm thick.

Their experimental transients and transit times are directly comparable due to similar thicknesses and are shown in Fig.VI.1. For similar applied voltages, transit times are larger in the

[1]The code (c++) has initially been written by Xin Jiang under Sean Shaheen's advising, in order to model and simulate charge transport in organic materials. They welcomed me for three months at the University of Denver in order to learn to use the code and adapt it to bulk heterojunctions. This research stay was made possible thanks to the financial help of the *Association Française des Femmes Diplômées d'Universités*, the French counterpart of the 'International Federation of University Women', which aim is to promote women's higher education throughout the world.

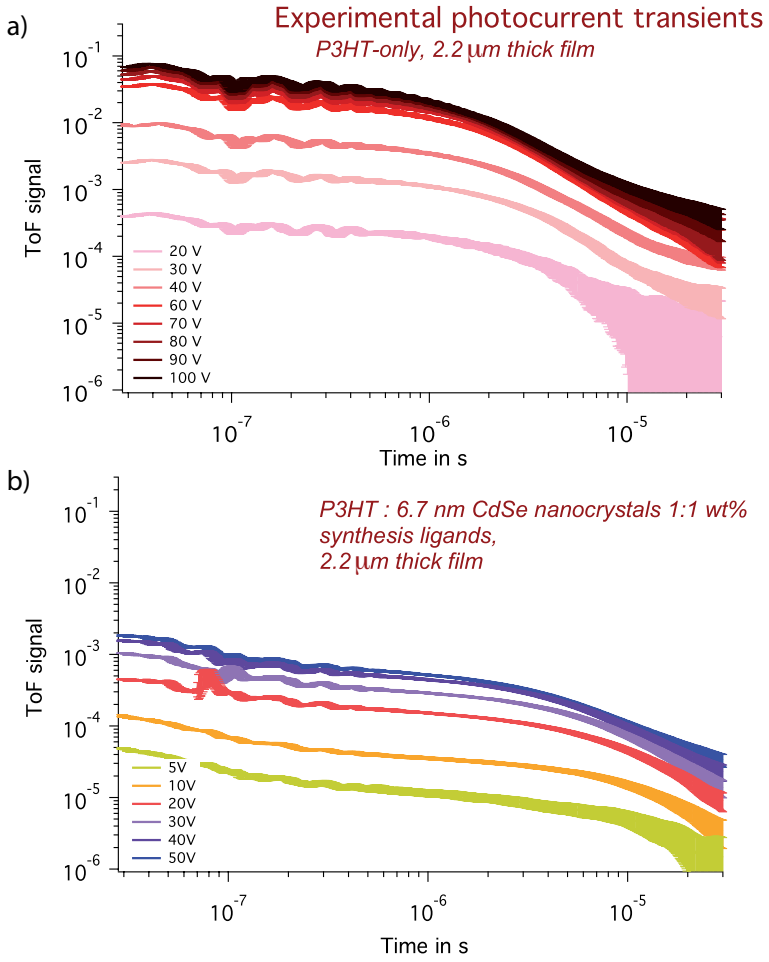

Figure VI.1 – Experimental photocurrent transients to be simulated. In a), hole transient in a P3HT1-only device and in b) a hybrid device based on P3HT1 and containing 50 wt%-16 vol% 6.7 nm CdSe nanocrystals with synthesis ligands. Both films are 2.2 μm thick.

hybrid than in pristine P3HT1. Moreover, photocurrents recorded in the hybrid are slightly more dispersive than in pristine P3HT1.

2 Short description of the simulation procedure

Space is discretized due to the localization of charge carriers (see Fig. VI.2). The active layer is represented by a 3D cubic lattice of lattice parameter a and limited by the electrodes in one direction and with periodic boundary conditions in the other two dimensions.

Each site (intersections in Fig. VI.2) is randomly assigned an energy value from en energy distribution centered on the HOMO level of P3HT, -5.2 eV and of width of tens to hundreds of meV, as we will detail below.

A number of free charge carriers is randomly generated on the lattice, following a charge-generation spatial distribution, that takes into account the penetration depth of the optical

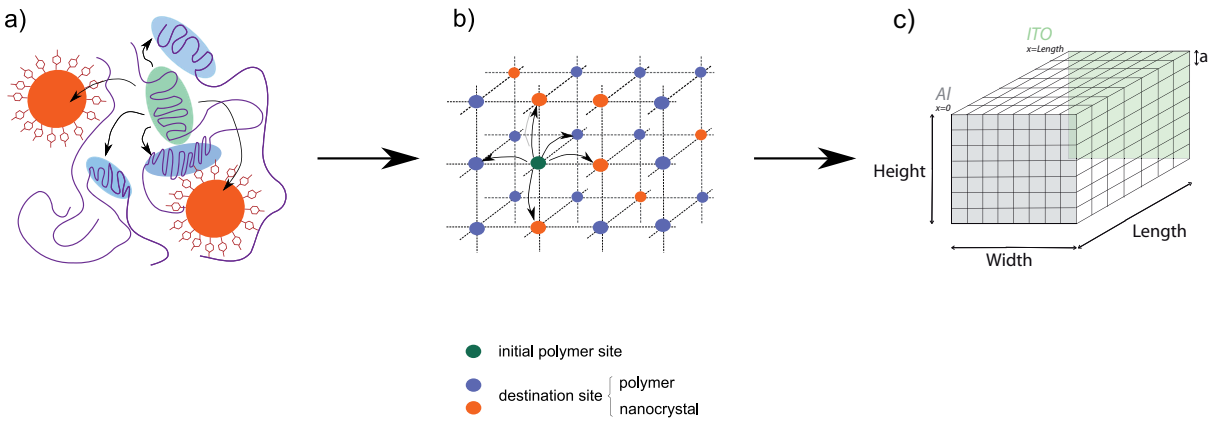

Figure VI.2 – From the active layer to the simulation cell In a), picture of the localization and hops of charge carriers in the active layer, from an initial polymeric site to a destination site, either polymeric or nanocrystalline. Intersections of a cubic lattice are used to represent each localization site, as shown in b). In c), we define lattice variables.

excitation and the exciton diffusion. In the frame of this work, we focus on one single type of charge carriers (electrons or holes): nor excitons dissociation, nor recombinations are treated in the simulation.

Hopping transport For each site i, hopping rates to the six first neighbors are calculated (only nearest neighbors hops are implemented) and the average probability of hopping away from each site is determined.

Charges are sorted in a queue: the charge with the highest average probability of hopping to an adjacent site is the first in the queue. Its actual hopping direction is randomly chosen, according to the respective magnitudes of hopping rates in each direction. The queue is then updated by removing this charge from the first position and placing it back in the queue, according to the average hopping rate of the site it has moved onto. This gives a new sorted queue, the first element of which is taken to hop in the following step.

At each time step t_n, determined by the user, the electrical current resulting from all hops during the interval $t_n - t_{n-1}$ is calculated.

When a charge reaches an electrode, it is taken out of the queue. The simulation stops when all charges have reached an electrode. This procedure is summarized schematically in Fig. V.1.

Simulation of experimental transients Fig. VI.3 summarizes the steps to simulate experimental transients. Running the whole simulation with different random seeds allows to explore site energy distributions, charge-generation spatial distributions and random directions of hops[2]. This exploration of probability distributions corresponds to finding a thermal average for the evolution of the system: this is the principle of Monte Carlo simulations.

[2] *i.e.* each time a random number is used in the simulation.

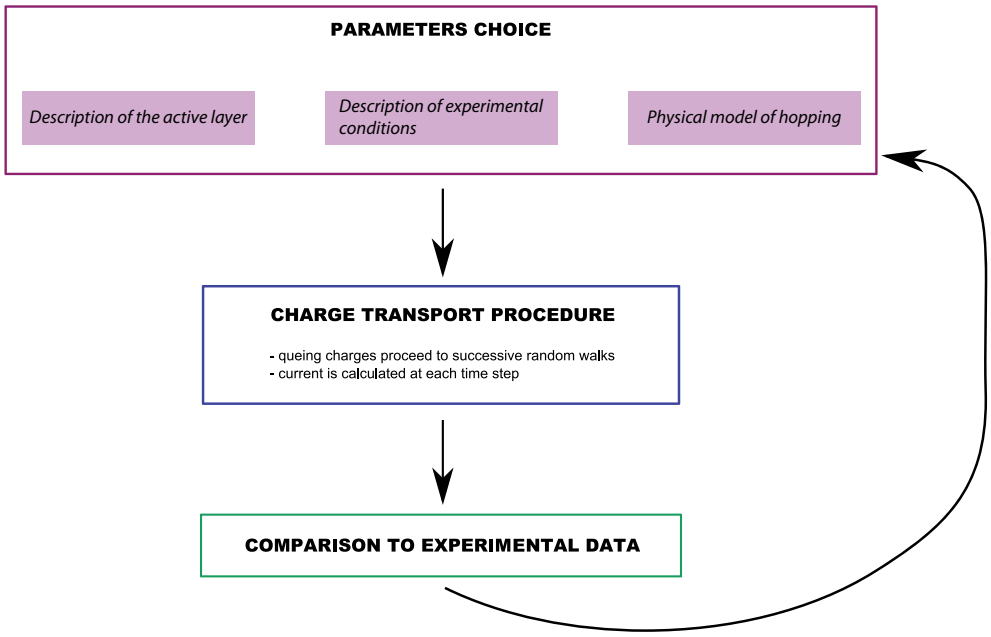

FIGURE VI.3 – Experimental transients simulation principle

3 Parameters of the simulations

In order to simulate the experimental current transients, reasonable range for each parameter have been evaluated from experimental hints and from the literature. Parameters are summarized in Table VI.1. Some are fixed by experimental conditions (temperature, voltage, illumination), while others belong to our description of the materials and need adjusting: initial spatial distribution of charges, density-of-state (DOS), transfer integrals, electron-phonon couplings (a.k.a. reorganization energy in the case of Marcus theory).

Here we discuss the order of magnitude of each parameter, as chosen from experiments or literature. We also discuss in more detail the effects of:

- the energy landscape, or DOS, for each material. They are static, describe the amount of disorder in the materials[3] and rule the general aspect of current transients, *i.e.* the slopes before and after the transit time.

- the hopping rate parameters. We describe hopping transport in the framework of :

  (i) thermally activated hopping, equivalent to Miller-Abrahams rate for a cut-off length equal to the lattice parameter. Miller-Abrahams hopping rates have been used for the simulation of transport in organic materials, for example in the OLED field, *e.g.* [23];

  (ii) Marcus theory, as in [1, 5, 18].

[3] Absolute energy values are not relevant since we only consider energy differences between adjacent sites, related to the strength of disorder.

As a reminder:

$$\nu_{i\to j}^{therm.act.} = \frac{2\pi}{\hbar}|t|^2\, e^{-\frac{\Delta E_{ij}}{kT}} \text{ with } \Delta E_{ij} = \begin{cases} E_j - E_i & \text{if } E_j > E_i \\ 0 & \text{else} \end{cases} \quad \text{(VI.1)}$$

$$\nu_{i\to j}^{Marcus} = \frac{2\pi}{\hbar}|t|^2 \frac{1}{\sqrt{4\pi\lambda k_B T}}\, e^{-\frac{\left(E_j - E_i + \lambda\right)^2}{4\lambda kT}} \text{, with } \lambda = S\hbar\omega_0 \quad \text{(VI.2)}$$

The transfer integral t and the reorganization energy λ need to be evaluated. As we will detail below, in the simulations based on Marcus model, the transfer integral mostly influences the position of the transit times, whereas the reorganization energy tunes the accessibility of traps, *i.e.* the dispersivity of transients.

Miller-Abrahams and Marcus hopping rates give comparable mobilities for lower fields and before the inverted region of Marcus rates is reached [12]. We have seen that Miller-Abrahams neglect polaronic effects. Marcus theory to the contrary includes them, by only in the low frequency regime. About Marcus theory, as is nicely put in [21] *'Despite all imperfections it is widely used for charge transfer in organic crystals and one can certainly assume that this theory is suitable for the purpose of a qualitative charge-transport analysis'*. Qualitative analysis will it be, which seems reasonable at this stage of our experimental study.

Table VI.1 – Parameters of the Monte Carlo simulation

Experimental conditions	- Electric field ↪ electrodes ↪ applied voltage - Temperature - Illumination ↪ density of photogenerated charges
Material description	- Site size and lattice dimensions - Energy landscape ↪ energy distribution of the active layer - Illumination penetration depth, exciton diffusion and dissociation
Model parameters	- Hopping rate parameters ↪ transfer integral ↪ reorganization energy (Marcus hopping rates)

3.1 Fixing experimental conditions

The choice of parameters is constrained by the field dependence of our transients: when varying the electric field, all other parameters should be kept fixed.

Electric field The built-in electric field due to the asymmetry in work functions between the ITO and the Al electrodes on the order of 3.10^3 V/cm for a 2.2 μm thick device. The applied electric field was varied between 5.10^4 V/cm and 5.10^5 V/cm in these samples.

$$\left| \begin{array}{rcl} E_F^{ITO} & = & -5.1\ eV,\ E_F^{Al} \ = \ -4.3\ eV \\ V_{app} & = & 10 - 100\ V \end{array} \right.$$

The electric field is the only non-random source of asymmetry in the hopping process. In the direction of the electric field, the electric energy difference between two adjacent sites is around 25 meV-250 meV depending on the applied voltage, which is comparable to the thermal energy, to the width of the energetical disorder and to the reorganization energy.

Temperature All simulated experiments were performed at room temperature.

$$\left| \begin{array}{rcl} k_B T & = & 0.025\ eV \end{array} \right.$$

Illumination Free charges are randomly positioned on lattice sites, following a probability distribution as shown in Fig. VI.4.

$$\left| \begin{array}{l} \text{penetration depth of 532 nm illumination in P3HT thin films} \approx\ 50\ nm \\ \text{exciton diffusion length in P3HT} \approx\ 10\ nm \end{array} \right.$$

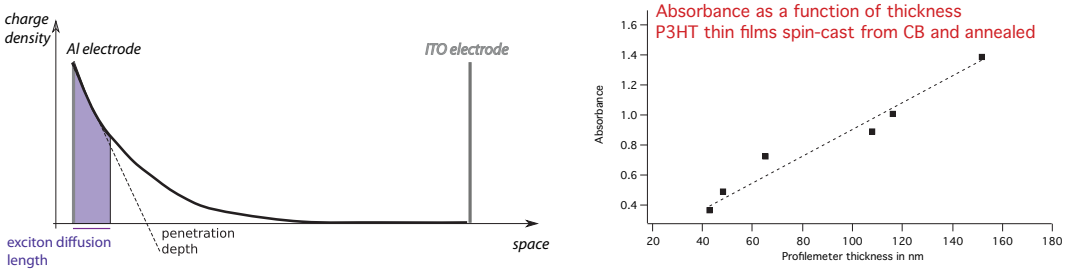

Figure VI.4 – Free charge generation Representation of the device when illuminated through Al electrode. Free charges are generated randomly in the purple space. The penetration depth is deduced from absorbance of P3HT thin films at $\lambda = 532\ nm$ and the exciton diffusion length from the literature [24].

In heterojunctions, exciton dissociation is favored by the chemical built-in electric field at the interfaces between the polymer and the nanocrystals. Thus :

- if the charge is generated on its preferred phase (*i.e.* the polymer for holes and the nanocrystals for electrons), it stays where it is;

- if the charge is generated on the other phase, it jumps to an adjacent site belonging to the preferred phase, if there is any. If there are several in the vicinity, the direction of the jump is randomly chosen.

3.2 Mimicking the active layer morphology: the lattice description

The localization length of charge-carriers & the discretization of the active layer The lattice parameter a corresponds to the localization length of charge-carriers. For example, in the case of CdSe nanocrystals' assemblies, a would be the mean distance between nanocrystals (the diameter+the ligand length). For P3HT, the case is more complex since the conjugation length depends on the material chemical quality, its regioregularity, molecular weight, crystallinity and processing conditions. Moreover, in semi-crystalline P3HT, the localization is non-homogeneous (amorphous *vs* crystalline domains) and anisotropic, at least in crystalline domains. It should be comprised between 1 nm (a few monomers, the interchain distance) and 15 nm (the typical size of crystalline domains, see Chapter II, Fig. II.14). Due to this uncertainty and to similar orders of magnitude, we chose to describe one nanocrystal as one site for hybrids and to keep the same parameters for pristine P3HT and hybrid films simulations.

$$a = d_{NX} = 6.7\ nm$$

Morphology of the active layer The simulated volume is 328 sites long (corresponding to the 2.2 μm thickness of the samples) and 200 $\times$ 200 sites in area, with periodic boundary conditions in these lateral directions.

We treat sites as independent in energy. Nonetheless, it must be remarked that since polymers are long, snake-like chains, energy correlations along polymer chains are likely to exist. Moreover, the presence of amorphous and crystalline domains implies a supplementary spatial inhomogeneity in the hopping rates. Some papers discuss this issue, using Monte Carlo algorithms to simulate polymeric morphologies and their evolutions [3, 5].

For the hybrid sample, assigning an energy value to each site corresponds to defining the heterojunction morphology: fractions of components and their spatial repartition (*e.g.* the degree of dispersion of nanocrystals in the polymer matrix). 16 % of sites with nanocrystals energies, *i.e.* the volume fraction of nanocrystals, are introduced randomly in the lattice (corresponding to a good dispersion of nanocrystals in the polymer matrix; spatial correlations could account for aggregation).

3.3 Depicting energy landscapes

Each site on the lattice is randomly attributed an energy value according to an energy distribution. In conjugated polymers, the energy distribution is often a Gaussian with added levels or band(s), either Gaussian or exponential [2, 4]. The secondary band is sometimes referred to

as the 'trap band'. The mean of the Gaussian corresponds to the HOMO/LUMO level of the material. Its width, $\sigma_{\mathrm{HOMO/LUMO}}$, the dispersion in energy, is essentially due to disorder:

- *thermal disorder* a function of the temperature and is related to the phonon influence on the electronic spectra.
- *spatial disorders* configurational/positional disorder (polymer chains orientations, unregular packing of nanocrystals) and energetical disorder due to size dispersion (polydispersities of polymers and nanocrystals). Its order of magnitude is tenths of meV to a hundred meV.
- *homogeneous broadening* single nanocrystal photoluminescence spectra exhibit a small width, of the order of 5 meV. This phenomenon is called spectral diffusion.

3.3.1 P3HT density-of-states

We have studied the effect of energy distributions on P3HT current transients, starting from the common 'Gaussian main band+Gaussian secondary band' model, in the framework of Marcus theory. We show representative simulated photocurrent transients in Fig. VI.5 in the log-log representation. The transit time is clearly defined by a change in the slope of the transient.

Fig. VI.5 a) shows that transport becomes more dispersive as the number of traps increases. This is coherent with a trap-driven picture of dispersive transport.

Fig. VI.5 b) shows current transients for different trap energy levels, from a level close to the HOMO, $-$ 4.96 eV (for which the mean energy of traps E_{trap} is separated form the main band by the reorganization energy λ), to a level close the middle of the gap, $-$ 4.4 eV, and this for two different fractions of traps, 1 and 10 vol%. Transport gets more dispersive as the secondary band gets further from the main band and this effect is far more important for a high fraction of traps.

Indeed, in the framework of Marcus theory, hops with an energy difference matching the reorganization energy are favored. When the difference between main and secondary bands strongly mismatches the reorganization energy, hops from one band to another are very unlikely. Consequently, for low fractions of sites in the secondary energy band, charge carriers in this energy band have low probabilities of hopping altogether: 1) the sites in the main band are far away in energy; 2) the sites from the secondary band are far away in space. Hence, a little accessible secondary energy band, with only nearest neighbor hops and relatively low densities of traps renders transport more dispersive. Variable range hopping may allow to study deep trap effects since charge carriers would be allowed to move through trap states even for low fractions of traps.

McMahon and Troisi computed a DOS for semicrystalline P3HT by a molecular dynamics method, using localized molecular orbitals [2]. The obtained DOS is is in agreement with other

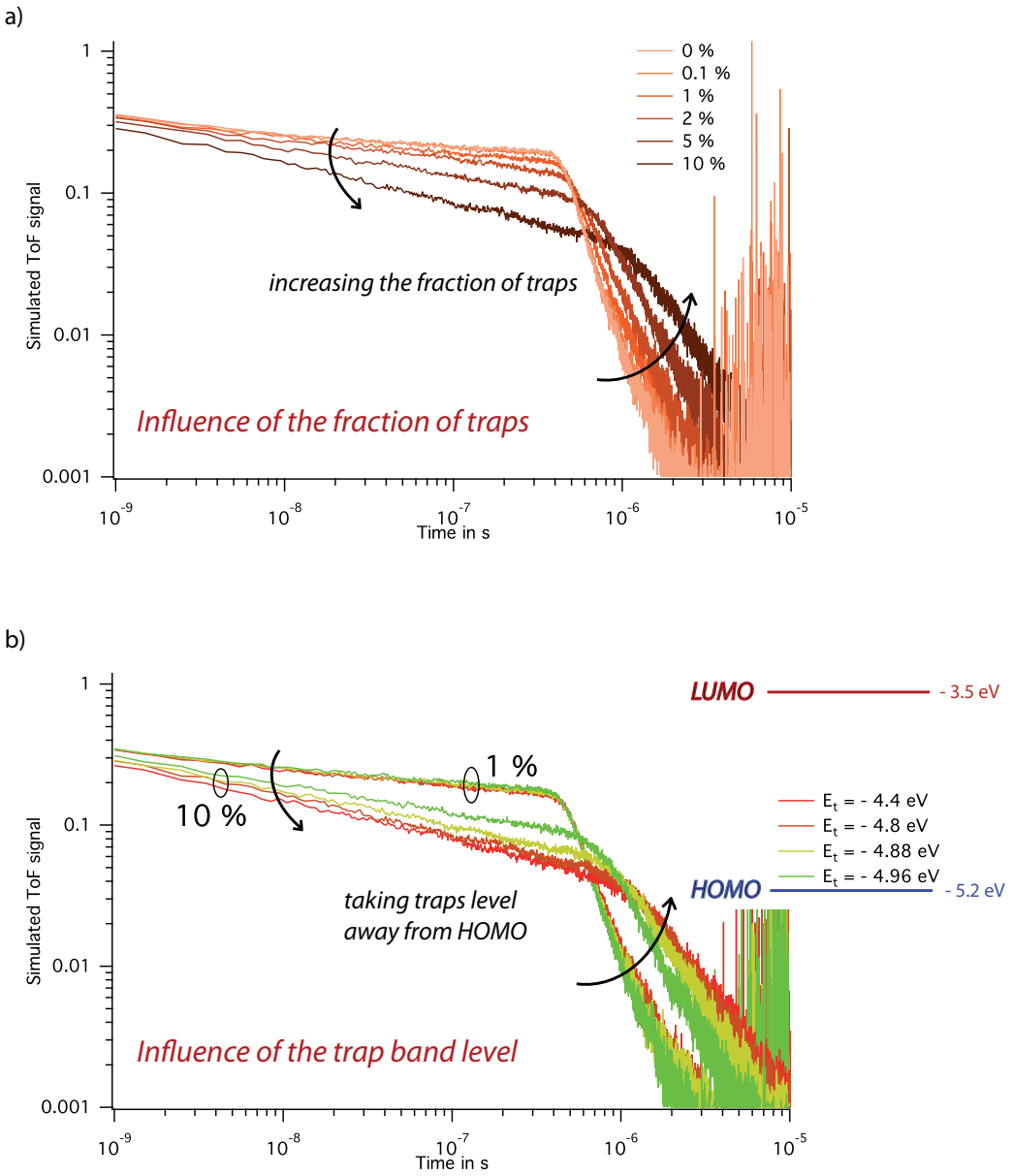

Figure VI.5 – Influence of traps on simulated current transients in the framework of Marcus theory with a main HOMO band at $-5.2\ eV$ and widths $0.09\ eV$ for both the HOMO and the secondary bands. In a), the secondary energy band was fixed at $-4.8\ eV$ and its volume fraction varied from 0 to 10 %. In b), the secondary energy level varied from $-4.96\ eV$, close to the HOMO, to $-4.4\ eV$, close to mid-gap states. We represented transients for two volume fractions of 'traps': 1 and 10 %. Reorganization energy was fixed to $0.24\ eV$ in all cases, meaning that the secondary level at $-4.96\ eV$ is separated from the main band by the reorganization energy.

theoretical and experimental energy distributions and is pictured in Fig. VI.6 a).

$$\left| \begin{array}{llll} E_0 = E_{\text{HOMO, P3HT}} = -5.2\ eV, & & \sigma_0 = \sigma_{\text{HOMO, P3HT}} = 0.1\ eV \\ E_{sec} = -4.95\ eV, & & \sigma_{sec} = 0.09\ eV \end{array} \right.$$

The width of the DOS is of the same order of magnitude than that found for spin-coated films by the analysis of optical spectra in Chapter II, 2.2.

Using the 'McMahon & Troisi' DOS, our simulated transients fitted our experimental data well, as we will detail in the Results section.

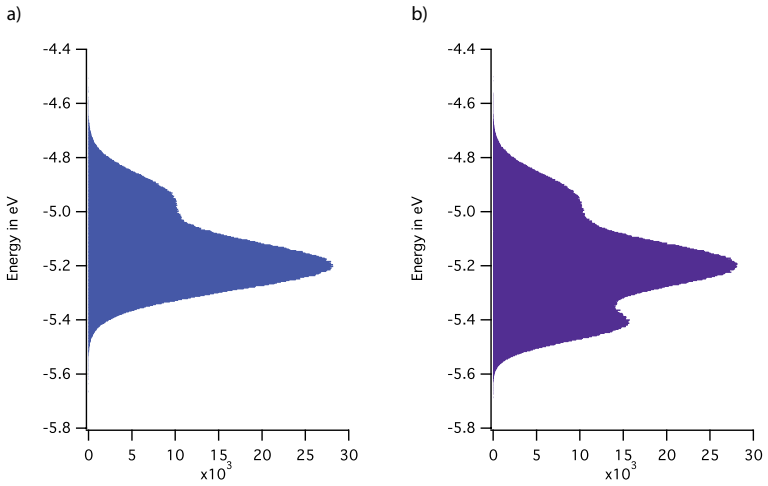

Figure VI.6 – Tested energy distributions for hole transport simulations in a), HOMO of P3HT as calculated in [2] (main band: mean at -5.2 eV, width 0.1 eV; secondary band: 20% of sites, mean at -4.95 eV, width 0.09 eV); in b), the same distribution with in addition the HOMO level of nanocrystals (mean at -5.42 eV from electrochemistry, width 0.06 eV from optical measurements).

3.3.2 Hybrids' energy landscape for hole transport

To simulate transient in hybrids, we tried two different approaches:

- holes transport occurs only in P3HT, the DOS for polymeric states is the one pictured in Fig. VI.6 a). Nanocrystals sites are 'dead sites', *i.e.* they are far away in energy (at the vacuum energy level).
- holes hop through the P3HT HOMO *and* through the nanocrystals' HOMO bands. The DOS is the one pictured in Fig. VI.6 b)[4].

In the second case, the resulting DOS is very wide, and transport becomes more dispersive. As we noticed experimentally, the addition of nanocrystals in P3HT1 did not make hole photocurrents a lot more dispersive. Moreover, as we will detail below, taking sites out of reach of

[4]The mean energy of the nanocrystals HOMO energy level has been reevaluated at energies $\leq$ -5.59 eV. This would lead to an even wider energy distribution for hole transport and does not modify qualitatively the results.

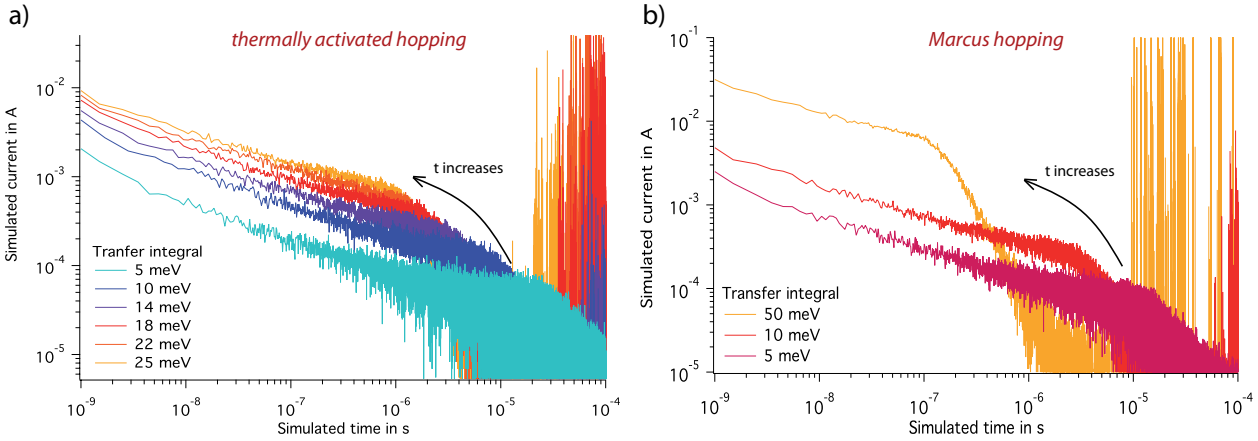

FIGURE VI.7 – Influence of the transfer integral a) thermally activated hopping ; b) Marcus hopping rate with reorganization energy 0.2 eV. All transients were computed with McMahon and Troisi DOS for an applied voltage of 20 V (electric energy between adjacent sites 56 meV).

holes allowed to fit experimental transients, increasing time transients by an amount comparable to what we observe experimentally. This confirms the idea that P3HT alone serves as the hole transporting layer.

3.4 Modeling the hopping process

Hopping transport arises from localization of charge-carriers, *i.e.* the transfer integral t is small in comparison to the electron-phonon coupling and to the thermal energy ($25\ meV$). Moreover, derivation of Marcus formula for hopping rates necessitates fulfilling of conditions (V.10), $t << \lambda$ and $\hbar\omega_0 << k_BT$, see Chapter V.

In Chapter II, we have determined the exciton bandwidth from spectroscopic features of P3HT to be around 100 meV. This value is four times the intermolecular coupling energy for a one-dimensional linear aggregate [25]. Moreover, Liu *et al.* have recently shown that transfer integrals between P3HT and PCBM are around 10 meV [26]. These studies give us an estimate of the order of magnitude of the transfer integral t.

Influence of the transfer integral t on current transients We present in FIG.VI.7 current transients for different values of the transfer integral. When the electronic transfer integral t increases, charges are less strongly localized and hopping probabilities are higher. Charges arrive faster to the electrode : transit times are smaller.

In both thermally activated hopping and Marcus model, slopes before the transit time increase slightly with decreasing t and slopes after the transit time increase slightly: transport is more dispersive for smaller t.

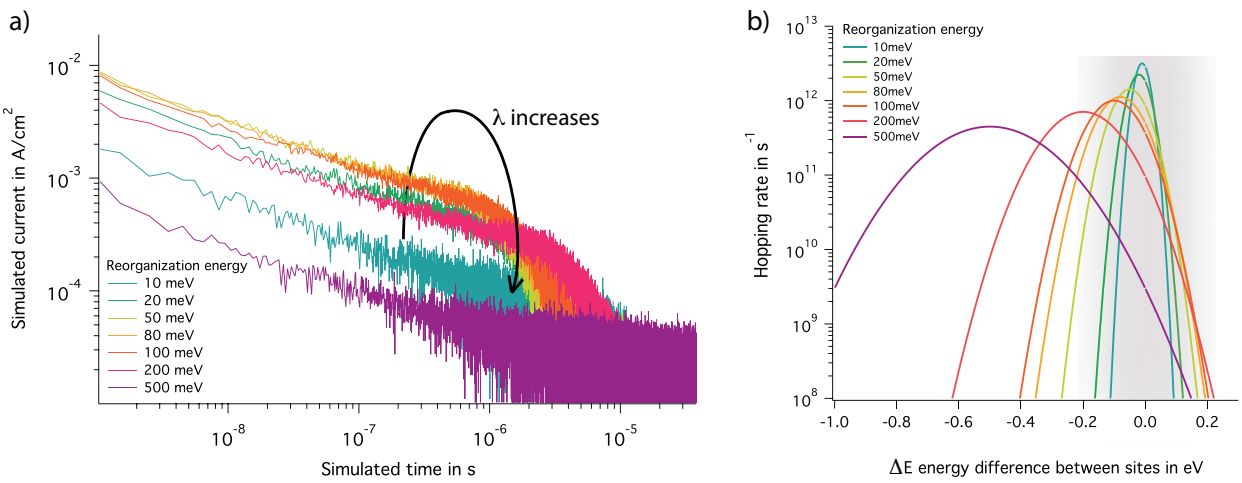

Figure VI.8 – Influence of the reorganization energy Marcus hopping rates with a transfer integral value of 10 meV. All transients were computed with McMahon and Troisi DOS for an applied voltage of 20 V (electric energy between adjacent sites 56 meV).

Influence of the reorganization energy λ on current transients The influence of the reorganization energy λ depends on the value of $\Delta E = E_j - E_i$. For a single value of ΔE, hopping rates reach a maximum for a certain value of λ. In energetically disordered materials, energy values are distributed, so ΔE is distributed as well. In Fig.VI.8 b), the gray zone represents the explored range of ΔE in the case of a Gaussian distribution. The range of hopping rate amplitudes varies with λ. For example, in this figure, hopping rates obtained for λ= 500 meV are lower than those for 200 meV. When λ decreases further, they reach a maximum, as can also be seen in the transients in Fig.VI.8 a), before decreasing again. When all other parameters are fixed, transit times thus first decrease with decreasing reorganization energy and then increase again.

In conclusion, we have reviewed all simulations parameters, with an emphasis on the influence of the DOS, transfer integral and electron-phonon coupling on the allure of current transients. We have seen that the wider the DOS (or equivalently, the more numerous the traps and/or the further they are from the main band), the more dispersive the simulated transients are. The value of the transfer integral rules mostly the arrival time of charges, and also slightly the dispersivity of simulated transients. Finally, the reorganization energy has a more complex, non monotonic influence on the transients, which reflects the balance between the energetical disorder and the reorganization energy.

4 Results and outlooks

We present the results of our simulations. First, we show simulations of the transients measured in the pristine P3HT1 sample, within the frameworks of the thermally activated model and of Marcus hopping. This allows to find the best value for the transfer integral t and the reorganization energy λ. Then we turn to the simulation of photocurrents in the hybrid thin film, with the P3HT parameters determined above, as nanocrystals as voids in the hole transporting layer. That way, we show that in this specific hybrid material, nanocrystals do not contribute to hole transport.

4.1 Hole currents in P3HT-only film

Thermally activated hopping FIG.VI.9 shows our fits of hole experimental transients in P3HT1 for thermally activated hopping. These fits are very satisfactory in terms of shape and values of the transit times.

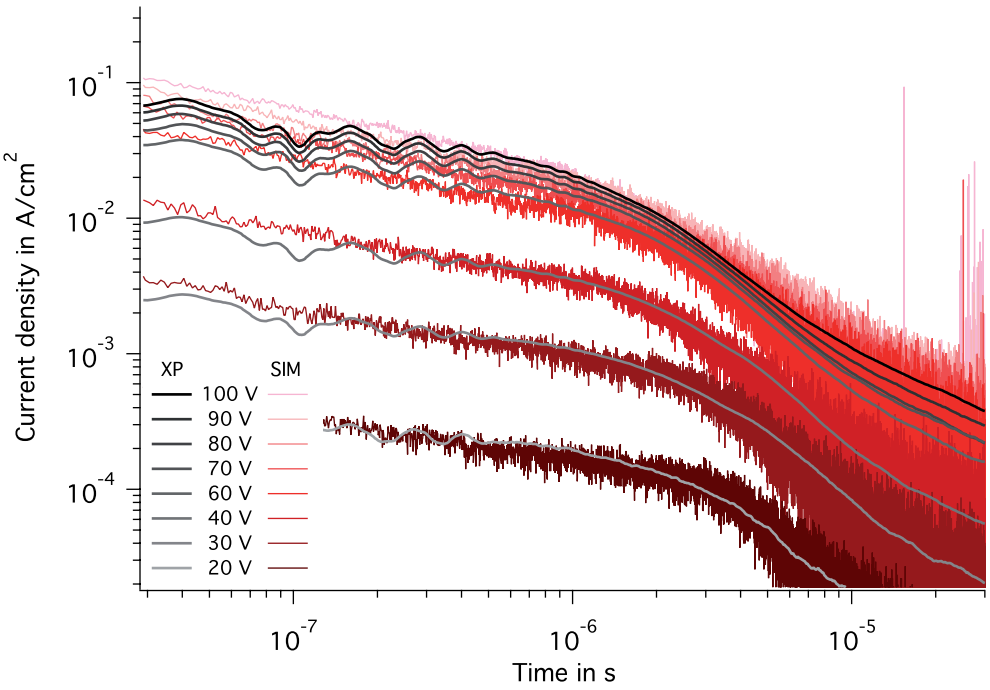

FIGURE VI.9 – Monte Carlo simulation of current transients in P3HT for different applied voltages and thermally activated hopping rates In gray, experimental curves (for a 2.2 μm P3HT1 film illuminated through Al by a 532 nm laser pulse ; averaged with a sliding box) and in red, the simulated transients. All transients were computed with McMahon and Troisi DOS and a transfer integral 3 $meV \leq t \leq 14\ meV$)

Nonetheless, the slope prior to the transit time is slightly too large in the simulations. It was moreover not possible to fit all transients with a single t. We indeed find that t varies between 14 meV and 3 meV (for applied voltages between 20 V to 100 V). t depends exponentially on the applied voltage : $t = t_0 e^{-\alpha V}$ with $t_0 = 21.8\ meV$ and $\alpha = -20.8\ .10^{-3}\ V^{-1}$. These variations are relatively low compared to uncertainties regarding knowledge of transfer integrals in P3HT and the different approximations of our model.

Marcus hopping We present fits of P3HT1 experimental hole transients obtained in the framework of Marcus theory in Fig.VI.10. Here as well, the fits are good in terms of shape of the transients and of values of transit times. The similarity of curves obtained with the two models shows that the shape of the simulated transients is dominated by the energy distribution. This said, in the case of Marcus hopping rates simulations, the slope prior to the transit time fits better experimental curves than in the case of thermally activated hopping.

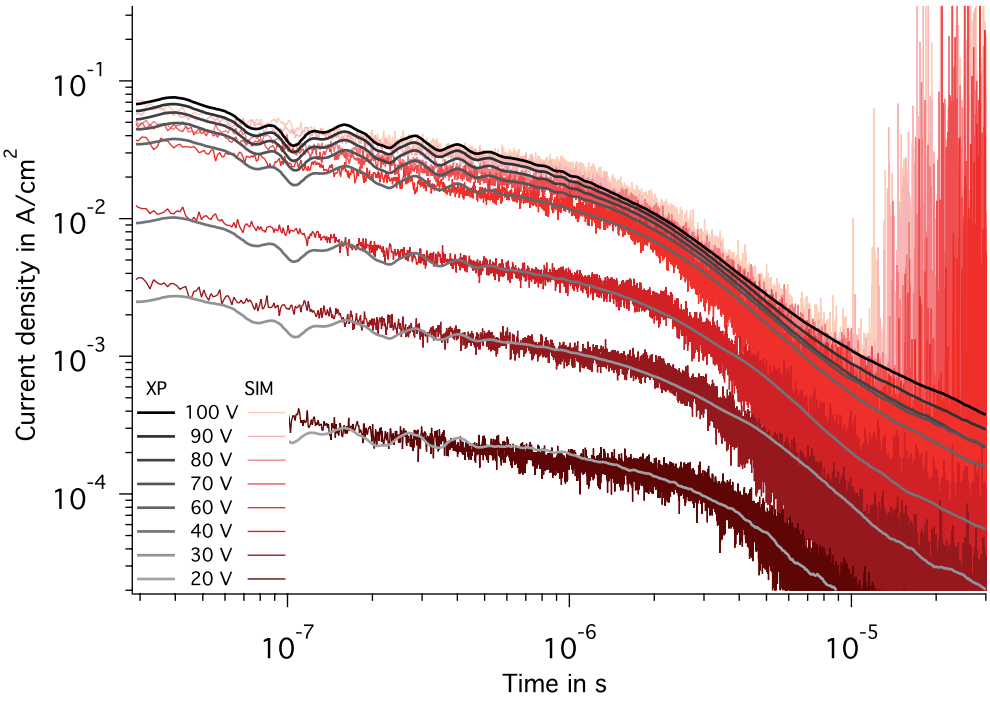

Figure VI.10 – Monte Carlo simulation of current transients in P3HT for different applied voltages and Marcus hopping rates In gray, experimental curves (for a 2.2 μm P3HT1 film illuminated through Al by a 532 nm laser pulse ; averaged with a sliding box) and in red, the simulated transients. All transients were computed with McMahon and Troisi DOS, a transfer integral $t = 10\ meV$ and the reorganization energy $200\ meV \leq \lambda \leq 590\ meV$).

In the case of high voltages particularly, these slopes are smaller than in the case of thermally activated hopping. Since transfer integral values used in the two models are similar for high voltages (10 meV for Marcus, between 3 and 6 meV for thermally activated hopping), the differences in the slopes does not arise from t, but from the influence of the reorganization energy.

Thus, Marcus hopping seems more appropriate to simulate hole transport in a P3HT-only film. Indeed, as mentioned above, thermally activated hopping describes phonon-assisted hopping but neglects polaronic effects, while Marcus theory formalizes the polaronic hopping of a charge dressed with a lattice deformation. Polaronic effects are important in π-conjugated polymers.

Interestingly, fits obtained with Marcus hopping rates were obtained with a single value of the transfer integral $t = 10\ meV$ but needed variation of the reorganization energy λ between 200 and 590 meV, depending on the voltage. We discuss the possible reasons for this voltage dependence at the end of the Chapter.

Using different values of the transfer integral (5 meV and 50 meV) led to different reorganization energy values, but with the same linear dependence on the applied voltage 5 meV/V, as shown in Fig.VI.11. Therefore, the condition $t << \lambda$ was always satisfied. Using a still lower value of the transfer integral t=1 meV did not allow fitting of experimental transients for any of the reorganization energies probed (between 1 eV and 10 meV): the transients were low in amplitude and transit times exceeded 10^{-4} s when they were detectable at all.

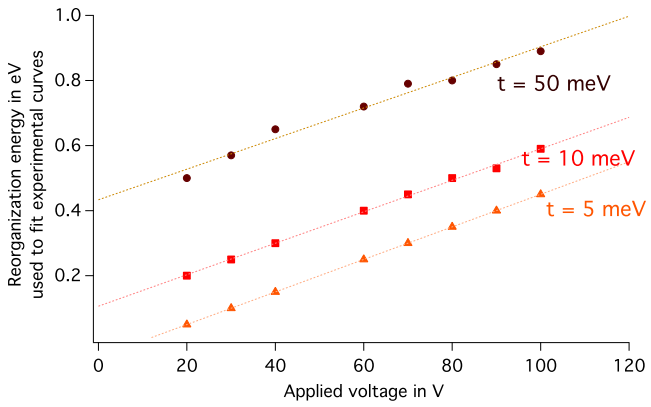

Figure VI.11 – Reorganization energies needed to fit the experimental transients for different applied voltages The reorganization energy needed to fit experimental transients depends linearly on the applied voltage by a factor 5 meV/V for all values of the transfer integral.

Finally, let us note that reorganization energy values are rather large and do not respect the second condition of Eq.V.10, stating that phonons can be treated classically: $\lambda = S\hbar\omega_0 << Sk_BT$ with S, the Huang-Rhys factor, equal to 1. This was also found in the works of J. Nelson's group (*e.g.* in [4, 18, 27]) and of Bisquert's group (in [28]) and is related to high polaron binding energies in organic materials (equal to $\lambda/2$).

4.2 Hole currents in an hybrid film

The best fits for the transients obtained in the hybrid thin film are shown in Fig.VI.12. Marcus hopping rates were used, all parameters were kept identical to those used for P3HT1 (t=10 meV) and nanocrystals were modeled as little accessible sites (at the vacuum energy, so that the hopping rates to and from nanocrystals are very small).

In conclusion, simulating nanocrystals as the far, far away land (low accessibility sites) allows to fit experimental transients in hybrids: the dispersivity of transport is comparable to that in the pristine P3HT sample and transit times are slightly longer with 16 % of sites occupied by nanocrystals.

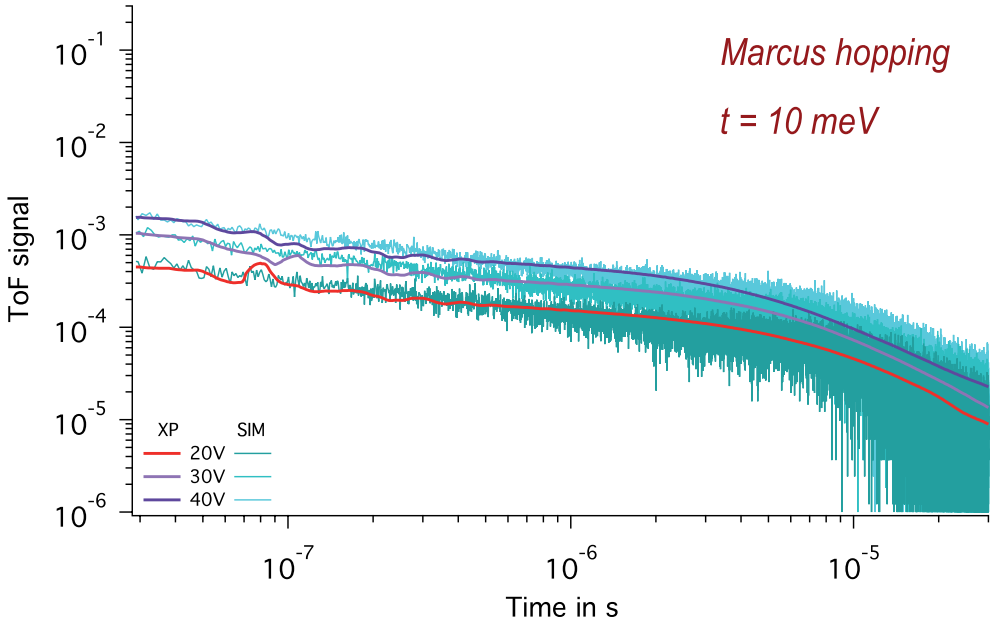

Figure VI.12 – Monte Carlo simulation of current transients in an hybrid thin film for different applied voltages In red and purple, experimental curves (for a 2.2 μm hybrid film made with P3HT1 and 50 wt%-16 vol% of 6.7 nm nanodots, illuminated through Al by a 532 nm laser pulse; averaged with a sliding box) and in blue, the simulated transients. All transients were computed with McMahon and Troisi DOS, with 16 % of sites as nanocrystals, and parameters identical to those used for P3HT1 in Fig.VI.10 b). We present here curves for 20, 30 and 40 V that are the voltages shared with the P3HT measurements and simulations.

4.3 Applied voltage dependence

We have seen that our fit parameters t and λ depend on the applied voltage.

This does not necessarily reflect variations of actual materials parameters on the applied voltage, but merely of our model. Indeed, we do not account for some physical phenomena that depend on the voltage, such as spatial inhomogeneity of the electric field, spatial inhomogeneity of hopping and recombinations.

Sean Shaheen's team is currently looking into the spatial dependance of the electric field through the thin film. Indeed, a depletion zone is known to form at the interface with the Al electrode. If the thin film is not completely depleted (its thickness being larger than the depletion width), charge transport occurs in two phases, by drift followed by diffusion. The depletion width depends on the applied voltage.

Implementing site energy correlations and a distribution of transfer integrals (arising from the positional disorder) would account for different factors possibly entering the voltage dependence: energetical disorder, but also directionality of crystallization (*e.g.* with different intra- and intermolecular transfer integrals), might reduce the voltage dependence of the fit values of transfer integrals and reorganization energies. Moreover, it would allow to investigate the effect on hole transport of the suspected presence of nanocrystals in amorphous domains, see Chapter IV.

Finally, recombinations also depend on the applied voltage (*e.g.* [29]), and recombination rates increase with increasing voltages.

5 Conclusion

In conclusion, Monte Carlo simulation of hole current transients in P3HT and hybrid thin films have been performed. We showed that the energy distribution rules the shape of simulated transients. The DOS derived by Troisi and McMahon in [2] permitted to reproduce the shape of our experimental transients. We used different models of hopping rates, namely thermally activated and Marcus rates and showed that Marcus hopping rates allowed better fitting of P3HT experimental curves. The best fits were obtained with a transfer integral t =10 meV and varying the reorganization energy between 200 and 590 meV. Finally, we showed that making it difficult for charges to hop to nanocrystals sites made transit times longer and allowed to reproduce experimental transients obtained for an hybrid thin film.

We discussed and used reasonable ranges for each parameter of the simulation. Several assumptions were made in our model, namely i) there is a single type of charge carriers, ii) hops occur towards nearest neighbors only, iii) there is no positional disorder, *i.e.* no distribution of transfer integral, iv) the active layer is uniform: site energies are spatially uncorrelated and the electric field is constant. More work is needed to include these effects into device simulations. Parallel theoretical and experimental works, at different space and time-scales, should bring insight into values of physical parameters in our real experimental devices. These values are expected to depend on processing conditions.

References of part III

[1] D. L. Cheung and A. Troisi. *Modelling charge transport in organic semiconductors: from quantum dynamics to soft matter.* Phys. Chem. Chem. Phys. **10**, 5941 (2008).

[2] P.D. McMahon and A. Troisi. *Organic semiconductors: impact of disorder at different timescales.* Chem. Phys. Chem. **11**, 2067 (2010). 122, 126, 135, 136, 138, 145

[3] N. Vukmirović and L-W. Wang. *Charge carrier motion in disordered conjugated polymers: a multiscale ab initio study.* Nano Lett. **9**(12), 3996 (2009).

[4] A. J. Chatten, S. M. Tuladhar, S. A. Choulis, D. D. C. Bradley, and J. Nelson. *Monte Carlo modelling of hole transport in MDMO-PPV: PCBM blends.* Journal of Materials Science **40**(6), 1393 (2005).

[5] J. Nelson, J. J. Kwiatkowski, J. Kirkpatrick, and J. M. Frost. *Modeling charge transport in organic photovoltaic materials: introduction.* Accounts of Chemical Research **42**(11) (2009).

[6] A. Assadi, C. Svensson, M. Willander, and O. Inganäs. *Field-effect mobility of poly(3-hexylthiophene).* Appl. Phys. Lett. **53**(3), 195 (1988).

[7] D. S. Ginger and N. C. Greenham. *Charge injection and transport in films of CdSe nanocrystals.* J. Appl. Phys. **87**(3), 1361 (2000).

[8] H. Liu, A. Pourret, and P. Guyot-Sionnest. *Mott and Efros-Shklovskii variable range hopping in CdSe quantum dots films.* ACS nano **4**(9), 5211 (2010).

[9] W. U. Huynh, J. J. Dittmer, N. Teclemariam, D. J. Milliron, A. P. Alivisatos, and K. W. Barnham. *Charge transport in hybrid nanorod-polymer composite photovoltaic cells.* Phys. Rev. B **67**, 115326 (2003).

[10] K. R. Choudhury, J. G. Winiarz, M. Samoc, and P. N. Prasad. *Charge carrier mobility in an organic-inorganic hybrid nanocomposite.* Appl. Phys. Lett. **82**(3), 406 (2003). 123

[11] J. Cottaar and P. Bobbert. *Calculating charge-carrier mobilities in disordered semiconducting polymers: Mean field and beyond.* Phys. Rev. B **74**(11), 1–6 (2006).

[12] H. Houili, E. Tutis, I. Batistic, and L. Zuppiroli. *Investigation of the charge transport through disordered organic molecular heterojunctions.* J. Appl. Phys. **100**(3), 033702 (2006).

[13] Z. G. Yu, D. L. Smith, A. Saxena, R. L. Martin, and A. R. Bishop. *Molecular geometry fluctuations and field-dependent mobility in conjugated polymers.* Phys. Rev. B **63**(8), 085202 (2001).

[14] A. Miller and E. Abrahams. *Impurity conduction at low concentrations.* Phys. Rev. **120**(3), 745 (1960).

[15] M. Bouhassoune, S. L. M. Van Mensfoort, P. A. Bobbert, and R. Coehoorn. *Carrier-density and field-dependent charge-carrier mobility in organic semiconductors with correlated Gaussian disorder.* Organic Electronics **10**(3), 437 (2009).

[16] J. Nelson. *Continuous-time random-walk model of electron transport in nanocrystalline TiO 2 electrodes.* Phys. Rev. B **59**(23), 374 (1999).

[17] R. E. Chandler, A. J. Houtepen, J. Nelson, and D. Vanmaekelbergh. *Electron transport in quantum dot solids: Monte Carlo simulations of the effects of shell filling, Coulomb repulsions, and site disorder.* Phys. Rev. B **75**, 085325 (2007).

[18] J. Nelson, J. Kirkpatrick, and P. Ravirajan. *Factors limiting the efficiency of molecular photovoltaic devices.* Phys. Rev. B **69**, 035337 (2004).

[19] J. M. Frost, F. Cheynis, S. M. Tuladhar, and J. Nelson. *Influence of polymer-blend morphology on charge transport and photocurrent generation in donor-acceptor polymer blends.* Nano Lett. **6**(8), 1674 (2006).

[20] A. A. Kocherzhenko, F. C. Grozema, S. A. Vyrko, N. A. Poklonski, and L. D. A. Siebbeles. *Simulation of hopping transport based on charge carrier localization times derived for a two-level system.* J. Phys. Chem. C **114**, 20424 (2010).

[21] V. Stehr, J. Pfister, R. F. Fink, B. Engels, and C. Deibel. *First-principles calculations of anisotropic charge-carrier mobilities in organic semiconductor crystals.* Phys. Rev. B **83**(15), 155208 (2011).

[22] F. C. Grozema and L. D. A. Siebbeles. *Mechanism of charge transport in self-organizing organic materials.* Intern. Rev. in Phys. Chem. **27**(1), 87 (2008).

[23] Y. Preezant and N. Tessler. *Carrier heating in disordered organic semiconductors.* Phys. Rev. B **74**(23), 1–5 (2006).

[24] P. Reiss, E. Couderc, J. De Girolamo, and A Pron. *Conjugated polymers/semiconductor nanocrystals hybrid materials–preparation, electrical transport properties and applications.* Nanoscale **3**(2), 446 (2011). 134

[25] J-F. Chang, J. Clark, N. Zhao, H. Sirringhaus, D. W. Breiby, J. W. Andreasen, M. M. Nielsen, M. Giles, M. Heeney, and I. Mcculloch. *Molecular-weight dependence of interchain polaron delocalization and exciton bandwidth in high-mobility conjugated polymers.* Phys. Rev. B **74**, 115318 (2006). 139

[26] T. Liu and A. Troisi. *Absolute rate of charge separation and recombination in a molecular model of the P3HT/PCBM interface.* J. Phys. Chem. C **115**, 2406 (2011).

[27] J. Kirkpatrick, V. Marcon, J. Nelson, K. Kremer, and D. Andrienko. *Charge mobility of discotic mesophases: a multiscale quantum and classical study.* Phys. Rev. Lett. **98**(22), 1–4 (2007).

[28] G. Garcia-Belmonte and J. Bisquert. *Open-circuit voltage limit caused by recombination through tail states in bulk heterojunction polymer-fullerene solar cells.* Appl. Phys. Lett. **96**(11), 113301 (2010).

[29] M. Kuik, H. T. Nicolai, M. Lenes, G-J. A. H. Wetzelaer, M. Lu, and P. W. M. Blom. *Determination of the trap-assisted recombination strength in polymer light emitting diodes.* Appl. Phys. Lett. **98**(9), 093301 (2011).

Conclusion and outlook

This thesis aims to improve the understanding of charge transport in hybrids made of P3HT and CdSe nanocrystals. To do so, we prepared samples, performed Time-of-Flight measurements of hole and electron transport in P3HT and hybrid films and simulated experimentally obtained photocurrent transients. In particular,

- We performed the gram-scale synthesis of spherical and branched nanocrystals by the hot-injection organometallic route and obtained samples of low polydispersity and of adjustable size.

- The surface ligands of the obtained CdSe nanocrystals were exchanged in the liquid phase or in the solid phase. We used small molecules as new ligands, namely pyridine, ethanedithiol, phenylenediamine, butylamine and benzenedithiol. Electrochemical measurements showed that this exchange resulted in a raise of the HOMO level for the first three ligands [1]. We showed that effective dielectric constants models are insufficient to explain the observed shifts of the absorption excitonic peak upon ligand exchange.

- We deposited and characterized P3HT and hybrid films and obtained layers of adjustable thicknesses. Thanks to optical and GIXRD measurements, we evaluated the degrees of disorder in the films.

- We measured P3HT and hybrid thin films with the Time-of-Flight method. The hole mobility is slightly improved for smaller fractions of nanocrystals, and decreases notably for larger amounts; the electron mobility to the contrary is enhanced by the presence of nanocrystals, as proposed by percolation models, and it does not increase further after a certain fraction of nanocrystals. These changes of mobilities actually depend on the nature of the P3HT matrix and on the nature of the nanocrystals, *i.e.* on their shapes and ligands.

- We showed that the optimal fraction of nanodots with synthesis ligands is 75 wt%-36 vol% for large and balanced mobilities of both electron and holes.

- We calculated hole photocurrent transients in P3HT using Monte Carlo simulations. We studied the influence of the density-of-states (DOS) on charge transport. The DOS for the HOMO of P3HT derived theoretically by McMahon and Troisi [2] allows to simulate our experimental transients nicely. We used two types of hopping rates, namely thermally activated hopping rates and hopping rates from Marcus theory. The second ones give better fits of our experimental results.

- We simulated hole photocurrent transients obtained in a hybrid sample containing 16 vol% of spherical nanocrystals with synthesis ligands. We represented nanocrystals by sites difficult to hop on and this resulted in larger transient times, as was observed experimentally.

Finally, we presented critical analyses of all these findings, with an emphasis on the relation of our results to the field of hybrid photovoltaics.

In the future, still many aspects need to be explored, in the preparation of hybrid components, in the formation of hybrid heterojunctions, in their characterizations and in device integration. Inspiration can be drawn from the field of all-organic heterojunctions.

As we explained at the beginning of this thesis, we chose for this work to use a well-documented hybrid heterojunction, *i.e.* made of CdSe nanocrystals and P3HT blended in solution. These materials are still investigated by different groups but a shift towards the use of lower band gap materials, both on the organic and on the inorganic side, extends the absorption range of hybrids. Much work is carried out by many research teams around the world to improve the quality of hybrid counterparts (in terms of polydispersity for example) and to develop new components of hybrids materials. Also, a great deal of research focuses on novel types of surface ligands allowing the good redispersion of nanocrystals required for solution processing of thin films of low roughness while achieving high conductivities. The used solvents should of course be compatible with conjugated polymers if the aim is to realize hybrid bulk heterojunctions.

The investigation of volume morphology of hybrid heterojunctions needs advanced characterisation tools. Electron tomography can bring insight into the spatial dispersion and possible orientation of nanocrystals in the matrix; in-plane and out-of-plane X-ray diffraction measurements enable to build a precise picture of the semi-crystalline structure of the conjugated polymer. In the case of P3HT, which is a conjugated polymer particularly sensitive to processing conditions, these techniques could particularly help understanding the correlations between structure and transport properties, and also facilitate the comparison of results from different groups. The evolution of the volume morphology during annealing should be studied, similarly as it was done recently in P3HT:PCBM active layers [3].

Understanding the different interfaces present in hybrid materials requires the use of complementary techniques, for example local probes, time-resolved spectroscopy and theoretical

calculations. These characterizations help clarifying our description of components, for example the influence of ligands on nanocrystals energy levels and wave functions, and our representation of hybrid junctions, concerning their energy distributions, the extend and magnitude of built-in electric fields, etc.

Electrodes and interlayers (charge blocking layers at electrodes or in tandem cells) are currently very actively investigated. The performances of hybrid solar cells could certainly be improved by the optimization of such layers specially designed for hybrids, as is done for all-organic active layers, see *e.g.* [4].

Concerning charge transport in hybrids, many effects still need to be investigated.

Charging effects under light and voltage influences are revealed for example by hysteresis behavior of current-voltage characteristics, and should be explored systematically, for example by temperature-dependent measurements, by the application of a background light or by the application of a background voltage. Temperature-dependence and dynamics of charging would allow to better understand the energetics of charging and/or trapping phenomena, through activation energies, lifetimes, relaxation mechanisms and their possible combination, etc.

Moreover, the influence of aging, oxygen and moisture on trap distributions, carrier densities and charge transport should be explored by performing temperature-dependent electrical studies in controlled atmosphere, particularly the measurements of transient currents. For example, thermally stimulated current measurements and the CELIV technique were used recently to study trap formation in P3HT:fullerenes heterojunctions [5].

Capacitance measurements against voltage and frequency give access to the profile of the electric field inside the active layer (depletion width, band bending).

More directly related to the TOF experiments presented in this work, it would be interesting to study the influence of the active layer thickness and of the electrode area, in order to probe volume and edge effects. A very thin, semi-transparent Al layer on top of the ITO electrode acts as a blocking contact and avoids hole injection, as recently shown in TOF investigation of P3HT:TiO_2 heterojunctions [6, 7]. This approach can be used to measure hole and electron mobilities by generating them from the same side (Al-coated ITO). The large photon transmission resulting from this configuration would allow studying electron and hole currents with different excitation wavelengths and intensities. A temperature-dependent study would also bring more insight into transport mechanisms in hybrids, and in particular allow to unravel the physical origins of energetic and positional disorders. Finally, it will of course be of great interest to shift to CELIV and integral TOF techniques to study samples of the same thickness as those used in hybrid solar cells.

Heterojunctions with specific architectures, for example comb-like structures, are also actively sought for. Orienting P3HT in the flat-on configuration (*i.e.* with the aromatic cycle parallel to the substrate) would favor hole transport perpendicular to the substrate; vertical arrays of inorganic nanowires would favor electron transport. The description of transport in

these more complicated architecture would most probably require some modeling efforts to avoid deriving meaningless effective mobilities.

Finally, as we mentioned previously, theoretical work at different space and time scales should shine light on the density-of-states in our materials, on transfer integrals and on electron-phonon couplings within nanocrystal assemblies, polymer thin films, and hybrid materials. The presented Monte Carlo simulations could be made even more relevant by implementing energy correlations to introduce the anisotropy of transport in the organic phase and study the effect of the possible aggregation of nanocrystals. It would be interesting as well to introduce some disorder in the transfer integral. The second type of charge carriers (electrons) can be introduced in the simulations, enabling at the same time the investigation of electron transport and of recombinations. In order to simulate low temperature photocurrents, variable range hopping needs to be implemented. Finally, these progresses would of course only be meaningful only if they were supported by a large amount of experimental data. Indeed, there is a large dispersion of values in disordered materials. Characteristics of hybrids depend on many parameters in the processing and history of the sample. While reducing the sources of non-reproductibility by careful handling is possible and necessary, some dispersion will remain, for example in the measured mobility values. The tedious but essential study of statistical dispersions is a daily concern in fields where complexity is at the heart of the studied objects, for example in life sciences. It has also started in the organic materials community, for example in G. Whitesides' group, in electrical studies of self-assembled monolayers [8].

In conclusion, the research on hybrid materials is driven by the quest for cheap energy converting devices. They also raise very interesting fundamental questions in physics and chemistry, and much theoretical and experimental studies are underway, most especially concerning interfaces and disorder.

References of the conclusion

[1] A. Lefrançois, E. Couderc, J. Faure-Vincent, S. Sadki, A. Pron, and P. Reiss. *Effect of the treatment with (di-)amines and dithiols on the spectroscopic, electrochemical and electrical properties of CdSe nanocrystals' thin films.* J. Mater. Chem. **21**, 11524 (2011).

[2] P.D. McMahon and A. Troisi. *Organic semiconductors: impact of disorder at different timescales.* Chem. Phys. Chem. **11**, 2067 (2010).

[3] S. Lilliu, T. Agostinelli, E. Pires, M. Hampton, J. Nelson, and J. E. Macdonald. *Dynamics of crystallization and disorder during annealing of P3HT/PCBM bulk heterojunctions.* Macromolecules **44**(8), 2725 (2011).

[4] E. L. Ratcliff, B. Zacher, and N. R. Armstrong. *Selective interlayers and contacts in organic photovoltaic cells.* J. Phys. Chem. Lett. **2**(1337) (2011).

[5] J. Schafferhans, A. Baumann, A. Wagenpfahl, C. Deibel, and V. Dyakonov. *Oxygen doping of P3HT:PCBM blends: influence on trap states, charge carrier mobility and solar cell performance.* Organic Electronics **11**(10), 1693 (2010). 153

[6] Chang C-H., Huang T-K., Lin Y-T., Lin Y-Y., Chen C-W., Chu T-H., and W-F. Su. *Improved charge separation and transport efficiency in P3HT-TiO2 nanorod bulk heterojunction solar cells.* J. Mater. Chem. **18**, 2201 (2008). 153

[7] Li S-S., C-P. Chang, Lin C-C., Lin Y-Y., Chang C-H., Yang J-R., Chu M-W., and Chen C-W. *Interplay of three dimensional morphologies and photocarrier dynamics of polymer/TiO2 bulk heterojunction solar cells.* JACS **133**, 11614 (2011). 153

[8] M. M. Thuo, W. F. Reus, C. A. Nijhuis, J. R. Barber, Kim C., M. D. Schulz, and G. M. Whitesides. *Odd-even effects in charge transport across self-assembled monolayers.* JACS **133**, 2962 (2011).

Experimental protocols and appendices

1 Nanocrystals synthesis

Synthesis of spherical CdSe nanocrystals of different diameters The synthesis is described in [1] and in M. Protière PhD dissertation [2] for different sizes of nanocrystals.

Synthesis of branched CdSe nanocrystals with arm and core diameters of 3.8 nm and arm length of 6.3 nm We use a slightly modified protocol, with a lower reaction temperature, than in the case of the synthesis of spherical nanocrystals.

Trioctylphosphine (TOP, 200 mL) and selenium powder (0.08 mol, 6.23g) are mixed in a flask in the glovebox and stirred overnight to obtain 200 mL of TOP-Se at 0.4 M.

Cadmium stearate (8 mmol, 5434.72 mg), stearic acid (184 mmol, 52312.58 mg), oleylamine (280 mL) and octadecene (186 mL) are introduced into the 2 L reactor, degazed for one hour and finally put under argon atmosphere.

The mixture is then heated to 230°C and mechanically stirred. When the reaction temperature is reached, 200 mL of TOP-Se are rapidly injected by means of a peristaltic pump and the injection tail is stopped rapidly by closing a valve. When the temperature of the mixture has reached 230° again, the reaction is left to take place for 18 minutes. The heat is then turned off.

After cooling the reaction mixture to 80°C, 500 mL of acetone are introduced, then 200 mL of ethanol when the temperature is 70°C and finally 300 mL of acetone when the temperature is 50°C. The nanocrystals are precipitated by addition of methanol, and recovered by centrifugation for 25 minutes at 11000 rpm.

Finally, nanocrystals are redispersed in hexane.

2 Ligand exchange in solution, with pyridine

For a nanocrystals radius r, the number of surface units $(n_{CdSe})_{surface}$ is determined by calculating first the total number of units in a nanocrystal and subtracting the number of core

units $(n_{CdSe})_{core}$, *i.e.* the number of units in a nanocrystal of radius $r - 0.263nm$ (0.263 nm the closest neighbor distance in bulk CdSe). It is given by [3]:

$$(n_{CdSe})_{surface} = n_{CdSe} - (n_{CdSe})_{core} \tag{1}$$

$$\text{with} \begin{cases} n_{CdSe} = \frac{\rho_{CdSe}}{m_{CdSe}} \times V_{NX} = \frac{5810}{191.37 \times 1.66054 \times 10^{-27}} \frac{4}{3}\pi r_{NX}^3 \\ \quad = 7.66 \times 10^{28} \times r_{NX}^3 \\ (n_{CdSe})_{core} = 7.66 \times 10^{28} \times (r_{NX} - 0.263 \times 10^{-9})^3 \end{cases} \tag{2}$$

For example, in 4 nm nanocrystals, the number of surface CdSe units is estimated around 215 (core units 410). It is moreover known that Cd atoms are 1.2 more numerous than Se atoms at the surface of CdSe nanocrystals. Thus, to obtain the number of mol needed for the ligand exchange, we take the number of CdSe surface units, multiplied by 1.2, multiplied by the excess factor.

Typically, 75 mL (0.93 mol) of pyridine is added to 35 mL of a 1.5 mg/mL nanocrystals dispersion (8. 10^{-5} mol Cd surface atoms) in 6:1 $CHCl_3$:hexane mixture in a 250 mL round-bottom flask. The solution under argon is stirred and heated under reflux at 110°C for 24 hours. Stirring is stopped and the heat is turned down to around 60°C to keep stearic acid in the liquid phase. When the solution has cooled, 120 mL of hexane are added and nanocrystals are left to precipitate for 10 minutes. The viscous surnatant is removed from the round-bottom flask with a 50 mL glass pipet. A small volume of pyridine is added and the solution is precipitated again in hexane and centrifuged for 2 minutes at 4000 rpm to recover most nanocrystals; the surnatant is centrifuged again for 2 minutes at 11000 rpm to recover the remaining nanocrystals. Finally, the precipitate is recovered and stored in pure pyridine and in the fridge until use. The concentration of the solution is determined by gravimetry, *i.e.* by weighting a known volume of solution dried under argon. Pyridine-treated nanocrystals are dispersed in a 9:1 S:pyridine solvent mix, where S was for example be chloroform or orthodicholorbenzene, depending on the intended use.

3 Ligand exchange after thin film deposition

Ligand exchange after thin film deposition was performed by soaking CdSe nanocrystals thin films (100 nm spin coated films for absorbance measurements; 1 μm drop cast films for FTIR and electrochemistry measurements) in an acetonitrile solution containing the new ligand. The exact concentration and soaking time were optimized for each ligand, and are detailed in Table A.1. These procedures were developed for CdSe nanocrystals in our lab by Aurélie Lefrançois [4]. Similar studies on PbSe nanocrystals were reported in [5, 6].

Table A.1 – Experimental conditions for ligand exchange after thin film deposition

Ligand in acetonitrile	Concentration in g/mol	Soaking time
Ethanedithiol	0.1	6 minutes
Butylamine	0.1	48 hours
Benzendithiol	0.025	24 hours
Phenylenediamine	0.1	48 hours
Pyridine	0.1	48 hours

4 P3HT preparation

Fractionation of 3 g of P3HT from Merck (with initial parameters M_n=12.8 kDa, M_n=37.2 kDa, D=2.90) was performed with a Soxhlet extractor and cellulose filters. The solvent sequence used was acetone, hexane, dichloromethane, tetrahydrofuran and chloroform [7]. Each fraction's solvent was evaporated in a rotavap and the polymer recovered in $CHCl_3$ before being dried under argon and weighted. Due to the high mass of P3HT initially, the full procedure took two weeks and we obtained respectively for each fraction a few mg (acetone), 101 mg (hexane), 140 mg (dichloromethane), 1160 mg (tetrahydrofuran) and 1513 mg (chloroform). The chloroform fraction is called P3HT2.

The regioregularity of P3HT1, from Sigma, was determined by H^1 NMR, following [8]. The NMR spectrum in $CDCl_3$ is presented in Fig. A.1. To obtain the regioregularity, the area of the dominated peak, corresponding to a head-to-tail coupling (darker blue rectangle in the zoom) is divided by the area of all aromatic peaks (both blue zones) [9].

When needed, P3HT was weighted and redispersed in an know volume of the appropriate solvent (chloroform, chlorobenzene, orthodichlorobenzene) by stirring and heating gently the solution (40°C). Just before use, the solution was filtered still warm, with a 0.45 μm PTFE filter. For warm chlorobenzene solutions, the filtration induced a 10 % mass loss, in the range of concentrations 10 mg/mL to 40 mg/mL.

5 Hybrid solutions

Hybrids made of CdSe nanocrystals and P3HT were blended in solution before deposition. Equal volumes V of polymer and nanocrystals suspensions were stirred and heated gently (40°C).

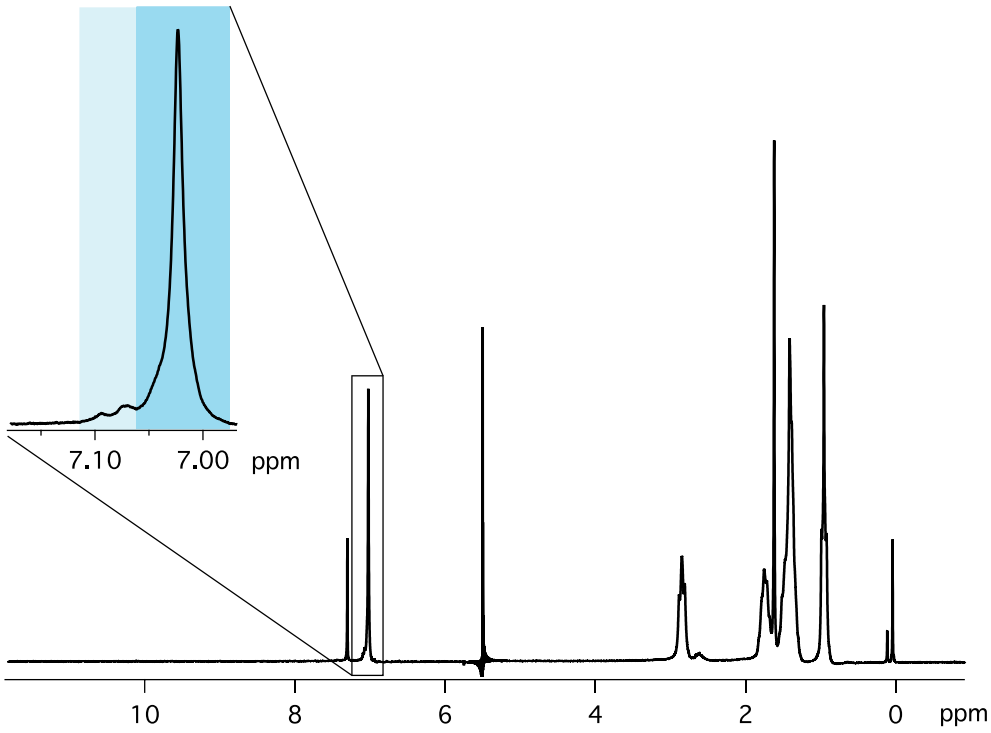

Figure A.1 – H^1 NMR spectrum of P3HT1

Initial concentrations were :

$$\begin{cases} c_{\text{pm init}} &= \frac{V_{\text{tot}}}{V_{\text{pm}}} c_{\text{pm final}} = 2c_{\text{pm final}} \\ \\ c_{\text{nx init}} &= \frac{V_{\text{tot}}}{V_{\text{nx}}} \frac{1}{R} c_{\text{pm final}} = \frac{2}{R} c_{\text{pm final}} \end{cases} \tag{3}$$

As we have seen above, the pyridine-treated nanocrystals are dispersed in a mixture of solvents with 10 vol% of pyridine. Our blending procedure always uses the same relative volumes of nanocrystals and polymer dispersions, *i.e.* also the same amount of pyridine (5 vol%).

Volume *vs* weight ratio With R the ratio of masses of nanocrystals and polymer ($R = m_{NX}/m_{pm}$), one has $V_{NX}/V = (R\rho_{pm})/(\rho_{NX} + R\rho_{pm})$ with V_{NX} the nanocrystals volume, V the total volume and ρ_i the density of phase i.

6 ITO substrate cleaning and patterning

ITO substrates are wiped with a clean tissue and acetone, cleaned by a wet procedure (ultrasonic bath in acetone for 15 minutes, rinsing with acetone; ultrasonic bath in isopropanol for 15 minutes, rinsing with isopropanol; drying under argon flux) and finally placed in a UV-ozone cleaner for 10 minutes at 130°C.

UV-curable SU8-2005 resist is spin coated (5 seconds at 500 rpm, 40 seconds at 3000 rpm, accelerations 200 rpm/s) on ITO substrates and annealed (1 minute at 65°C, 2 minutes at 95°C). The subtrates are insolated through mechanical masks at λ =365 nm and 6 mW/cm^2 nm for 60 seconds with a Süss Microtech MJB4 and annealed again (1 minute at 65°C, 1 minute at 95°C). Finally, the resist is developed in SU8-developer (30 seconds-1 minute), rinsed with isopropanol and dried under argon flux.

ITO appears were the resist has been developed and is etched chemically in warm aqua regia (1 minute at 35°C); the etching is stopped by rinsing with deionized water.

The UV-cured resist is removed with N-methylpyrolidinone in an ultrasonic bath (30 minutes at 70°C).

Finally, ITO substrates are cleaned again with the procedure indicated at the begining of the section. A schematical representation the different steps of the substrate preparation is given in Chapter IV, Fig. IV.2.

7 Functionalization of ITO and SiO_2 substrates

Substrates were functionalized by a wet procedure.

ITO substrates were soaked for 1 hour into a 0.1 M mercaptopropyltriethoxysilane or ethanedithiol solution in acetonitrile in the glovebox, rinsed with acetonitrile and baked at 60°C for 10 minutes.

Similarly, SiO_2 substrates were functionalized by mercaptopropyltriethoxysilane by soaking for one hour in a 5 mM solution in acetonitrile and baked at 120° [10].

8 Thin films depositions methods

We used different wet deposition methods summarized in Fig. A.2.

Spin coating

Depositions of nanocrystals thin films were carried out in a single spinning step, with the following parameters:

1. deposition of enough of the nanocrystals dispersion to cover the substrate, typically 200-300 μL for a 1.2 $\times$ 1.7 cm^2 substrate;

2. spinning 10 seconds at 4000 rpm, acceleration 3000 rpm/s.

We studied the obtained thickness as a function of the solution concentration in hexane, as shown of Fig. A.3. A 100 nm thick film can be realized on ITO substrate with a 30 mg/mL nanocrystals solution in hexane.

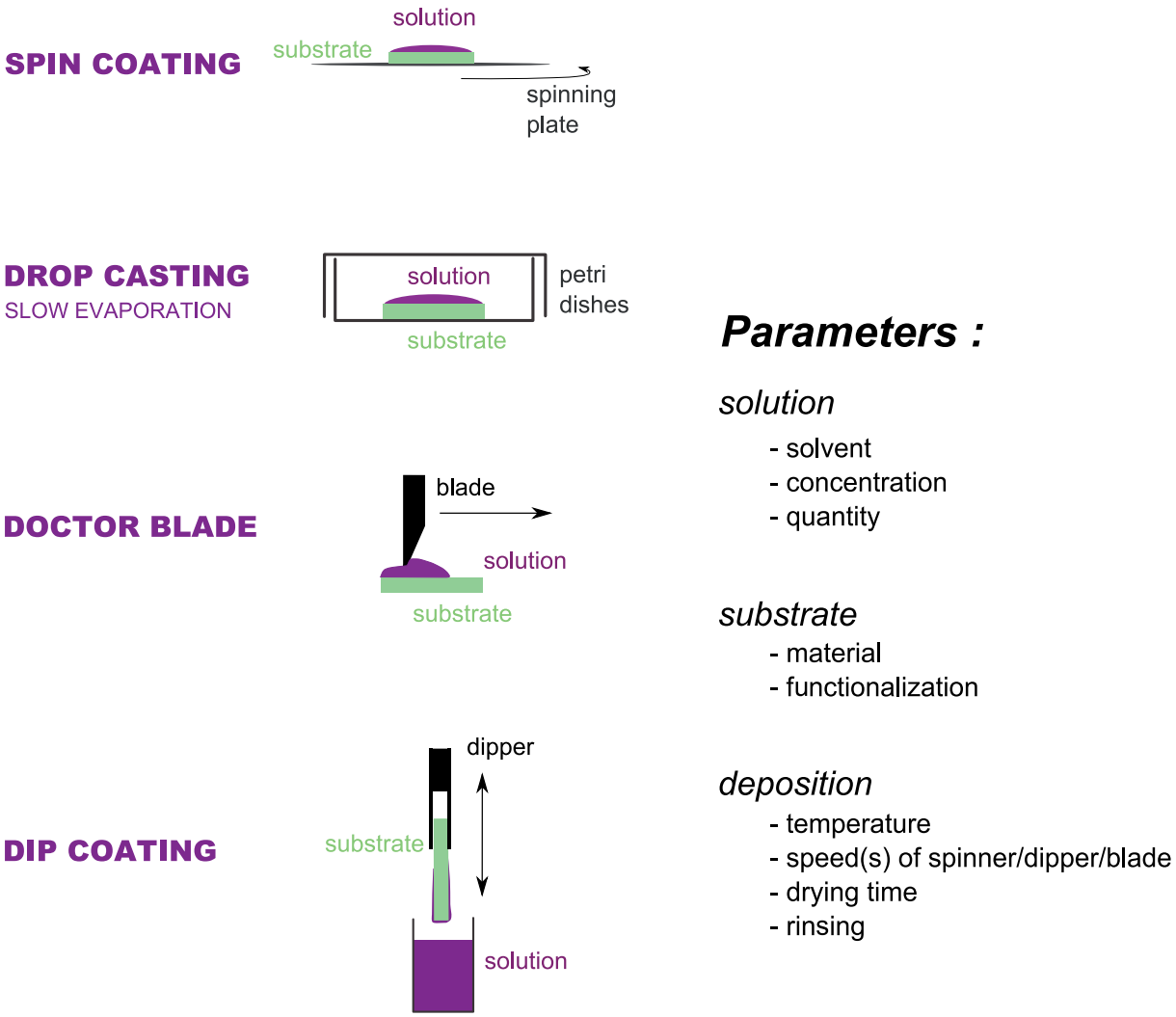

FIGURE A.2 – Thin films deposition methods

All depositions of P3HT and hybrid thin films were performed with the following parameters.

1. deposition of enough of the polymer dispersion to cover the substrate, typically 200-300 μL for a 1.2 $\times$ 1.7 cm^2 substrate;
2. Spreading: 10 seconds at 500 rpm, acceleration 200 rpm/s;
3. Coating: 40 seconds at 1500 rpm, acceleration 200 rpm/s;
4. Drying: 60 seconds at 2500 rpm, acceleration 200 rpm/s.

FIG. A.4 indicates the thicknesses obtained with chlorobenzene solutions of P3HT for different concentrations.

Moreover, depending on the solvent used, thicknesses of P3HT thin films vary a lot for the same concentration. For example, using a concentration of 40 mg/mL, dissolving P3HT upon

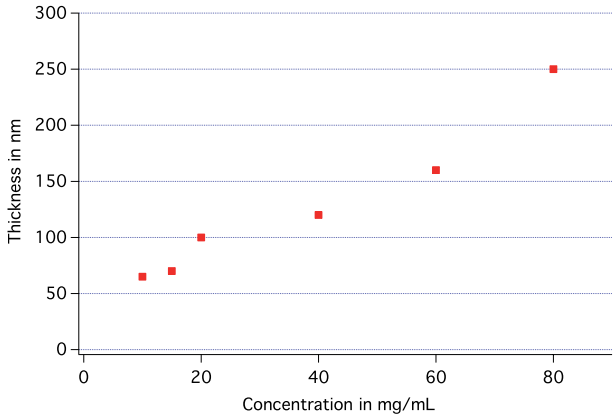

Figure A.3 – Thicknesses of nanocrystals spin coated films as a function of the concentration in hexane

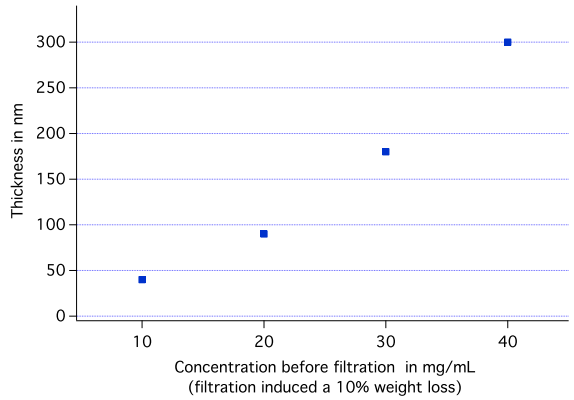

Figure A.4 – Thicknesses of P3HT spin coated films as a function of the concentration in chlorobenzene

gentle heating (40-50°C) and filtering with a 0.45 μm PTFE filter, we obtained thicknesses of 570 nm, 300 nm and 135 nm for $CHCl_3$, chlorobenzene and ortho-dichlorobenzene (ODCB), respectively. The viscosities of these solvents, respectively 0.57, 0.8 and 1.32, show that the more viscous the solvent, the thinner the obtained film.

Drop casting

The ITO substrate is placed at the bottom of a Petri dish. A pipet is used to deposit the solution on the substrate. A second, slightly larger Petri dish is delicately deposited upside down on top, and a cover (aluminum foil) is used to allow the films to dry in the dark. Drying takes place at room temperature in the glove box and takes around 8 days for ODCB solutions.

The films were more homogeneous when the pipetted solution is almost ready to overflow. With our 1.2 $\times$1.7 cm^2 substrates, this was usually achieved for 180 to 240 μL of solution.

For P3HT films, a concentration of 5 mg/mL was used, resulting in film thicknesses above 1 μm (the film thickness also depends on the substrate size and the volume of solution). This resulted in RMS roughnesses of 50 nm, *i.e.* 1 % of the thickness.

For nanocrystals, a 9:1 hexane:octane solvent mixture was used [10], which strongly affects the evaporation process: while hexane tends to flow towards the border of the drop during evaporation, the small amount of octane results in a slow, almost ghost-like spreading of the drop. As a result, the commonly observed coffee-stain effect can be avoided and a more homogeneous deposition is obtained. For drop casting on ITO substrates as explained above, low concentrations around 8 mg/mL were used; for other uses in which substrates have much smaller areas (1 mm^2 for electrochemistry, 0.25 mm^2 for FTIR spectroscopy), larger concentrations and smaller volumes on small substrates were used, namely 80 mg/mL and 10 μL for substrates sized below 10 mm^2. At a microscopic scale, nanocrystals tend to aggregate into superstructures and films obtained by this method are usually less homogeneous in thickness and roughness than P3HT films; this could be overcome by substrate functionalization.

Finally, for hybrids, a global polymer concentration of 5mg/mL was used and the concentration of the nanocrystals solution was adapted according to the desired weight ratio between components. Thicknesses in these conditions were between 5 and 8 μm. RMS roughnesses were above 7 %, and notably more important for hybrids based on nanocrystals treated with pyridine, which were on average 16 % *vs* 9 % for hybrid with nanocrystals capped with the synthesis ligands.

Doctor blade

We optimized doctor blade deposition for nanocrystals on ITO and Si or SiO_2 substrates. To reduce the influence of seasonal temperature variations, we perform doctor blading on a heating plate at 23°. 2 to 5 μL of solution are deposited at one end of the substrate just before the automatic blade sets in movement, at a height of 50 μm above the substrate, with a speed of 25 mm/s. We used an 9:1 hexane:octane solvent mixture; a nanocrystals' concentration of 15 mg/mL allows to deposit very thin films, around 50 nm.

Dip coating

Dip coating is a cyclic method that can be used to deposit very small amounts of material (sub-monolayers) at each cycle. We performed dip coating for two types of samples: to obtain sub-monolayers and study the repartition of nanocrystals onto the substrate on one hand, and to deposit hybrid thin films in a Layer-by-Layer fashion on the other hand.

To deposit sub-monolayers of nanocrystals, we use very dilute solutions (10 mg/mL) and dip the substrate once in the nanocrystals solution, rinse it with the nanocrystals solvent (typically hexane) and dry it under argon flux.

Using the dip-coating robot allows to perform numerous deposition cycles. Very dilute

solutions are in beakers, themselves on a rotating plate. The substrate is mounted to a dipper. A program selects the first beaker and plunges the dipper with a regulated speed; the substrate is left in the solution for a definite amount of time, before being lifted, left to dry for a certain amount of time, and possibly plunged again in the same beaker or another one.

To deposit hybrid samples, very specific components were used: both polymer and nanocrystals were functionalized to allow for a molecular recognition between components, see Fig. II.18. This system was developed and optimized by Julia De Girolamo during her PhD thesis, including manual dip coating [3]. Nanocrystals and polymer are dispersed in orthogonal solvents, forbidding solution blending and avoiding the redispersion of any of the two phases in the second one during deposition. Here we focused on the automatization of the dip-coating procedure. The polymer solvent was changed from chloroform to chlorobenzene in order to slow down the evaporation of the polymer solution during the deposition process and consequently maintain a constant concentration. Nanocrystals were dispersed in a 10:1 solvent mix of dimethylformamide:methanol. Rincing steps after each deposition of one of the two composents avoid the presence of aggregates on the substrate, for a cleaner, more homogeneous deposition; drying steps avoid mixing solvents and even nanocrystals and polymer. Since each components is not soluble in the other solvent, any mixing of the solution resulting in precipitation. We used the following parameters:

1. Polymer deposition: speed down: 60 mm/min; time down (in the solution): 2 minutes; speed up: 60 mm/min; time up (drying): 1 minute;

2. Rinsing in the polymer solvent: speed down: 60 mm/min; time down: 0 ; speed up: 60 mm/min; time up: 2 minutes;

3. Nanocrystals deposition: speed down: 60 mm/min; time down: 5 minutes; speed up: 60 mm/min; time up: 1 minute;

4. Rinsing in the nanocrystals solvent: speed down: 60 mm/min; time down: 0; speed up: 60 mm/min; time up: 3 minutes.

This cycle was repeated N times, resulting in the deposition of a $3N$ nm thick films, within around $25N$ minutes.

Annealing

Annealing is done in a Büchi oven under primary vacuum (0.01 to 0.06 mbar). The sample undergoes a slow temperature rise, spending 15 minutes with a setting temperature of 80°C, then 30 minutes with a setting temperature at 130°C, finally followed by a 'slow' temperature decrease to room temperature, namely 15 minutes at 80°C and a final rest to room temperature.

Annealing improved the reproducibility of profilometer measurements.

9 Counter electrode evaporation

150 nm of Aluminum were evaporated under secondary vacuum through a mechanical mask, at a deposition rate of 0.1 Å/s for the first 50 nm and 0.5 Å/s for the remaining 100 nm.

10 Experimental characterization setups

Profilometer measurements For thick films, thickness and surface roughness measurements were realized with an Ambios XP2 profilometer, with a stylus force of 0.8 mg, a scanning speed of 0.1 mm/s and a scan length of 1 mm.

Atomic Force Microscopy For thickness and roughness determination of our thinnest nanocrystals' films (below 100 nm) and for substrate roughness measurements, we used a Nanosurf AFM with its software.

Scanning electron microscopy Scanning electron imaging of thin films was done with a MEB Zeiss Ultra 55 at relatively low voltage values, in order to limit the degradation of organic counterparts (2.5 kV for polymer, 5 kV for nanocrystals-only films and in between for hybrids), and at a working distance of 4 nm to 5 mm.

Transmission electron microscopy TEM imaging was performed by P. Reiss and F. Chandezon on a Jeol 4000EX TEM at 400 kV.

UV-visible absorbance measurements Optical absorbance spectra were measured and recorded with an HP8452A Diode Array Spectrophotometer (range 190 nm-820 nm).

Photoluminescence measurements Optical photoluminescence spectra were measured and recorded with an Hitachi F-4500 Fluorescence Spectrophotometer (range nm). The excitation wavelength was usually set to 480 nm and the scanning speed to 1200 nm/minutes. For solution measurements, the incidence and detection slit widths were both 5 nm, respectively. For thin films measurements, a special film holder was used and incidence and detection slit widths were 10 nm and 20 nm respectively.

Fourier Transform Infrared Spectroscopy measurements FTIR spectra were recorded on a Perkin-Elmer Paragon 500 FT-IR Spectrometer equipped with an Attenuated Total Reflectance (ATR) setup. The penetration depth of the evanescent wave is between 0.5 and 5 μm, so we used thick films ($\geq$ 1 μm, drop cast).

Nuclear Magnetic Resonance measurements Proton NMR were recorded on a Bruker AC 200 MHz spectrometer, using deuterated chloroform.

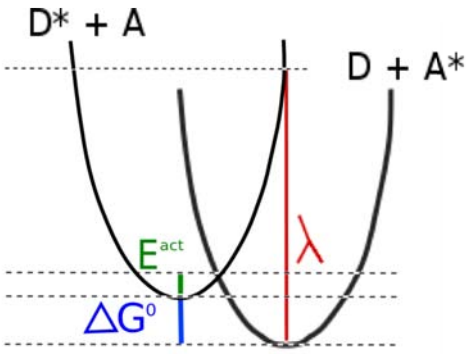

Figure A.5 – Definitions of energies in Marcus theory

X-ray diffraction XRD profiles have been measured using a Philips X'pert diffractometer with a Co source ($\lambda = 1.789$Å), at 40 kV and 40 mA. For GIXRD measurements, an incidence angle of 0.15° was used. The typical 2θ step was 0.04° with a 35s counting time per step.

Current-voltage characteristic measurements I(V) characteristic were performed with an automated Keithley 2636A probe station and the corresponding software.

Electrochemistry Electrochemical measurements were carried out under argon by A. Lefrançois, with an Autolab potentio-galvanostat. Ag/Ag^+ was used as a pseudo-reference, and the counter and work electrodes were Pt. Reduction cycles were measured with voltages from 0.5 V to -1.5 V and oxydation cycles were performed with applied voltages from -0.5 V to 1.5 V. Reduction and oxidation measurements were performed each time on newly deposited films, due to the irreversibility of the redox process.

Unless a specific software was required for the instrument, all data were treated with Igor Pro.

11 Back to Marcus theory [11–13]

We recall here two derivations of the Marcus rates, historically developed for electron transfers between molecules in a solvent. Fig. A.5 depicts free energy curves of the donor and acceptor for asymmetrical electron transfer.

The electron transfer is thermally activated and its probability writes:

$$\nu = A\, e^{\frac{-E^{act}}{k_B T}} \tag{4}$$

By rewriting E^{act} thanks to ΔG^0 and λ, Marcus transition rate becomes:

$$\nu = A\, e^{\frac{-(\Delta G^0+\lambda)^2}{4\lambda k_B T}} \tag{5}$$

with ν the transfer rate, A a prefactor that depends on the frequency of attempt to cross the barrier, ΔG^0 the free energy difference between acceptor and donor excited states and λ the reorganization energy. λ includes two components:

$$\lambda = \lambda_i + \lambda_o \tag{6}$$

λ_i is the inner sphere component and describes vibrations of the molecules (intramolecular reorganization energy). λ_o is the outer sphere component and includes polarization changes in the dielectric environment (solvent reorganization energy). The latter is often neglected and $\lambda \approx \lambda_i$.

Equation 5 is derived from classical energetic considerations. It assumes that the energy barrier is crossed thanks to thermal energy and it does not account for coupling to quantified vibronic levels (phonons).

A quantum treatment allows to find a more precise expression of the prefactor A and to detail the electron-phonon coupling λ_i.

The Fermi Golden rule to the electronic transition between donor and acceptor excited states writes:

$$\nu_{ij} = \frac{2\pi}{\hbar}|V_{el-el,ij}|^2 \delta(\epsilon_i - \epsilon_j) \tag{7}$$

with $V_{el-el,ij} = -t a_i^\dagger a_j$ the coupling between electrons on sites i and j (t is the transfer integral). We have made the Condon approximation, *ie* the assumption that the transfer integral does not depend on nuclear coordinates.

In the classical limit (high temperature/low frequency mode), for a single harmonic mode ω_0, one finds an expression equivalent to Equation 5 with:

$$\nu = \frac{2\pi}{\hbar}|t|^2 \frac{1}{\sqrt{4\pi\lambda k_B T}} e^{\frac{-(\Delta G^0+\lambda)^2}{4\lambda k_B T}} \text{ with } \lambda \approx S\hbar\omega_0 \tag{8}$$

where S is the the electron-phonon coupling constant, also called the Huang-Rhys factor.

12 Hopping rates calculations

Hopping rates give the rate of hopping to an adjacent site. They depend on the energies of the departure and destination sites, including the influence of the electric field. In Time-of-Flight experiments, the applied voltage is constant in time, so hopping rates need be calculated only

once for all possible hops on the lattice.

In the simulation, hopping rates are normalized by the total probability for hopping in any direction to a nearest neighbor. For example, the Marcus hopping rate for a forward jump $x \to x+1$ is:

$$\nu^{sim}_{i=(x,y,z)\to(x+1,y,z)} = \frac{\frac{2\pi}{\hbar}|t|^2 \frac{1}{\sqrt{4\pi\lambda k_B T}} e^{-\frac{\left(E_{(x+1,y,z)}-E_{(x,y,z)}+\lambda\right)^2}{4\lambda kT}}}{\sum_j \nu^{Marcus}_{i=(x,y,z)\to j}} \tag{9}$$

where j is an index over the nearest neighbors of the departure site and $E_{(x,y,z)}$ is the energy of the site (x,y,z).

Finally, for each site i, the average hopping rate $< \nu_i^{sim} >$ is calculated and associated to dwell time τ_i:

$$< \nu_i^{sim} >= \frac{\sum_j \nu^{Marcus}_{i\to j}}{6} = \tau_i^{-1} \tag{10}$$

Charges are sorted in a queue according to the site dwell time.

13 Abbreviations used in the text

AFM	Atomic force microscopy
CB	Chlorobenzene
CELIV	Current extraction by linearly increased voltage
CV	Cyclovoltammetry
DMF	Dimethylformamide
DOS	Density-of-state
DPV	Differential pulse voltammetry
EDT	1,2-ethanedithiol
FET	Field-effect transistor
FTIR	Fourier transform infrared spectroscopy
HOMO	Highest occupied molecular orbital
KPFM	Kelvin probe force microscopy
ITO	Indium Tin Oxide
JCPDS	Joint Committee on Powder Diffraction Standards
LESR	Light-induced electron spin resonance
LUMO	Lowest unoccupied molecular orbital
MEH-PPV	Poly[2-methoxy-5-(2'-ethylhexyloxy)-p-phenylenevinylene]
MeOTAD	2,20,7,70-tetrakis(N,N-di-p-methoxyphenylamine)-9,90-spirobifluorene
MDMO-PPV	Poly[2-methyloxy-5-(30,70-dimethyloctyloxy)- p-phenylenevinylene]
MHT	1-(6-mercaptohexyl)thymine
MPTES	Mercaptopropyltriethoxysilane
NMR	Nuclear magnetic resonance
ODCB	*ortho*-dichlorobenzene
OPV	Organic photovoltaics
PCBM	Phenyl-C61-butyric acid methyl ester
PCDTBT	Poly[[9-(1-octylnonyl)-9H-carbazole-2,7-diyl]-2,5-thiophenediyl-2,1,3-benzothiadiazole-4,7-diyl-2,5-thiophenediyl]
PCPDTBT	Poly[2,6-(4,4-bis-(2-ethylhexyl)-4H-cyclopenta[2,1-b;3,4b0]dithiophene)-alt-4,7-(2,1,3-benzothiadiazole)]
PCE	Power conversion efficiency
PEDOT:PSS	poly(3,4-ethylenedioxythiophene):poly(styrenesulfonate)
PTB7	Poly[[4,8-bis[(2-ethylhexyl)oxy]benzo[1,2-b:4,5-b0]dithiophene-2,6-diyl] [3-fluoro-2-[(2-ethylhexyl)carbonyl]- thieno[3,4-b]thiophenediyl]]
PTFE	Polytetrafluoroethylene (or teflon)
P3HT	Poly(3-hexylthiophene)
PL	Photoluminescence
RMS	Root mean square
SCLC	Space-charge limited current
SEC	Steric-exclusion chromatography
SEM	Scanning electron microscopy
TCO	Transparent conductive oxide
TEM	Transmission electron microscopy
TOF	Time-of-Flight
XRD	X-ray diffraction

References of appendices

[1] M. Protière, N. Nerambourg, and P. Reiss. *Rational design of the gram-scale synthesis of nearly monodisperse semiconductor nanocrystals.* Nanoscale Research Letters **6**, 472 (2011).

[2] Myriam Protière. *Synthèse de nanocristaux fluorescents de semi-conducteurs II-VI et III-V. Augmentation de l'échelle de synthèse.* PhD dissertation, Université Joseph Fourier (2007).

[3] Julia De Girolamo. *Architectures hybrides auto-assemblées à base de systèmes polyconjugués et de nanocristaux de semi-conducteurs pour le photovoltaïque plastique.* PhD dissertation, Université Joseph Fourier (2007).

[4] A. Lefrançois, E. Couderc, J. Faure-Vincent, S. Sadki, A. Pron, and P. Reiss. *Effect of the treatment with (di-)amines and dithiols on the spectroscopic, electrochemical and electrical properties of CdSe nanocrystals' thin films.* J. Mater. Chem. **21**, 11524 (2011).

[5] J. M. Luther, M. Law, M. C. Beard, Q. Song, M. O. Reese, R. J. Ellingson, and A. J. Nozik. *Schottky solar cells based on colloidal nanocrystal films.* Nano Lett. **8**(10), 3488 (2008).

[6] M. Law, J. M. Luther, Q. Song, B. K. Hughes, C. L. Perkins, and A. J. Nozik. *Structural, optical, and electrical properties of PbSe nanocrystal solids treated thermally or with simple amines.* JACS **130**(18), 5974 (2008).

[7] M. Trznadel, A. Pron, and M. Zagorska. *Preparation and properties of fractionated regioregular poly(3-alkylthiophenes).* Synthetic Metals **101**, 118 (1999).

[8] G. Barbarella, A. Bongini, and M. Zambianchi. *Regiochemistry and conformation of poly(3-hexylthiophene) via the synthesis and the spectroscopic characterization of the model configuration triads.* Macromolecules **27**, 3039 (1994).

[9] J-M. Verilhac. *Transistors organiques à base de dérivés du polythiophène, effets de la structure moléculaire et supramoléculaire.* PhD dissertation, Université Joseph Fourier (2006).

[10] B. L Wehrenberg, D. Yu, J. Ma, and P. Guyot-Sionnest. *Conduction in charged PbSe nanocrystal films.* J. Phys. Chem. B **109**(43), 20192 (2005).

[11] R.A. Marcus. *Nonadiabatic processes involving quantum-like and classical-like coordinates with applications to nonadiabatic electron transfer.* J. Chem. Phys. **81**(10), 4494 (1984).

[12] P. F. Barbara, T. J. Meyer, and M. A. Ratner. *Contemporary issues in electron transfer research.* J. Phys. Chem. **100**, 13148 (1996).

[13] A. Tokmakoff. *Marcus theory class.* http://www.mit.edu/ tokmakof/TDQMS/Notes/12.2. Marcus.pdf (2008).

Transport de charge dans des matériaux hybrides composés de polymères π-conjugués et de nanocristaux de semi-conducteurs Cette thèse a pour but d'étudier le transport de charges photogénérées dans des matériaux hybrides composés de polymères π-conjugués et de nanocristaux de semi-conducteurs, conçus pour des applications en opto-électronique. La synthèse chimique permet d'obtenir des nanocristaux de CdSe à l'échelle du gramme ayant une faible polydispersité et des formes contrôlées (sphériques, branchées). Les ligands de surface des nanocristaux de CdSe sont échangés par de petites molécules (pyridine, éthanedithiol, phénylènediamine, butylamine, benzènedithiol) afin d'augmenter leur conductivité. L'échange de ligands modifie les niveaux énergétiques des nanocristaux, comme le montrent des études optiques et électrochimiques. Le poly(3-hexylthiophène) déposé sous forme de couches minces présente différents degrés de couplage intermoléculaire et de désordre énergétique selon la méthode de dépôt et le solvant utilisé. Dans les films hybrides, des mesures de diffraction de rayons X en incidence rasante montrent que la structuration cristalline de la matrice organique est modifiée par la présence des nanocristaux. Les mesures de Temps-de-Vol dans les couches hybrides montrent que les mobilités des trous et des électrons varient avec le contenu en nanocristaux, ainsi qu'avec leur forme et leurs ligands. De faibles fractions de nanocristaux provoquent une amélioration de la mobilité des trous, tandis que de plus grandes fractions la détériorent. Les mobilités électroniques sont soumises à une fraction-seuil, assimilable à un seuil de percolation. La fraction optimale de nanocristaux, du point de vue des mobilités des trous et des électrons, est de 36% en volume pour les nanocristaux sphériques avec les ligands de synthèse. Enfin, les simulations Monte-Carlo des courants transitoires photo-générés, dans un échantillon de poly(3-hexylthiophène) et dans un hybride, montrent d'une part que la distribution énergétique du poly(3-hexylthiophène) domine l'allure des courants simulés et d'autre part que les nanocristaux peuvent être assimilés à des sites difficilement accessibles du réseau cubique.

Mots-clés : nanocristaux de semi-conducteurs, polymères π-conjugués, transport de charge, Temps-de-Vol, simulation Monte-Carlo

Charge transport in hybrid films of π-conjugated polymers and semiconductor nanocrystals The aim of this work is the study of photogenerated charge transport in hybrid films composed of π-conjugated polymers and of semiconductor nanocrystals, designed for applications in optoelectronics. Chemical synthesis provides gram-scale samples of CdSe nanocrystals, of low polydispersity and controlled shapes (spherical, branched). In order to enhance their conductivity, the surface ligands of CdSe nanocrystals (stearic acid, oleylamine) are exchanged by smaller molecules, namely pyridine, ethanedithiol, phenylenediamine, butylamine and benzenedithiol. Optical and electrochemical studies show that the ligand exchange modifies the nanocrystals' energy levels. Poly(3-hexylthiophene) thin films exhibit varying degrees of energetical disorder and of intermolecular coupling, depending on the processing method and on the solvent used. In hybrid films, the crystallinity of P3HT, probed by grazing incidence X-ray diffraction, is modified by the presence of nanocrystals. Time-of-Flight measurements of hybrid films show that electron and hole mobilities vary with the content of nanocrystals, with their shape, and with their ligands. Small volume fractions of nanocrystals enhance the hole mobility, and large fractions degrade it. Electron mobilities are percolation-limited: they reach a stable value for a threshold fraction of nanocrystals. The optimal fraction of nanocrystals for electron and hole mobilities is 36 vol% in hybrids made of spherical nanocrystals with their synthesis synthesis ligands. Finally, Monte Carlo simulations of photogenerated current transients in pristine poly(3-hexylthiophene) and in a hybrid sample show on one hand that the energy distribution of poly(3-hexylthiophene) rules the shape of the simulated transients, and on the other hand that nanocrystals can be described as little accessible sites of the hopping lattice.

Keywords : semi-conductor nanocrystals, π-conjugated polymers, charge transport, Time-of-Flight, Monte Carlo simulation